Discovery and Biosynthesis of Novel Bioactive Microbial Natural Products

DISSERTATION

zur

Erlangung des Doktorgrades (Dr. rer. nat.)

der

Fachbereichs Agrarwissenschaften, Ökotrophologie und Umweltmanagement

der

Justus-Liebig-Universität Gießen

vorgelegt von

Lei Wang

Aus

Hubei, P. R. China

Gießen, 2023

Mit Genehmigung des Fachbereichs Agrarwissenschaften, Ökotrophologie und Umweltmanagement der Justus-Liebig-Universität Gießen

1. Gutachter **Professor Dr. Till F. Schäberle**

Institut für Insektenbiotechnologie

Fachbereich Agrarwissenschaften, Ökotrophologie und Umweltmanagement

Justus-Liebig-Universität Gießen

2. Gutachter **Professor Dr. Gerd Hamscher**

Institut für Lebensmittelchemie und Lebensmittelbiotechnologie

Fachbereich Biologie und Chemie

Justus-Liebig-Universität Gießen

Erklärung gemäß der Promotionsordnung des Fachbereichs 09 vom 07. Juli 2004 § 17 (2)

Ich erkläre:

Ich habe die vorgelegte Dissertation selbständig und ohne unerlaubte fremde Hilfe und nur mit den Hilfen angefertigt, die ich in der Dissertation angegeben habe.

Alle Textstellen, die wörtlich oder sinngemäß aus veröffentlichten Schriften entnommen sind, und alle Angaben, die auf mündlichen Auskünften beruhen, sind als solche kenntlich gemacht.

Bei den von mir durchgeführten und in der Dissertation erwähnten Untersuchungen habe ich die Grundsätze guter wissenschaftlicher Praxis, wie sie in der „Satzung der Justus-Liebig-Universität Gießen zur Sicherung guter wissenschaftlicher Praxis“ niedergelegt sind, eingehalten.

_____ _____

Datum Unterschrift

Acknowledgements

First of all, I would like to express my deepest appreciation to Prof. Dr. Till F. Schäberle for giving me this precious opportunity to pursue my doctoral research in such excellent working conditions and good facilities at the Institute for Insect Biotechnology of Justus-Liebig-University Giessen and Fraunhofer Institute for Molecular Biology and Applied Ecology (IME). His patient guidance, scientific advice, profound knowledge, and comprehensive support have greatly helped me successfully complete the research and learn a lot of new knowledge. Moreover, his serious and responsible work attitude, meticulous scientific research spirit, and sincere belief in the pursuit of truth are the models for me to learn throughout my life. It was a great privilege and honour to work and study under his guidance, it is impossible to conclude my work without his encouragement and constructive advice.

I am deeply indebted to Dr. Yang Liu (Institute for Insect Biotechnology, Justus-Liebig-University of Giessen) for introducing me to Prof. Dr. Till F. Schäberle and for her valuable suggestion, fruitful discussion and rich knowledge in the experimental operation, structure elucidation and manuscript preparation, and comprehensive support for my life in Giessen.

My special thanks to thank my former supervisor Prof. Dr. Kun Zou (Hubei Key Laboratory of Natural Products Research and Development, College of Biological and Pharmaceutical Sciences, China Three Gorges University) for his help, support, and generous advice during my study.

I would also like to extend my sincere gratitude to my colleagues in the working group of Prof. Schäberle: Dr. Zerlina Gabriela Wuisan, Dr. Riyanti, Dr. I Dewa Made Kresna, Dr. Ute Mettal, Jil-Christine Kramer and Flaviana C. Susanto for their help and the fruitful scientific discussion.

My deep thanks to Dr. Nils Böhringer and Dr. Luis Linares-Otoya for their help and support in the molecular biology field. Moreover, special thanks to Ms. Alexandra Bender for her kindly help in administrative process and my life in Giessen.

Many thanks should also go to Felix Getzke and Dr. Stéphane Hacquard (Department of Plant Microbe Interactions, Max Planck Institute for Plant Breeding Research) for their productive collaborations.

I would like to say thanks to employees of Fraunhofer Institute for Molecular Biology and Applied Ecology (IME), Dr Michael Marner for his help in the testing antimicrobial activity. Christoph Hartwig for providing valuable assistance in mass spectrometry analysis. Dr. Maria A. Patras for her support in the Marfey's analysis. Dr. Sanja Mihajlovic for providing the fungus strain.

I would like to thank Dr. Heike Hausmann (Justus-Liebig-University Giessen, Germany) for measuring NMR spectra for structure elucidation. I also appreciate Dr.(RUS) Sergei Ivlev (Fachbereich Chemie, Philipps-Universität Marburg) for his help in X-ray crystallographic analyses.

I am extending my thanks to China Scholarship Council for funding my study in Giessen.

In the end, I would like to express my heartfelt thanks to my family for their encouragement, understanding and full support.

Abstract

Natural products derived from microorganisms like bacteria and fungi, are structurally diverse and represent a rich source for the discovery of new drugs to treat various human diseases, including infections and cancer. Many microorganisms derived bioactive compounds have been eventually developed into agents for clinical use. During our continuous research on bioactive secondary/specialized metabolites from microorganisms, the marine flavobacterium *Tenacibaculum discolor* sv11, the plant endophytic bacterium *Pseudomonas brassicacearum* Root401 and the fungus *Palmiascoma qujingense* ST006189 were investigated for their potential to produce specialized metabolites. Obligate marine flavobacteria of the genus *Tenacibaculum* play an important role in marine habitats. However, not much is known about natural products produced by these bacteria. *T. discolor* sv11 was chosen based on antimicrobial activity against *B. subtilis*. The *P. brassicacearum* Root401 genome indicated a high biosynthetic potential to produce specialized metabolites, especially for nonribosomal peptides (NRPs). The bacterium can cause disease in salt-stressed *Arabidopsis thaliana.* The extract of *P. qujingense* ST006189 contains a variety of chromone derivatives as revealed by LC-MS analysis. In this dissertation the focus was on the isolation and identification of bioactive secondary metabolites from the cultures of *T. discolor* sv11, *P. brassicacearum* Root401 and *P. qujingense* ST006189. Furthermore, the antimicrobial activity and virulence in *A. thaliana*, as well as the biosynthetic routes of these metabolites were tested and elucidated in this thesis.

In summary, thirteen new alkaloids were isolated from *T. discolor* sv11. A novel sub group of cyclic lipopeptides was identified from *P. brassicacearum* Root401. Ten compounds were obtained from *P. qujingense* ST006189. The structures of the pure compounds were

unambiguously elucidated on the basis of one- and two-dimensional NMR spectroscopy and mass spectrometry, together with Marfey's analysis and X-ray crystallography. The pure compounds were investigated for their antimicrobial activity against bacteria and fungi. For selected compounds, their anthelmintic activity and virulence in plants was investigated. Putative biosynthetic gene clusters (BGCs), corresponding to the respective isolated compounds, were identified based on the bioinformatics analysis of the whole genome data, and the biosynthetic route was investigated using *in vivo* and *in vitro* experiments.

In advance Publications of the Dissertation

(1) **Wang, L**, Linares-Otoya V, Liu Y, Mettal U, Marner M, Armas-Mantilla L, Willbold S, Kurtán T, Linares-Otoya L, **Schäberle TF**. (**2022**). Discovery and biosynthesis of antimicrobial phenethylamine alkaloids from the marine Flavobacterium *Tenacibaculum discolor* sv11. *Journal of Natural Products*, 85(4), 1039-1051.

(2) **Wang L**, Marner M, Mettal U, Liu Y, **Schäberle TF**. (**2022**). Seven New Alkaloids Isolated from Marine Flavobacterium *Tenacibaculum discolor* sv11. *Marine Drugs,* 20(10), 62.

(3) Getzke F, Hassani A, Crüsemann M, Malisic M, Zhang P, Ishigaki Y, Böhringer N, Jiménez Fernández A, **Wang L**, Ordon J, Ma KW, Wesseler H, Miyauchi S, Garrido-Oter R, Shirasu K, **Schäberle TF**, Hacquard S*, Schulze-Lefert P*. (**2023**). Cofunctioning of bacterial exometabolites drives root microbiota establishment. *Proceedings of the National Academy of Sciences*, 120(15), e2221508120.

(4) Felix Getzke[#], **Lei Wang**[#], Nienke Denissen, Fantin Mesny, Hidde Wesseler, Paul Schulze-Lefert, **Till F. Schäberle**[*], Stéphane Hacquard[*]. Physiochemical interaction between osmotic stress and a bacterial exometabolite promotes plant disease. ([#]co-first author, in revision for *Nature Communications*)

Conference contributions

Wang L., Liu Y., Linares-Otoya V., et al. Antimicrobial Natural Products from *Tenacibaculum discolor* sv11[A]. Biology of Microorganisms Producing Natural Products-International VAAM Workshop 2019, Jena.

Table of Contents

Chapter 1. Introduction

1.1 Natural products in drug discovery

Natural products represent the most promising resource for the detection of novel bioactive chemical scaffolds which are exhibiting structural diversity and multifarious bioactivities (Koehn et al., 2005). Such natural products and their structural analogues have historically made a major contribution to pharmacotherapy (Atanasov et al., 2021), especially for cancer and infectious diseases (Atanasov et al., 2015; Harvey et al., 2015). Of the totally 1881 new approved drugs over the four decades from 1981 to 2019, roughly 40 % of them were unaltered natural products (3.8 %), semisynthetic natural product derivatives (18.9 %), total synthetic drugs which the pharmacophore from a natural product (3.2 %), natural product mimic (11 %) and botanical drug (defined mixture, 0.8 %) (Newman et al., 2020).

Dating from the discovery of penicillin in 1928 by Alexander Fleming (Fleming, 1929), natural products have long been considered as the key source of new drugs against infectious diseases, especially antibiotics (Hutchings et al., 2019; Miethke et al., 2021; Rossiter et al., 2017). As a most successful example of recent years, the natural product antibiotic daptomycin should be named. It is a cyclic lipopeptide that belongs to a class of antibiotics produced by *Streptomyces roseosporus* (Debono et al., 1988; Eliopoulos et al., 1986), which was introduced onto the market in 2003 and now sales more than $1 billion a year (Hutchings et al., 2019). Daptomycin exhibits selectively antimicrobial activity against most Gram-positive organisms (Steenbergen et al., 2005). It is also active against multiple antibiotic-resistant strains including methicillin-resistant *Staphylococcus aureus* (MRSA), vancomycin-resistant *Enterococcus faecium* (VREF), and vancomycin-resistant *Staphylococcus aureus* (VRSA) (Jevitt et al., 2003). Another example is Fidaxomicin, which is a

narrow-spectrum macrocyclic antibiotic isolated from the fermentation broth of *Dactylosporangium aurantiacum* subspecies *hamdenensis* (Hochlowski et al., 1987). It has been approved by the FDA for the treatment of *Clostridium difficile* infection (CDI) in 2011 (Venugopal et al., 2012). This compound showed strong activity against *Clostridium difficile* with minimum inhibitory concentration (MIC) ranging from 0.001 to 1 μg/mL (Goldstein et al., 2012). Fidaxomicin works as an inhibitor of the initiation of bacterial RNA synthesis to block the initiation only if it binds to its target before the formation of the "open promoter complex," in which the template DNA strands have separated but RNA synthesis has not yet begun (Artsimovitch et al., 2012).

Homoharringtonine, a plant cephalotaxus alkaloid from *Cephalotaxus* species, was long time investigated by Chinese researchers from the 1970s on as an active anticancer agent in acute myeloid leukemia (AML) (Cephalotaxus Research Coordinating Group, 1976; Liu et al., 2009; Zhang, 1981), myelodysplastic syndrome (MDS) (Wu et al., 2009), acute promyelocytic leukemia (APL) (Ye et al., 1988), polycythemia vera (Lu et al., 1983), and as intrathecal therapy for central nervous system (CNS) leukemia (Hou et al., 1981). Over 40 years, a semisynthetic homoharringtonine compound, omacetaxine mepesuccinate, has been studied and was approved in 2012 by the FDA for patients with chronic myeloid leukemia (CML) refractory to treatment or intolerant to two or more tyrosine kinase inhibitors (Winer et al., 2018). Plitidepsin is an unmodified marine natural product, which was approved in Australia for the treatment of multiple myeloma (Gomes et al., 2020). It most likely acts by binding to the target eukaryotic Elongation Factor 1A2 (eEF1A2) to exert its antitumor activity (Losada et al., 2016). Besides the treatment of cancer, homoharringtonine and plitidepsin also showed potent preclinical efficacy against SARS-CoV-2 (Chen et al., 2021; White et al., 2021). The safety and pharmacokinetic data for them are

already available and renders these drugs candidates for repurposing approaches, since this should help to expedite the human clinical trials designed to combat active COVID-19 infection.

Additional to those antibacterial and anticancer agents, many other important drugs, such as the multiple sclerosis agents siponimod (Scott, 2020) and fingolimod (Brinkmann et al., 2010), the antidiabetic drugs voglibose (Kawamori et al., 2009) and acarbose (Laube, 2002), as well as the hypolipidemic agents pravastatin (Jungnickel et al., 1992), lovastatin (Illingworth, 1994) and its semisynthetic analog simvastatin (Singh et al., 2017), are natural products per se or are derived from natural products.

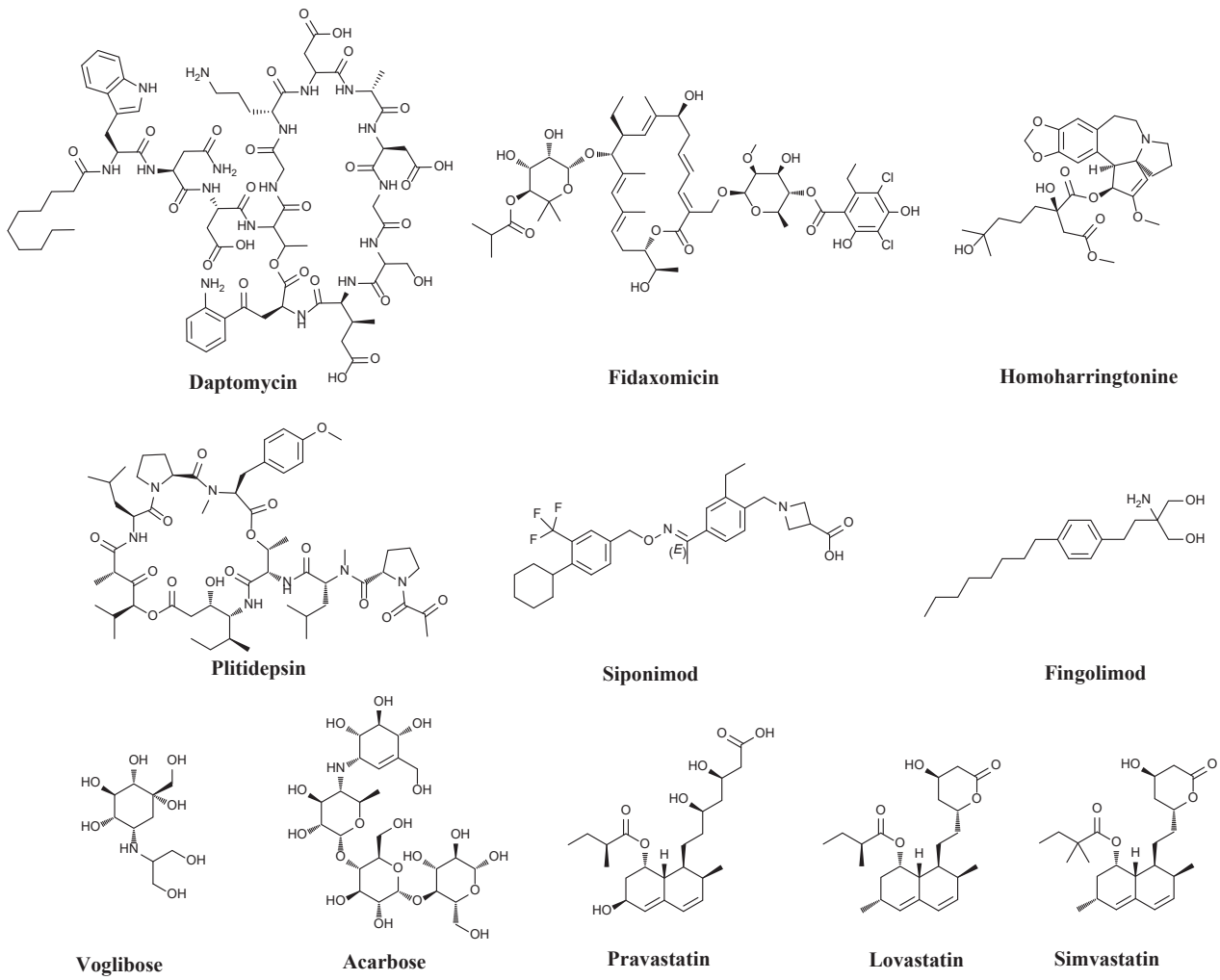

Figure 1.1 Chemical structures of selected drugs of natural origin in clinical use.

The fact that a huge number of natural products or natural product-derived compounds have been introduced to the market or are in clinical trials can highlight the existing viability and significance of the use of natural products as source of new drug candidates (Veeresham, 2012); obviously, natural products will always remain the most important source of future drug discovery (Cragg et al., 2013; Newman, 2019). Meanwhile, with the continuing development of novel technologies such as DNA sequencing, genomics/metagenomics, synthetic biology, genome editing technologies, computational biology techniques, and artificial intelligence, the discovery of new natural products and the development of new drugs are greatly accelerated (Atanasov et al., 2021; Thomford et al., 2018; Zhang et al., 2017).

1.2 Bacteria and fungi as important source of bioactive compounds

Bacteria and fungi, which account for the second and third most of the biomass next to plants on Earth, respectively, have been always considered as a valuable source of bioactive natural products (Bar-On et al., 2018; Bills et al., 2016; Sekurova et al., 2019). Microorganisms produced around 10% (around 22 000) of bioactivity natural products, of which around 62% (about 17% are metabolites of unicellular bacteria and 45% are products of actinomycetes fermentation) were produced by bacteria and 38% were produced by fungi (Solecka et al., 2012). These natural products play an important role in lead discovery and drug development against human diseases, such as infections, cancer and immune system-related diseases (Sekurova et al., 2019).

The order of filamentous actinomycetales produces about 10,100 (45%) bioactive microbial compounds, thereunder about 75% (7,600) derived from *Streptomyces* and 25% (2,500) from the so called rare actinomycetes (rare actinos), which represents the largest group of bioactive

microbial metabolites (Solecka et al., 2012). One of the most famous bioactive metabolites obtained from actinomycetales is streptomycin, an aminoglycoside antibiotic, which was first discovered by Selman Abraham Waksman and introduced to clinical use for the treatment of tuberculosis (Schatz et al., 1944). Together with his co-worker H. Boyd Woodruff, Waksman also discovered actinomycin D from a soil *Actinomyces*, which has been used as an anticancer drug, particularly in the treatment of Wilms' tumor and soft tissue sarcomas in children for more than 50 years (Waksman et al., 1940; Wang et al., 2017). Bleomycin is an anticancer drug currently used in the treatment of head and neck squamous cell carcinoma, Hodgkin and non-Hodgkin lymphomas, testicular carcinoma. It is a water soluble glycopeptide produced by *Streptomyces verticillus*, which is always associated with many other drugs in the clinical use (Mir et al., 1996; Umezawa et al., 1967). Mitomycin C was isolated from the broth of *Streptomyces caespitosus.* This drug has been approved for treatment of cancers of the bladder, head and neck, lungs, breast, cervix, colon and rectum, hepatic cell carcinoma and melanoma in addition to stomach and pancreatic (Bradner, 2001). Besides the use in the cancer treatment, mitomycin C was also widely used as a chemotherapeutic agent in glaucoma filtration surgery (Wolters et al., 2021). Tetracyclines are a class of compounds bearing the same octahydrotetracene-2-carboxamide skeleton, which are either isolated directly from several species of *Streptomyces* or produced semi-synthetically from those natural compounds. As an important class of antibiotics, tetracyclines were used widely in the prophylaxis and therapy of human and animal infections due to their wide range of activity against Gram-positive and Gram-negative bacteria, chlamydiae, mycoplasmas, rickettsiae and protozoan parasites. The most recently approved tetracyclines are tigecycline and omadacycline, which were approved by the FDA in 2005 and 2018, respectively (Burgos et al., 2019; Chopra et al., 2001; Pankey, 2005). The anthracyclines are a class of antitumor drugs

extracted from *Streptomyces* with the widest spectrum of activity in human cancers, and only a few cancers (e.g., colon cancer) are unresponsive to them. Doxorubicin reigns in this drug class as the one having the most proven cancerocidal effect at present (Venkatesh et al., 2019). Rapamycin, also known as sirolimus, is a macrolide isolated from *Streptomyces hygroscopicus* and used as immunosuppressive agent to prevent organ transplant rejection. This drug is also used to treat (Wagner et al., 2021) a rare lung disease called lymphangioleiomyomatosis (Landh et al., 2022; Mahalati et al., 2001; Vezina et al., 1975). Streptozotocin was discovered from the fermentation broth of *Streptomyces achromogenes* in 1959 and approved by the FDA for the treatment of pancreatic neuroendocrine tumors (panNETs) in 1982. 40 years after its approval, this agent remains one of the first-line treatment of patients with panNETs (Capdevila et al., 2022). Other than the clinical use, streptozotocin also has been used for inducing insulitis and diabetes on experimental animals and for modeling Alzheimer's disease through memory loss in mice (Costa et al., 2016; Furman, 2015; Rossini et al., 1977).

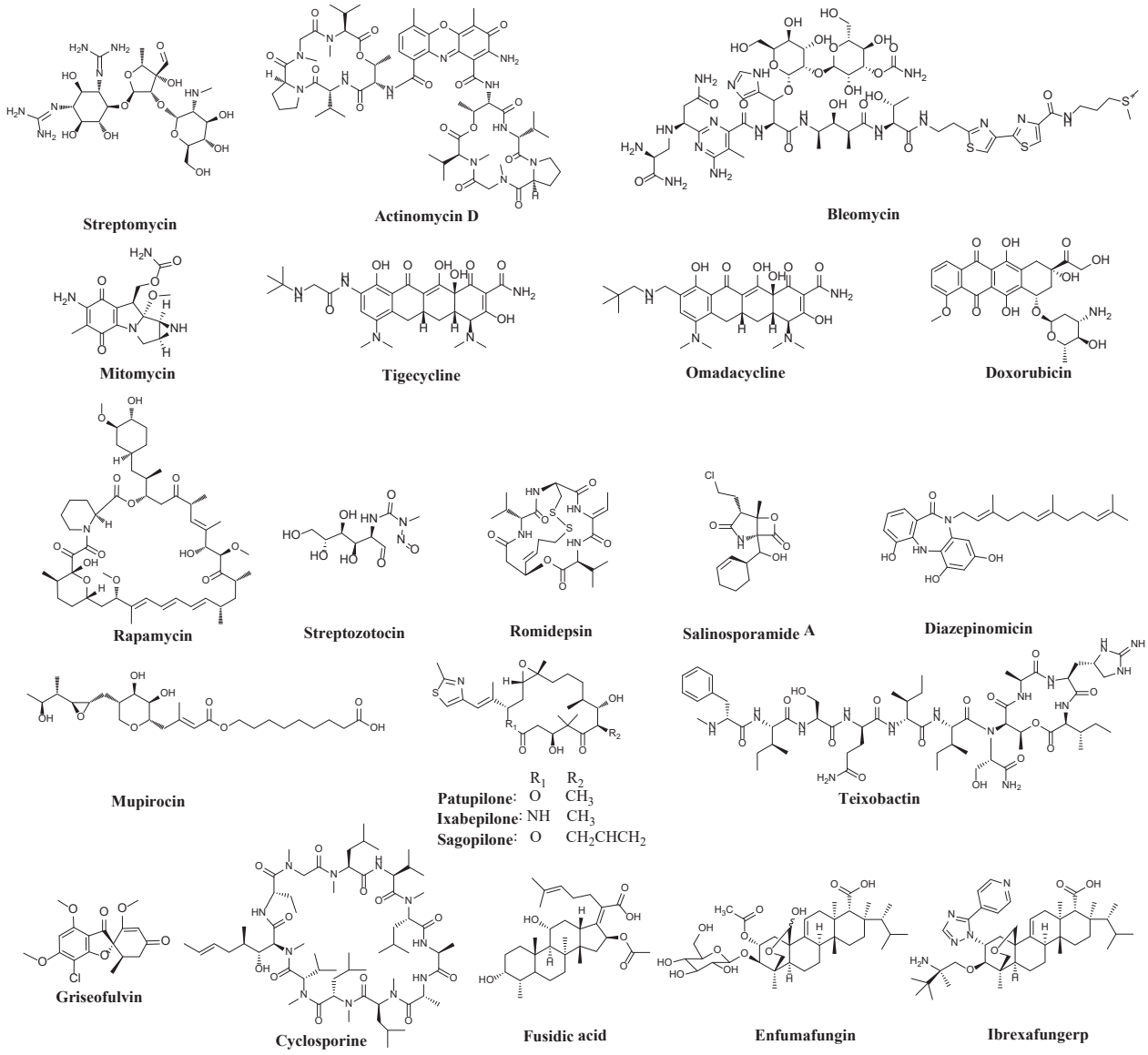

Figure 1.2 Chemical structures of selected natural products originated in bacteria.

Except for those important drugs developed from *Streptomyces*, other bacteria also produce a lot of bioactive compounds. These natural products or their derivatives have been introducedto the market or are in clinical trials, these include, but are by no means limited to, romidepsin, salinosporamide A, diazepinomicin, mupirocin, patupilone and its synthetic derivative ixabepilone and sagopilone. Romidepsin is a histone deacetylase inhibitor isolated from *Chromobacterium violaceum* and used for the treatment of adult patients with cutaneous T-cell lymphoma (CTCL)

or peripheral T-cell lymphoma (PTCL) (Shigematsu et al., 1994; Ueda, Manda, et al., 1994; Ueda, Nakajima, et al., 1994; Yang, 2011). Salinosporamide A is a potent proteasome inhibitor isolated from a marine bacterium *Salinispora tropica* CNB-392in 2003 (Feling et al., 2003), which entered in human clinical trials for the treatment of multiple myeloma and newly diagnosed glioblastoma (Badros et al., 2017; Bota et al., 2021; Roth et al., 2021). Diazepinomicin is a dibenzodiazepine alkaloid originally isolated from marine *Micromonospora* strain DPJ12 (Charan et al., 2004). It was generally safe and well tolerated in a Phase II trial in patients with Glioblastoma Multiforme (Mason et al., 2010). Mupirocin, a topical antibiotic agent isolated from *Pseudomonas fluorescens* and used in the treatment of impetigo caused by *Staphylococcus aureus* and *Streptococcus pyogenes* and traumatic skin lesions due to secondary skin infections caused by *S. aureus* and *S. pyogenes* (Lamb, 1991). Patupilone is produced by a myxobacterial *Sorangium cellulosum* strain (Conlin et al., 2007). A Phase III study by Novartis to assess the ability of patupilone to extend the survival time and potential beneficial effects in women who have nonresponsive or recurrent ovarian, primary fallopian, or primary peritoneal cancer was completed in 2010, while it has not yet been approved for clinical use (Colombo et al., 2012). Ixabepilone is a semi-synthetic analog of patupilone, which has been approved for use as a monotherapy or in combination with capecitabine for the treatment of metastatic or locally advanced breast cancer after failure of an anthracycline and a taxane therapy (Ibrahim, 2021). Sagopilone is another synthetic derivative of patupilone, which has completed a Phase II study for the treatment of patients with recurrent malignant gliomas (Silvani et al., 2009).

Fungal secondary metabolites also have revolutionized medicine, yielding blockbuster drugs and drug leads of enormous therapeutic potential. Hence, a series of structural diverse bioactive metabolites has played a vital role in the pharmaceutical industry. An example is griseofulvin that

is derived from the mold *Penicillium griseofulvum* and has been in clinical use for treatment of fungal infections of the skin, hair, and nails. It acts by binding to tubulin, interfering with microtubule function, thus inhibiting mitosis (Grove et al., 1952; Gull et al., 1973). Recently, griseofulvin has attracted renewed attention due to reports of complementary bioactivity including antiviral and anticancer effects (Jin et al., 2008; Rebacz et al., 2007). Cyclosporine is a peptide composed of 11 amino acids, which was first isolated from the soil fungus *Tolypocladium inflatum Gams* in 1972 (Borel et al., 1995). It is used as an immunosuppressant in organ and tissue transplantation surgery, to prevent rejection following bone marrow, kidney, liver and heart transplantations (Cohen et al., 1984; Tribe, 1998). Fusidic acid was isolated for the first time in 1962 from the fermentation broth of *Fusidium coccineumis* (Godtfredsen et al., 1962), it is a steroid-like antibiotic, which is active against resistant bacterial strains, including penicillin-, methicillin-, ampicillin- and cloxacillin-resistant *Staphylococcus aureus* (Bonamonte et al., 2014; Long, 2008). In addition, it shows *in vitro* activity against many Gram-positive bacteria, including *Nocardia* spp., *Mycobacteriumn tuberculosis*, *Neisseria* spp. and some anaerobic bacterial pathogens (Akinpelu et al., 2020; Black et al., 1971; Canzi et al., 1987; Collignon et al., 1999). Due to its strong antibiotic activity, fusidic acid was introduced to the market with a variety of formulations for oral, intravenous and topical use (Turnidge, 1999). Enfumafungin is a triterpene glycoside natural product produced by the fungus *Hormonema carpetanum*, which was found to have potent antifungal activity *in vitro* (Kuhnert et al., 2018; Peláez et al., 2000; Schwartz et al., 2000). However, it showed limited stability *in vivo*. Semi-synthetic modification of enfumafungin resulted in improvement of oral bioavailability and PK properties; thereby, leading to the discovery of ibrexafungerp, which was approved for medical use in 2021 for the treatment of vulvovaginal

candidiasis and considered to be a first-in-class medication (Gamal et al., 2021; Lee, 2021; Phillips et al., 2023).

Traditionally, novel compounds produced by bacteria and fungi were discovered via conventional bioprospecting based on isolation of potential producers and screening their bioactivities, which lead to the rediscovery of known compounds over and over again. However, there is an increasing demand for new lead structures due to the global antibiotic resistance crisis and the side effects of many approved agents. One approach to tackle this challenge is mining the potential of uncultured environmental microbes, which were previously unknown or unculturable to produce bioactive secondary metabolites (Liu et al., 2022; Sekurova et al., 2019).The discovery of teixobactin is a good example in which a novel approach was used to mine the potential of previously unculturable bacteria. Teixobactin is a peptide isolated from *Eleftheria terrae* with activity against Gram-positive organisms. The producer strain was isolated using a new tool, the iChip which allows to place individual bacterial cells from environmental samples into specially designed diffusion chambers (Ling et al., 2015). The future for scientists to discovery novel drug candidates from unknown or unculturable bacteria and fungi looks bright due to the high genetic potential of those bacteria to produce secondary metabolites (Crits-Christoph et al., 2018; Paoli et al., 2022; Scherlach et al., 2021; Wiemann et al., 2014).

1.3 Nitrogen-containing heterocycles is a special and important class of bioactive compounds

Nitrogen-containing heterocycles are a class of structurally diverse small molecules that can be commonly encountered in natural products and these natural products and their derivatives are often found to show diverse significant biological activities (Ebenezer et al., 2022; Jin, 2016).

Besides for their structural and biological activities diversity, nitrogen-containing scaffolds also showed their amenability to semi-synthesis, total-synthesis and further structural modification (Henary et al., 2020). Many of these naturally occurring heterocycles and their derivatives have gained special attention with a remarkable history of therapeutic applications.

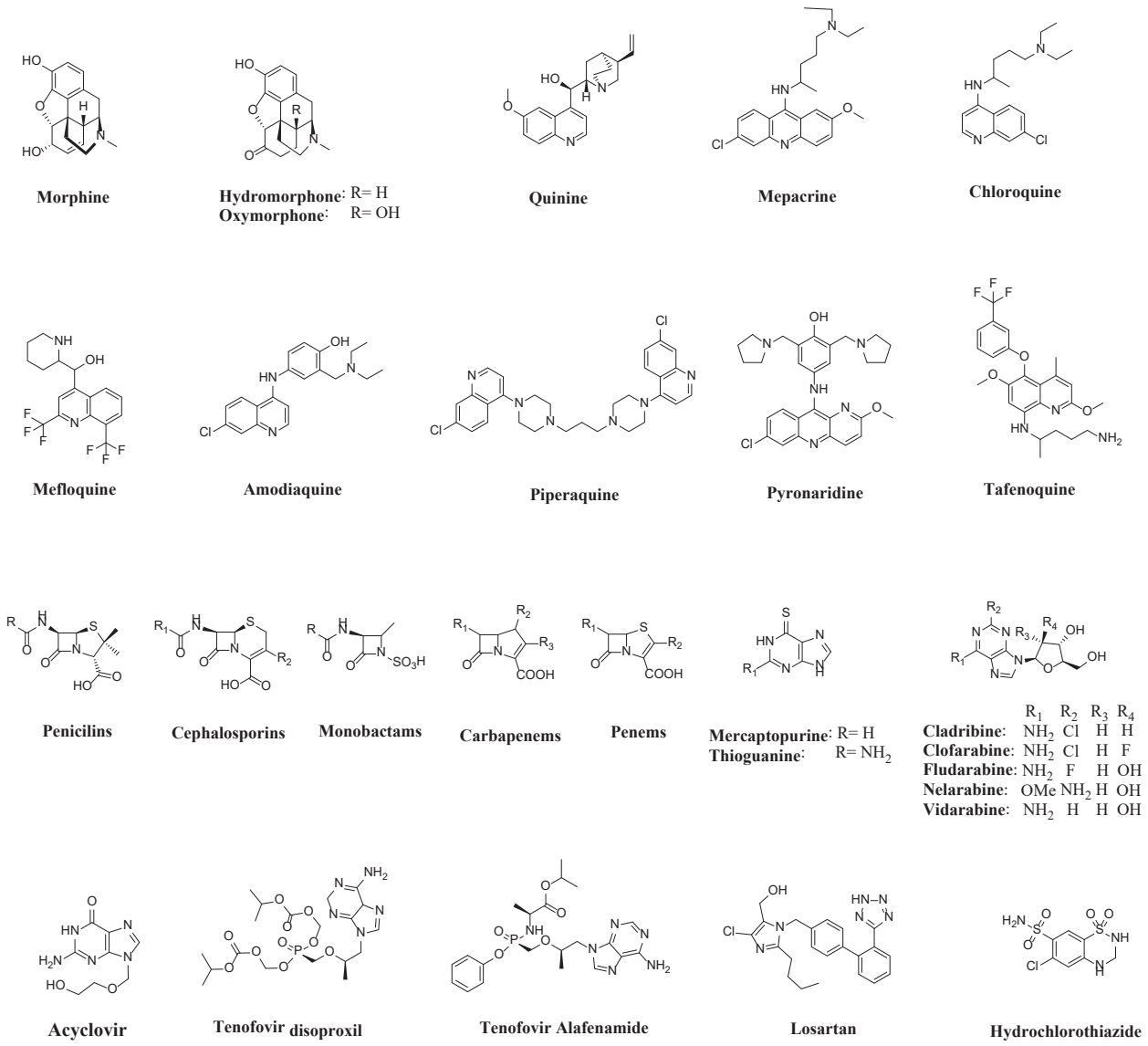

Figure 1.3 Chemical structures of selected nitrogen-containing heterocycles in clinical use.

One of such famous compounds is the well-known compound morphine, which is bearing a piperidine ring and was mainly used as analgesic since 1827. It is generally considered to be the

first active natural product from plants, which was isolated as pure compound - already in 1804 (Joule, 2016). Another famous plant plant-derived natural product, which has a long history in clinical use is quinine, an alkaloid with a quinoline moiety which that remains an important anti-malarial drug almost 400 years after its effectiveness was first documented (Achan et al., 2011). Since the isolation of quinine in 1820, a number of other natural and synthetic quinoline-containing heterocycles have been developed as anti-malarial drugs, they are e.g. mepacrine, chloroquine, mefloquine, amodiaquine, piperaquine, pyronaridine and tafenoquine (Tse et al., 2019). The classes of β-lactam antibiotics, in which the nitrogen atom is attached to the β-carbon atom relative to the carbonyl are preeminent in the treatment of bacterial infection due to their unparalleled clinical efficacy and clinical safety. Following the discovery of the penicillin, a serious of β-lactam antibiotics has been introduced to therapy. They are classified into the following families based on the chemical nature of the ring fused to the β-lactam pharmacophore unit: penicillins family, cephalosporins family, monobactams family, carbapenems family and penems family (Lima et al., 2020). These antibiotic agents have evolved over the last 70 years and remain one of the most commonly prescribed drug classes (Turner et al., 2022). It has been calculated that the annual expenditure for these antibiotics amounts to approximately $15 billion USD, and it makes up 65% of the total antibiotics market (Thakuria et al., 2013).

Purine analogs are an important class of drugs, all of the purine drugs are either approved as anticancer or antiretroviral agents (Vitaku et al., 2014). These agents, such as mercaptopurine, thioguanine, cladribine, clofarabine, fludarabine and nelarabine, display high efficacy in the treatment of hematological malignancies, especially in chronic lymphocytic leukemia (CLL) and low-grade non-Hodgkin’s lymphomas (LG-NHL) (Robak et al., 2005). Vidarabine and acyclovir are used in the treatment of varicella-zoster virus (VZV) infection (Miwa et al., 2005). Tenofovir

disoproxil and tenofovir alafenamide are newer, more tolerable, nucleotide reverse transcriptase inhibitors for the treatment of HIV infection and are used in combination with other drugs, such as emtricitabine, lamivudine, elvitegravir and cobicistat (Wassner et al., 2020). Sartans are a class of Angiotensin II type 1 receptor antagonists (ARBs), which were introduced in the treatment of cardiovascular diseases. These agents are used alone or in combination with other classes of antihypertensives for the treatment of hypertension and are used in the treatment of diabetic nephropathy ion hypertensive patients with type 2 diabetes mellitus, as well as in the treatment of congestive heart failure (Muszalska et al., 2014). Losartan is the prototype of this class of drugs, which was approved in 1995. Thiazide diuretics are another important class of tolerated efficient antihypertensive drugs. These diuretics effectively decrease blood pressure in hypertensive patients, and reduce in adults with hypertension the risk of adverse cardiovascular outcomes (Blowey, 2016). Among them, hydrochlorothiazide is the most common used thiazide diuretic in the treatment of primary hypertension. It has been used clinically for more than half a century and is relatively very safe (Herman et al., 2021).

The number of nitrogen-containing heterocycles applied in medicine is growing daily and their diverse analogs provide a viable and important path for the discovery of drugs with various biological applications. Therefore, a large amount of work has been made towards N-heterocyclic skeleton medicinal chemistry (Kerru et al., 2020). According to the in-depth analysis of Jon's Group based on the database of all U.S. FDA approved pharmaceuticals, 59% (640) of unique small-molecule drugs (1035) contain at least one nitrogen heterocycle (Vitaku et al., 2014). Research and development of nitrogen-containing heterocycles in medicinal chemistry has become and will still be a rapidly developing and increasingly active topic.

1.4 Mining the biosynthetic potential as a promising strategy to enlarge the repertoire of bioactive compounds

Traditionally, natural products were isolated from microbes and plants mainly by bioactivity-guided approaches. However, in the last decades it became more challenging to detect novel compounds, since re-discovery rates of the known metabolites increased (Katz et al., 2016). The search for novel drugs turned to chemical synthesis and modification of known structures. Initially, the success rates were high; however, antibiotics represent a special case, since no new compound that entered the market was identified by this approach (Geers et al., 2021; Shoichet, 2004). On the other hand, many drugs currently in use are losing their efficacy due to resistance development (Davies et al., 2010). Therefore, there is still an unmet need for novel lead structures. Therefore, beside bioactivity-guided approaches, other promising strategies must be employed to enlarge the repertoire of bioactive compounds: One is mining the biosynthetic potential of microorganisms.

The progress in sequencing technologies enabled us to get insights into the biosynthetic potential of bacteria, fungi and even higher organisms to produce specialized metabolites. It became clear that the genetic potential is much larger than what is observed under laboratory conditions (Scherlach & Hertweck, 2021). Activating the expression of biosynthetic gene clusters (BGCs), which are silent under standard laboratory growth conditions is important to achieve the full potential for the discovery of novel microbial natural products. For this purpose, pleiotropic methods have been developed, including variation of growth conditions, engineering the transcription and translation machinery, manipulating global regulators and epigenetic perturbation, together with different pathway-specific methods such as manipulating pathway-

specific regulators, reporter-guided mutant selection, refactoring and heterologous expression (Rutledge et al., 2015).

Historically, microorganisms from the soil (especially soil-derived actinobacteria, see above) played an important role in the drug discovery which led the "Golden era of antibiotic discovery", while most of these drugs are derived from a few microbial taxa, the biosynthetic potential of the vast majority of bacteria in soil has rarely been investigated (Geers et al., 2021). Genome-mining based on the construction and screening of complex libraries derived from the soil metagenome provides opportunities to fully explore and exploit the enormous genetic and metabolic diversity of soil microorganisms (Daniel, 2004). Alexander and his co-workers reconstructed hundreds of near-complete genomes from grassland soil metagenomes and identify microorganisms including the newly identified members of the *Acidobacteria*, *Verrucomicobia* and *Gemmatimonadetes*, and the candidate phylum *Rokubacteria* from previously understudied phyla, large numbers of biosynthetic genes were characterized in these newly identified members (Crits-Christoph et al., 2018). Apart from soil microorganisms, the ocean microorganisms also possess high biosynthetic potential. Lucas et al. investigated the diversity and novelty of biosynthetic gene clusters in the ocean by integrating around 10,000 microbial genomes from cultivated and single cells with more than 25,000 newly reconstructed draft genomes from more than 1,000 seawater samples, Their research revealed approximately 40,000 putatively new biosynthetic gene clusters, several of which were found in previously unsuspected phylogenetic groups (Paoli et al., 2022).

Advances in genomics and bioinformatics will reinvigorate the natural product research from bioactivity-guided strategy to genome-guided strategy. A huge number of novel chemical scaffolds has been and will be discovered through mining the biosynthetic potential hidden in the silent BGCs and both culturable and unculturable microorganisms. There will be a golden age of

genomics-driven drug and agrochemical discovery with the ongoing development of innovative culturing methods, efficient genome sequencing and editing, and optimized expression systems, along with more sensitive chemical analytics.

Chapter 2. Publication 1

Discovery and Biosynthesis of Antimicrobial Phenethylamine Alkaloids from the Marine Flavobacterium *Tenacibaculum discolor* sv11

Lei Wang, Virginia Linares-Otoya, Yang Liu,* Ute Mettal, Michael Marner, Lizbeth Armas-Mantilla, Sabine Willbold, Tibor Kurtán, Luis Linares-Otoya,* and Till F. Schäberle*

J. Nat. Prod. 2022, 85, 1039−1051

In this chapter, we investigated *T. discolor* sv11, a marine flavobacterium isolated from seaweed *Chandracanthus chamisoii* collected from the Huanchaco estuarine region located at Paracas Bay in Peru, to produce antimicrobial metabolites. We described the bacterial strain isolation and bioactivity-guided compound purification, as well as the structure elucidation and antimicrobial activity of isolated compounds. We also investigated the biosynthetic route toward two new imidazolium-containing alkaloids named discolins A and B, using *in vivo* and *in vitro* experiments. Furthermore, the proposed biosynthetic pathway of other isolated compounds is discussed.

In summary, 26 strains belonging to four different *Tenacibaculum* species were isolated from the seaweed *Chandracanthus chamisoii* from the Huanchaco estuarine region and Paracas Bay, Peru. Initial screening for antimicrobial activity revealed that the culture of *T. discolor* sv11 displayed strong inhibitory activity against *Bacillus subtilis* JH642. *T. discolor* sv11 was selected for culture optimization and bioactivity-guided isolation that enabled the identification of six new

phenethylamine (PEA)-containing alkaloids: discolins A and B, dispyridine, dispyrrolopyridine A-B and dispyrrole. Their antimicrobial activity was investigated against bacteria (*Bacillus subtilis* DSM10, *Mycobacterium smegmatis* ATCC607, *Listeria monocytogenes* DSM20600, *Staphylococcus aureus* ATCC25923, and *Escherichia coli* ATCC25922 wild type and efflux pump deficient ΔtolC strain), against fungi (*Candida albicans* FH2173 and *Aspergillus flavus* ATCC9170), and anthelmintic activity against the model organism *Caenorhabditis elegans* N2. Among them, discolin A and discolin B showed moderate activity against *B. subtilis* and *M. smegmatis* with MIC values ranging from 8 µg/mL to 32 µg/mL. Dispyrrolopyridine A and dispyrrolopyridine B exhibited strong activity against all tested gram-positive indicator strains (i.e., *B. subtilis*, *M. smegmatis*, *L. monocytogenes* and *S. aureus*) with MIC values ranging from 0.5 µg/mL to 4 µg/mL and moderate activity against the yeast *C. albicans* and the spore forming mold *A. flavus* (MIC values from 1 µg/mL to 16 µg/mL). Dispyrrole showed antibacterial activities against all tested gram-positive bacteria with MIC values from 4 µg/mL to 8 µg/mL. Furthermore, dispyrrolopyridine A was also active against *E. coli* ATCC25922 *ΔtolC* (8 µg/mL), while the wild type strain was not inhibited at the highest tested concentration. Moreover, dispyrolopyridine A was also the only tested metabolite possessing bioactivity against *C. elegans* N2 with a MIC value of 32 µg/mL. Dispyridine was inactive against the all the tested microorganisms.

The *in vivo* (heterologous expression) and *in vitro* (enzymatic reactions) experiments indicated that PEA was an intermediate building block in the biosynthesis of discolin A and discolin B. It comprises an enzymatic decarboxylation of phenylalanine to PEA, catalyzed by the decarboxylase DisA, followed by a non-enzymatic condensation to form the central imidazolium ring. This spontaneous formation of the imidazolium core was verified by means of a synthetic one pot reaction using the respective building blocks.

JOURNAL OF NATURAL PRODUCTS

pubs.acs.org/jnp Article

Discovery and Biosynthesis of Antimicrobial Phenethylamine Alkaloids from the Marine Flavobacterium *Tenacibaculum discolor* sv11

Lei Wang, Virginia Linares-Otoya, Yang Liu,* Ute Mettal, Michael Marner, Lizbeth Armas-Mantilla, Sabine Willbold, Tibor Kurtán, Luis Linares-Otoya,* and Till F. Schäberle*

Cite This: *J. Nat. Prod.* 2022, 85, 1039−1051 Read Online

ACCESS | Metrics & More | Article Recommendations | Supporting Information

ABSTRACT: The bacterial genus *Tenacibaculum* has been associated with various ecological roles in marine environments. Members of this genus can act, for example, as pathogens, predators, or episymbionts. However, natural products produced by these bacteria are still unknown. In the present work, we investigated a *Tenacibaculum* strain for the production of antimicrobial metabolites. Six new phenethylamine (PEA)-containing alkaloids, discolins A and B (**1** and **2**), dispyridine (**3**), dispyrrolopyridine A and B (**4** and **5**), and dispyrrole (**6**), were isolated from media produced by the predatory bacterium *Tenacibaculum discolor* sv11. Chemical structures were elucidated by analysis of spectroscopic data. Alkaloids **4** and **5** exhibited strong activity against Gram-positive *Bacillus subtilis* DSM10, *Mycobacterium smegmatis* ATCC607, *Listeria monocytogenes* DSM20600, and *Staphylococcus aureus* ATCC25923, with minimum inhibitory concentration (MIC) values ranging from 0.5 to 4 μg/mL, and moderate activity against *Candida albicans* FH2173 and *Aspergillus flavus* ATCC9170. Compound **6** displayed moderate antibacterial activities against Gram-positive bacteria. Dispyrrolopyridine A (**4**) was active against efflux pump deficient *Escherichia coli* ATCC25922 Δ*tolC*, with an MIC value of 8 μg/mL, as well as against *Caenorhabditis elegans* N2 with an MIC value of 32 μg/mL. Other compounds were inactive against these microorganisms. The biosynthetic route toward discolins A and B (**1** and **2**) was investigated using *in vivo* and *in vitro* experiments. It comprises an enzymatic decarboxylation of phenylalanine to PEA catalyzed by DisA, followed by a nonenzymatic condensation to form the central imidazolium ring. This spontaneous formation of the imidazolium core was verified by means of a synthetic one-pot reaction using the respective building blocks. Six additional strains belonging to three *Tenacibaculum* species were able to produce discolins, and several DisA analogues were identified in various marine flavobacterial genera, suggesting the widespread presence of PEA-derived compounds in marine ecosystems.

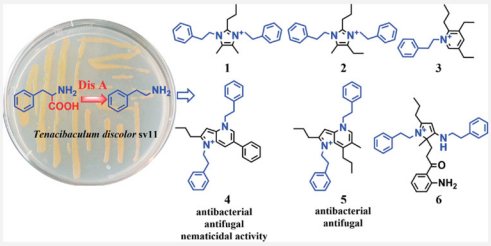

Marine bacteria have already proven themselves as a promising source of novel bioactive molecules with great potential for application in pharmaceutical and biotechnological industries.[1] For instance, the actinobacterial genus *Salinispora* has been recognized as a great producer of bioactive compounds including salinosporamide A, a potential anticancer agent currently undergoing phase I human clinical trials.[2] Other taxa such as *Proteobacteria* (e.g., *Pseudoalteromonas*,[3] *Myxobacteria*,[4] *Phaeobacter*[5]) and cyanobacteria[6] were also reported as producers of dozens of diverse bioactive specialized metabolites.

In the last years, there has been increasing evidence for the relevant role of marine bacteria belonging to the Bacteroidetes phylum in the chemical ecology of the oceans.[7] Besides their contribution to the nutrient cycling and degradation of complex polymers,[7] their role as mediators of different interorganismic interactions has been highlighted.[8] For instance, marine flavobacterial strains belonging to the *Euzebyella*[9] (annotated as *Cytophaga* sp.) and *Maribacter*[10] genera produce thallusin, a morphogenetic sesquiterpene that induces thallus differentiation in macroalgae, e.g., germination of the green *Ulva* algae even at picomolar concentrations.[10] The flavobacterial strain *Candidatus Endobryopsis kahalalidefaciens* is an obligate endosymbiont of the green algae genus *Bryopsis*. This bacterium produces several cytotoxic peptides, i.e., the kahalalides,[11] that are later ingested and accumulated by the mollusk *Elysia rufescens*, which uses it for its own chemical defense.

Received: December 10, 2021
Published: April 13, 2022

https://doi.org/10.1021/acs.jnatprod.1c01173
J. Nat. Prod. 2022, 85, 1039−1051

Obligate marine flavobacteria belonging to the genus *Tenacibaculum* have been isolated ubiquitously from the surface of larger organisms such as sea squirt,[12] fish,[13] algae, and sponge.[14] It has been reported as the etiologic agent of tenacibaculosis, a disease that affects several fish species and causes serious economic losses for the fish industry.[15] It was also connected to a recent outbreak of the sea star wasting disease (SSWD), one of the largest marine epizootics in history.[16] In addition, the genus *Tenacibaculum* exhibits an epiphytic predatory behavior against several marine bacterial strains.[17]

Despite this impact on marine habitats, not much is known about natural products produced by these bacteria. In the present work, we investigated the potential of *Tenacibaculum discolor* sv11 for the production of antimicrobial metabolites. For this purpose, an isolation project was carried out using samples of the seaweed *Chandracanthus chamisoii* collected from the Huanchaco estuarine region and Paracas Bay, Peru. Therefrom, a collection of 26 strains belonging to four different *Tenacibaculum* species was obtained. Initial screening for antimicrobial activity revealed that over half of the strains produced compounds with inhibitory activity. *T. discolor* sv11 was selected for culture optimization and bioactivity-guided isolation that enabled the identification of new alkaloids **1**−**6**, of which compounds **4**−**6** showed promising bioactivity. Furthermore, the biosynthetic basis for the production of these molecules was investigated.

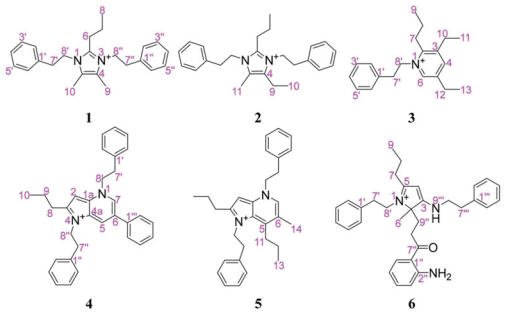

RESULTS AND DISCUSSION

Bacterial Strain Isolation and Bioactivity-Guided Compound Purification. Overall, 450 axenic bacterial strains were obtained in a bacteria strains isolation campaign. Samples were collected from the Huanchaco estuarine region (dominated by the seaweed *C. chamisoii*) and a sand beach located at Paracas Bay, Peru. From these isolates, 32 strains were selected based on the iridescent pattern characteristic of several flavobacterial genera.[18] The identification of selected strains by 16S rRNA gene sequencing confirmed that 26 strains belonged to the *Tenacibaculum* genus (*T. discolor*, *T. mesophilum*, *T. litoreum*, and *T. ascidiacicola*).

First, activity screening was performed using ethyl acetate (EtOAc) extracts of the cultures. In an agar diffusion test, 15 out of 26 strains showed antimicrobial activity against several Gram-positive test strains (i.e., *Micrococcus luteus* ATCC4698, *Bacillus subtilis* JH642, and *Bacillus megaterium* DSM32). Among the most active isolates, *T. discolor* sv11 was chosen for culture optimization, e.g., using different media (n = 3) and variable times of growth (1−10 days). The highest activity against *B. subtilis* was observed after cultivation in LB medium prepared with artificial seawater and supplemented with trace elements and vitamin B_{12}.

On the basis of these results, *T. discolor* sv11 was cultivated on a large scale (36 L) at 30 °C and 180 rpm for 8 days. It was subsequently extracted with EtOAc to yield 11.9 g of crude extract. By activity-guided isolation, the crude extract was subjected to chromatographic purification, using first reversed-phase silica gel and Sephadex LH-20, followed by semi-preparative high-performance liquid chromatography (HPLC) to yield six new minor constituents.

Structure Elucidation. Compound **1** was obtained as a colorless oil. The UV absorption (λ_{max} 280 nm) was attributable to substituted aromatic chromophores. According to the ^{1}H NMR and correlated spectroscopy (COSY) spectra, hydrogen signals at δ_H 7.32 and δ_H 7.19 ppm were connected to aromatic rings (Table 1). Furthermore, the heteronuclear single quantum coherence (HSQC) spectrum of compound **1** revealed six methylene groups resonating at δ_H 4.29 (H-8′/8″), δ_H 2.94 (H-7′/7″), δ_H 2.55 (H-6), and δ_H 1.39 ppm (H-7), as well as three methyl groups resonating at δ_H 2.12 (H-9/10) and δ_H 0.89 ppm (H-8). Analysis of the one-dimensional (1D) and two-dimensional (2D) NMR spectra of compound **1** indicated two identical phenylethyl moieties, elucidated based on the heteronuclear multiple bond correlations (HMBC) from H-7′ to C-1′, C-2′, and C-6′ and from H-8′ to C-7′ and C-1′, as well as from H-7″ to C-1″, C-2″, and C-6″ and from H-8″ to C-7″ and C-1″. In the COSY spectrum, a propyl spin system was observed from H-8 to H-7 to H-6, which was further confirmed by HMBC correlations from H-8 to C-6 and from H-7 to C-2, as well as from H-6 to C-2. The remaining two methyl groups, and the two above-mentioned phenylethyl moieties, were located on the imidazolium ring, as deduced by HMBC correlations from both H-9 and H-10 to C-4 and C-5, from H-8′ to C-2 and C-5, and from H-8″ to C-2 and C-4 (Figure 1). The high-resolution electrospray mass spectrometry (HR-ESI-MS) spectrum of **1** showed a molecular ion peak $[M]^+$ at m/z 347.2472, indicating that the molecule itself is positively charged and possesses a molecular formula of $C_{24}H_{31}N_2^+$. On the basis of the analysis of spectroscopic data, compound **1** was identified as 4,5-dimethy-1,3-diphenylethyl-2-propylimidazolium, for which we propose the name discolin A.

Compound **2** was also obtained as a colorless oil. The prominent peak $[M]^+$ at m/z 361.2640 in the HR-ESI-MS spectrum indicated a 14 Da difference compared to compound **1**, supporting the molecular formula of $C_{25}H_{33}N_2^+$. The NMR data of **2** revealed a close similarity to those of **1** (Table 1), except for one additional methylene group at δ_H 2.59 ppm and one methyl group shifted from δ_H 2.12 to δ_H 1.16 ppm. These spectral differences suggest that **2** features the same molecular skeleton as **1** but bears an ethyl group rather than a methyl group, which accounts for the 14 Da molecular weight difference observed between both compounds. The differences of compound **2** were confirmed by COSY correlation between H-9 and H-10, as well as by HMBC correlations from H-9 to C-4 and C-5 (Figure 1). Hence, compound **2** was identified as 4-ethyl-5-methyl-1,3-diphenylethyl-2-propylimidazolium, for which the name discolin B was proposed.

To the best of our knowledge, such a class of alkaloids has not been reported before from any bacterial source. However, structurally related alkaloids named lepidilines A−D were isolated from the roots of the Andean plant *Lepidium meyenii*

https://doi.org/10.1021/acs.jnatprod.1c01173
J. Nat. Prod. 2022, 85, 1039−1051

Table 1. ^{1}H and ^{13}C NMR Data of Compounds 1 and 2

	1[a]			2[b]	
no.	δ_C, type	δ_H, mult. (J in Hz)	δ_H, mult. (J in Hz)[c]	δ_C, type	δ_H, mult. (J in Hz)
2	144.92, C			146.64, C	
4	125.64, C			132.77, C	
5	125.64, C			127.78, C	
6	23.98, CH_2	2.55, t (8.2)	2.37, t (8.2)	25.87, CH_2	2.39, t (8.2)
7	20.77, CH_2	1.39, dq (15.1, 7.3)	1.42, dq (15.1, 7.3)	21.93, CH_2	1.46, dq (15.1, 7.4)
8	13.44, CH_3	0.89, t (7.3)	0.93, t (7.3)	13.91, CH_3	0.94, t (7.3)
9	7.93, CH_3	2.12, s	2.11, s	16.97, CH_2	2.59, q (7.6)
10	7.93, CH_3	2.12, s	2.11, s	13.95, CH_3	1.16, t (7.6)
11				8.39, CH_3	2.01, s
1′/1″	136.93, C			138.01/130.08, C	
2′/2″	129.03, CH	7.19, m	7.12, dd (7.8, 1.5)	130.02/130.12, CH	7.12, m
3′/3″	128.62, CH	7.32, m	7.33, m	130.14/130.18, CH	7.34, m
4′/4″	127.06, CH	7.30, dt (7.0, 1.5)	7.31, m	128.62/128.65, CH	7.31, m
5′/5″	128.62, CH	7.32, m	7.33, m	130.14/130.18, CH	7.34, m
6′/6″	129.03, CH	7.19, m	7.12, dd (7.8, 1.5)	130.02/130.12, CH	7.12, m
7′/7″	35.04, CH_2	2.94, t (7.2)	3.01, t (6.8)	36.74/37.42, CH_2	3.01, td (6.9, 1.8)
8′/8″	46.04, CH_2	4.29, t (7.2)	4.30, t (6.8)	47.81/47.88, CH_2	4.31, t (6.9)

[a]^{1}H at 400 MHz and ^{13}C at 100 MHz in DMSO-d_6. [b]^{1}H at 600 MHz and ^{13}C at 150 MHz in CD_3OD. [c]^{1}H at 400 MHz in CD_3OD.

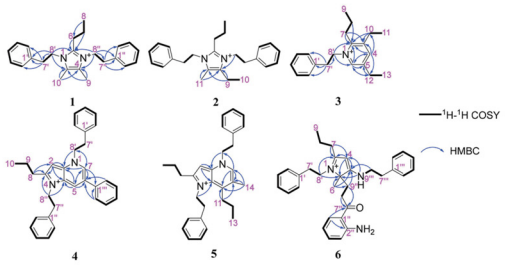

Figure 1. Selected HMBC and ^{1}H–^{1}H COSY correlations of compounds **1**–**6**.

"maca".[19,20] Despite the topological similarity, some structural differences can be noted: The carbon chains connecting the phenyl moiety to the central imidazolium ring are elongated by one C atom in discolins A and B. In addition, the aliphatic side chains of the imidazolium ring differ in size between discolins and lepidilines. In the case of lepidiline C and D an additional methoxylation of the phenyl ring is observed.

Compound **3** was obtained as a colorless oil. The HR-ESI-MS of **3** showed a molecular ion peak $[M]^+$ at m/z 282.2215, indicating a molecular formula $C_{20}H_{28}N^+$ with a degree of unsaturation of 8. Detailed analysis of the 1D and 2D NMR spectra revealed one phenylethyl moiety, one propyl group, and two ethyl groups. Compared to compound **1**, the phenylethyl moiety was confirmed by HMBC correlations

Table 2. ^{1}H NMR and ^{13}C NMR Data of Compound 3

no.	δ_C, type[a]	δ_H, mult. (J in Hz)[a]	δ_C, type[b]	δ_H, mult. (J in Hz)[b]
2	155.28, C		154.83, C	
3	145.20, C		144.49, C	
4	146.39, CH	8.22, s	146.00, CH	8.36, d (1.8)
5	143.22, C		142.73, C	
6	143.69, CH	8.22, s	144.05, CH	8.81, d (1.9)
7	31.34, CH_2	2.92, m	31.10, CH_2	3.10, m
8	23.34, CH_2	1.67, dq (16.2, 7.3)	23.02, CH_2	1.76, m
9	14.34, CH_3	1.12, t (7.3)	14.35, CH_3	1.12, t (7.3)
10	26.24, CH_2	2.85, q (7.5)	25.89, CH_2	2.94, q (7.5)
11	14.89, CH_3	1.30, t (7.5)	14.87, CH_3	1.31, t (7.5)
12	26.24, CH_2	2.69, t (7.6)	25.89, CH_2	2.78, q (7.6)
13	14.68, CH_3	1.17, t (7.6)	14.66, CH_3	1.21, t (7.6)
1′	137.04, C		137.1, C	
2′	130.10, CH	7.05, dd (6.6, 2.9)	130.04, CH	7.22, m
3′	128.75, CH	7.28, m	128.24, CH	7.30, m
4′	130.18, CH	7.29, m	129.74, CH	7.30, m
5′	128.75, CH	7.28, m	128.24, CH	7.30, m
6′	130.10, CH	7.05, dd (6.6, 2.9)	130.04, CH	7.22, m
7″	37.99, CH_2	3.28, t (6.9)	37.85, CH_2	3.41, t (7.2)
8′	60.53, CH_2	4.83, t (6.9)	60.03, CH_2	5.07, t (7.2)

[a]^{1}H at 400 MHz and ^{13}C at 100 MHz in CD_3OD. [b]^{1}H at 400 MHz and ^{13}C at 100 MHz in acetone-d_6.

https://doi.org/10.1021/acs.jnatprod.1c01173
J. Nat. Prod. 2022, 85, 1039−1051

Table 3. ^{1}H and ^{13}C NMR Data of Compounds 4 and 5

	4[a]		5[b]	
no.	δ_C, type	δ_H, mult. (J in Hz)	δ_C	δ_H, mult. (J in Hz)
1a	136.45, C		138.94, C	
2	95.09, CH	6.79, s	95.32, CH	6.64, s
3	156.83, C		156.10, C	
4a	135.54, C		132.61, C	
5	123.94, CH	8.18, s	143.95, C	
6	131.33, C		127.62, C	
7	136.22, CH	8.24, d (1.2)	137.46, CH	8.04, s
8	29.89, CH_2	2.73, t (7.7)	30.10, CH_2	2.49, t (7.8)
9	22.20, CH_2	1.82, m	21.98, CH_2	1.70, m
10	14.21, CH_3	1.07, t (7.4)	14.15, CH_3	0.99, t (7.4)
11			31.06, CH_2	3.13, m
12			24.62, CH_2	1.62, m
13			14.17, CH_3	1.08, t (7.3)
14			16.48, CH_3	2.40, s
1′	137.75, C		137.77, C	
2′	130.02, CH	7.23, m	129.89, CH	6.99, m
3′	128.50, CH	6.98, dd (6.6, 2.8)	129.79, CH	7.20, m
4′	129.95, CH	7.23	128.38, CH	7.20, m
5′	128.50, CH	6.98, dd (6.6, 2.8)	129.79, CH	7.20, m
6′	130.02, CH	7.23, m	129.89, CH	6.99, m
7′	36.48, CH_2	3.35, t (6.5)	36.46, CH_2	3.29, t (6.8)
8′	59.46, CH_2	4.99, t (6.5)	58.57, CH_2	4.85, t (6.8)
1″	139.36, C		138.52, C	
2″	129.75, C	7.15, m	130.06, CH	6.95, m
3″	130.33, C	6.93, dd (8, 1.6)	129.86, CH	7.24, m
4″	128.14, C	7.11, m	128.30, CH	7.24, m
5″	130.33, C	6.93, dd (8, 1.6)	129.86, CH	7.24, m
6″	129.75, C	7.15, m	130.06, CH	6.95, m
7″	37.36, CH_2	3.14, t (6.1)	38.49, CH_2	3.07, t (6.9)
8″	46.93, CH_2	4.70, t (6.1)	47.76, CH_2	4.57, t (6.9)
1‴	131.33			
2‴	130.27, C	7.48, m		
3‴	128.45, C	7.37, dd (7.9, 1.6)		
4‴	129.95, C	7.45, m		
5‴	128.45, C	7.37, dd (7.9, 1.6)		
6‴	130.27, C	7.48, m		

[a] ^{1}H at 400 MHz and ^{13}C at 100 MHz in CD_3OD. [b] ^{1}H at 600 MHz and ^{13}C at 150 MHz in CD_3OD.

from H-7′ to C-8′, C-1′, C-2′, and C-6′ and from H-8′ to C-1′ (Figure 1). The remaining five sp^2 carbons resonated at δ_C 155.28 (C-2), 145.20 (C-3), 146.39 (C-4), 143.22 (C-5), and 143.69 ppm (C-6) (Table 2). In combination with the degree of unsaturation, this suggested one pyridinium ring in the structure instead of an imidazolium ring. Such assumption was confirmed by the observation of HMBC correlations from H-6 to C-2, C-4, and C-5 and from H-4 to C-2, C-3, and C-6. The two ethyl groups were assigned to be attached to C-3 and C-5, due to the HMBC correlations of one ethyl group from H-10 to C-2 and C-3, as well as the COSY correlation between H-10 and H-11, while the other ethyl group showed correlations from H-12 to C-5 and C-6 and from both H-4 and H-6 to C-12, as well as a COSY correlation between H-12 and H-13. The propyl group, which is indicated by a COSY spin system from H-9 to H-8 to H-7, was located on C-2 based on the HMBC correlations from H-7 to C-2 and C-3 and from H-8 to C-2. Furthermore, the elucidated phenylethyl moiety is connected to the 3,5-diethyl-2-propylpyridinium moiety through a C−N linkage based on the HMBC correlations from H-8′ to C-2 and C-6 (Figure 1). Therefore, compound **3** was determined to be 3,5-diethyl-1-phenylethyl-2-propylpyridinium, for which we propose the name dispyridine.

Compound **4** was obtained as a yellowish oil. The molecular formula $C_{32}H_{33}N_2^+$ was deduced by HR-ESI-MS analysis ($[M]^+$, m/z 445.2647). Two phenylethyl moieties and one propyl group were disclosed from the similar ^{1}H NMR and COSY data compared with those of compounds **1** and **2**. The additional signals in the ^{1}H NMR spectrum were representative of one singlet sp^2 proton resonating at δ_H 6.79 ppm and two protons resonating at δ_H 8.24 and δ_H 8.18 ppm, as well as one monosubstituted phenyl ring (Table 3). A 1*H*-pyrrolo[3,2-*b*]pyrimidinium moiety was assigned by HMBC correlations from H-2 to C-1a, C-3, and C-4a, from H-5 to C-1a, C-4a, C-6, and C-7, and from H-7 to C-1a, C-5, and C-6. The two phenylethyl moieties were assigned to be located at positions 1 and 4 based on the HMBC correlations from H-8′ to C-1a and C-7 and from H-8″ to C-3 and C-4a. The remaining phenyl ring was connected to C-6, supported by the HMBC correlations from H-2‴ (overlapping with H-6‴) to C-6 and from H-7 to C-1‴ (Figure 1). Therefore, compound **4** was elucidated to be 1,4-diphenethyl-6-phenyl-3-propyl-1*H*-

https://doi.org/10.1021/acs.jnatprod.1c01173
J. Nat. Prod. 2022, 85, 1039−1051

Table 4. ^{1}H and ^{13}C NMR Data of Compound 6

no.	δ_C, type[a]	δ_H, mult. (J in Hz)[b]	no.	δ_C, type[a]	δ_H, mult. (J in Hz)[b]
2	74.52, C		1″	116.84, C	
3	177.66, C		2″	151.54, C	
4	91.49, CH	5.67, s	3″	117.72, CH	6.75, d (8.4)
5	181.88, C		4″	135.24, CH	7.23, dd (8.4, 1.3)
6	23.55, CH_3	1.50, s	5″	115.38, CH	6.50, m
7	30.34, CH_2	2.62, m 2.54, m	6″	131.64, CH	7.42, dd (8.2, 1.3)
8	20.19, CH_2	1.64, m	7″	200.34, C=O	
9	14.17, CH_3	0.95, t (7.3)	8″	31.77, CH_2	2.42, m; 2.17, m
1′	138.34, C		9″	30.97, CH_2	2.42, m; 2.17, m
2′	129.38/129.58, CH	7.32, m	1‴	138.93	
3′	129.38/129.58, CH	7.32, m	2‴	129.44, CH	7.24, m
4′	127.58, CH	7.24, m	3‴	128.94, CH	7.18, m
5′	129.38/129.58, CH	7.32, m	4‴	127.13, CH	7.07, t (7.3)
6′	129.38/129.58, CH	7.32, m	5‴	128.94, CH	7.18, m
7′	36.27, CH_2	2.85, m	6‴	129.44, CH	7.24, m
8′	44.31, CH_2	3.82, ddd (16.1, 10.1, 6.4); 3.69, ddd (15.8, 10.2, 6.1);	7‴	34.55, CH_2	2.88, t (6.9)
			8‴	46.73, CH_2	3.57, m
			9‴-NH		8.98, t (5.1)

[a]^{1}H at 600 MHz in DMSO-d_6. [b]^{13}C at 150 MHz in DMSO-d_6.

Table 5. MIC Values (μg/mL) for Compounds 1−6

	MIC (μg/mL, n = 3)					
test organism	1	2	3	4	5	6
B. subtilis DSM10	16	32	>64	1	4	8−4
M. smegmatis ATCC607	8	16−8	>64	1−0.5	4	8
L. monocytogenes DSM20600	>64	>64	>64	0.5	2	4
S. aureus ATCC25923	64	64	>64	1−0.5	4	8
E. coli ATCC25922	>64	>64	>64	64	>64	>64
E. coli ATCC25922 Δ*tolC*	>64	>64	>64	8	64	>64
C. albicans FH2173	>64	>64	>64	8−4	16−8	32−16
A. flavus ATCC9170	>64	>64	>64	4−1	8	32−16
C. elegans N2	>64	>64	>64	32	>64	64

pyrrolo[3,2-*b*]pyridinium, for which the name dispyrrolopyridine A is suggested.

Compound **5** was isolated as a colorless powder. Its molecular formula was established as $C_{30}H_{37}N_2^+$ based on the prominent ion peak $[M]^+$ observed at m/z 425.2949 in the HR-ESI-MS spectrum. The NMR data of **5** were similar to those of **4**, except for the additional signals of one methyl group (δ_H 2.40 ppm) and one propyl group (spin system from δ_H 1.08 to δ_H 1.62 to δ_H 3.13 ppm) instead of a proton resonating at δ_H 8.18 ppm and one monosubstituted aromatic ring, indicating that the structure of **5** is modified at C-5 and C-6 compared to **4**. In the HMBC spectrum, correlations from H-14 to C-5, C-6, and C-7, as well as from H-11 to C-5 and C-6, support that the methyl group is located at C-6, while the propyl group is located at C-5 (Figure 1). Therefore compound **5** was elucidated to be 6-methyl-1,4-diphenethyl-3,5-dipropyl-1*H*-pyrrolo[3,2-*b*]pyridinium, for which we recommend the name dispyrrolopyridine B.

Compound **6** was isolated as a yellowish oil. With the prominent molecular ion peak $[M]^+$ detected in the HR-ESI-MS at m/z 494.3165, the molecular formula of $C_{33}H_{40}N_3O^+$ was deduced. When the NMR spectra of **6** were compared with the previously isolated compounds, two phenylethyl moieties and one propyl group were clearly identified. The remaining signals of compound **6** in the ^{1}H NMR spectrum were assigned to a secondary amine proton (δ_H 8.98 ppm), a phenyl moiety (δ_H 7.42, 7.23, 6.75, and 6.50 ppm), an olefinic proton (δ_H 5.67 ppm), two methylene groups (δ_H 2.17 and δ_H 2.42 ppm), and one methyl group (δ_H 1.50 ppm) (Table 4). The HMBC correlations from H-9‴ to C-2 and C-4, from H-7 to C-5 and C-4, as well as from H-4 to C-2, C-3, and C-5 revealed the substructure of a pyrrolium ring. When combined with further HMBC correlations from H-8‴ to C-3, it was established that one of the phenylethyl moieties was linked to the secondary amine located on C-3. In the HMBC spectrum, the correlations from H-6 to C-2 and C-3 determined the location of the methyl group at C-2 on the pyrrolium ring. On the basis of the molecular formula and the chemical shift of a carbon signal at δ_C 151.54 ppm (C-2″) of an aromatic ring,[21] a primary amine group was deduced to be located at C-2″ of the aromatic ring. Furthermore, the part of a 3-(2-aminophenyl)-3-oxypropyl side chain was determined to be located at C-2 of the pyrrolium ring as supported by the HMBC correlations from H-8″ to C-9″ and from H-9″ to C-7″ and C-8″, as well as from H-6 to C-9″ (Figure 1). Therefore, compound **6** was elucidated to be 2-(3-(2-aminophenyl)-3-oxypropyl)-2-methyl-1-phenethyl-3-(phenethylamino)-5-propyl-2*H*-pyrrol-1-ium, which we named dispyrrole. Electronic circular dichroism (ECD) analysis gave a featureless baseline curve indicating compound **6** to be a racemate.

Bioactivity of Isolated Compounds. Compounds **1**−**6** were investigated for their bioactivity against six different

https://doi.org/10.1021/acs.jnatprod.1c01173
J. Nat. Prod. 2022, 85, 1039−1051

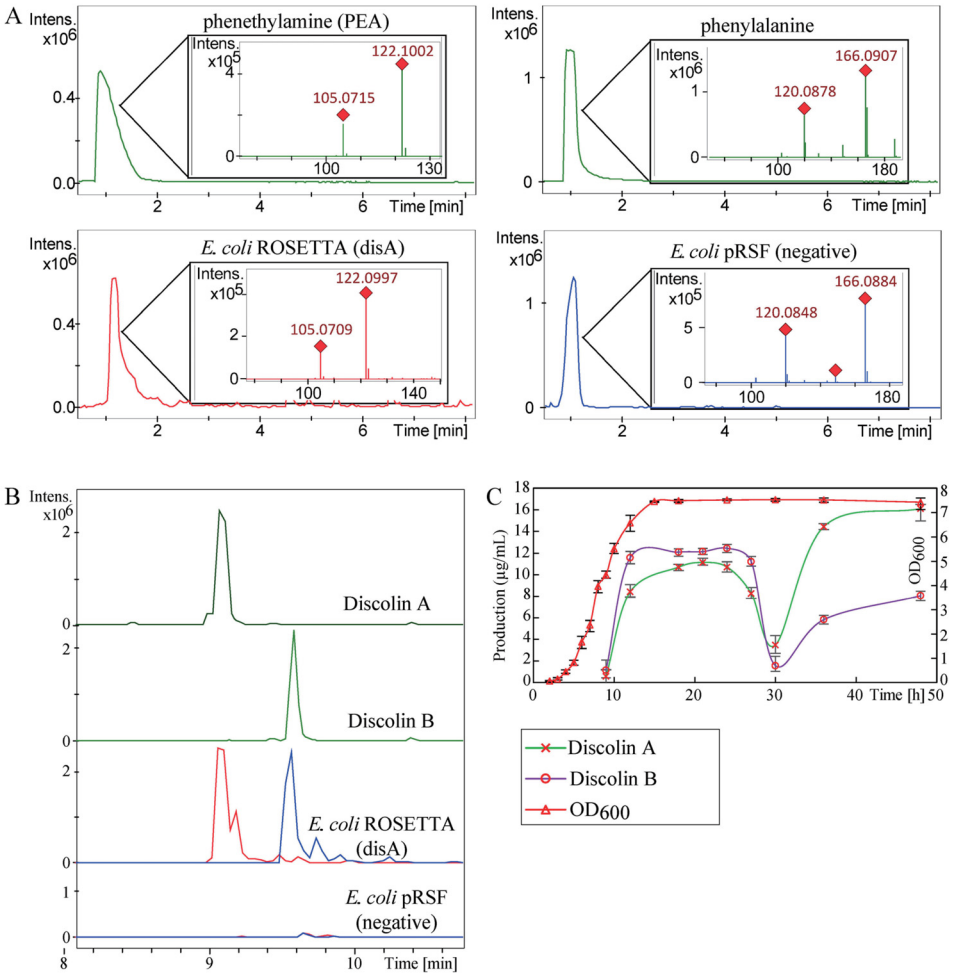

Figure 2. Heterologous expression of the *disA* gene in *E. coli* Rosetta. (A) *In vivo* decarboxylation of phenylalanine to PEA catalyzed by DisA, when 0.06 mM phenylalanine was added to the medium. Extracted ion chromatograms (EICs) of phenylalanine ($C_9H_{11}NO_2$, 166.0863 $[M + H]^+$) and PEA ($C_8H_{11}N$, 122.0964 $[M + H]^+$). (B) EICs of discolin A (**1**, *m*/*z* 347.2482 $[M]^+$) and discolin B (**2**, *m*/*z* 361.2638 $[M]^+$). (C) Growth curve of *E. coli* Rosetta (disA) and production (μg/mL) of discolin A and B (**1** and **2**); data is presented as averages from triplicate measurements; error bars show the standard deviation.

bacteria (*B. subtilis* DSM10, *Mycobacterium smegmatis* ATCC607, *Listeria monocytogenes* DSM20600, *Staphylococcus aureus* ATCC25923, and *Escherichia coli* ATCC25922 wild type and efflux pump deficient strain Δ*tolC*). Antifungal activity was assessed against *Candida albicans* FH2173 and *Aspergillus flavus* ATCC9170. The anthelmintic activity of the purified compounds was determined against the model organism *Caenorhabditis elegans* N2.

As shown in Table 5, discolin A (**1**) and discolin B (**2**) showed moderate activity against *B. subtilis* and *M. smegmatis* with minimum inhibitory concentration (MIC) values ranging from 8 to 32 μg/mL. Dispyrrolopyridine A (**4**) and dispyrrolopyridine B (**5**) exhibited strong activity against all tested Gram-positive indicator strains (i.e., *B. subtilis*, *M. smegmatis*, *L. monocytogenes*, and *S. aureus*) with MIC values ranging from 0.5 to 4 μg/mL and moderate activity against the yeast *C. albicans* and the spore-forming mold *A. flavus* (MIC values ranging from 1 to 16 μg/mL). Dispyrrole (**6**) showed antibacterial activities against all tested Gram-positive bacteria with MIC values ranging from 4 to 8 μg/mL. Furthermore, dispyrrolopyridine A (**4**) was also active against *E. coli* ATCC25922 Δ*tolC* (8 μg/mL), while the wild-type strain was not inhibited at the highest tested concentration. This finding indicates that pump-mediated compound efflux might be the primary mechanism of resistance of *E. coli* toward the herein described dispyrolopyridine A (**4**). Moreover, dispyrolopyridine A (**4**) was also the only tested metabolite possessing bioactivity against *C. elegans* N2 with an MIC

https://doi.org/10.1021/acs.jnatprod.1c01173
J. Nat. Prod. 2022, 85, 1039−1051

value of 32 μg/mL. Dispyridine (**3**) was inactive against the all the tested microorganisms.

While the previously mentioned structurally related compounds lepidiline A and B and some synthetic analogues showed cytotoxic activity against different cancer cell lines, no data regarding their antimicrobial activity was reported.[19] In the case of dispyridine (**3**) no similar compound of bacterial origin was identified. However, some related compounds from synthetic origin were described.[22] Related synthetic counterparts previously showed strong antibiotic activity against *S. aureus*.[23] Yet, no activity against bacterial or fungal strains was observed for dispyridine (**3**). For the dispyrrolopyridines (**4** and **5**), a series of pyrrolo[2,3-*b*]pyrimidine derivatives has been synthesized and showed promising inhibitory effects against fluoroquinolone-resistant MRSA and other bacteria.[24,25] Other synthetic pyrrolo[2,3-*b*]pyrimidine derivatives proved to be positive allosteric modulators (PAM) of the M1 receptor and displayed high 5-HT_{1F} receptor affinity, which may be useful for the treatment of diseases mediated by the M1 receptor, such as Alzheimer's disease, cognitive impairment, schizophrenia, pain, sleep disorders, and migraine.[26,27]

Biosynthetic Basis of Discolins. In a next step, we investigated the biosynthetic basis for discolin production in *T. discolor* sv11. We considered that phenethylamine (PEA) was an intermediate building block in the biosynthesis of **1**−**6**. It was reported that several other bacteria such as *Enterococcus* produce PEA via decarboxylation of phenylalanine.[28] In *Enterococcus faecalis* R612Z1, phenylalanine is decarboxylated to PEA by a pyridoxal 5′ phosphate (PLP)-dependent enzyme named TDC.[29] In order to determine if a similar enzyme is involved in the biosynthesis of **1**−**6**, the *T. discolor* sv11 genome was sequenced, yielding a 3.4 Mbp draft genome (25 contigs). *In silico* search for phenylalanine decarboxylases revealed three candidates which shared 34%, 24%, and 27% similarity to *E. faecalis* R612Z1 TDC. The first one corresponded to a characterized lysine/ornithine decarboxylase involved in the biosynthesis the siderophore bisucaberin.[30] The second one was a putative decarboxylase domain embedded in a large nonribosomal peptide synthetase, therefore likely involved in peptide biosynthesis. The third one was annotated as putative decarboxylase and did not cluster with any other genes. Our hypothesis was that the latter is involved in PEA biosynthesis.

To test this hypothesis, the candidate decarboxylase from *T. discolor* sv11 (here named DisA) was expressed in *E. coli* Rosetta (disA) under the control of an inducible promoter. After 1 day of cultivation the cultures of *E. coli* Rosetta (disA) and *E. coli* pRSF (negative empty vector control) were extracted and analyzed by LC−ESI-MS/MS.

Initial results using standard LB medium showed no clear differences between *E. coli* Rosetta (disA) and the negative control. We reasoned that the substrate for DisA (i.e., phenylalanine) was present in low concentration in the used culture medium so that the PEA production was likely below detection levels. In a second experiment, 0.06 mM phenylalanine was added to the medium. This time PEA was detected in the extracts of *E. coli* Rosetta (disA) while no production was found the in negative control strain (Figure 2A).

Interestingly, not only PEA but also discolins A and B were detected in the *E. coli* Rosetta (disA) culture (Figure 2B). It was observed that the concentrations of **1** and **2** reached a plateau at 13 h, when *E. coli* Rosetta (disA) reached the stationary phase, and an equilibrium production was observed until 24 h. After that an oscillation in the production can be observed from 24 to 36 h (Figure 2C). This oscillation might be caused by feedback inhibition where discolins could be degraded by other enzymes from the heterologous host.

In order to confirm that DisA is responsible for the decarboxylation of phenylalanine, an *in vitro* enzymatic characterization was carried out. A His-tagged DisA was expressed in *E. coli* and subsequently purified using affinity chromatography. Following *in vitro* assays showed that PEA was produced from phenylalanine only in the presence of DisA, thereby confirming the previous results observed using *in vivo* experiments (Figure 3).

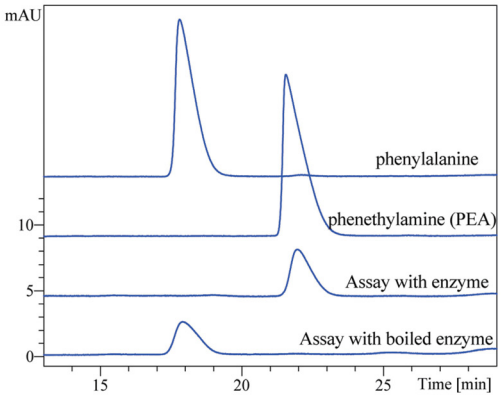

Figure 3. *In vitro* formation of PEA. Comparative HPLC analysis of the standards phenylalanine and phenethylamine (PEA), assay with enzyme, and assay with boiled enzyme. The UV absorbance at 254 nm is shown.

Spontaneous Formation of Discolins. These *in vivo* and *in vitro* experiments indicate that DisA is likely the only enzyme involved in the production of the discolins A and B. Thus, the remaining biosynthetic steps should occur in a nonenzymatic way. It was previously reported how bacteria apply spontaneous reactions in order to complete biosyntheses (e.g., of rubrolone[31]) to generate diversity (e.g., APPAs[32]). It can be assumed that the production of a reactive intermediate, which can result in a large variety of bioactive metabolites, may be a strategy used more often in the bacterial specialized metabolism.

In order to confirm the spontaneous formation of discolins, a one-pot reaction was carried out at room temperature in H_2O. The substrates PEA, butyraldehyde, and 2,3-butanedione (for the formation of discolin A) or 2,3-pentanedione (for the formation of discolin B) were combined. Indeed, discolins A (**1**) and B (**2**) were detected after 3 h of reaction time (Figure 4).

Proposed Biosynthetic Pathway of Compounds 1−5 from PEA. In general, there are two likely pathways toward the monocyclic PEA-containing alkaloids **1**−**3** (Figure 5). The Chichibabin pyridine synthesis could afford the formation of the pyridinium core of dispyridine (**3**) by reaction of 2-phenethylamine with 3 equiv of *n*-butyraldehyde (pathway 1, Scheme S1), while a Radziszewski-type reaction could be responsible for the formation of discolins having an imidazolium core structure (pathways 2a and 2b, Scheme S2).

https://doi.org/10.1021/acs.jnatprod.1c01173
J. Nat. Prod. 2022, 85, 1039−1051

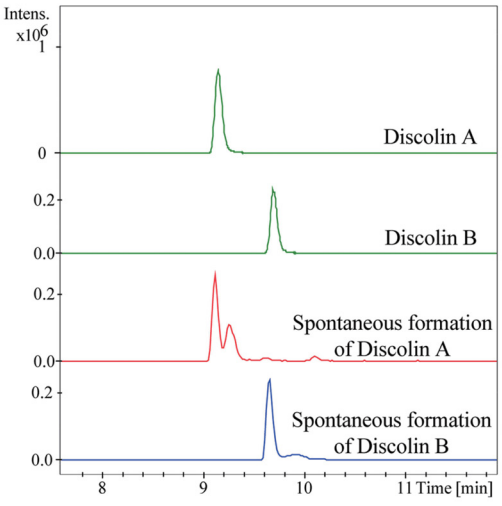

Figure 4. Spontaneous formation of discolin A (**1**) and discolin B (**2**). Extracted ion chromatograms (EICs) of **1** (m/z 347.2482 $[M]^+$) and **2** (m/z 361.2638 $[M]^+$).

The role of the Chichibabin pyridine synthesis in the biosynthesis of natural products has so far been controversially discussed, especially when benzylic aldehydes are involved.[33,34] On the other hand, the situation appears less controversial in the case of aliphatic aldehydes. The biomimetic syntheses described for the alkaloid ficuseptine[35] and the elastin cross-linker isodesmosine[36] give an implication for the Chichibabin pyridine synthesis in biosynthetic pathways.

Discolins A and B on the other hand might be the result of a Radziszewski-type reaction.[37] The classical Radziszewski reaction is a condensation reaction of an α-dicarbonyl compound, an aldehyde, and 2 equiv of ammonia, affording an imidazole.[38] Primary amines are also suitable for the reaction. Thus, replacement of 1 equiv of ammonia by 1 equiv of a primary amine enables the formation of tetrasubstituted imidazoles.[39] In case of discolins A (**1**) and B (**2**) the necessary 1,2-dicarbonyl compounds would be 2,3-butanedione (for **1**) and 2,3-pentadienone (for **2**). Both of these compounds are known metabolites of yeast.[40] Furthermore, 1,2-diketones and their acyloin precursors were discussed for the biosynthesis of pyrazines in *Corynebacterium glutamicum*.[41] In essence, the α-hydroxyketones are side products from the biosynthesis of the amino acids valine, leucine, and isoleucine, arising from the decarboxylation of (*S*)-2-acetolactate and its congeners. Oxidation of the α-hydroxyketones in turn yields the corresponding 1,2-diketones.[41] The reaction has furthermore been successfully exploited for the synthesis of the structurally similar natural product lepidiline B.[42] Yet, only the imidazole core was installed by the Radziszewski reaction, while *N*-alkylation was achieved in a second reaction step. Thus, to the best of our knowledge, the Radziszewski reaction has never before been reported to produce pentasubstituted imidazolium ions by use of 2 equiv of a primary amine as the starting material.

As the azaindole **4** appears to consist of the same building blocks as compounds **1**−**3** plus an additional aldehyde component, we assume a similar origin (pathway 3, Scheme S3). In the case of the structurally related compound **5**, not only the aldehyde component but also the diketone differs in comparison to the other compounds. The diketone 2,3-heptanedione necessary for the production of **5** has previously been reported to be present in the headspace extracts of *C. glutamicum* and was discussed in the context of pyrazine biosynthesis.[41]

The biosynthesis of compound **6** still remains elusive. It might be speculated that 4-(2-aminophenyl)-2,4-dioxobutanoic

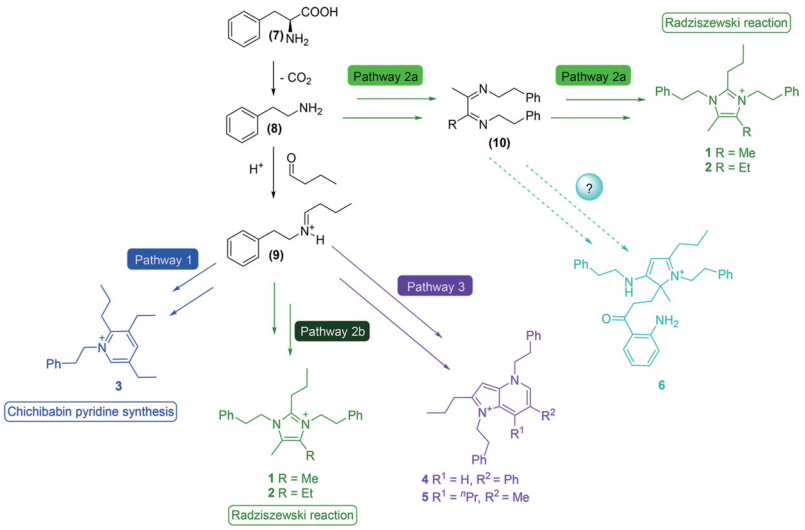

Figure 5. General outline for the proposed biosynthesis of compounds **1**−**6**.

https://doi.org/10.1021/acs.jnatprod.1c01173
J. Nat. Prod. 2022, 85, 1039−1051

acid, a product of the tryptophan metabolism,[43−45] reacts in a thiamine phosphate dependent manner with the intermediate **10**, thus initiating a reaction sequence leading to **6**, whereby thiamine phosphate promotes the necessary polarity inversion.

Overall, our experiments support the hypothesis that phenylalanine-derived PEA is a building block in the biosynthesis of compounds **1**−**6**. The proposed aldehyde and 1,2-diketone reaction partners presumably originate from the primary metabolism, but further experimental proof is required. As shown above, these building blocks possess suitable reactivity to produce compounds **1**−**3** in a non-enzymatic fashion. For compounds **4** and **5** on the other hand, additional oxidation reactions are needed, which might require enzymatic control. As no redox enzymes were found clustering with DisA, those would need to be stand-alone enzymes. Alternatively, the redox processes might take place among the different reaction intermediates itself, leading to additional, so far uncharacterized, products. In general, due to the multitude of possible reactions taking place between the key building blocks, further natural product derivatives might be expected.

Distribution of *disA*-like Genes in Other Bacteria. To investigate the distribution of DisA within the *Tenacibaculum* genus or even among other flavobacterial genera, we searched for DisA orthologues using BLASTP. Several related enzymes (>98% coverage and above 70% identity) were found in the majority of the *Tenacibaculum* genomes available in the NCBI database. Furthermore, several flavobacterial genera were found to possess enzymes similar to DisA (Figure 6). Interestingly, most of the hits correspond to strictly marine flavobacterial genera such as *Aequorivita*, *Aquimarina*, *Croceibacter*, *Maribacter*, *Muricauda*, *Polaribacter*, and *Ulvibacter*.[46] From our collection of 26 *Tenacibaculum* strains, discolin production could be detected in six of the EtOAc extracts (belonging to the species *T. discolor*, *T. ascidiascicola*, and *T. mesophilum*).

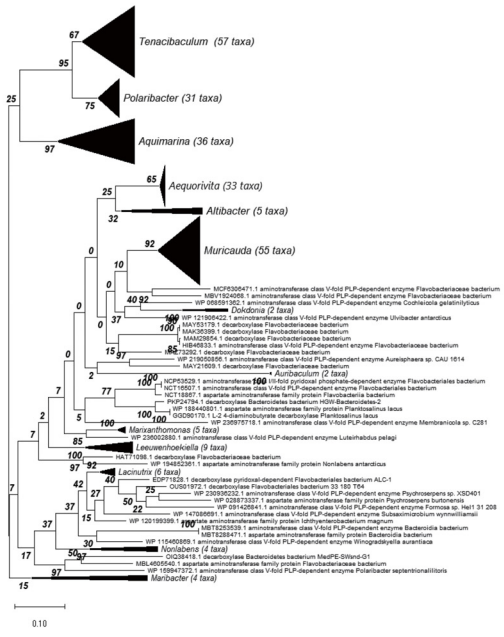

Figure 6. Distribution of *disA*-like genes in bacteria.

Our finding, together with previous reports, indicates that the production of PEA-containing alkaloids is likely a widespread characteristic within the marine flavobacteria. For instance, in a previous report five PEA derivatives were isolated from the flavobacterial strain *Arenibacter*.[47] In addition, PEA was proposed as a taxonomic biomarker within the free-living Bacteroidetes phylum.[48] These studies together with our findings revealed that the genus *Tenacibaculum* and other flavobacterial strains are able to produce this type of arylamine. Despite that an antimicrobial, antifungal, and nematicidal activity could be assigned to PEA-containing alkaloids, their real ecological role in the marine ecosystems is still unknown. Further studies, for instance, associating the expression of DisA homologues with several environmental conditions using metatranscriptomics or metabolomics, could provide additional insights about the ecological role of these natural products.

■ EXPERIMENTAL SECTION

General Experimental Procedures. The UV spectra of compounds **1**−**3** were measured in methanol (MeOH) solution on a Jasco V760 spectrometer (JASCO Deutschland GmbH, Pfungstadt, Germany). The 1D and 2D NMR spectra were recorded in CD_3OD, acetone-d_6, or DMSO-d_6 using Bruker Avance II 400 MHz and Bruker Avance III 600 MHz spectrometers equipped with a Prodigy cryoprobe (Bruker, Ettlingen, Germany). The LC−HRMS data for compounds **1**−**3** were recorded on a micrOTOF-QII mass spectrometer (Bruker, Billerica, MA, U.S.A.) with an ESI source coupled to a Dionex Ultimate 3000 HPLC system (Thermo Scientific, Darmstadt, Germany) using an EC10/2 Nucleoshell C18 2.7 μm column (Macherey-Nagel, Dueren, Germany). The LC−HRMS data for the heterologous expression was recorded on a micrOTOF-QII mass spectrometer (Bruker, Billerica, MA, U.S.A.) equipped with an ESI source coupled to an Agilent Infinity 1290 UHPLC system using an ACQUITY UPLC BEH C18 column, 130 Å, 1.7 μm, 2.1 mm × 100 mm (Waters, Eschborn, Germany) with an ACQUITY UPLC BEH C18 VanGuard precolumn, 130 Å, 1.7 μm, 2.1 mm × 5 mm (Waters, Eschborn, Germany). HPLC was performed using a Shimadzu HPLC system (Shimadzu Deutschland GmbH, Duisburg, Germany) for analysis (EC 250/4.6 Nucleodur C18 Gravity-SB, 5 μm; Macherey-Nagel, Düren, Germany) and for semipreparative purification (VP 250/10 Nucleodur C18 Gravity-SB, 5 μm; Macherey-Nagel, Düren, Germany). MPLC was performed on the Interchim Puriflash 4125 chromatography system (Interchim, Montluçon, France).

Bacterial Strain Isolation. The seaweed *C. chamisoii* was collected from the Huanchaco estuarine region and a sand beach located at Paracas Bay, Peru. Epidermal mucus from the seaweed was rinsed with SSW (sterile seawater) for 10 s. An amount of 1 mL of mucus was diluted in 1 mL of SSW, vortex-mixed, and diluted 1:10 in SSW, and 25 μL was inoculated onto P7 (5 g of starch, 2 g of yeast extract, 1 g of peptone, 1 L of filtered seawater, 100 μg/mL cycloheximide, 18 g of agar) agar plates. The agar plates were incubated at room temperature for 2−3 months and checked weekly for new colony formation using a Leicia MZ6 stereomicroscope. A total of 32 strains were selected based on the characteristic iridescent pattern characteristic of several flavobacterial genera,[18] of which 26 strains belonged to the *Tenacibaculum* genus (*T. discolor*, *T. mesophilum*, *T. litoreum*, and *T. ascidiacicola*) based on the 16S rRNA gene sequencing result. A small-scale cultivation (50 mL) was carried out in marine broth 2216 for 4 days at 30 °C to determine the antimicrobial activity of the isolated *Tenacibaculum* strains. The cultures were extracted using 1:1 EtOAc, and the EtOAc phase was dried by rotary evaporation. These crude extracts were further

https://doi.org/10.1021/acs.jnatprod.1c01173
J. Nat. Prod. 2022, 85, 1039−1051

dissolved in MeOH with a concentration of 10 mg/mL for activity testing against *M. luteus* ATCC4698, *B. subtilis* JH642, and *B. megaterium* DSM32 using the agar diffusion method, whereby 50 μL was applied for testing. *T. discolor* sv11 showed the best activity and was chosen for culture optimization.

OSMAC Approach. The media used for the one strain many compounds (OSMAC) approach of strain *T. discolor* sv11 were LB (10 g of peptone, 5 g of yeast extract, 1 L of artificial seawater), MB (40 g of marine broth, 1 L of distilled water), and MYE (10 g of glucose, 3 g of yeast extract, 3 g of malt extract, 5 g of peptone, 1 L of artificial seawater). The kinetics of the antibacterial activity of each culture were observed over 10 days against *B. subtilis* JH642. The results of the OSMAC approach and the kinetics studies showed that the strongest antibacterial activity was observed on the eighth day of fermentation in LB medium. Therefore, large-scale fermentation (36 L) of *T. discolor* sv11 was performed in 5 L flasks which contained 1.5 L of LB medium and were incubated at 30 °C and 140 rpm for 8 days.

Extraction and Isolation. The 36 L culture was extracted with EtOAc with the volume ratio of 1:1 three times, thereby generating 11.9 g of crude extract. The EtOAc crude extract was fractionated by reversed-phase flash chromatography (Interchim Puriflash 4125 chromatography system with a Puriflash C18-AQ30 μm F0120 column) with an elution gradient starting from 10% MeOH/H_2O to 100% MeOH over 1.5 h and yielded 13 fractions (Fr. 1−13). Fr. 11 showed good antimicrobial activities against *B. subtilis* in the agar diffusion test. Therefore, Fr. 11 (973.8 mg) was further subjected to size exclusion chromatography on a Sephadex LH-20 column and eluted with 100% MeOH to give 10 subfractions (Frr. 11.1−11.10). Frr. 11.3 was further subjected to reversed-phase flash chromatography (Interchim Puriflash 4125 chromatography system with a Puriflash C18-HP30 μm F0025 flash column) using an elution gradient from 10% MeOH/H_2O to 100% MeOH over 3 h to give 14 subfractions (Frrr. 11.3.1−11.3.14). Frrr. 11.3.7 was further purified by semipreparative HPLC (0−5 min, 35% MeOH; 5−18 min, gradient increased from 35% to 60% MeOH; 19−25 min, 100% MeOH) to yield compounds **1** (6.3 mg, t_R = 32 min) and **2** (1.2 mg, t_R = 34.5 min). Frrr. 11.3.9 was also fractionated by semipreparative HPLC (0−38.5 min, gradient increased from 35% to 73.5% MeOH) to give three subfractions (Frrrr. 11.3.9.1−11.3.9.3). Frrrr. 11.3.9.1 was again purified by semipreparative HPLC (0−57 min, gradient increased from 30% to 58.5% MeCN) to yield compounds **4** (1.6 mg, t_R = 53.8 min) and **5** (0.9 mg, t_R = 56.2 min). Purification of Frrrr. 11.3.9.2 by semipreparative HPLC (0−57 min, gradient increased from 25% to 63% MeCN) yielded compound **6** (1.6 mg, t_R = 54.7 min). Compound **3** (2.5 mg, t_R = 16 min) was obtained from Frr. 11.2 by semipreparative HPLC (MeOH/H_2O: 0−5 min, 35%; 5−18 min, from 35% to 60%; 19−25 min, 100% MeOH).

*Discolin A (**1**).* Colorless oil; UV (MeOH) λ_{max} (log ε) 256.8 (0.62), 263.9 (0.49), 267.7 (0.44), 281.1 (0.39), 290.1 (0.36) nm; ^{1}H NMR (DMSO-d_6 and CD_3OD, 400 MHz) and ^{13}C NMR (DMSO-d_6, 100 MHz) data are given in Table 1; HR-ESI-MS *m*/*z* 347.2472 $[M]^+$ (calcd for $C_{24}H_{31}N_2^+$, 347.2482).

*Discolin B (**2**).* Colorless oil; UV (MeOH) λ_{max} (log ε) 202.2 (3.08), 206.8 (2.54), 232.9 (0.78) nm; ^{1}H NMR (CD_3OD, 600 MHz) and ^{13}C NMR (CD_3OD, 150 MHz) data are given in Table 1; HR-ESI-MS *m*/*z* 361.2640 $[M]^+$ (calcd for $C_{25}H_{33}N_2^+$, 361.2638).

*Dispyridine (**3**).* Colorless oil; UV (MeOH) λ_{max} (log ε) 241.4 (1.34), 224.8 (1.71), 281.9 (1.81) nm; ^{1}H NMR (CD_3OD and acetone-d_6, 400 MHz) and ^{13}C NMR (CD_3OD and acetone-d_6, 100 MHz) data are given in Table 2; HR-ESI-MS *m*/*z* 282.2215 $[M]^+$ (calcd for $C_{20}H_{28}N^+$, 282.2216).

*Dispyrrolopyridine A (**4**).* Yellowish oil; UV (MeOH) λ_{max} 251, 364 nm; ^{1}H NMR (CD_3OD, 400 MHz) and ^{13}C NMR (CD_3OD, 100 MHz) data are given in Table 3; HR-ESI-MS *m*/*z* 445.2647 $[M]^+$ (calcd for $C_{32}H_{33}N_2^+$, 445.2638).

*Dispyrrolopyridine B (**5**).* Colorless powder; UV (MeOH) λ_{max} 228, 294, 345 nm; ^{1}H NMR (CD_3OD, 600 MHz) and ^{13}C NMR (CD_3OD, 150 MHz) data are given in Table 3; HR-ESI-MS *m*/*z* 425.2949 $[M]^+$ (calcd for $C_{30}H_{37}N_2^+$, 425.2951).

*Dispyrrole (**6**).* Yellowish oil; $[\alpha]_D^{25}$ − 4.9 (*c*, 0.14; CH_3OH); UV (MeOH) λ_{max} 208, 333 nm; ^{1}H NMR (DMSO-d_6, 600 MHz) and ^{13}C NMR (DMSO-d_6, 150 MHz) data are given in Table 4; HR-ESI-MS *m*/*z* 494.3165 $[M]^+$ (calcd for $C_{33}H_{40}N_3O^+$, 494.3166).

Plasmid Construction. The DNA template for amplification of the DisA BGC was isolated using the innuPREP bacteria DNA kit (Analytik Jena AG, Jena, Germany). The polymerase chain reaction (PCR) mixture (total volume 50 μL) contained 1 μL of dNTPs, 0.3 μL of each primer (primers used: *ten-decarbx-f* 5′-CAG CGG CCT GGT GCC GCG CGG CAG CAT GAG CGC TCA TTT TGA TTT ATC AA-3′; *ten-decarbx-r* 5′-TCA GTG GTG GTG GTG GTG GTG CTT ATT ATT TTT CTT TTA AAA TTT CTT CTC CAA ACTG-3′), 10 μL of Q5 buffer, 0.5 μL of Q5 polymerase (Promega, Madison, WI, U.S.A.), 37.5 μL of ddH_2O, 2 μL of dimethyl sulfoxide (DMSO), and 1 μL of DNA template. PCR was performed in a Biometra TRIO thermal cycler (Analytik Jena AG, Jena, Germany) using the following program: initial denaturation at 95 °C for 10 min; 34 cycles of denaturation at 95 °C for 45 s, annealing at 50 °C for 60 s, extension at 72 °C for 90 s; final extension at 72 °C for 5 min. The fragment with the desired size of ∼1.5 kbp was purified from 1% agarose gel using SV gel and the PCR Clean-Up system (Promega Corporation, Madison, WI, U.S.A.). PCR product (3 μL) was assembled into pRSF duet vector using Gibson assembly at 50 °C for 1 h. The *E. coli* TOP10 cells were thawed on ice for 5 min, and 3 μL of the Gibson product was added, mixed, and left on ice for 20 min. Subsequently, a heat shock at 42 °C for 90 s was applied to the mixture and 800 μL of LB medium was added to the mixture, followed by incubation at 37 °C for 60 min. Finally, the culture was centrifuged at 4000 rpm for 3 min resulting in a 100 μL cell pellet in the vial. The cell pellet was spread on LB agar plates containing 50 μg/mL kanamycin for clone selection. After overnight incubation colonies were transformed to 1 mL of LB medium containing 50 μg/mL kanamycin and cultivated at 37 °C overnight. A volume of 10 μL of this preculture was used to inoculate 5 mL of LB broth containing the same antibiotics followed by incubation at 37 °C overnight. Cells were recovered from 2 mL of LB broth by centrifugation and used for the plasmid isolation with the innuPREP plasmid mini kit 2.0 (Analytik Jena AG, Jena, Germany). The validated plasmid pRSF was transferred into *E. coli* Rosetta by chemical transformation as described above. The host strain was further plated onto kanamycin-containing (50 μg/mL) LB agar plates and incubated at 37 °C overnight. Colonies were picked and used for cultivation in 5 mL of kanamycin-containing (50 μg/mL) LB medium at 37 °C overnight, and cryocultures were prepared for *in vivo* assays or protein purification.

Heterologous Expression and Purification of DisA. The transgenic *E. coli* Rosetta (disA) was grown overnight in 30 mL of kanamycin-containing (50 μg/mL) LB medium at 37 °C. An inoculum of 15 mL of these cultures was used to inoculate 1.5 L of kanamycin-containing (50 μg/mL) LB medium; 0.1 mM isopropyl β-D-1-thiogalactopyranoside (IPTG) was added to the medium when the cultures reached an OD_{600} of 0.5, and the mixture was cultured overnight. Then, cells were collected by centrifugation at 4 °C and 10 000 rpm and resuspended in lysis buffer (50 mM NaH_2PO_4, 300 mM NaCl, and 10 mM imidazole; pH 8.0). The resulting suspensions were sonicated, followed by centrifugation at 4 °C at maximum speed for 30 min. The supernatant was loaded onto a pre-equilibrated 500 μL Qiagen Ni−NTA column. After washing with 2 mL of lysis buffer and 2 mL of wash buffer (20 mM imidazole lysis buffer), the His-tagged protein DisA was eluted from the column using elution buffer (250 mM imidazole lysis buffer) (Figure S45). The protein was resuspended into an imidazole-free buffer (50 mM NaH_2PO_4, 300 mM NaCl; pH 8.0) and concentrated using an Amicon Ultra-15 centrifugation membrane column.

Production of Discolin A and Discolin B in *E. coli* Rosetta (disA). The *E. coli* Rosetta (disA) was cultured in 30 mL of kanamycin-containing (50 μg/mL) LB medium at 30 °C overnight as preculture. A volume of 15 mL of this preculture was used to inoculate in 1.5 L of kanamycin-containing (50 μg/mL) LB medium at 37 °C; 0.1 mM IPTG was added into the medium when the cultures reached an OD_{600} of 0.5, and the mixture was cultured at 30

https://doi.org/10.1021/acs.jnatprod.1c01173
J. Nat. Prod. 2022, 85, 1039−1051

°C for 48 h. An amount of 5 mL of medium was harvested and extracted with EtOAc every 3 h after the sixth hour of cultivation and analyzed by UPLC−HRMS to calculate the concentration of discolin A and discolin B. The OD_{600} of the strain was measured every hour after the second hour of cultivation. The *E. coli* pRSF Rosetta cells without the target *disA* gene were cultivated under the same conditions and analyzed by UPLC−HRMS at 18, 24, and 30 h as the negative control. Data were collected from three replicates.

Enzymatic Activity of DisA. Enzymatic reactions were performed in 50 mM lysis buffer without imidazole (50 mM NaH_2PO_4, 300 mM NaCl, pH 8.0) containing 100 μM phenylalanine and 4 μM DisA in a total volume of 1 mL. After incubation at 30 °C overnight, the same volume of MeOH was added to quench the reactions. The reaction mixture was then centrifuged, and the supernatant was dried and redissolved in 50 μL of MeOH and analyzed by analytical HPLC (0−20 min, 5% MeCN; 20−30 min, gradient increased from 5% to 7.5% MeCN; 30−40 min, gradient increased from 7.5% to 100% MeCN).

Spontaneous Formation of Discolins. The reaction was performed in H_2O containing 200 mM PEA, 100 mM butyraldehyde, and 100 mM 2,3-butanedione (for discolin A) or 100 mM 2,3-pentanedione (for discolin B) in a total volume of 2 mL. The reaction mixture was stirred (1000 rpm) at room temperature for 3 h. Subsequently, the reaction mixture was evaporated to dryness, redissolved in MeOH, and analyzed by UPLC−HRMS.

Bioactivity Tests. Determination of the MICs of purified compounds **1**−**6** was carried out by micro broth dilution assays in 96-well plates. All compounds were dissolved in DMSO with a concentration of 6.4 mg/mL and tested in triplicate. For *E. coli* ATCC 25922 (wild type and efflux pump deficient strain Δ*tolC*), *B. subtilis* DSM10, and *S. aureus* ATCC25923, an overnight culture (37 °C, 180 rpm) was diluted to 5×10^5 cells/mL in cation-adjusted Mueller Hinton II medium (Becton Dickinson). *L. monocytogenes* DSM20600 was incubated for 2 days before the assay inoculum was adjusted. As positive controls, dilution series of rifampicin, tetracycline, and gentamycin (all Sigma-Aldrich) were prepared (64−0.03 μg/mL). Cell suspensions without test sample or antibiotic control were used as negative controls. After incubation (18 and 48 h for *L. monocytogenes*, 37 °C, 180 rpm, 80% RH) cell growth was assessed by turbidity measurement with a microplate spectrophotometer at 600 nm (LUMIstar Omega BMG Labtech GmbH, Ortenberg, Germany). The cell viability of *L. monocytogenes* was determined by ATP quantification (BacTiter-Glo, Promega GmbH, Walldorf, Germany) according to the manufacturer's instructions.

The preculture of *M. smegmatis* ATCC607 was incubated in brain−heart infusion broth (Becton Dickinson GmbH, Heidelberg, Germany) supplemented with Tween 80 [1.0% (v/v)] for 48 h at 37 °C and 180 rpm before the cell concentration was adjusted in cation-adjusted Mueller Hinton II medium. Isoniazid (Honeywell) was used instead of gentamycin as a third positive control. Cell viability was evaluated after 48 h (37 °C, 180 rpm, 80% RH) via ATP quantification (BacTiter-Glo, Promega GmbH, Walldorf, Germany) according to the manufacturer's instructions. *C. albicans* FH2173 was incubated for 48 h at 28 °C and 180 rpm before the preculture was diluted to 1×10^6 cells/mL in cation-adjusted Mueller Hinton II medium. For *A. flavus* ATCC9170, a previously prepared spore solution was used to prepare the assay inoculum of 1×10^5 spores/mL. Yeast and mold assays were incubated at 37 °C, 180 rpm, and 80% RH for 24 h (*A. flavus*) or 48 h (*Ca. albicans*). For both, tebuconazole (Cayman Chemical Company, Ann Arbor, MI, U.S.A.) and amphotericin B (Sigma-Aldrich) were used as the positive control (64−0.03 μg/mL). Readout was carried out by ATP quantification.

Determination of the antihelmithic activity of purified compounds **1**−**6** against the model organism *C. elegans* N2 was carried out by micro broth dilution assays.[49] *C. elegans* was kept on NGM agar plates with *E. coli* OP50 as the food source. After 4 days the plates contained sufficient gravid worms. The worms were washed from the plate by M9 buffer and collected in a polypropylene tube. Subsequently, egg isolation was carried out by treating the harvested worms with an alkaline hypochlorite solution (5 M NaOH and 5% NaClO 1:2). Larvae and adult worms do not tolerate this treatment, while the eggs survive. After several washing steps with M9 buffer, eggs were incubated overnight in NGM on a rotator. This synchronized suspension of hatched L1/L2 larvae was adjusted to 100 worms/mL and supplemented with cholesterol (5 μg/mL), carbenicillin (25 μg/mL), and *E. coli* OP50 (0.5%). This assay solution was distributed into 96-well plates and incubated with a dilution series of compounds **1**−**6** (64−0.03 μg/mL). An eight-point dilution series of ivermectin (40−0.3 ng/mL), colistin (64−0.03 μg/mL), and nisin (64−0.03 μg/mL) was used as a positive control to examine the different degrees of potency ranging from high (ivermectin) to none (nisin). Worm cultures without any treatment were cultured as a negative control. Solvent background was controlled by supplementation with pure DMSO without any compound. After 2 days of incubation at room temperature, the worm motility was determined with a binocular dissecting microscope.

■ ASSOCIATED CONTENT

Supporting Information

The Supporting Information is available free of charge at https://pubs.acs.org/doi/10.1021/acs.jnatprod.1c01173.

Proposed biosynthetic pathways of compounds **1**−**5**, HR-ESI-MS and NMR spectra for compounds **1**−**6**, SDS−PAGE gel of the purified His-tagged DisA, and HPLC spectra of *in vitro* formation of PEA (PDF)

■ AUTHOR INFORMATION

Corresponding Authors

Till F. Schäberle − *Institute for Insect Biotechnology, Justus-Liebig-University Giessen, 35392 Giessen, Germany; Fraunhofer Institute for Molecular Biology and Applied Ecology, Branch for Bioresources, 35392 Giessen, Germany; German Center for Infection Research, Partner Site Giessen-Marburg-Langen, 35392 Giessen, Germany;* orcid.org/0000-0001-9947-8079; Email: till.f.schaeberle@agrar.uni-giessen.de

Yang Liu − *Institute for Insect Biotechnology, Justus-Liebig-University Giessen, 35392 Giessen, Germany; Fraunhofer Institute for Molecular Biology and Applied Ecology, Branch for Bioresources, 35392 Giessen, Germany;* Email: Liu.Yang@agrar.uni-giessen.de

Luis Linares-Otoya − *Institute for Insect Biotechnology, Justus-Liebig-University Giessen, 35392 Giessen, Germany; Fraunhofer Institute for Molecular Biology and Applied Ecology, Branch for Bioresources, 35392 Giessen, Germany; Department of Pharmacology, National University of Trujillo, 13011 Trujillo, Peru*; Email: llinareso@unitru.edu.pe

Authors

Lei Wang − *Institute for Insect Biotechnology, Justus-Liebig-University Giessen, 35392 Giessen, Germany; Fraunhofer Institute for Molecular Biology and Applied Ecology, Branch for Bioresources, 35392 Giessen, Germany*

Virginia Linares-Otoya − *Department of Pharmacology, National University of Trujillo, 13011 Trujillo, Peru; Research Centre for Sustainable Development Uku Pacha, 13011 Trujillo, Peru*

Ute Mettal − *Institute for Insect Biotechnology, Justus-Liebig-University Giessen, 35392 Giessen, Germany; Fraunhofer Institute for Molecular Biology and Applied Ecology, Branch for Bioresources, 35392 Giessen, Germany*

https://doi.org/10.1021/acs.jnatprod.1c01173
J. Nat. Prod. 2022, 85, 1039−1051

Michael Marner − *Fraunhofer Institute for Molecular Biology and Applied Ecology, Branch for Bioresources, 35392 Giessen, Germany;* orcid.org/0000-0002-1024-1567
Lizbeth Armas-Mantilla − *Department of Pharmacology, National University of Trujillo, 13011 Trujillo, Peru; Research Centre for Sustainable Development Uku Pacha, 13011 Trujillo, Peru*
Sabine Willbold − *Central Institute for Engineering, Electronics and Analytics, Analytics, Forschungszentrum Juelich GmbH, 52425 Juelich, Germany*
Tibor Kurtán − *Department of Organic Chemistry, University of Debrecen, H-4002 Debrecen, Hungary;* orcid.org/0000-0002-8831-8499

Complete contact information is available at: https://pubs.acs.org/10.1021/acs.jnatprod.1c01173

Notes

The authors declare no competing financial interest.

■ ACKNOWLEDGMENTS

This work was supported by the China Scholarship Council (CSC No. 201908080177). Furthermore, the authors would like to thank the Deutscher Akademischer Austauschdienst (DAAD) for funding under the framework of PROPERU, and L.L.-O., V. L.-O., and L.A.-M. are thankful to FONDECYT (Proyecto 041-2019 FONDECYT-BM). The Schäberle lab is part of the German Center of Infection Research (DZIF) and supported by the Hessen State Ministry of Higher Education, Research and the Arts (HMWK) via the LOEWE Center for Insect Biotechnology and Bioresources.

■ REFERENCES

(1) Schinke, C.; Martins, T.; Queiroz, S. C. N.; Melo, I. S.; Reyes, F. G. R. *J. Nat. Prod.* **2017**, *80*, 1215−1228.
(2) Jensen, P. R.; Moore, B. S.; Fenical, W. *Natural product reports* **2015**, *32*, 738−751.
(3) Offret, C.; Desriac, F.; Le Chevalier, P.; Mounier, J.; Jégou, C.; Fleury, Y. *Marine drugs* **2016**, *14*, 129.
(4) Amiri Moghaddam, J.; Crüsemann, M.; Alanjary, M.; Harms, H.; Dávila-Céspedes, A.; Blom, J.; Poehlein, A.; Ziemert, N.; König, G. M.; Schäberle, T. F. *Sci. Rep.* **2018**, *8*, 16600.
(5) Buijs, Y.; Bech, P. K.; Vazquez-Albacete, D.; Bentzon-Tilia, M.; Sonnenschein, E. C.; Gram, L.; Zhang, S.-D. *Natural product reports* **2019**, *36*, 1333−1350.
(6) Demay, J.; Bernard, C.; Reinhardt, A.; Marie, B. *Mar. Drugs* **2019**, *17*, 320.
(7) Fernández-Gómez, B.; Richter, M.; Schüler, M.; Pinhassi, J.; Acinas, S. G.; González, J. M.; Pedrós-Alió, C. *ISME journal* **2013**, *7*, 1026−1037.
(8) Krüger, K.; Chafee, M.; Ben Francis, T.; Glavina Del Rio, T.; Becher, D.; Schweder, T.; Amann, R. I.; Teeling, H. *ISME journal* **2019**, *13*, 2800−2816.
(9) Matsuo, Y.; Imagawa, H.; Nishizawa, M.; Shizuri, Y. *Science (New York, N.Y.)* **2005**, *307*, 1598.
(10) Alsufyani, T.; Califano, G.; Deicke, M.; Grueneberg, J.; Weiss, A.; Engelen, A. H.; Kwantes, M.; Mohr, J. F.; Ulrich, J. F.; Wichard, T. *Journal of experimental botany* **2020**, *71*, 3340−3349.
(11) Zan, J.; Li, Z.; Tianero, M. D.; Davis, J.; Hill, R. T.; Donia, M. S. *Science* **2019**, *364*, eaaw6732.
(12) Kim, Y.-O.; Park, I.-S.; Park, S.; Nam, B.-H.; Park, J.-M.; Kim, D.-G.; Yoon, J.-H. *International journal of systematic and evolutionary microbiology* **2016**, *66*, 1174−1179.
(13) Bridel, S.; Olsen, A.-B.; Nilsen, H.; Bernardet, J.-F.; Achaz, G.; Avendaño-Herrera, R.; Duchaud, E. *Genome biology and evolution* **2018**, *10*, 452−457.
(14) Suzuki, M.; Nakagawa, Y.; Harayama, S.; Yamamoto, S. *International journal of systematic and evolutionary microbiology* **2001**, *51*, 1639−1652.
(15) Avendaño-Herrera, R.; Toranzo, A. E.; Magariños, B. *Diseases of aquatic organisms* **2006**, *71*, 255−266.
(16) Lloyd, M. M.; Pespeni, M. H. *Sci. Rep.* **2018**, *8*, 16476.
(17) Banning, E. C.; Casciotti, K. L.; Kujawinski, E. B. *FEMS Microbiol. Ecol.* **2010**, *73*, 254−270.
(18) Kientz, B.; Ducret, A.; Luke, S.; Vukusic, P.; Mignot, T.; Rosenfeld, E. *PLoS One*, **2012**, *7*, e52900.
(19) Cui, B.; Zheng, B. L.; He, K.; Zheng, Q. Y. *J. Nat. Prod.* **2003**, *66*, 1101−1103.
(20) Jin, W.; Chen, X.; Dai, P.; Yu, L. *Phytochem. Lett.* **2016**, *17*, 158−161.
(21) Rennison, D.; Conole, D.; Tingle, M. D.; Yang, J.; Eason, C. T.; Brimble, M. A. *Bioorg. Med. Chem. Lett.* **2013**, *23*, 6629−6635.
(22) Balaban, A. T.; Dinculescu, A.; Elguero, J.; Faure, R. *Magn. Reson. Chem.* **1985**, *23*, 553−558.
(23) Pesnot, T.; Gershater, M. C.; Edwards, M.; Ward, J. M.; Hailes, H. C. *Molecules* **2017**, *22*, 626.
(24) Zhang, J.; Yang, Q.; Cross, J. B.; Romero, J. A. C.; Poutsiaka, K. M.; Epie, F.; Bevan, D.; Wang, B.; Zhang, Y.; Chavan, A.; et al. *J. Med. Chem.* **2015**, *58*, 8503−8512.
(25) Veselov, M. S.; Ivanenkov, Y. A.; Yamidanov, R. S.; Osterman, I. A.; Sergiev, P. V.; Aladinskiy, V. A.; Aladinskaya, A. V.; Terentiev, V. A.; Ayginin, A. A.; Skvortsov, D. A.; et al. *Mol. Diversity* **2020**, *24*, 233−239.
(26) Blass, B. *ACS Med. Chem. Lett.* **2015**, *6*, 726−728.
(27) Filla, S. A.; Mathes, B. M.; Johnson, K. W.; Phebus, L. A.; Cohen, M. L.; Nelson, D. L.; Zgombick, J. M.; Erickson, J. A.; Schenck, K. W.; Wainscott, D. B.; et al. *J. Medicinal Chem.* **2003**, *46*, 3060−3071.
(28) Marcobal, A.; De Las Rivas, B.; Landete, J. M.; Tabera, L.; Muñoz, R. *Critical Rev. Food Sci. Nutr.* **2012**, *52*, 448−467.
(29) Liu, F.; Xu, W.; Du, L.; Wang, D.; Zhu, Y.; Geng, Z.; Zhang, M.; Xu, W. *Journal of food protection* **2014**, *77*, 592−598.
(30) Fujita, M. J.; Goto, Y.; Sakai, R. *Mar. Drugs* **2018**, *16*, 342.
(31) Yan, Y.; Yang, J.; Yu, Z.; Yu, M.; Ma, Y.-T.; Wang, L.; Su, C.; Luo, J.; Horsman, G. P.; Huang, S.-X. *Nat. Commun.* **2016**, *7*, 13083.
(32) Linares-Otoya, L.; Liu, Y.; Linares-Otoya, V.; Armas-Mantilla, L.; Crüsemann, M.; Ganoza-Yupanqui, M. L.; Campos-Florian, J.; König, G. M.; Schäberle, T. F. *ACS Chem. Biol.* **2019**, *14*, 176−181.
(33) Burns, N. Z.; Baran, P. S. *Angewandte Chemie (International ed. in English)* **2008**, *47*, 205−208.
(34) Dagorn, F.; Yan, L.-H.; Gravel, E.; Leblanc, K.; Maciuk, A.; Poupon, E. *Tetrahedron Lett.* **2011**, *52*, 3523−3526.
(35) Snider, B. B.; Neubert, B. J. *Org. Lett.* **2005**, *7*, 2715−2718.
(36) Usuki, T.; Sugimura, T.; Komatsu, A.; Koseki, Y. *Org. Lett.* **2014**, *16*, 1672−1675.
(37) Radziszewski, B. *Ber. Dtsch. Chem. Ges* **1882**, *15*, 1493−1496.
(38) Wang, Z., Ed. *Comprehensive Organic Name Reactions and Reagents*; John Wiley & Sons, Inc.: Hoboken, NJ, 2010.
(39) Gelens, E.; Kanter, F. J. J.; Schmitz, R. F.; Sliedregt, L. A. J. M.; van Steen, B. J.; Kruse, C. G.; Leurs, R.; Groen, M. B.; Orru, R. V. A. *Mol. Diversity* **2006**, *10*, 17−22.
(40) Stewart, G. *Fermentation* **2017**, *3*, 63.
(41) Dickschat, J. S.; Wickel, S.; Bolten, C. J.; Nawrath, T.; Schulz, S.; Wittmann, C. *Eur. J. Org. Chem.* **2010**, *2010*, 2687−2695.
(42) Wolkenberg, S. E.; Wisnoski, D. D.; Leister, W. H.; Wang, Y.; Zhao, Z.; Lindsley, C. W. *Org. Lett.* **2004**, *6*, 1453−1456.
(43) Kanehisa, M.; Goto, S. *Nucleic acids research* **2000**, *28*, 27−30.
(44) Kanehisa, M. *Protein Sci.* **2019**, *28*, 1947−1951.
(45) Kanehisa, M.; Furumichi, M.; Sato, Y.; Ishiguro-Watanabe, M.; Tanabe, M. *Nucleic acids research* **2021**, *49*, D545−D551.
(46) Rosenberg, E.; Schleifer, K. H.; Stackebrandt, E.; Dworkin, M. *The Prokaryotes: A Handbook on the Biology of Bacteria*, 3rd ed.; Springer: New York, 2006.
(47) Chen, Y.; Tang, J.; Tang, X.; Wang, C.; Lian, Y.; Shao, Z.; Yao, X.; Gao, H. *Journal of antibiotics* **2013**, *66*, 655−661.

(48) Hamana, K.; Itoh, T.; Benno, Y.; Hayashi, H. *Journal of general and applied microbiology* **2008**, *54*, 229−236.
(49) Stiernagle, T. Maintenance of *C. elegans*. In *WormBook*; The C. elegans Research Community, 2006.

https://doi.org/10.1021/acs.jnatprod.1c01173
J. Nat. Prod. 2022, 85, 1039−1051

Supporting Information of Publication 1

Supplementary Information

Discovery and Biosynthesis of Antimicrobial Phenethylamine Alkaloids from the Marine Flavobacterium *Tenacibaculum discolor* sv11

Lei Wang,[†,‡] *Virginia Linares-Otoya,*[§,^] *Yang Liu,*[†,‡,*] *Ute Mettal,*[†,‡] *Michael Marner,*[‡] *Lizbeth Armas-Mantilla,*[§,^] *Sabine Willbold,*[‖] *Tibor Kurtán,*[O] *Luis Linares-Otoya,*[†,‡,§,*] *Till F. Schäberle* [†,‡,▽,*]

[†]Institute for Insect Biotechnology, Justus-Liebig-University Giessen, 35392 Giessen, Germany

[‡]Fraunhofer Institute for Molecular Biology and Applied Ecology (IME), Branch for Bioresources, 35392 Giessen, Germany

[§]Department of Pharmacology, Faculty of Pharmacy and Biochemistry, National University of Trujillo, 13011 Trujillo, Peru

[^]Research Centre for Sustainable Development Uku Pacha, 13011 Trujillo, Peru

[‖]Central Institute for Engineering, Electronics and Analytics, Analytics (ZEA-3), Forschungszentrum Juelich GmbH, 52425 Juelich, Germany.

[▽]German Center for Infection Research (DZIF), Partner Site Giessen-Marburg-Langen, 35392 Giessen, Germany.

[O]Department of Organic Chemistry, University of Debrecen, H-4002 Debrecen, Hungary.

Contents

Proposed biosynthetic pathways of compounds 1-5 from PEA. Several mechanisms have been published for the Chichibabin pyridine synthesis[1–5] . Basically, all rely on a set of condensation reactions followed by a final auto-oxidation. The mechanism shown in **Figure S1** is based upon the publication by Dagorn *et al.*.[6] The initial step is the formation of an iminium ion (**9**) by the reaction of *n*-butyraldehyde with 2-phenylethylamine, which according to our experiments is derived from the DisA catalyzed decarboxylation of phenylalanine. This iminium ion subsequently undergoes a Mannich reaction with the enol form of a second molecule of *n*-butyraldehyde, yielding compound **13**. This secondary amine (**13**) reacts again with *n*-butyraldehyde to furnish the enamine **14**, which in its turn cyclizes to afford compound **15**. Subsequent elimination of water yields a dihydropyridinium species **16**, which finally undergoes auto-oxidation to afford dispyridine **3**.

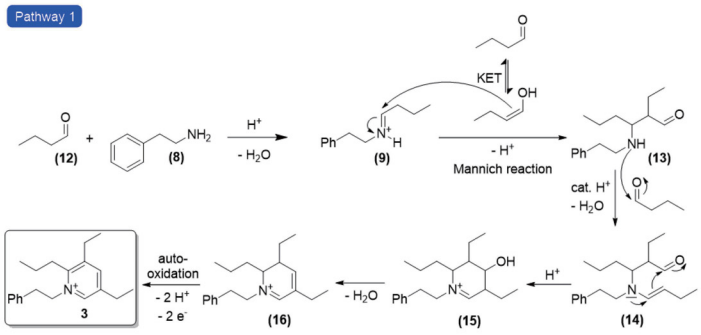

Scheme S1. Detailed description of the possible pathways leading to compound **3**.

1

Concerning the mechanism of the Radziszewski reaction, different routes are possible, depending on whether the amine first reacts with the aldehyde or the dicarbonyl compound and thus reflects their relative reactivities.[7, 8] In this respect, the different reaction routes have also been reported to have an impact on the substitution pattern when unsymmetrical diketones are used in the reaction.[8] In **Figure S2** two possible pathways for the non-enzymatic formation of discolins A and B are depicted. In both cases PEA, which is produced by DisA catalyzed decarboxylation of phenylalanine, serves as starting material. According to Baldwin's rules，[9, 10] pathway 2a would result in a kinetically disfavored 5-endo-trig cyclization, so that pathway 2b seems more likely as it proceeds via a kinetically favored 5-exo-trig ring closure.

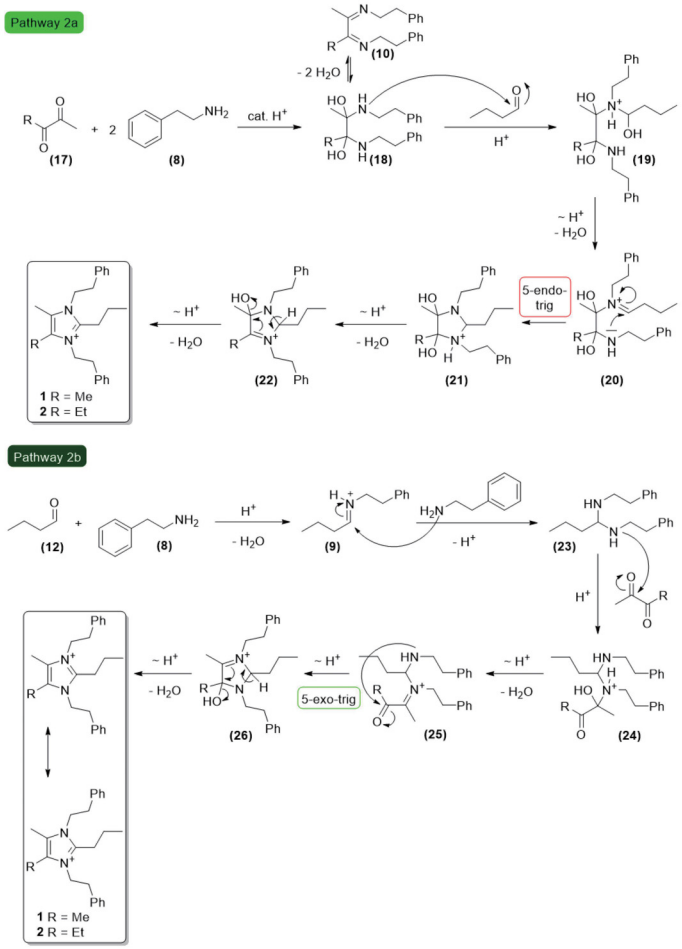

Scheme S2. Detailed description of the possible pathways leading to compounds **1** and **2**.

In analogy to pathways 1 and 2a, theoretically two different reaction mechanisms would be viable for the biosynthesis of **4** and **5**, depending on whether the initial reaction partner of PEA is *n*-butyraldehyde (pathway 3, **Figure S3**) or a suitable 1,2-diketone (pathway not shown). Yet, pathway 3 appears to be the more likely of both potential mechanisms as it comprises a kinetically favored 5-exo-trig cyclization instead of a disfavored 5-endo-trig cyclization. The last stage of the reaction appears to include oxidative steps, as described for dispyridine **3**. But unlike dispyridine, here two oxidation reactions, a $2H^+$,$2e^-$ oxidation and a $1H^+$,$2e^-$ oxidation, would need to take place, which might necessitate the involvement of the redox cofactors FAD and NAD^+.

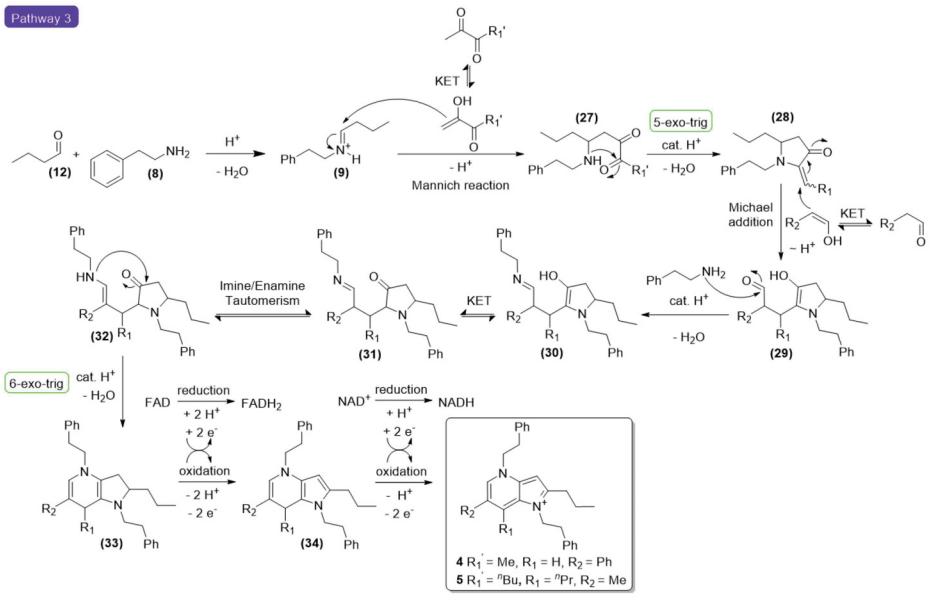

Scheme S3. Possible pathway leading to compounds **4**-**5**.

Supplementary Figures

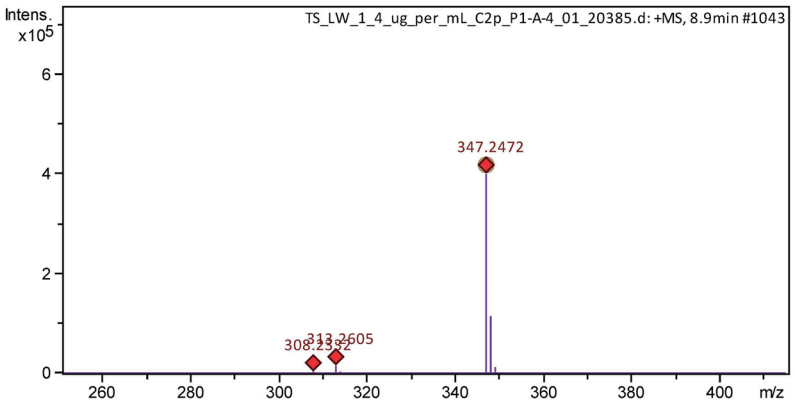

Meas. m/z	#	Ion Formula	m/z	err [ppm]	mSigma	# mSigma	Score	rdb	eÂ¯Conf	N-Rule
347.2472	1	C24H31N2	347.2482	2.9	10.2	1	100.00	10.5	even	ok
347.2472	2	C19H31N4O2	347.2442	-8.6	36.9	2	12.05	6.5	even	ok

Figure S1. The HR-ESI-MS of compound **1**.

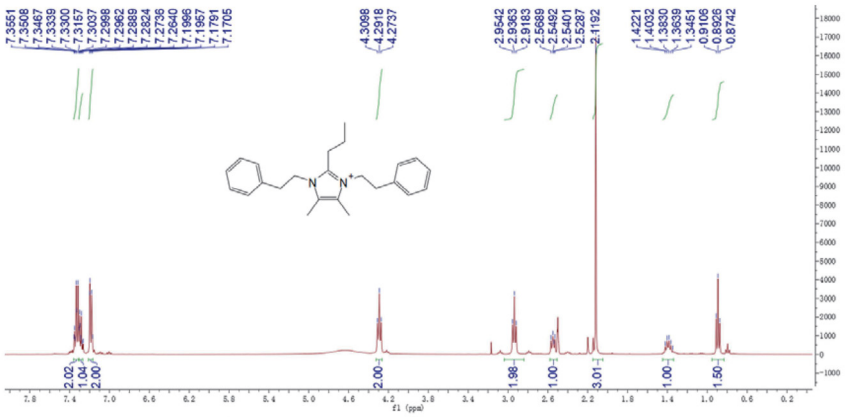

Figure S2. The ^{1}H-NMR (400 MHz, DMSO-*d*$_6$) spectrum of compound **1**.

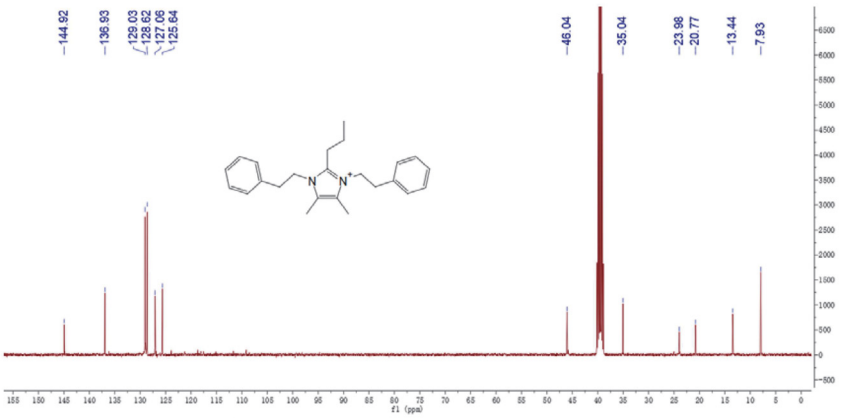

Figure S3. The ^{13}C-NMR (100 MHz, DMSO-*d*$_6$) spectrum of compound **1**.

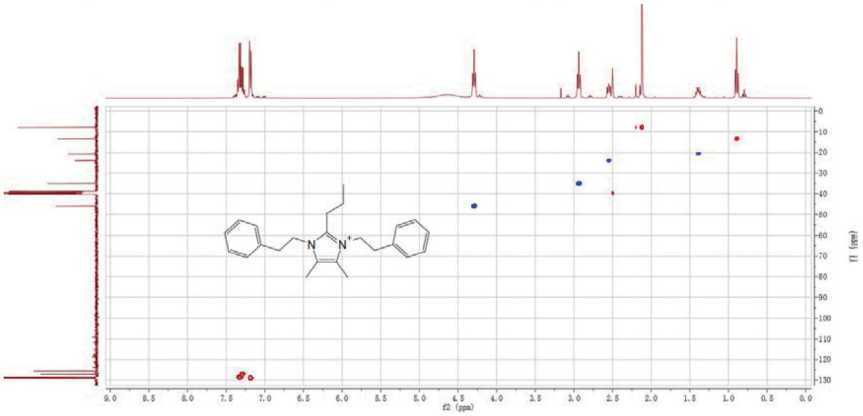

Figure S4. The HSQC (400 MHz, DMSO-*d*$_6$) spectrum of compound **1**.

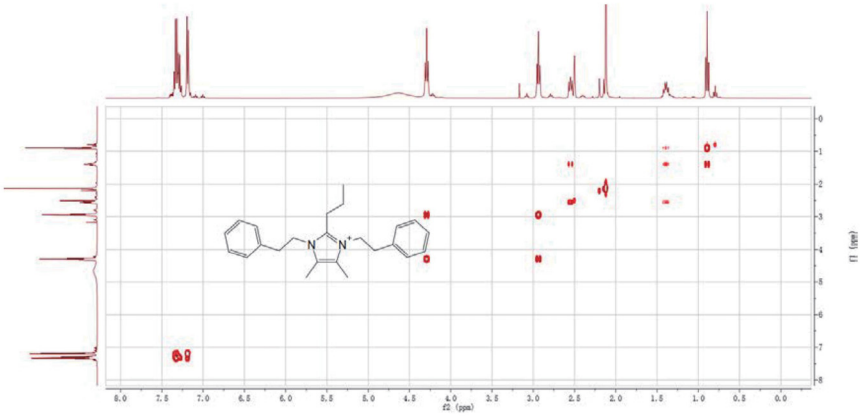

Figure S5. The ^{1}H-^{1}H COSY (400 MHz, DMSO-*d*$_6$) spectrum of compound **1**.

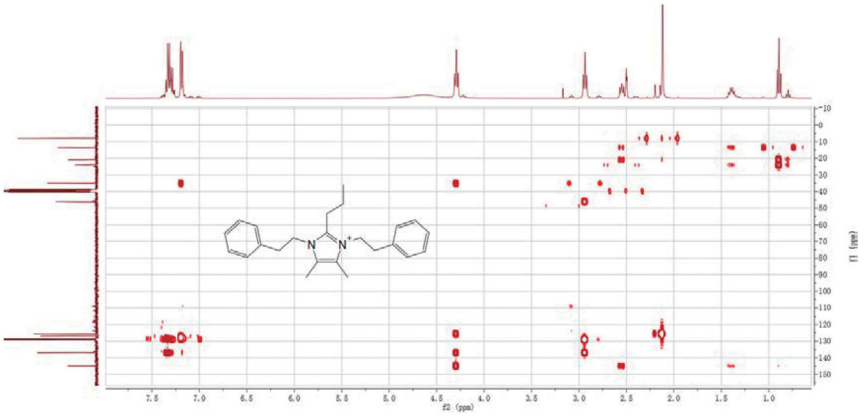

Figure S6. The HMBC (400 MHz, DMSO-d_6) spectrum of compound **1**.

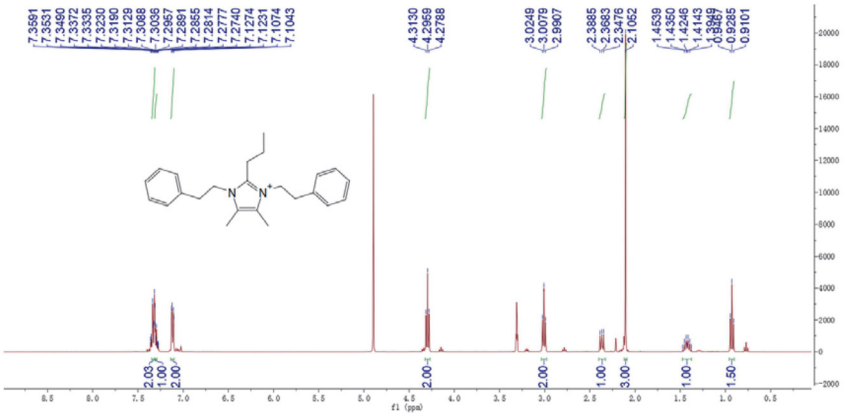

Figure S7. The ^{1}H-NMR (400 MHz, CD_3OD) spectrum of compound **1**.

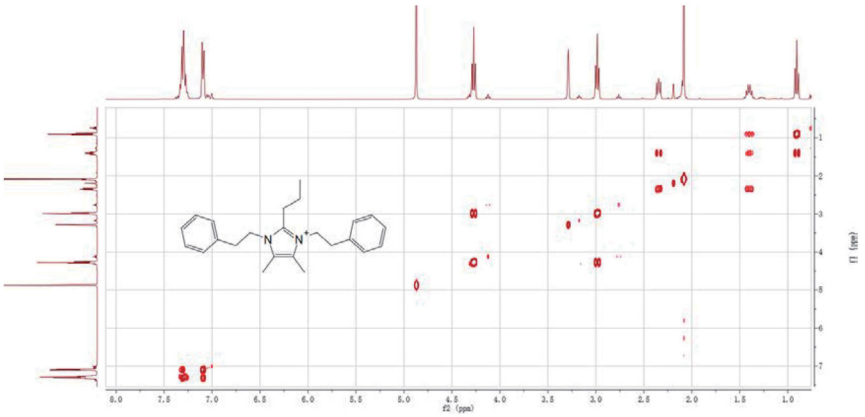

Figure S8. The ^{1}H-^{1}H COSY (400 MHz, CD_3OD) spectrum of compound **1**.

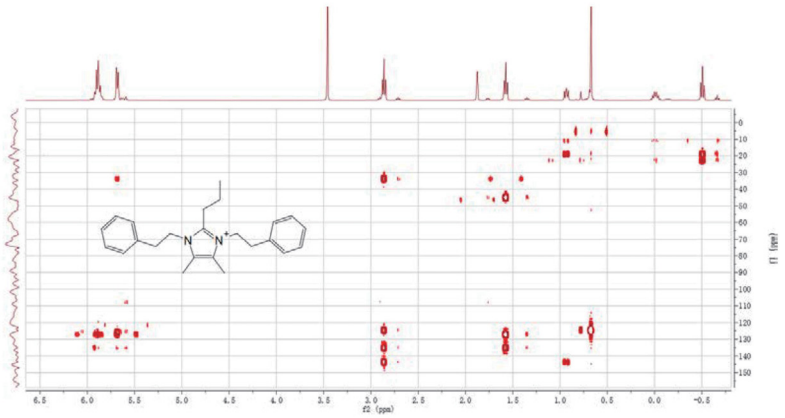

Figure S9. The HMBC (400 MHz, CD_3OD) spectrum of compound **1**.

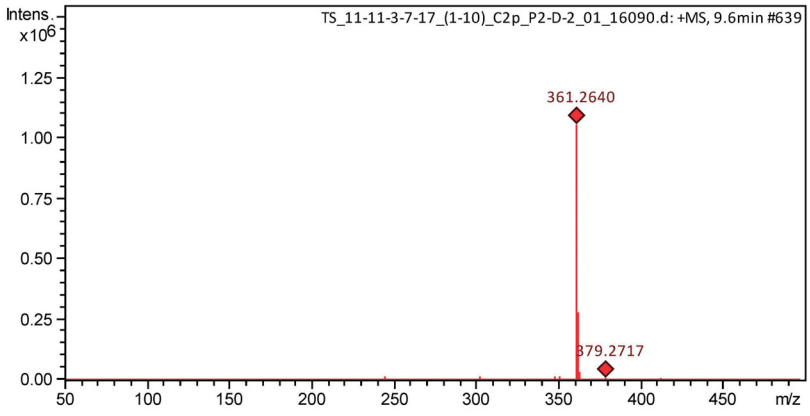

Meas. m/z	#	Ion Formula	m/z	err [ppm]	mSigma	# mSigma	Score	rdb	eÂ¯Conf	N-Rule
361.2640	1	C25H33N2	361.2638	-0.5	7.3	1	100.00	10.5	even	ok
361.2640	2	C20H33N4O2	361.2598	-11.6	19.6	2	3.05	6.5	even	ok

Figure S10. The HR-ESI-MS of compound **2**.

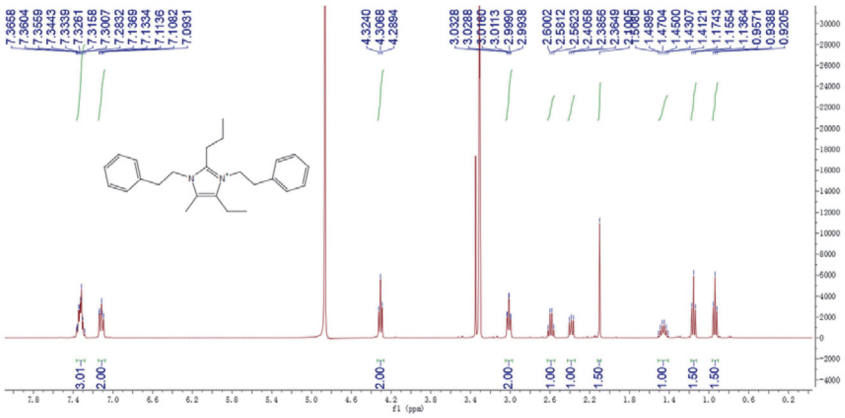

Figure S11. The ^{1}H-NMR (400 MHz, CD_3OD) spectrum of compound **2**.

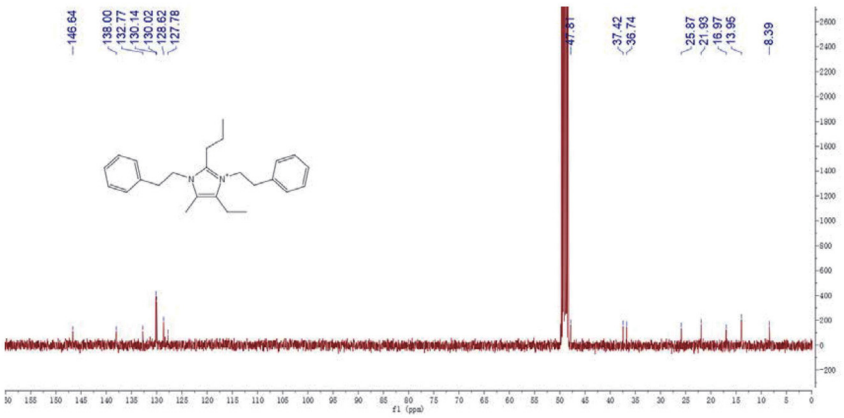

Figure S12. The ^{13}C-NMR (100 MHz, CD_3OD) spectrum of compound **2**.

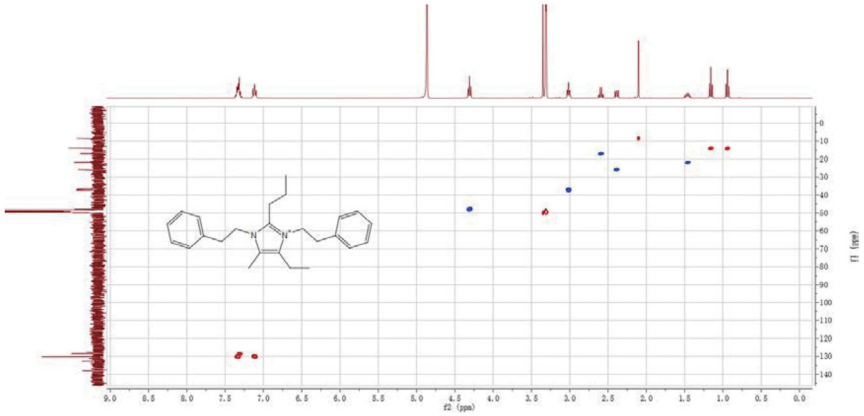

Figure S13. The HSQC (400 MHz, CD_3OD) spectrum of compound **2**.

10

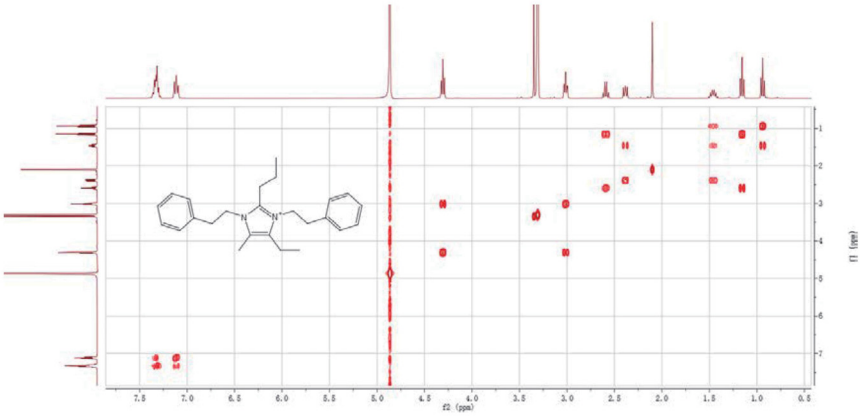

Figure S14. The ^{1}H-^{1}H COSY (400 MHz, CD_3OD) spectrum of compound **2**.

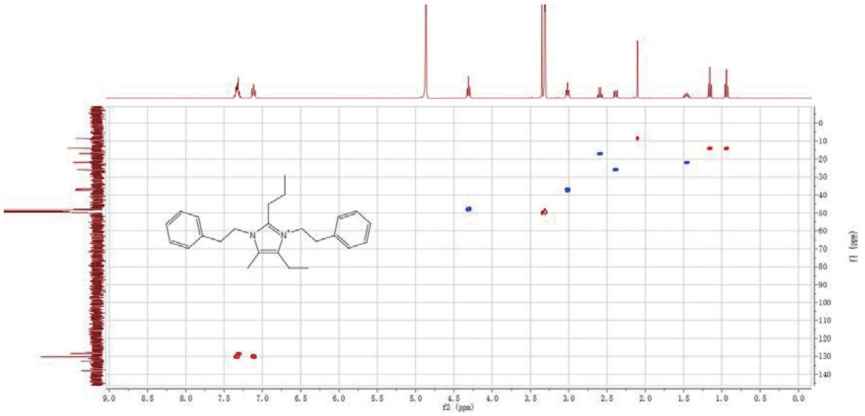

Figure S15. The HMBC (400 MHz, CD_3OD) spectrum of compound **2**.

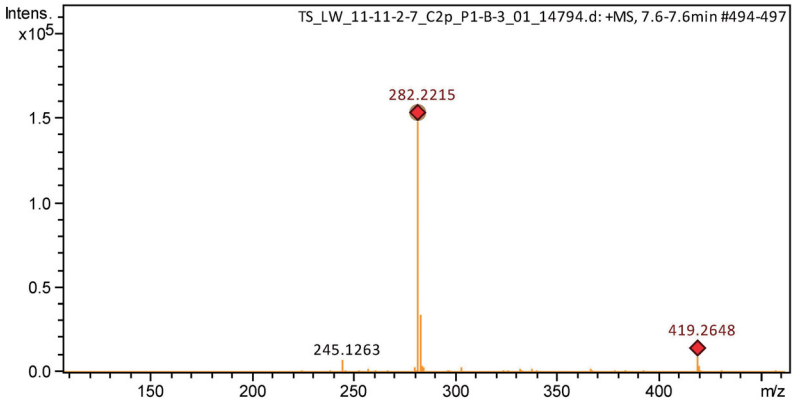

Meas. m/z	#	Ion Formula	m/z	err [ppm]	mSigma	# mSigma	Score	rdb	eÂ¯Conf	N-Rule
282.2215	1	C20H28N	282.2216	0.6	4.2	1	100.00	7.5	even	ok
282.2215	2	C15H28N3O2	282.2176	-13.7	30.9	2	3.31	3.5	even	ok

Figure S16. The HR-ESI-MS of compound **3**.

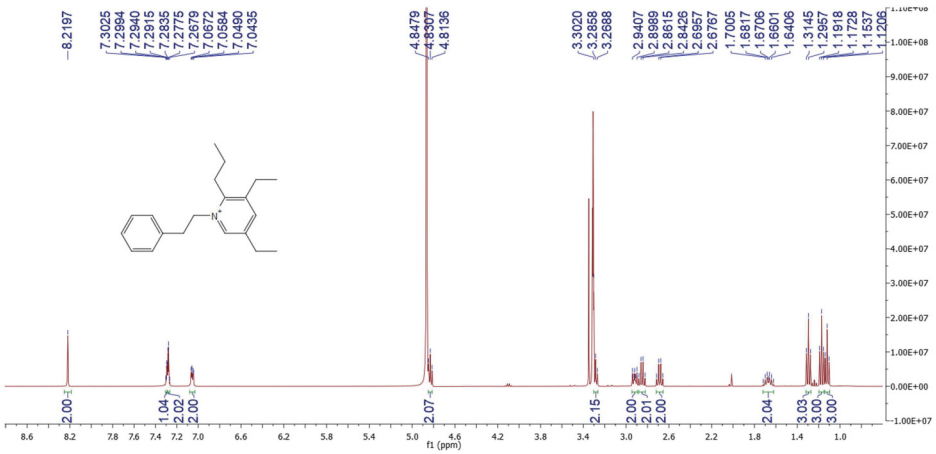

Figure S17. The ^{1}H-NMR (400 MHz, CD_3OD) spectrum of compound **3**.

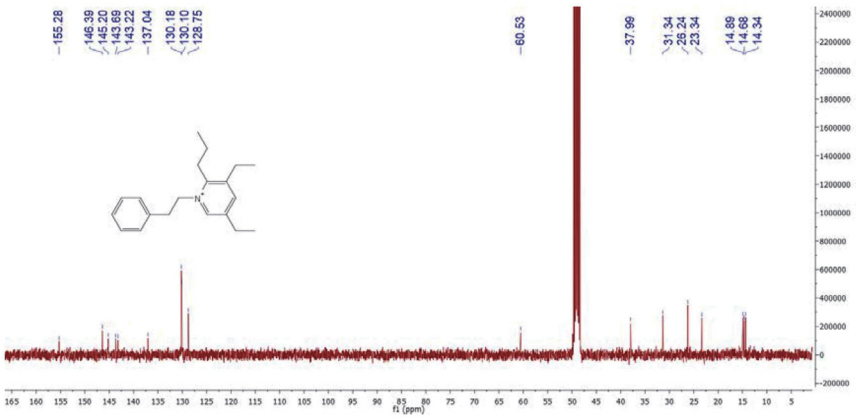

Figure S18. The ^{13}C-NMR (100 MHz, CD_3OD) spectrum of compound **3**.

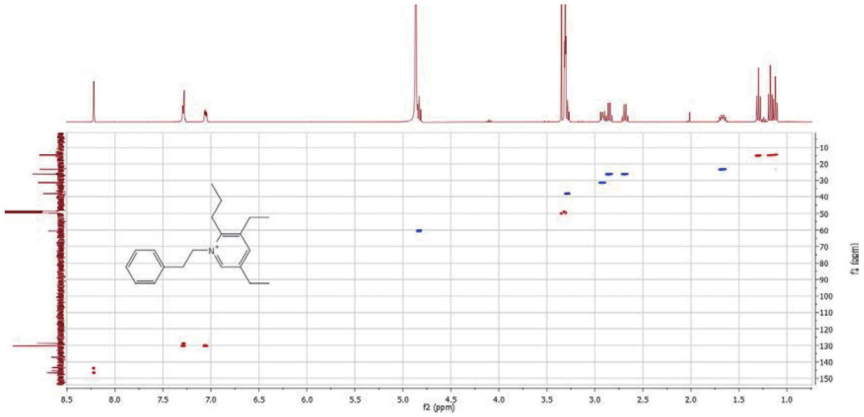

Figure S19. The HSQC (400 MHz, CD_3OD) spectrum of compound **3**.

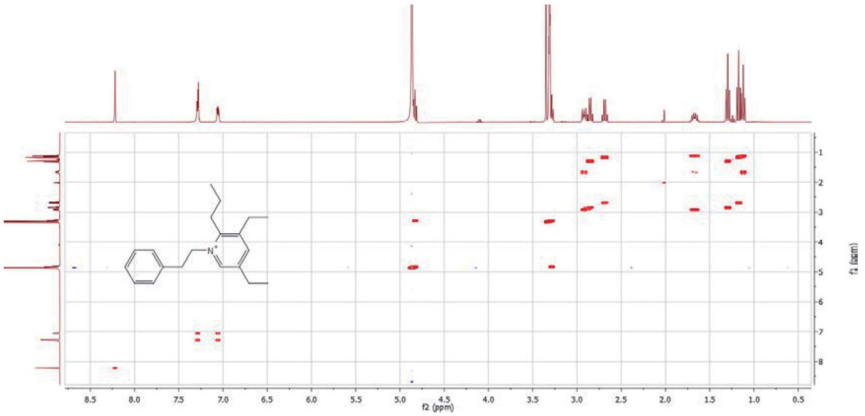

Figure S20. The ^{1}H-^{1}H COSY (400 MHz, CD_3OD) spectrum of compound **3**.

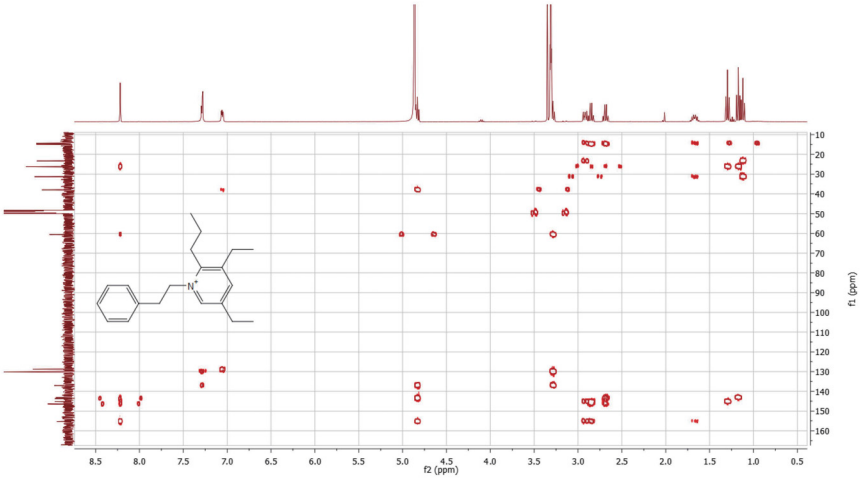

Figure S21. The HMBC (400 MHz, CD_3OD) spectrum of compound **3**.

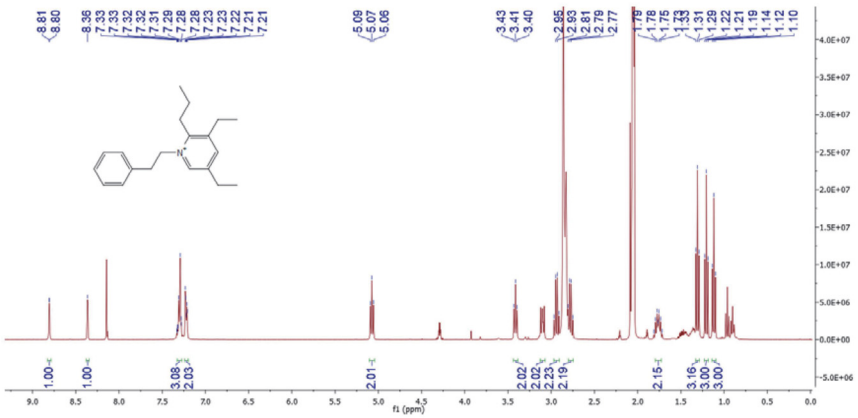

Figure S22. The ^{1}H-NMR (400 MHz, acetone-d_6) spectrum of compound **3**.

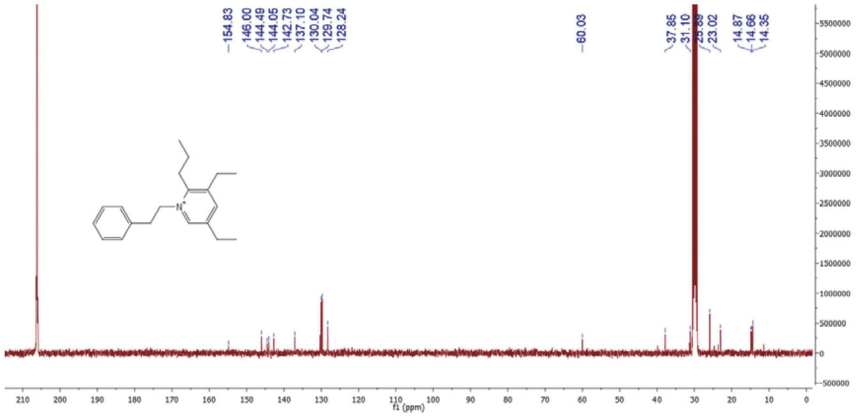

Figure S23. The ^{13}C-NMR (100 MHz, acetone-d_6) spectrum of compound **3**.

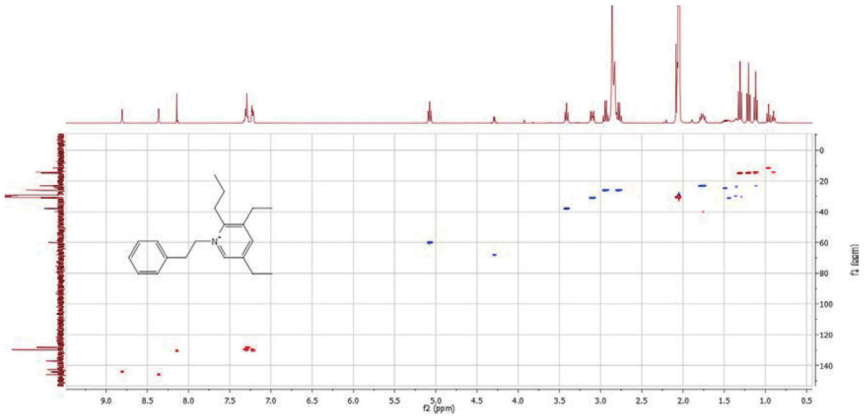

Figure S24. The HSQC (400 MHz, acetone-d_6) spectrum of compound **3**.

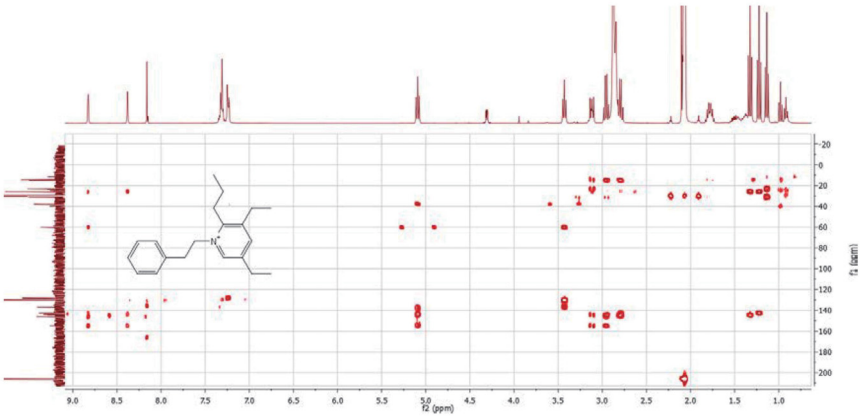

Figure S25. The HMBC (400 MHz, acetone-d_6) spectrum of compound **3**.

16

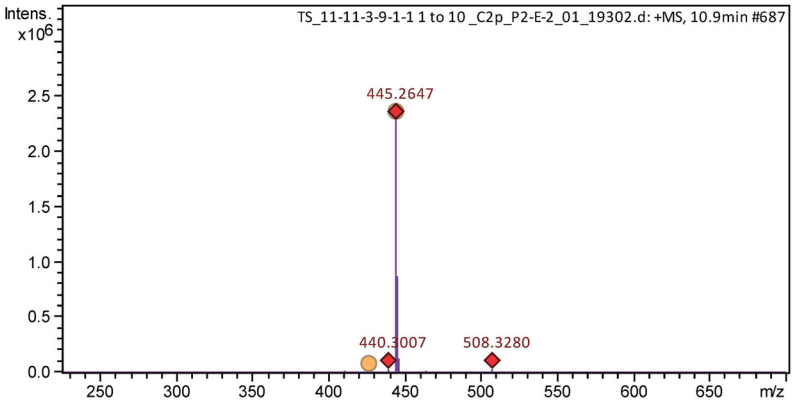

Meas. m/z	#	Ion Formula	m/z	err [ppm]	mSigma	# mSigma	Score	rdb	eÂ¯ Conf	N-Rule
445.2647	1	C32H33N2	445.2638	-2.0	15.1	1	100.00	17.5	even	ok
445.2647	2	C27H33N4O2	445.2598	-11.1	41.2	2	1.14	13.5	even	ok

Figure S26. The HR-ESI-MS of compound **4**.

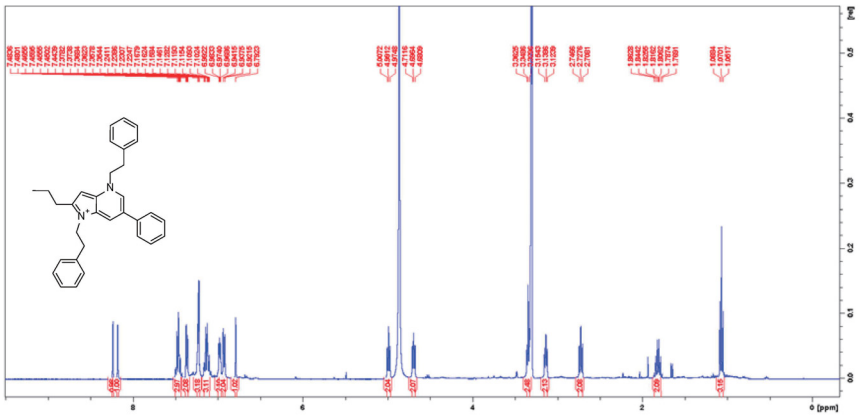

Figure S27. The ^{1}H-NMR (400 MHz, CD_3OD) spectrum of compound **4**.

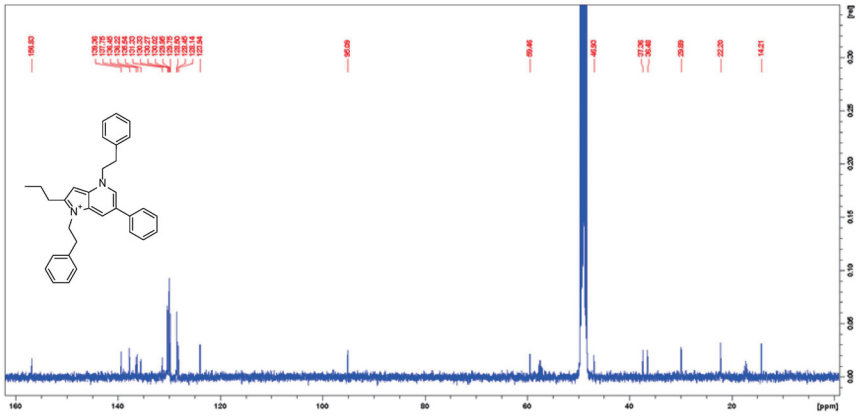

Figure S28. The ^{13}C-NMR (100 MHz, CD_3OD) spectrum of compound **4**.

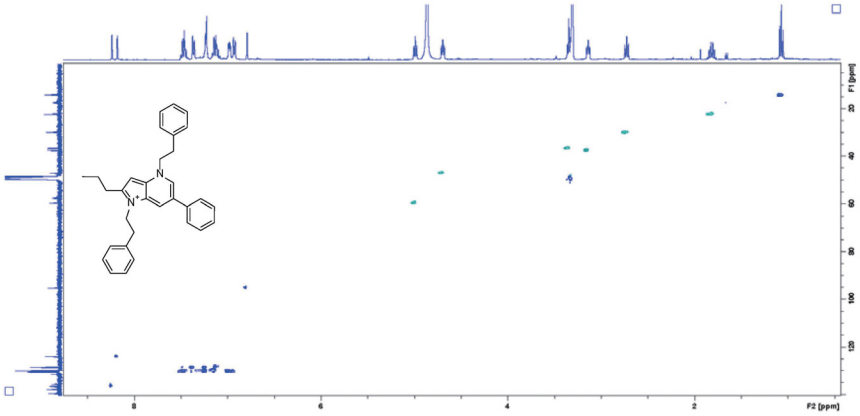

Figure S29. The HSQC (400 MHz, CD_3OD) spectrum of compound **4**.

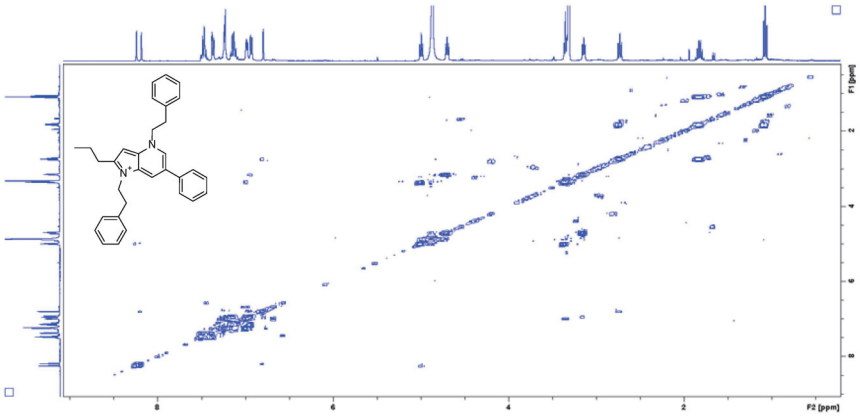

Figure S30. The ^{1}H-^{1}H COSY (400 MHz, CD_3OD) spectrum of compound **4**.

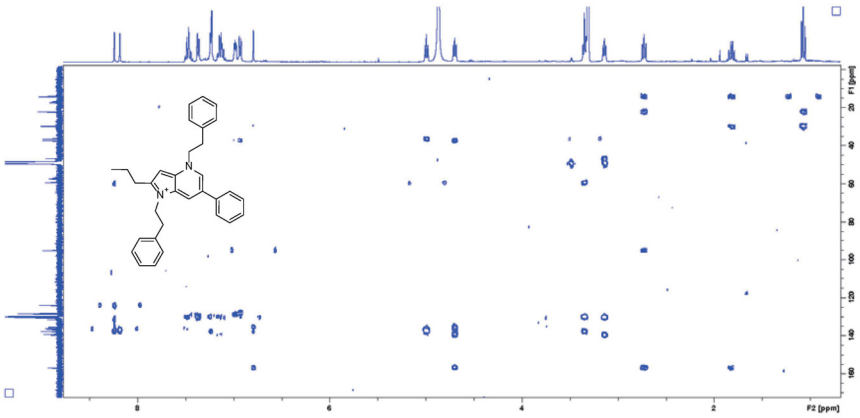

Figure S31. The HMBC (400 MHz, CD_3OD) spectrum of compound **4**.

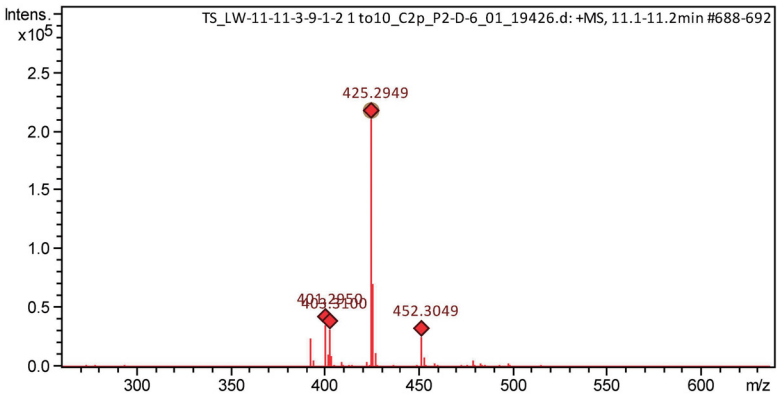

Meas. m/z	#	Ion Formula	m/z	err [ppm]	mSigma	# mSigma	Score	rdb	eÂ¯Conf	N-Rule
425.2949	1	C30H37N2	425.2951	0.6	1.3	1	100.00	13.5	even	ok
425.2949	2	C25H37N4O2	425.2911	-8.9	25.9	2	4.00	9.5	even	ok

Figure S32. The HR-ESI-MS of compound **5**.

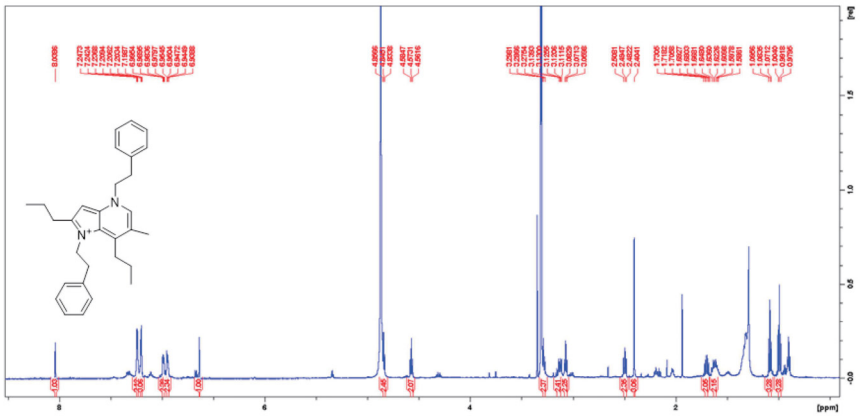

Figure S33. The ^{1}H-NMR (600 MHz, CD_3OD) spectrum of compound **5**.

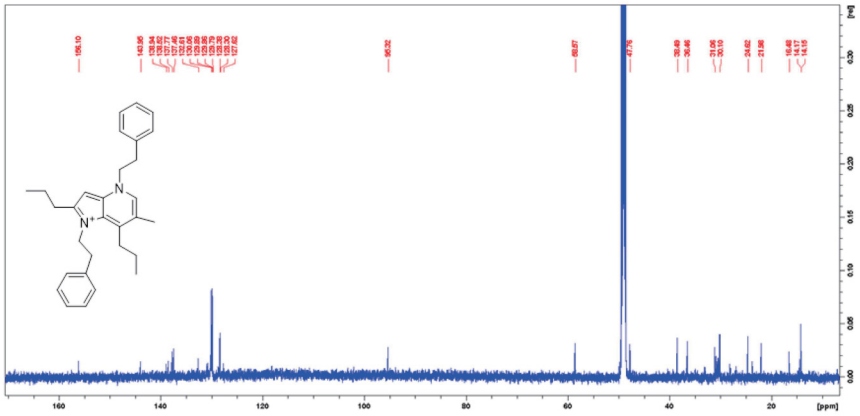

Figure S34. The ^{13}C-NMR (150 MHz, CD_3OD) spectrum of compound **5**.

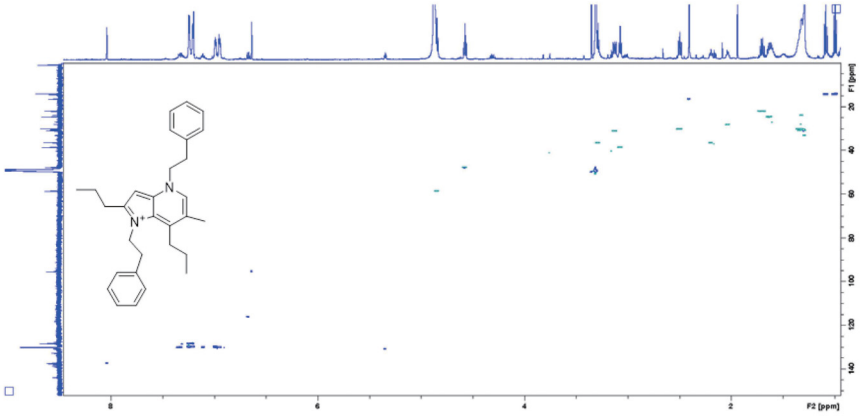

Figure S35. The HSQC (600 MHz, CD_3OD) spectrum of compound **5**.

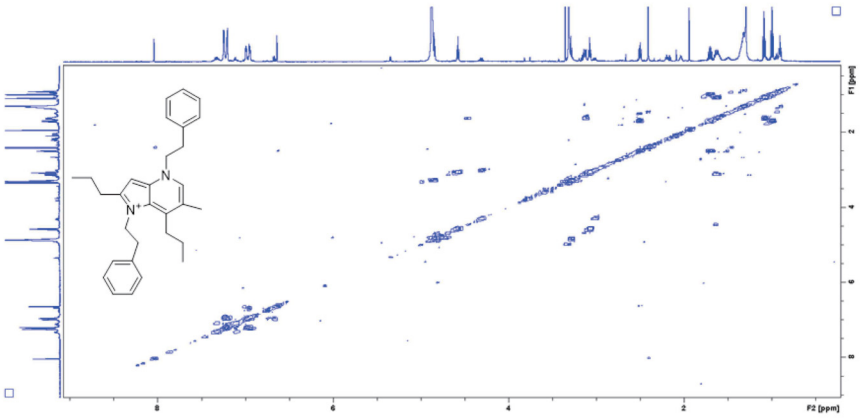

Figure S36. The ^{1}H-^{1}H COSY (600 MHz, CD_3OD) spectrum of compound **5**.

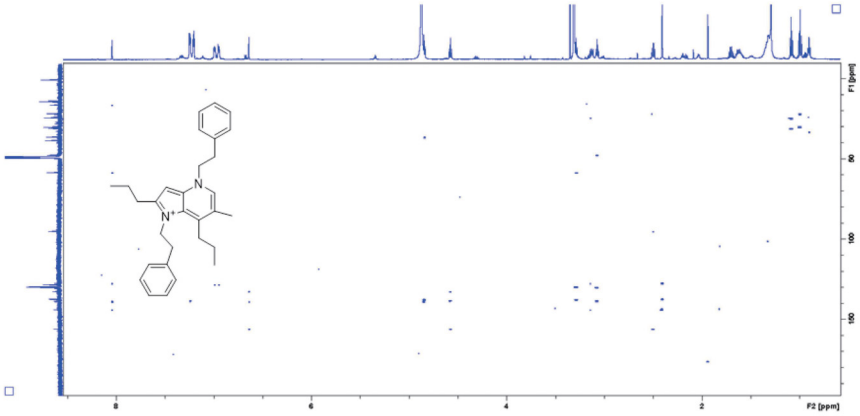

Figure S37. The HMBC (600 MHz, CD_3OD) spectrum of compound **5**.

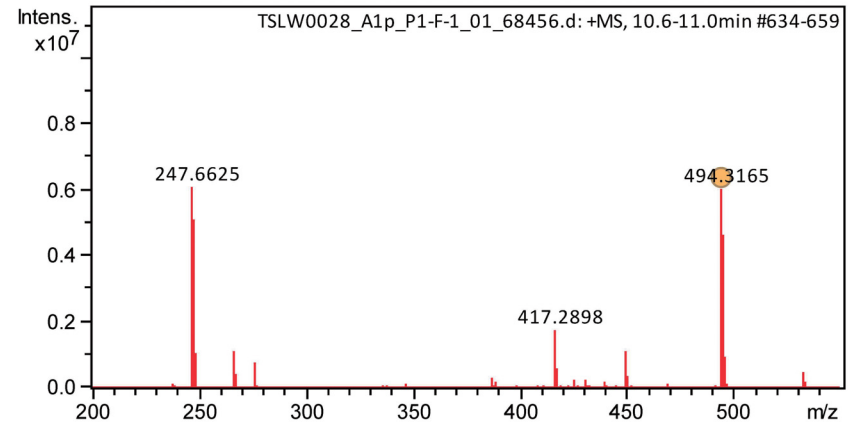

Meas. m/z	#	Ion Formula	m/z	err [ppm]	mSigma	# mSigma	Score	rdb	eÂ¯ Conf	N-Rule
494.3165	1	C33H40N3O	494.3166	0.2	203.3	1	100.00	15.5	even	ok
494.3165	2	C28H40N5O3	494.3126	-7.9	227.1	2	0.63	11.5	even	ok

Figure S38. The HR-ESI-MS of compound **6**.

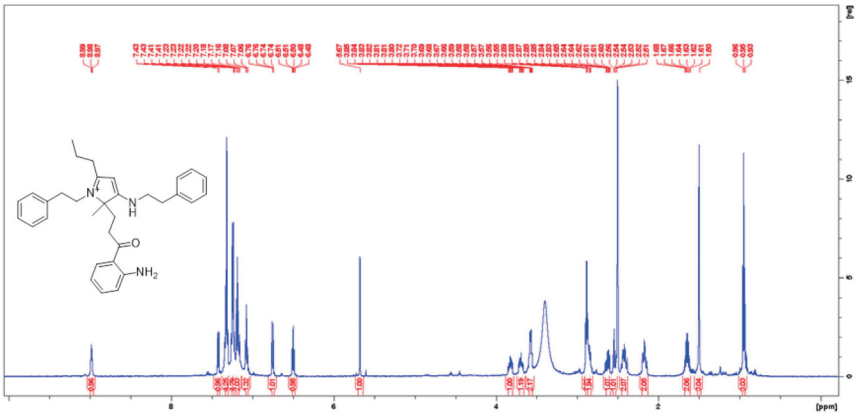

Figure S39. The ^{1}H-NMR (600 MHz, DMSO-d_6) spectrum of compound **6**.

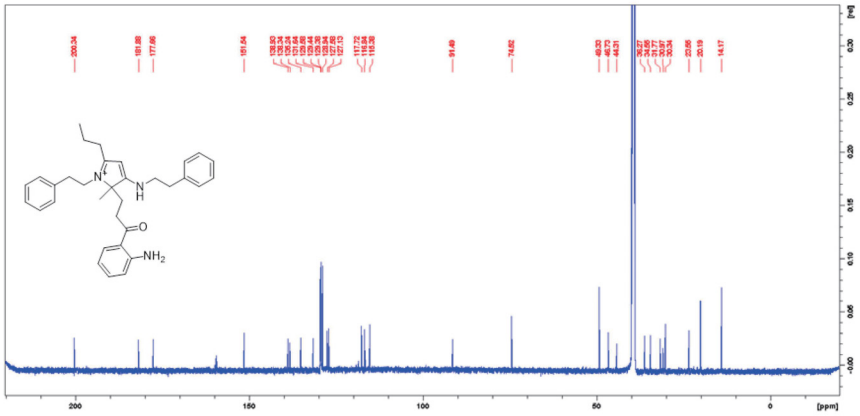

Figure S40. The ^{13}C-NMR (150 MHz, DMSO-*d*$_6$) spectrum of compound **6**.

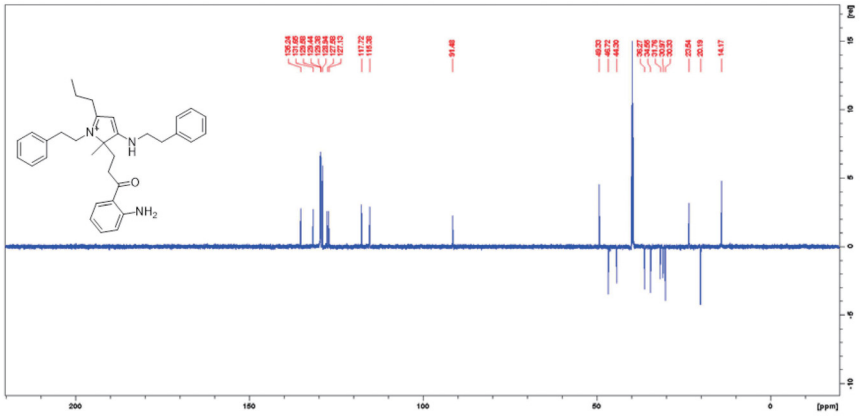

Figure S41. The DEPT135 (150 MHz, DMSO-*d*$_6$) spectrum of compound **6**.

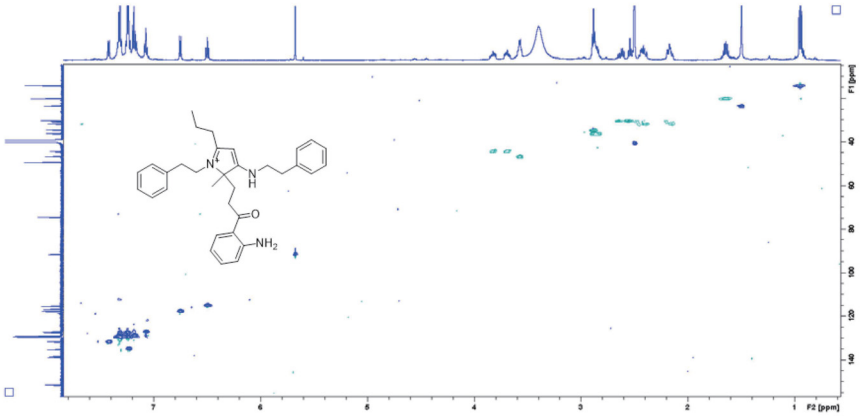

Figure S42. The HSQC (600 MHz, DMSO-*d*$_6$) spectrum of compound **6**.

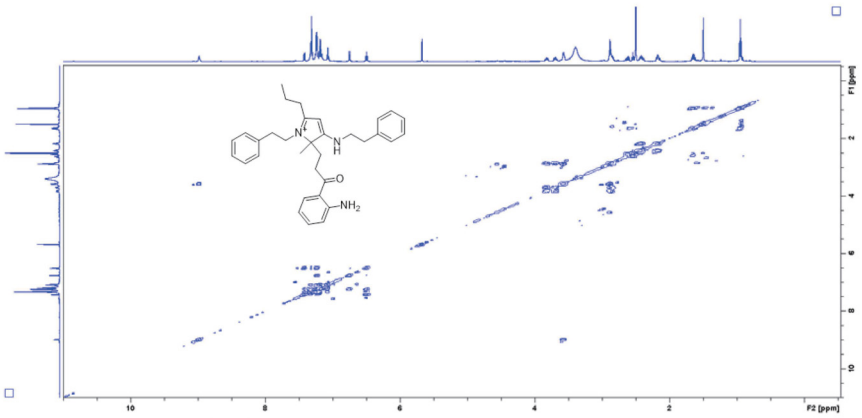

Figure S43. The ^{1}H-^{1}H COSY (600 MHz, DMSO-*d*$_6$) spectrum of compound **6**.

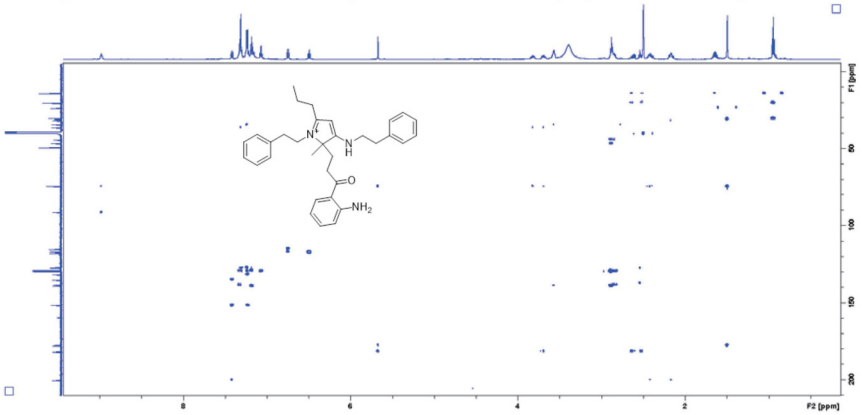

Figure S44. The HMBC (600 MHz, DMSO-*d*$_6$) spectrum of compound **6**.

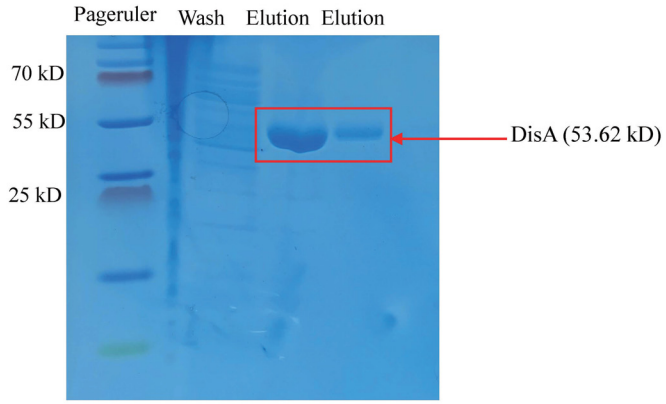

Figure S45. SDS-PAGE gel showing the purification of His-tagged DisA from *E. coli* ROSETTA (washing and elution steps).

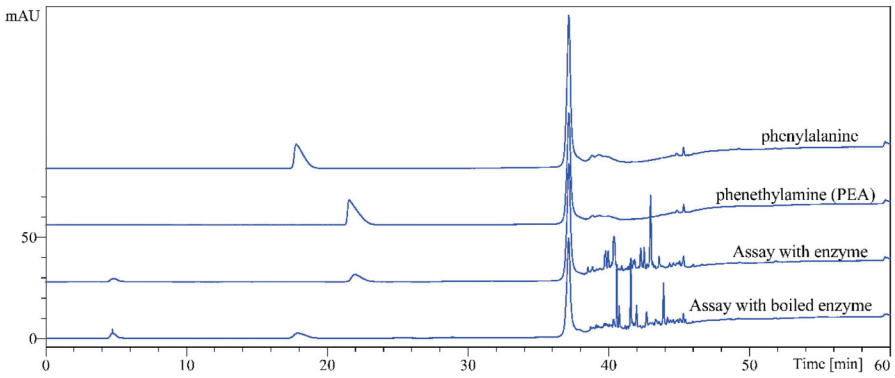

Figure S46. *In vitro* formation of PEA. Comparative HPLC analysis of the standards 2-phenethylamine (PEA), phenylalanine, assay with enzyme, and assay with boiled enzyme. The UV absorbance at 254 nm is shown.

References

1. Burns, N. Z.; Baran, P. S. *Angewandte Chemie (International ed. in English)* **2008,** *47*, 205–208.
2. Frank, R. L.; Seven, R. P. *J. Am. Chem. Soc.* **1949,** *71*, 2629–2635.
3. Li, J. J., Ed. *Name Reactions;* Springer International Publishing, 2014. DOI: 10.1007/978-3-319-03979-4.
4. Li, J.; Thiara, P. S.; Mrksich, M. *Langmuir : the ACS journal of surfaces and colloids* **2007,** *23*, 11826–11835.
5. Imura, A.; Tanaka, N.; Usuki, T. *Tetrahedron Letters* **2019,** *60*, 489–492.
6. Dagorn, F.; Yan, L.-H.; Gravel, E.; Leblanc, K.; Maciuk, A.; Poupon, E. *Tetrahedron Letters* **2011,** *52*, 3523–3526.
7. Wang, Z., Ed. *Comprehensive Organic Name Reactions and Reagents;* John Wiley & Sons, Inc, 2010. DOI: 10.1002/9780470638859.
8. Gelens, E.; Kanter, F. J. J. de; Schmitz, R. F.; Sliedregt, L. A. J. M.; van Steen, B. J.; Kruse, C. G.; Leurs, R.; Groen, M. B.; Orru, R. V. A. *Molecular diversity* **2006,** *10*, 17–22.
9. Baldwin, J. E. *J. Chem. Soc., Chem. Commun.* **1976**, 734–736.
10. Gilmore, K., Alabugin, I. V. *Chem. Rev.* **2011,** *111*, 6513–6556.

Chapter 3. Publication 2

Seven New Alkaloids Isolated from Marine Flavobacterium *Tenacibaculum* discolor sv11

Lei Wang, Michael Marner, Ute Mettal, Yang Liu,* and Till F. Schäberle*

Mar. Drugs 2022, 20, 620.

As a continuous investigation of *Tenacibaculum discolor* sv11 for the production of more bioactive nitrogen-containing heterocycles, another LC-MS guided isolation project was performed. In this chapter, we described the purification, structure elucidation and antimicrobial activity of new nitrogen-containing heterocycles. Furthermore, we also described the *in vivo* and *in vitro* experiments of enzymatic decarboxylation of tryptophan and tyrosine to tryptamine and tyramine catalyzed by the decarboxylase DisA.

In summary, six new imidazolium-containing alkaloids (i.e., discolins C–H) and one pyridinium-containing alkaloid (i.e., dispyridine A) were isolated from the culture of *T. discolor* sv11. All isolated compounds were investigated for their bioactivity against bacteria (*B. subtilis* DSM10, *M. smegmatis* ATCC607, *L. monocytogenes* DSM20600, *S. aureus* ATCC25923, and *E. coli* ATCC25922) and fungi (Candida albicans FH2173). Discolin C showed activity against *M. smegmatis* ATCC607 and *B. subtilis* DSM10 with MIC values ranging from 4 µg/mL to 8 µg/mL and moderate to weak activity against *S. aureus* ATCC25923 and *L. monocytogenes* DSM20600 with MIC values ranging from 16 µg/mL to 32 µg/mL. Discolin E exhibited activity against four

tested Gram-positive bacteria with MIC values ranging from 4 μg/mL to 8 μg/mL and moderate activity against *C. albicans* FH2173 with an MIC value of 16 μg/mL.

The biosynthetic route of the isolated imidazolium-containing alkaloids discolins C–H was investigated based on both *in vivo* and *in vitro* experiments. The decarboxylase DisA first catalyzes the decarboxylation of the aromatic-L-amino acids phenylalanine, tryptophan and tyrosine to phenethylamine, tryptamine and tyramine, respectively, followed by a nonenzymatic condensation to form the central imidazolium ring.

marine drugs

MDPI

Article

Seven New Alkaloids Isolated from Marine Flavobacterium *Tenacibaculum discolor* sv11

Lei Wang [1,2], Michael Marner [2], Ute Mettal [1,2], Yang Liu [1,2,*] and Till F. Schäberle [1,2,3,*]

[1] Institute for Insect Biotechnology, Justus-Liebig-University Giessen, 35392 Giessen, Germany
[2] Fraunhofer Institute for Molecular Biology and Applied Ecology (IME), Branch for Bioresources, 35392 Giessen, Germany
[3] German Center for Infection Research (DZIF), Partner Site Giessen-Marburg-Langen, 35392 Giessen, Germany
* Correspondence: liu.yang@agrar.uni-giessen.de (Y.L.); till.f.schaeberle@agrar.uni-giessen.de (T.F.S.); Tel.: +49-(0)641-97219-140 (T.F.S.)

Abstract: Marine flavobacterium *Tenacibaculum discolor* sv11 has been proven to be a promising producer of bioactive nitrogen-containing heterocycles. A chemical investigation of *T. discolor* sv11 revealed seven new heterocycles, including the six new imidazolium-containing alkaloids discolins C-H (**1**–**6**) and one pyridinium-containing alkaloid dispyridine A (**7**). The molecular structure of each compound was elucidated by analysis of NMR and HR-ESI-MS data. Furthermore, enzymatic decarboxylation of tryptophan and tyrosine to tryptamine and tyramine catalyzed by the decarboxylase DisA was investigated using in vivo and in vitro experiments. The antimicrobial activity of the isolated compounds (**1**–**7**) was evaluated. Discolin C and E (**1** and **3**) exhibited moderate activity against Gram-positive *Bacillus subtilis* DSM10, *Mycobacterium smegmatis* ATCC607, *Listeria monocytogenes* DSM20600 and *Staphylococcus aureus* ATCC25923, with MIC values ranging from 4 µg/mL to 32 µg/mL.

Keywords: Bacteroidetes; *Tenacibaculum*; nitrogen-containing heterocycles; imidazolium-containing alkaloids; pyridinium-containing alkaloid; antimicrobial activity

Citation: Wang, L.; Marner, M.; Mettal, U.; Liu, Y.; Schäberle, T.F. Seven New Alkaloids Isolated from Marine Flavobacterium *Tenacibaculum discolor* sv11. *Mar. Drugs* **2022**, *20*, 620. https://doi.org/10.3390/md20100620

Academic Editor: Asunción Barbero

Received: 4 September 2022
Accepted: 28 September 2022
Published: 30 September 2022

1. Introduction

Structurally diverse nitrogen-containing heterocycles, such as pyrroles, imidazoles, oxazoles, pyridines, and quinolones, are widely distributed in marine organisms and microorganisms. These naturally occurring secondary metabolites often exhibit significant pharmacological activities, including antibacterial, antifungal, antiparasitic, and anticancer activities [1–6]. Furthermore, these compounds are often amenable to further structural modifications [7–10]. Currently, marine-derived imidazole alkaloids are reported mainly to be isolated from sponges, while reports of marine bacteria as bioresource are relatively rare [2,6,11–14].

As a member of the family *Flavobacteriaceae* within the phylum *Bacteroidetes*, isolates of the genus *Tenacibaculum* have been mainly obtained from marine environments, such as sea water, tidal flat, and aquaculture systems, as well as marine organisms like bryozoan, sea anemone, oyster, sponge and green algae [15–22]. Bacteria of this genus are the etiological agent of an ulcerative disease known as tenacibaculosis, which affects a large number of marine fish species in the world [23]. Up to now, the natural products isolated from *Tenacibaculum* strains comprise only siderophores that showed beside their chelating activity also cytotoxicity [24–26], and phenethylamine-containing heterocycles. The latter include two imidazole alkaloids identified in our previous search for antimicrobial metabolites from marine flavobacteria. It was shown that they could be synthesized by decarboxylation of phenylalanine, catalyzed by the enzyme DisA [27]. Likewise, the tryptamine and phenethylamine moieties of imidazole alkaloids isolated from a marine sponge-associated *Bacillus* strain were proposed to be formed by an aromatic amino acid

decarboxylase-dependent reaction [28]. In order to further expand the array of available nitrogen-containing heterocycles, the metabolome of *T. discolor* sv11 was further investigated. Herein, we present the isolation, structure elucidation and biological activity of new alkaloids from the bacterium, and link the enzymatic activity of DisA to their biosynthesis using both, in vivo and in vitro assays.

2. Results

In our continuous search for new bioactive molecules, the six new imidazolium-containing alkaloids discolins C–H (**1–6**) and one pyridinium-containing alkaloid dispyridine A (**7**) were isolated from the marine-derived bacterium *T. discolor* sv11 (Figure 1). The antimicrobial activity of these new compounds was investigated, among which, compounds **1** and **3** exhibited moderate activity against Gram-positive *Bacillus subtilis* DSM10, *Mycobacterium smegmatis* ATCC607, *Listeria monocytogenes* DSM20600 and *Staphylococcus aureus* ATCC25923. In vivo and in vitro experiments indicated that phenethylamine, tryptamine and tyramine residues of the new alkaloids are derived from an enzymatic decarboxylation.

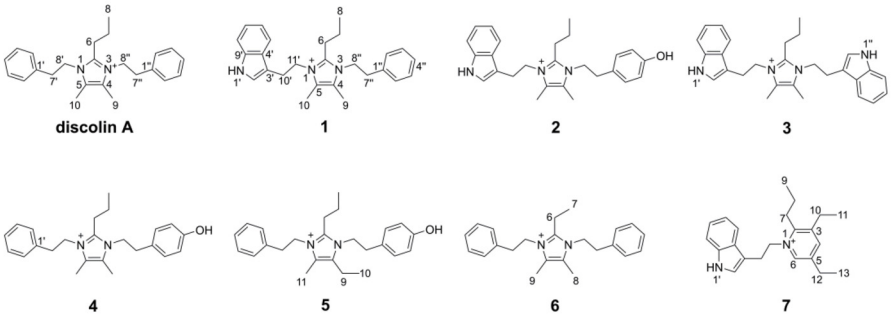

Figure 1. Discolin A and new compounds isolated from *T. discolor* sv11.

Compound **1** was obtained as a yellowish oil. The HR-ESI-MS spectrum of **1** showed a molecular formula of $C_{26}H_{32}N_3^+$ based on the prominent peak $[M]^+$ at *m/z* 386.2606 (calculated 386.2591, Figure S1). The analysis of ^{1}H NMR and HSQC spectra of **1** revealed three methyl groups at δ_H 0.80 (H-8), δ_H 2.15 (H-9) and δ_H 2.20 (H-10), six methylene groups at δ_H 1.34 (H-7), δ_H 2.41 (H-6), δ_H 2.80 (H-7″), δ_H 3.08 (H-10′), δ_H 4.22 (H-8″) and δ_H 4.30 (H-11′), as well as ten aromatic protons that resonated from δ_H 7.00 to δ_H 7.39 (Table 1). These NMR data exhibited a high similarity with the previously reported compound discolin A that was also isolated from *T. discolor* sv11 [27]. Therefore, a core structure of the 4,5-dimethyl-2-propyl imidazolium skeleton of **1** was elucidated based on the COSY spin system from H-6 to H-7 to H-8, as well as on HMBC correlations from both H-6 and H-7 to C-2, and from both, H-9 and H-10 to C-4 and C-5. The same phenylethyl moiety as present in discolin A was deducted from compound **1** based on the COSY spin system between H-7″ and H-8″, as well as between five benzene ring protons 7.16 (2H, H-2″ and H-6″), 7.28 (H-4″) and δ_H 7.32 (2H, H-3″ and H-5″), together with the core HMBC correlations from H-7″ to C-1″ and C-2″, and from H-8″ to C-1″ (Figure 2). The significant difference between compound **1** and discolin A are the HMBC correlations from a singlet aromatic proton resonating at δ_H 7.17 (H-2′) to C-3′, C-4′ and C-9′, from H-5′ to C-3′, C-4′, C-7′ and C-9′ (Figure 2), as well as the COSY spin system from H-5′ to H-6′, to H-7′ to H-8′. These results suggested an indole moiety instead of a phenyl residue in compound **1**. Together with the remaining COSY spin system between the two methylene groups H-10′ and H-11′ and the HMBC correlations from H-10′ to C-2′, C-3′, C-4′ and C-11′, a 3-ethylindole moiety ($C_{10}H_{10}N$) was elucidated from compound **1**, which is further supported by the MS/MS fragment $[C_{10}H_{10}N]^+$ detected at *m/z* 144.0813 (calculated 144.0813, Figure S1). With the HMBC correlations from H-8″ to C-2 and C-4,

and from H-11′ to C-2 and C-5, the above mentioned phenylethyl moiety and 3-ethylindole were supposed to be located at position 3 and 1 of the imidazolium skeleton (Figure 2). This assumption was proven by ^{1}H-^{15}N HMBC correlations from H-6, H-9, H-7″ and H-8″ to N-3 and from H-6, H-10, H-10′ and H-11′ to N-1 (Figure 2). The N-atom at position 1 was considered to be positively charged based on the detected chemical shift at δ_N 178.5, while N-3 was at δ_N 177.3 (Figures S7 and S8) [29–31]. An additional NMR measurement with added trifluoracetic acid (TFA) in DMSO-d_6 (ratio 1:3) was carried out to further prove this conclusion (Figures S9–S13). The methylene groups of H-8″ and H-7″ shifted to up-field with a deviation $\Delta\delta_{H\text{-}8''}$ value of 0.13 and $\Delta\delta_{H\text{-}7''}$ value of 0.10 ppm, while the deviation $\Delta\delta_{H\text{-}11'}$ and $\Delta\delta_{H\text{-}10'}$ values were 0.09 and 0.05 ppm, respectively. The addition of TFA lead to the protonation of the tertiary N-atom at position 3, which gives a higher influence on the chemical shift [32]. The detected different chemical shift deviations $\Delta\delta_{N\text{-}3}$ (155.1) and $\Delta\delta_{N\text{-}1}$ (154.1) further support this result (Figures S7, S8 and S13). Thus, the structure of compound **1** was elucidated as shown in Figure 1 and named discolin C.

Table 1. ^{1}H (700 MHz) and ^{13}C (175 MHz) NMR data of compounds **1–3** (DMSO-d_6, δ in ppm).

Position	1			2		3	
	δ_C, Type	δ_H, (*J* in Hz)	δ_H, (*J* in Hz) [a]	δ_C, Type	δ_H, (*J* in Hz)	δ_C, Type	δ_H, (*J* in Hz)
2	144.8, C			144.7, C		144.7, C	
4	125.5, C			125.5, C		125.5, C	
5	125.5, C			125.5, C		125.5, C	
6	23.8, CH_2	2.41, t (8.0)	2.20, m	23.8, CH_2	2.40, t (7.8)	23.7, CH_2	2.30, t (8.1)
7	20.6, CH_2	1.34, m	1.25, m	20.6, CH_2	1.34, m	20.5, CH_2	1.29, m
8	13.3, CH_3	0.80, t (7.3)	0.69, t (7.3)	13.3, CH_3	0.80, t (7.2)	13.2, CH_3	0.71, t (7.3)
9	7.9, CH_3	2.15, s	2.03, s	7.9, CH_3	2.13, s	8.0, CH_3	2.22, s
10	8.0, CH_3	2.20, s	2.10, s	8.0, CH_3	2.19, s	8.0, CH_3	2.22, s
1′ NH		11.11, s	10.80, s		11.02, s		11.03, s
2′	123.9, CH	7.17, s [b]	7.02, s [b]	123.8, CH	7.16, s	123.8, CH	7.16, s
3′	109.1, C			109.1, C		109.1, C	
4′	126.8, C			126.8, C		126.8, C	
5′	117.5, CH	7.39, d (7.3)	7.27, d (7.9)	117.5, CH	7.40, d (7.9)	117.5, CH	7.38, m
6′	118.6, CH	7.00, t (7.7)	6.93, d (7.5)	118.6, CH	7.00, t (7.4)	118.6, CH	7.01, t (7.5)
7′	121.2, CH	7.09, t (7.5)	7.02, m [b]	121.2, CH	7.09, t (7.4)	121.2, CH	7.09, t (7.5)
8′	111.6, CH	7.38, d (7.6)	7.32, d (8.1)	111.6, CH	7.38, d (8.0)	111.6, CH	7.38, m
9′	136.1, C			136.1, C		136.1, C	
10′	25.0, CH_2	3.08, t (7.0)	3.03, t (6.8)	25.0, CH_2	3.07, t (6.7)	24.9, CH	2.95, t (7.2)
11′	45.8, CH_2	4.30, t (7.0)	4.21, t (6.7)	45.7, CH_2	4.29, t (6.7)	45.6, CH	4.23, t (7.3)
1″ [c]	136.8, C			126.7, C			11.03, s
2″	128.9, CH	7.16, m [b]	7.02, m [b]	129.9, CH	6.91, d (7.9)	123.8, CH	7.16, s
3″	128.6, CH	7.32, t (7.3)	7.21, m	115.3, CH	6.70, d (8.0)	109.1, C	
4″	127.0, CH	7.28, m	7.17, m	156.5, C		126.8, C	
5″	128.6, CH	7.32, t (7.3)	7.21, m	115.3, CH	6.70, d (8.0)	117.5, CH	7.38, m
6″	128.9, CH	7.16, m [b]	7.02, m [b]	129.9, CH	6.91, d (7.9)	118.6, CH	7.01, t (7.5)
7″	35.0, CH_2	2.80, t (7.5)	2.70, t (7.3)	34.2, CH_2	2.69, t (6.9)	121.2, CH	7.09, t (7.5)
8″	45.8, CH_2	4.22, t (7.5)	4.09, t (7.2)	46.2, CH_2	4.14, t (6.9)	111.6, CH	7.38, m
9″						136.1, C	
10″						24.9, CH	2.95, t (7.2)
11″						45.6, CH	4.23, t (7.3)

[a] ^{1}H NMR data of compound **1** with TFA added. [b] Signals overlapped. [c] NH at 1″ for compound **3**.

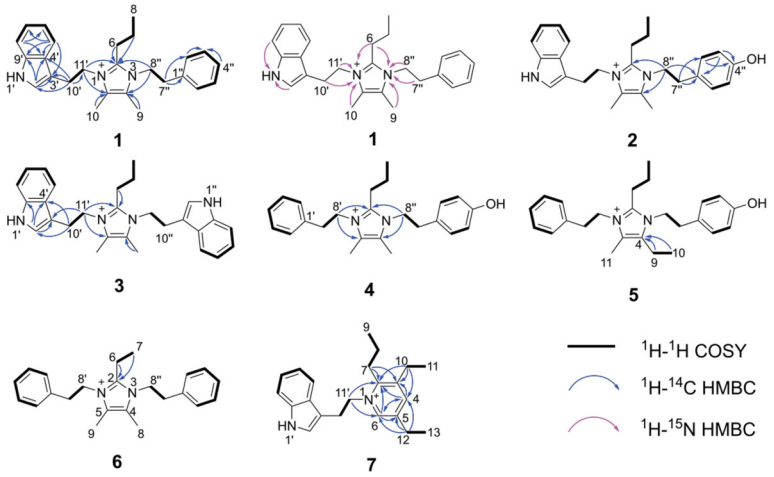

Figure 2. Key HMBC and ^{1}H-^{1}H COSY correlations of compounds **1**–**7**.

Compound **2** was obtained as a yellowish oil. The molecular formula of **2** was determined to be $C_{26}H_{32}ON_3^+$ (*m/z* = 402.2543, $[M]^+$, calcd. 402.2540, Figure S14) based on the HR-ESI-MS spectrum. Comprehensive comparison of NMR data of compounds **1** and **2** revealed the high similarity except for the chemical shift of C-4″, which was shifted from 126.96 to 156.48, and one missing aromatic proton. Together with the detected 16 Da increase in the HR-ESI-MS spectrum of compound **2**, this suggested the presence of a 4-hydroxyphenylethyl moiety located at position 3 instead of a phenylethyl moiety (Table 1). This assumption was confirmed by the upfield chemical shifts of the benzene ring protons at δ_H 6.70 (2H, H-3″ and H-5″) and δ_H 6.91 (2H, H-2″ and H-6″), which showed similar behavior as the reported 4-hydroxyphenylethyl-containing compound *N*-Acetyltyramine [33]. This effect is explained by the fact that the hydroxyl group is an electron donor, which shields the protons of the benzene nucleus more strongly and leads to an upfield shift of the corresponding signals. Second, the hydroxyl group that appeared at C-4″ in compound **2** changes the spin system of this radical, and therefore influenced the shape of the proton multiplets of the benzene nucleus. Furthermore, the COSY spin system between H-2″ and H-3″, as well as the HMBC correlations from H-7″ to C-1″, C-2″, from H-3″ to C-1″, C-4″, and from H-8″ to C-2, C-4 and C-1″ proved the 4-hydroxyphenylethyl group in compound **2**. The detected MS/MS fragment at *m/z* 282.1963 ($[C_{18}H_{23}N_3 + H]^+$, calcd. 282.1965, Figure S14) of compound **2**, which lost the 4-hydroxyphenylethyl group ($-C_8H_9O$), strongly indicated the above mentioned assumption. Thus, the structure of compound **2** was elucidated as shown in Figure 1 and named discolin D.

Compound **3** was also obtained as a yellowish oil. The molecular formula of **3** was determined to be $C_{28}H_{33}N_4^+$ (*m/z* = 425.2702, $[M]^+$, calculated 425.2700, Figure S20) based on the HR-ESI-MS spectrum. The core scaffold of compound **3** shared the 4,5-dimethyl-2-propyl imidazolium skeleton with compound **1** as deduced from a comparison of both, 1D and 2D NMR data (Table 1), which also indicated compound **3** to be a symmetric structure. Integration of the proton signals in the ^{1}H NMR spectrum together with the COSY spin system of the aromatic protons and the HMBC correlations from H-2′ to C-3′, C-4′ and C-9′, from H-10′ to C-2′, C-4′ and C-11′, as well as from H-11′ to C-3′, C-10′, C-2, and C-5 proved that two identical 3-ethylindole moieties were connected to the central imidazolium ring as shown in Figure 2. Hence, compound **3** is a member of the discolin family and was named discolin E.

Compounds **4** and **5** were each obtained as a yellowish oil. The molecula formulae of compounds **4** and **5** were identified as $C_{24}H_{31}ON_2^+$ and $C_{25}H_{33}ON_2^+$, respectively,

based on the HR-ESI-MS signals $[M]^+$ at *m/z* = 363.2442 (calculated 363.2431, compound **4**, Figure S26) and *m/z* = 377.2593 (calculated 377.2587, compound **5**, Figure S32), respectively. One phenylethyl moiety, one 4-hydroxyphenylethyl moiety and the 4,5-dimethyl-2-propyl imidazolium skeleton were disclosed as constituents of compound **4** by comparing the 1D and 2D NMR data with those of compounds **1** and **2** (Tables 1 and 2). The phenylethyl moiety and the 4-hydroxyphenylethyl moiety were assigned to be located at positions 1 and 3 of the imidazolium skeleton of compound **4**, based on the HMBC correlations from H-8′ to C-2 and C-5 and from H-8″ to C-2 and C-4 (Figure 2). In compound **5**, identical phenylethyl and 4-hydroxyphenylethyl moieties were assigned to be located at the same positions as in compound **4**. Comparing the 1D and 2D NMR data of compounds **4** and **5**, the only difference is one ethyl group present in compound **5**, while compound **4** carries a methyl group (Table 2). The presence of an ethyl group in compound **5** is corroborated by the COSY correlation between H-9 and H-10, and the HMBC correlations from both, H-9 and H-10 to C-4. In contrast, in compound **4**, the methyl group is directly connected to the unsaturated carbon C-4 (Figure 2), thus verifying the assumed structural relationship between compounds **4** and **5**. The 14 Da molecular weight difference between both compounds further supports their structural relationship. Thus, the structures of compounds **4** and **5** were elucidated as shown in Figure 1, and the names discolin F and discolin G were proposed, respectively.

Table 2. ^{1}H (700 MHz) and ^{13}C (175 MHz) NMR data of compounds **4**–**6** (DMSO-d_6, δ in ppm).

Position	4		5		6	
	δ_C, Type	δ_H, (*J* in Hz)	δ_C, Type [a]	δ_H, (*J* in Hz)	δ_C, Type	δ_H, (*J* in Hz)
2	144.8, C		144.8, C		146.0, C	
4	125.5, C		130.5, C		125.5, C	
5	125.6, C		125.7, C		125.5, C	
6	23.9, CH_2	2.53, t (7.9)	23.8, CH_2	2.55, m	16.1, CH_2	2.67, q (7.6)
7	20.7, CH_2	1.40, m	20.4, CH_2	1.43, m	11.8, CH_3	1.02, t (7.6)
8	13.4, CH_3	0.89, t (7.2)	13.1, CH_3	0.90, t (7.2)	7.9, CH_3	2.11, s
9	7.9, CH_3	2.10 or 2.11, s	15.1, CH_2	2.57, q (7.6)	7.9, CH_3	2.11, s
10	7.9, CH_3	2.10 or 2.11, s	13.3, CH_3	1.07, td (7.5, 1.9)		
11			7.6, CH_3	2.10, d (1.5)		
1′	136.9, C		136.8, C		136.9, C	
2′	129.0, CH	7.19, d (7.2)	128.7, CH	7.20 or 7.17, d (7.1)	129.0, CH	7.19, d (7.1)
3′	128.6, CH	7.33, t (7.3)	128.4, CH	7.33, m	128.6, CH	7.33, t (7.3)
4′	127.0, CH	7.28, t (7.2)	126.8, CH	7.29, m	127.0, CH	7.28, t (7.3)
5′	128.6, CH	7.33, t (7.3)	128.4, CH	7.33, m	128.6, CH	7.33, t (7.3)
6′	129.0, CH	7.19, d (7.2)	128.7, CH	7.20 or 7.17, d (7.1)	129.0, CH	7.19, d (7.1)
7′	35.0, CH_2	2.93, t (7.0)	35.2, CH_2	2.93, m	35.0, CH_2	2.95, t (7.3)
8′	46.0, CH_2	4.28, t (7.0)	45.6, CH_2	4.29, m	45.9, CH_2	4.28, t (7.3)
1″	126.5, C		126.4, C		136.9, C	
2″	129.9, CH	6.92, d (8.1)	129.6, CH	6.93 or 6.90, d (8.2)	129.0, CH	7.19, d (7.1)
3″	115.4, CH	6.70, d (8.1)	115.2, CH	6.71 or 6.70, d (8.4)	128.6, CH	7.33, t (7.3)
4″	156.8, C		156.7, C		127.0, CH	7.28, t (7.3)
5″	115.4, CH	6.70, d (8.1)	115.2, CH	6.71 or 6.70, d (8.4)	128.6, CH	7.33, t (7.3)
6″	129.9, CH	6.92, d (8.1)	129.6, CH	6.93 or 6.90, d (8.2)	129.0, CH	7.19, d (7.1)
7″	34.2, CH_2	2.81, t (6.8)	34.3, CH_2	2.81, m	35.0, CH_2	2.95, t (7.3)
8″	46.4, CH_2	4.21, t (6.9)	46.0, CH_2	4.21, m	45.9, CH_2	4.28, t (7.3)

[a] Deduced from HSQC and HMBC spectra.

Compound **6** was also obtained as a yellowish oil. The molecular formula of compound **6** was established as $C_{23}H_{29}N_2^+$ based on the prominent $[M]^+$ peak in HR-ESI-MS spectrum at *m/z* = 333.2329 (calculated 333.2325, Figure S37). Two identical phenylethyl moieties were deduced from the NMR spectra of compound **6** and connected at positions 1 and 3 of the core ring based on the HMBC correlations from H-8′ to C-2 and C-5, as well as from H-8″ to C-2 and C-4. The remaining signals of **6** were assigned to the 4,5-dimethyl-2-ethyl imidazolium scaffold, which showed an ethyl group rather than a propyl group at position 2. This difference was clarified by the COSY correlation between H-6 and H-7, as well as the HMBC correlations from both, H-6 and H-7 to C-2 (Figure 2). Therefore, compound **6** proved to be a representative of the discolin family and was named discolin H.

Compound **7** was isolated as a colorless powder. Its molecular formula was established as $C_{22}H_{29}N_2^+$ based on the prominent ion peak $[M]^+$ observed at *m/z* 321.2322 (calcd. 321.2325, Figure S43). Comprehensive analysis of 1D and 2D NMR data of compound **7** revealed one 3-ethylindole moiety as found in compounds **1**–**3**, as well as two ethyl groups and one propyl group (Table 3). The remaining two aromatic protons at δ_H 8.20 (H-4) and δ_H 8.40 (H-6) in the ^{1}H NMR spectrum and five aromatic carbons at δ_C 153.07 (C-2), δ_C 142.58 (C-3), δ_C 144.54 (C-4), δ_C 140.61 (C-5) and δ_C 142.62 (C-6) in the ^{13}C NMR spectrum were attributed to a pyridinium ring as apparent from comparison with the data of dispyridine, a pyridinium-containing alkaloid isolated previously [27]. The location of the 3-ethylindole moiety was determined from the HMBC correlations from H-11′ to C-2 and C-6, which also confirmed the location of the aromatic proton H-6 resonating at δ_H 8.40. The second aromatic proton resonating at δ_H 8.20 was attributed to position 4, based on the HMBC correlations from H-4 to C-2, C-3 and C-6. The propyl group and the two ethyl groups attached to the pyridinium ring were located at C-2, C-3 and C-5, as inferred from HMBC correlations from H-7 to C-2 and C-3, from H-10 to C-2, C-3 and C-4, and from H-12 to C-4, C-5 and C-6 (Figure 2). Therefore, compound **7** was found to be a new member of the dispyridine family and named dispyridine A.

Table 3. ^{1}H (700 MHz) and ^{13}C (175 MHz) NMR data of compound **7** (DMSO-d_6, δ in ppm).

Position	δ_C, Type	δ_H, (*J* in Hz)	Position	δ_C, Type	δ_H, (*J* in Hz)
2	153.1, C		1′ NH		11.06, s
3	142.6, C		2′	124.2, CH	7.13, s
4	144.5, CH	8.20, s	3′	108.3, C	
5	140.6, C		4′	126.8, C	
6	142.6, CH	8.40, s	5′	117.3, CH	7.25, d (7.9)
7	29.5, CH_2	2.83, t (8.2)	6′	118.6, CH	6.91, t (7.4)
8	21.8, CH_2	1.56, m	7′	121.2, CH	7.06, t (7.3)
9	13.8, CH_3	1.00, t (7.0)	8′	111.6, CH	7.35, d (8.1)
10	24.5, CH_2	2.73, q (7.5)	9′	136.0, C	
11	14.4, CH_3	1.13, t (7.5)	10′	26.5, CH_2	3.35, m [a]
12	24.5, CH_2	2.57, q (7.5)	11′	58.5, CH_2	4.78, t (6.5)
13	13.9, CH_3	1.01, t (7.5)			

[a] Signal overlapped with H_2O.

Based on previous research, it was known that phenylalanine can be converted to phenethylamine by the catalytic action of the decarboxylase DisA. This molecule could serve as building block to yield different derivatives [27]. Hence, the newly isolated imidazolium-containing alkaloids (**1**–**6**) were also supposed to be produced via the same biosynthetic route, i.e., first an enzymatic decarboxylation of the aromatic-*L*-amino acid tryptophan or tyrosine yielding tryptamine or tyramine, respectively, followed by a non-enzymatic condensation to form the central imidazolium ring. To confirm this hypothesis, the candidate enzyme DisA from *T. discolor* sv11 was analyzed in vivo in a heterologous system. Therefore, the previously constructed transgenic host strain *E. coli* ROSETTA (disA) carrying the respective *disA* gene and *E. coli* ROSETTA (pRSF) (negative empty vector control) were cultivated in LB medium, whereby 2 mM tryptophan and tyrosine

were added as substrates, respectively. After 24 h incubation, tryptamine and tyramine were only detected in the extract of *E. coli* ROSETTA (disA), while only the substrates, i.e., tryptophan and tyrosine were detected in the negative control (Figure 3). To further validate these results, a His-tagged version of DisA was purified using affinity chromatography and assayed in vitro. This confirmed that tryptamine and tyramine can be obtained from tryptophan and tyrosine by a DisA-dependent catalytic conversion (Figure 3).

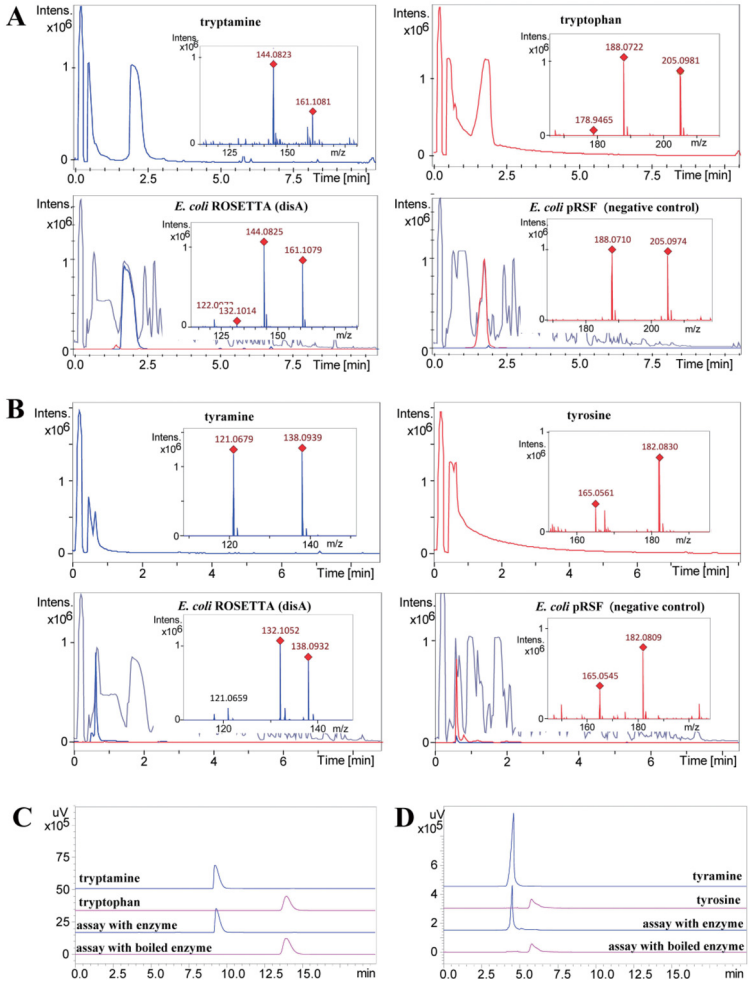

Figure 3. In vivo and in vitro decarboxylation of tryptophan and tyrosine catalyzed by DisA. (**A**) In vivo decarboxylation of tryptophan to tryptamine. Extracted ion chromatograms (EICs) of tryptophan ($C_{11}H_{13}N_2O_2$ 205.0977 $[M + H]^+$, in red) and tryptamine ($C_{10}H_{13}N_2$ 161.1079 $[M + H]^+$, in blue). (**B**) In vivo decarboxylation of tyrosine to tyramine. Extracted ion chromatograms (EIC) of tyrosine ($C_9H_{12}NO_3$ 182.0817 $[M + H]^+$, in red) and tyramine ($C_8H_{12}NO$ 138.0919 $[M + H]^+$, in blue). In A and B, the base peak chromatogram of the extracts is given in grey. (**C**) Comparative HPLC analysis of the in vitro decarboxylation of tryptophan. (**D**) Comparative HPLC analysis of the in vitro decarboxylation of tyrosine. In C and D, the UV absorbance at 254 nm is shown.

All isolated compounds **1–7** were investigated for their bioactivity against bacteria (*B. subtilis* DSM10, *M. smegmatis* ATCC607, *L. monocytogenes* DSM20600, *S. aureus* ATCC25923, and *E. coli* ATCC25922) and fungi (*Candida albicans* FH2173). As shown in Table 4, discolin C (**1**) showed activity against *M. smegmatis* ATCC607 and *B. subtilis* DSM10 with MIC values ranging from 4 µg/mL to 8 µg/mL and moderate to weak activity against *S. aureus* ATCC25923 and *L. monocytogenes* DSM20600 with MIC values ranging from 16 µg/mL to 32 µg/mL. Discolin E (**3**) exhibited activity against four tested Gram-positive bacteria with MIC values ranging from 4 µg/mL to 8 µg/mL and moderate activity against *C. albicans* FH2173 with an MIC value of 16 µg/mL. The other compounds (**2**, **4–7**) were inactive against all the tested microorganisms in the range tested.

Table 4. MIC values (µg/mL) for Compounds **1–7**.

Test organism	MIC (µg/mL, *n* = 3)									
	1	**2**	**3**	**4**	**5**	**6**	**7**	**Rifampicin**	**Tetracycline**	**Gentamicin**
B. subtilis DSM10	8	>32	8	>32	32	32	>32	<0.031	2–4	0.06
M. smegmatis ATCC607	4	>32	4	>32	>32	16	>32	8–16	0.25–0.5	4–8 [a]
L. monocytogenes DSM20600	32	>32	8	>32	>32	>32	>32	<0.031	0.5–1	<0.031
S. aureus ATCC25923	16	>32	8	>32	>32	32	>32	<0.031	0.25–0.5	0.06–0.125
E. coli ATCC25922	>32	>32	>32	>32	>32	>32	>32	4	2–4	0.06
C. albicans FH2173 [b]	>32	>32	16	>32	>32	>32	>32	Nystatin 1–2	Tebuconazole 0.25	Amphotericin B 0.5–1

[a] Isoniazid was used as positive control. [b] Nystatin, tebuconazole and amphotericin B were used as positive controls.

3. Conclusions and Discussion

In conclusion, seven new alkaloids were obtained from the crude extract of *T. discolor* sv11 after fermentation in LB medium. In vivo and in vitro experiments proved the decarboxylase DisA to catalyze the decarboxylation of the aromatic-*L*-amino acids phenylalanine, tryptophan and tyrosine to phenethylamine, tryptamine and tyramine, respectively. These molecules serve as substrates for the formation of the central imidazolium ring of discolins A–H through a non-enzymatic condensation. Hence, by combining an enzyme-catalyzed and a non-enzymatic reaction, the bacterium generates a mix of structurally related molecules. Besides the understanding of the biosynthetic mechanisms of the discolins, some insights into the structure–activity relationship of the antibacterial discolins A-H were also obtained [27]. Discolin A and discolin H feature the same molecular skeleton, except for the length of the carbon chain linked to C-2 of the central imidazolium ring. Both molecules showed the similar moderate bioactivity, which suggests that the substructure at position 2 can be altered without affecting the activity. The structural differences and changes in the bioactivity of discolins C-F and discolin A indicated that the substructures at position 1 and 3 of the central ring instead play an important role concerning antibacterial activity. Earlier evidence indicated that the activity of imidazolium salts is highly dependent upon the substituents on the nitrogen atoms of the imidazolium cation [34], which is in agreement with our observation. In summary, our finding, together with previous reports, clearly indicates that the genus *Tenacibaculum* exhibits a high potential to produce nitrogen-containing heterocycles with a unique structure and various biological activities. This includes positively charged imidazolium-containing natural products.

4. Materials and Methods

4.1. General Experimental Procedures

The 1D and 2D NMR spectra were recorded in DMSO-d_6 using a Bruker Avance Neo 700 MHz spectrometer equipped with a 5 mm CryoProbe Prodigy TCI (^{1}H,^{15}N,^{13}C Z-GRD) (Bruker, Ettlingen, Germany). The LC-HRMS data for new compounds were recorded on a micrOTOF-QII mass spectrometer (Bruker, Billerica, MA, USA) equipped with an ESI-source coupled to an Agilent Infinity 1290 UHPLC system using an ACQUITY UPLC BEH C18 Column, 130 Å, 1.7 µm, 2.1 mm×100 mm (Waters, Eschborn, Germany) with

an ACQUITY UPLC BEH C18 VanGuard Pre-column, 130 Å, 1.7 µm, 2.1 mm × 5 mm (Waters, Eschborn, Germany). HPLC was performed using a Shimadzu HPLC system (Shimadzu Deutschland GmbH, Duisburg, Germany) for analysis (EC 250/4.6 Nucleodur C18 Gravity-SB, 5 µm; Macherey-Nagel, Düren, Germany), and for semi-preparative purification (VP 250/10 Nucleodur C18 Gravity-SB, 5 µm; Macherey-Nagel, Düren, Germany). MPLC was performed on the Interchim Puriflash 4125 chromatography system (Interchim, Montluçon, France).

4.2. Extraction and Isolation

A fermentation (36 L) of *T. discolor* S11 was performed in 5 L flasks that contained 1.5 L of LB medium and were incubated at 30 °C and 140 rpm for 8 days, followed by an extraction using EtOAc (volume ratio 1:1) for three times, affording 11.9 g crude extract. Thirteen fractions (Fr. 1–13) were collected from reversed phase flash chromatography (Interchim Puriflash 4125 chromatography system with Puriflash C18-AQ30 µm F0120 column) with an elution gradient starting from 10% MeOH/H_2O to 100% MeOH over 1.5 h. Fr. 11 (973.8 mg) was further subjected to size exclusion chromatography on a Sephadex LH-20 column and eluted with 100% MeOH to give 10 subfractions (Frr. 11.1–11.10). Frr. 11.4 (229.4 mg) was further subjected to reversed phase flash chromatography (Interchim Puriflash 4125 chromatography system with Puriflash C18-HP30 µm F0025 Flash column) using an elution gradient from 10% MeOH/H_2O to 100% MeOH over 4 h to give 10 subfractions (Frrr. 11.4.1–11.4.10). Frrr. 11.4.6 was further purified by semi-preparative HPLC (0–1 min, 22% MeCN; 1–46 min, gradient increased from 22% to 37% MeCN) to yield compounds **1** (2.0 mg, t_R = 43 min) and **3** (0.6 mg, t_R = 45 min). Frrr. 11.4.5 was fractionated by semi-preparative HPLC (0–38.5 min, gradient increased from 10% to 46% MeOH) to give 6 subfractions (Frrrr. 11.4.5.1–11.4.5.6). Frrrr. 11.4.5.3 was again purified by semi-preparative HPLC (0–57 min, isocratic gradient with 29% MeOH) to yield compounds **2** (1.2 mg, t_R = 48.5 min), **4** (2.1 mg, t_R = 39 min) and **7** (1.5 mg, t_R = 44.4 min). Purification of Frrrr. 11.4.5.1 by semi-preparative HPLC (0–5 min, 5% MeCN; 5–50 min, gradient increased from 5% to 35% MeCN) yielded compound **5** (0.3 mg, t_R = 49.3 min). Compound **6** (0.3 mg, t_R = 51.2 min) was obtained from Frrrr. 11.4.5.6 by semi-preparative HPLC (0–5 min, 5% MeCN; 5–56 min, gradient increased from 5% to 39% MeCN).

Discolin C (**1**): yellowish oil; the ^{1}H NMR (DMSO-d_6, 700 MHz) and ^{13}C NMR (DMSO-d_6, 175 MHz) data are given in Table 1; HR-ESI-MS *m/z* 386.2606 $[M]^+$ (calculated for $C_{26}H_{32}N_3^+$, 386.2591, Figure S1).

Discolin D (**2**): yellowish oil; the ^{1}H NMR (DMSO-d_6, 700 MHz) and ^{13}C NMR (DMSO-d_6, 175 MHz) data are given in Table 1; HR-ESI-MS *m/z* 402.2543 $[M]^+$ (calculated for $C_{26}H_{32}ON_3^+$, 402.2540, Figure S14).

Discolin E (**3**): yellowish oil; the ^{1}H NMR (DMSO-d_6, 700 MHz) and ^{13}C NMR (DMSO-d_6, 175 MHz) data are given in Table 1; HR-ESI-MS *m/z* 425.2702 $[M]^+$ (calculated for $C_{28}H_{33}N_4^+$, 425.2700, Figure S20).

Discolin F (**4**): yellowish oil; the ^{1}H NMR (DMSO-d_6, 700 MHz) and ^{13}C NMR (DMSO-d_6, 175 MHz) data are given in Table 2; HR-ESI-MS *m/z* 363.2442 $[M]^+$ (calculated for $C_{24}H_{31}ON_2^+$, 363.2431, Figure S26).

Discolin G (**5**): yellowish oil; the ^{1}H NMR (DMSO-d_6, 700 MHz) and ^{13}C NMR (DMSO-d_6, 175 MHz) data are given in Table 2; HR-ESI-MS *m/z* 377.2593 $[M]^+$ (calculated for $C_{25}H_{33}ON_2^+$, 377.2587, Figure S32).

Discolin H (**6**): yellowish oil; the ^{1}H NMR (DMSO-d_6, 700 MHz) and ^{13}C NMR (DMSO-d_6, 175 MHz) data are given in Table 2; HR-ESI-MS *m/z* 333.2329 $[M]^+$ (calculated for $C_{23}H_{29}N_2^+$, 333.2325, Figure S37).

Dispyridine A (**7**): colorless powder; the ^{1}H NMR (DMSO-d_6, 700 MHz) and ^{13}C NMR (DMSO-d_6, 175 MHz) data are given in Table 3; HR-ESI-MS *m/z* 321.2322 $[M]^+$ (calculated for $C_{22}H_{29}N_2^+$, 321.2325, Figure S43).

4.3. Enzymatic Activity of Dis A

To investigate the enzymatic activity of Dis A in vivo, *E. coli* ROSETTA (disA) was cultured in 30 mL kanamycin-containing (50 μg mL^{-1}) LB medium at 30 °C overnight as pre-culture. A volume of 100 μL of this pre-culture was used to inoculate at 37 °C in two 300 mL Erlenmeyer flasks with 100 mL kanamycin-containing (50 μg mL^{-1}) LB medium; 0.1 mM IPTG was added into the medium when the cultures reached an OD_{600} of 0.5 and were cultured at 30 °C for 3 h. Then, 2 mM tryptophan or tyrosine were added to the medium and cultured at 30 °C overnight. Next, 2 mL medium was harvested, dried *in vacuo*, re-dissolved in 200 μL DMSO and analyzed by UPLC-HRMS. The *E. coli* ROSETTA strain harboring the empty vector pRSF without the target *disA* gene was cultivated under the same conditions and analyzed by UPLC-HRMS as the negative control.

An in vitro enzymatic characterization was carried out after the purification of the His-tagged DisA. An inoculum of 15 mL of same pre-culture prepared for in vivo assay was used to inoculate 1.5 L kanamycin-containing (50 μg mL^{-1}) LB medium; 0.1 mM IPTG was added to the medium when the cultures reached an OD_{600} of 0.5 and were cultured overnight. Cells were collected by centrifugation at 4 °C with 10,000 rpm and resuspended in lysis buffer (50 mM NaH_2PO_4, 300 mM NaCl and 10 mM imidazole; pH 8.0). The resulting suspensions were sonicated and centrifuged at 4 °C at maximum speed for 30 min. The supernatant was loaded onto a pre-equilibrated 750 μL Qiagen® Ni-NTA column. After washing with a 3 mL lysis buffer and 3 mL wash buffer (20 mM imidazole lysis buffer), the His-tagged protein DisA was eluted from the column using an elution buffer (250 mM imidazole lysis buffer) (Figure S49). The protein was resuspended into an imidazole-free buffer (50 mM NaH_2PO_4, 300 mM NaCl; pH 8.0) and concentrated using the Amicon® Ultra-15 centrifugation membrane column.

Enzymatic reactions were performed in 50 mM lysis buffer without imidazole (50 mM NaH_2PO_4, 300 mM NaCl, pH 8.0), containing 100 μM tryptophan (or 20 μM tyrosine) and 5 μM DisA in a total volume of 0.5 mL. After incubation at 30 °C overnight, the same volume of MeOH was added to quench the reactions. The reaction mixture was then centrifuged and the supernatant was dried and re-dissolved in 50 μL 50% MeOH and analyzed by analytical HPLC (0–16 min, 5% MeCN; 16–26 min, gradient increased from 5% to 100% MeCN).

4.4. Bioactivity Tests

Determination of the minimum inhibitory concentration (MIC) of purified compounds **1–7** was carried out by micro broth dilution assays in 96 well plates as described previously [27]. All compounds were dissolved in dimethyl sulfoxide (DMSO, Carl Roth GmbH + Co., Karlsruhe, Germany) with a concentration of 3.2 mg/mL and tested in triplicate. Dilution series (64−0.03 μg/mL) of rifampicin, tetracycline, and gentamicin (all Sigma-Aldrich, St. Louis, MS, USA) were prepared as positive controls for *B. subtilis* DSM10, *L. monocytogenes* DSM20600, *S. aureus* ATCC25923, and *E. coli* ATCC25922. Same dilution series of rifampicin, tetracycline, and isoniazid for *M. smegmatis* ATCC607. For fungi (*C. albicans* FH2173), tebuconazole (Cayman Chemical Company, Ann Arbor, MI, USA.), amphotericin B (Sigma-Aldrich, St. Louis, MS, USA) and nystatin (Sigma-Aldrich, St. Louis, MS, USA) were used as the positive control with same dilution series.

Supplementary Materials: The supporting information is available free of charge at: https://www.mdpi.com/article/10.3390/md20100620/s1, Figures S1–S48: HR-ESI-MS, HR-ESI-MS/MS and NMR spectra for compounds 1–7; Figure S49: SDS-PAGE gel of the purified His-tagged DisA (PDF).

Author Contributions: Conceptualization, L.W. and T.F.S.; methodology, L.W. and M.M.; data analysis, L.W., M.M., U.M. and Y.L.; writing—original draft preparation, L.W. and Y.L.; writing—review and editing, all authors; visualization, L.W.; supervision, project administration, and funding acquisition, T.F.S. All authors have read and agreed to the published version of the manuscript.

Funding: L.W. was funded by the China Scholarship Council (CSC NO. 201908080177). The Schäberle lab is part of the German Center of Infection Research (DZIF) and supported by the Hessen State Ministry of Higher Education, Research and the Arts (HMWK) via the LOEWE Center for Insect Biotechnology and Bioresources.

Acknowledgments: The authors would like to thank Heike Hausmann (Justus-Liebig-University Giessen, Germany) for measuring NMR spectra for structure elucidation.

Conflicts of Interest: The authors declare no conflict of interest.

References

1. Seipp, K.; Geske, L.; Opatz, T. Marine Pyrrole Alkaloids. *Mar. Drugs* **2021**, *19*, 514. [CrossRef] [PubMed]
2. Jin, Z. Muscarine, imidazole, oxazole and thiazole alkaloids. *Nat. Prod. Rep.* **2016**, *33*, 1268–1317. [CrossRef] [PubMed]
3. Chen, J.; Lv, S.; Liu, J.; Yu, Y.; Wang, H.; Zhang, H. An Overview of Bioactive 1, 3-Oxazole-Containing Alkaloids from Marine Organisms. *Pharmaceuticals* **2021**, *14*, 1274. [CrossRef] [PubMed]
4. O'Hagan, D. Pyrrole, pyrrolidine, pyridine, piperidine and tropane alkaloids. *Nat. Prod. Rep.* **2000**, *17*, 435–446. [CrossRef]
5. Ma, X.; Liang, X.; Huang, Z.H.; Qi, S.H. New alkaloids and isocoumarins from the marine gorgonian-derived fungus *Aspergillus* sp. SCSIO 41501. *Nat. Prod. Res.* **2000**, *34*, 1992–2000. [CrossRef]
6. Hassan, W.; Edrada, R.; Ebel, R.; Wray, V.; Berg, A.; Soest, R.V.; Wiryowidagdo, S.; Proksch, P. New imidazole alkaloids from the Indonesian sponge *Leucetta chagosensis*. *J. Nat. Prod.* **2004**, *67*, 817–822. [CrossRef]
7. Dyson, L.; Wright, A.D.; Young, K.A.; Sakoff, J.A.; McCluskey, A. Synthesis and anticancer activity of focused compound libraries form the natural product lead, oroidin. *Bioorg. Med. Chem.* **2014**, *22*, 1690–1699. [CrossRef]
8. Liu, L.P.; Zong, M.H.; Linhardt, R.J.; Lou, W.Y.; Li, N.; Huang, C.; Wu, H. Mechanistic insights into the effect of imidazolium ionic liquid on liquid production by *Geotrichum fermentas*. *Biotechnol. Biofuels* **2016**, *9*, 266. [CrossRef]
9. Johnson, N.A.; Southerland, M.R.; Youngs, W.J. Recent Developments in the Medicinal Applications of Silver-NHC Complexes and Imidazolium Salts. *Molecules* **2017**, *22*, 1263. [CrossRef]
10. Kirchhecker, S.; Antonietti, M.; Esposito, D. Hydrothermal decarboxylation of amino acid derived imidazolium zwitterions: A sustainable approach towards ionic liquids. *Green Chem.* **2014**, *16*, 3705–3709. [CrossRef]
11. Roué, M.; Domart-Coulon, I.; Ereskovsky, A.; Djediat, C.; Perez, T.; Bourguet-Kondracki, M.L. Cellular localization of clathridimine, an antimicrobial 2-aminoimidazole alkaloid produced by the Mediterranean calcareous sponge *Clathrina clathrus*. *J. Nat. Prod.* **2010**, *73*, 1277–1282. [CrossRef] [PubMed]
12. Bjørsvik, H.; Sandtorv, A. Synthesis of Imidazole Alkaloids Originated in Marine Sponges. In *Studies in Natural Products Chemistry*; Elsevier: Amsterdam, The Netherlands, 2014; Volume 42, pp. 33–57.
13. Dunbar, D.C.; Rimoldi, J.M.; Clark, A.M.; Kelly, M.; Hamann, M.T. Anti-cryptococcal and nitric oxide synthase inhibitory imidazole alkaloids from the calcareous sponge *Leucetta cf chagosensis*. *Tetrahedron* **2000**, *56*, 8795–8798. [CrossRef]
14. Gross, H.; Kehraus, S.; König, G.M.; Woerheide, G.; Wright, A.D. New and biologically active imidazole alkaloids from two sponges of the genus *Leucetta*. *J. Nat. Prod.* **2002**, *65*, 1190–1193. [CrossRef] [PubMed]
15. Bernardet, J.F. Family I. Flavobacteriaceae Reichenbach 1992. In *Bergey's Manual of Systematic Bacteriology*, 2nd ed.; Krieg, N.R., Staley, J.T., Brown, D.R., Hedlund, B.P., Paster, B.J., Ward, N.L., Ludwig, W., Whitman, W.B., Eds.; Springer: New York, NY, USA, 2011; Volume 4, pp. 106–111.
16. Frette, L.; Jørgensen, N.O.; Irming, H.; Kroer, N. *Tenacibaculum skagerrakense* sp. nov., a marine bacterium isolated from the pelagic zone in Skagerrak, Denmark. *Int. J. Syst. Evol. Microbiol.* **2004**, *54*, 519–524. [CrossRef]
17. Yoon, J.H.; Kang, S.J.; Jung, S.Y.; Oh, H.W.; Oh, T.K. *Gaetbulimicrobium brevivitae* gen. nov., sp. nov., a novel member of the family *Flavobacteriaceae* isolated from a tidal flat of the Yellow Sea in Korea. *Int. J. Syst. Evol. Microbiol.* **2006**, *56*, 115–119. [CrossRef]
18. Heindl, H.; Wiese, J.; Imhoff, J.F. *Tenacibaculum adriaticum* sp. nov., from a bryozoan in the Adriatic Sea. *Int. J. Syst. Evol. Microbiol.* **2008**, *58*, 542–547. [CrossRef]
19. Wang, J.T.; Chou, Y.J.; Chou, J.H.; Chen, C.A.; Chen, W.M. *Tenacibaculum aiptasiae* sp. nov., isolated from a sea anemone *Aiptasia pulchella*. *Int. J. Syst. Evol. Microbiol.* **2008**, *58*, 761–766. [CrossRef]
20. Lee, Y.S.; Baik, K.S.; Park, S.Y.; Kim, E.M.; Lee, D.H.; Kahng, H.Y.; Jeon, C.O.; Jung, J.S. *Tenacibaculum crassostreae* sp. nov., isolated from the Pacific oyster, *Crassostrea gigas*. *Int. J. Syst. Evol. Microbiol.* **2009**, *59*, 1609–1614. [CrossRef]
21. Pineiro-Vidal, M.; Riaza, A.; Santos, Y. *Tenacibaculum discolor* sp. nov. and *Tenacibaculum gallaicum* sp. nov., isolated from sole (*Solea senegalensis*) and turbot (*Psetta maxima*) culture systems. *Int. J. Syst. Evol. Microbiol.* **2008**, *58*, 21–25. [CrossRef]
22. Suzuki, M.; Nakagawa, Y.; Harayama, S.; Yamamoto, S. Phylogenetic analysis and taxonomic study of marine *Cytophaga*-like bacteria: Proposal for *Tenacibaculum* gen. nov. with *Tenacibaculum maritimum* comb. nov. and *Tenacibaculum ovolyticum* comb. nov., and description of *Tenacibaculum mesophilum* sp. nov. and *Tenacibaculum amylolyticum* sp. nov. *Int. J. Syst. Evol. Microbiol.* **2001**, *51*, 1639–1652.
23. Avendaño-Herrera, R.; Toranzo, A.E.; Magariños, B. Tenacibaculosis infection in marine fish caused by *Tenacibaculum maritimum*: A review. *Dis. Aquat. Organ.* **2006**, *71*, 255–266. [CrossRef] [PubMed]
24. Igarashi, Y.; Ge, Y.; Zhou, T.; Sharma, A.R.; Harunari, E.; Oku, N.; Trianto, A. Tenacibactins K–M, cytotoxic siderophores from a coral-associated gliding bacterium of the genus *Tenacibaculum*. *Beilstein. J. Org. Chem.* **2022**, *18*, 110–119. [CrossRef] [PubMed]

25. Jang, J.H.; Kanoh, K.; Adachi, K.; Matsuda, S.; Shizuri, Y. Tenacibactins a-d, hydroxamate siderophores from a marine-derived bacterium, *Tenacibaculum* sp. a4k-17. *J. Nat. Prod.* **2007**, *70*, 563–566. [CrossRef] [PubMed]
26. Fujita, M.J.; Nakano, K.; Sakai, R. Bisucaberin B, a Linear Hydroxamate Class Siderophore from the Marine Bacterium *Tenacibaculum mesophilum*. *Molecules* **2013**, *18*, 3917–3926. [CrossRef] [PubMed]
27. Wang, L.; Linares-Otoya, V.; Liu, Y.; Mettal, U.; Marner, M.; Armas Mantilla, L.; Willbold, S.; Kurtán, T.; Linares-Otoya, L.; Schäberle, T.F. Discovery and Biosynthesis of Antimicrobial Phenethylamine Alkaloids from the Marine Flavobacterium *Tenacibaculum discolor* sv11. *J. Nat. Prod.* **2022**, *85*, 1039–1051. [CrossRef]
28. Yan, J.X.; Wu, Q.; Helfrich, E.J.N.; Chevrette, M.G.; Braun, D.R.; Heyman, H.; Ananiev, G.E.; Rajski, S.R.; Currie, C.R.; Clardy, J.; et al. Bacillimidazoles A-F, Imidazolium-Containing Compounds Isolated from a Marine *Bacillus*. *Mar. Drugs* **2022**, *20*, 43. [CrossRef]
29. Silverstein, R.M.; Webster, F.X.; Kiemle, D.J.; Bryce, D.L. *Spectrometric Identification of Organic Compounds*, 8th ed.; John Wiley & Sons, Inc.: New York, NY, USA, 2015; pp. 299–305.
30. Zeng, Z.; Qasem, A.M.A.; Woodman, T.J.; Rowan, M.G.; Blagbrough, I.S. Impacts of Steric Compression, Protonation, and Intramolecular Hydrogen Bonding on the ^{15}N NMR Spectroscopy of Norditerpenoid Alkaloids and Their Piperidine-Ring Analogues. *ACS Omega* **2020**, *5*, 14116–14122. [CrossRef]
31. Wang, F.P.; Chen, D.L.; Deng, H.Y.; Chen, Q.H.; Liu, X.Y.; Jian, X.X. Further revisions on the diterpenoid alkaloids reported in a JNP paper (**2012**, *75*, 1145–1159). *Tetrahedron* **2014**, *70*, 2582–2590. [CrossRef]
32. Güntzel, P.; Schilling, K.; Hanio, S.; Schlauersbach, J.; Schollmayer, C.; Meinel, L.; Holzgrabe, U. Bioinspired Ion Pairs Transforming Papaverine into a Protic Ionic Liquid and Salts. *ACS Omega* **2020**, *5*, 19202–19209. [CrossRef]
33. Wu, L.X.; Xu, X.D.; Chen, X.; Miao, C.P.; Chen, Y.W.; Xu, L.H.; Zhao, L.X.; Li, Y.Q. Indole and tyramine alkaloids produced by an endophytic actinomycete associated with Artemisia annua. *Chem. Nat. Compd.* **2017**, *53*, 999–1001. [CrossRef]
34. Wright, B.D.; Deblock, M.C.; Wagers, P.O.; Duah, E.; Robishaw, N.K.; Shelton, K.L.; Southerland, M.R.; DeBord, M.A.; Kersten, K.M.; McDonald, L.J.; et al. Anti-tumor activity of lipophilic imidazolium salts on select NSCLC cell lines. *Med. Chem. Res.* **2015**, *24*, 2838–2861. [CrossRef] [PubMed]

Supporting Information of Publication 2

Supplementary Information

Seven New Alkaloids Isolated from Marine Flavobacterium *Tenacibaculum discolor* sv11

Lei Wang [1,2], Michael Marner [2], Ute Mettal [1,2], Yang Liu [1,2,*] and Till F. Schäberle [1,2,3,*]

1 Institute for Insect Biotechnology, Justus-Liebig-University Giessen, 35392 Giessen, Germany

2 Fraunhofer Institute for Molecular Biology and Applied Ecology (IME), Branch for Bioresources, 35392 Giessen, Germany

3 German Center for Infection Research (DZIF), Partner Site Giessen-Marburg-Langen, 35392 Giessen, Germany

* Correspondence: Till.F.Schaeberle@agrar.uni-giessen.de; Tel.: +49-(0)641-97219-140 (T.F.S.); Liu.Yang@agrar.uni-giessen.de (Y.L.)

Contents

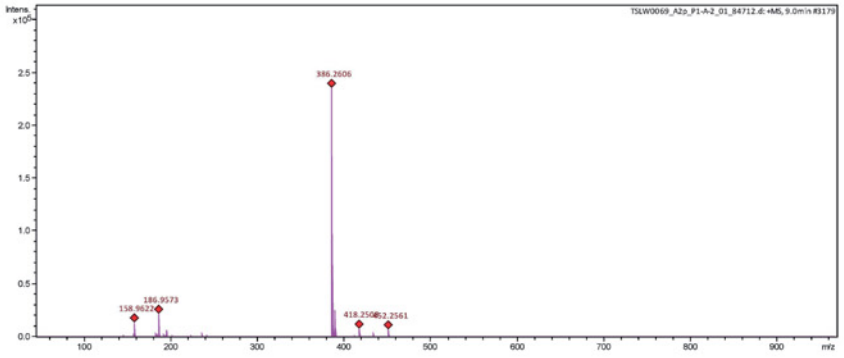

Meas. m/z	#	Ion Formula	m/z	err [ppm]	mSigma	# mSigma	Score	rdb	eÂ¯ Conf	N-Rule
386.2606	1	C26H32N3	386.2591	-4.0	5.4	1	100.00	12.5	even	ok

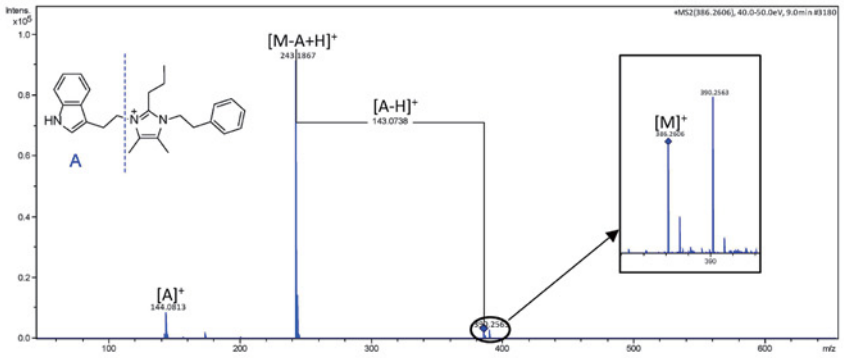

Figure S1. The HR-ESI-MS and HR-ESI-MS/MS of compound 1.

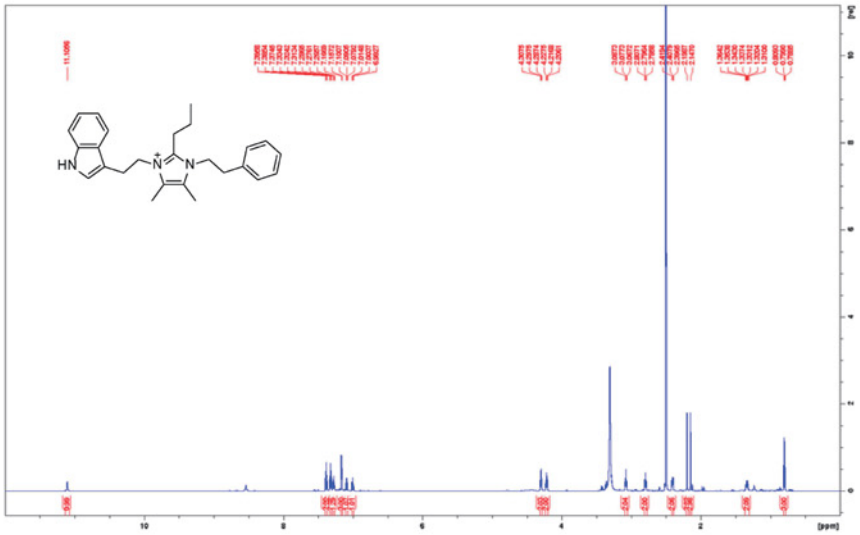

Figure S2. The ^{1}H-NMR (700 MHz, DMSO-d_6) spectrum of compound 1.

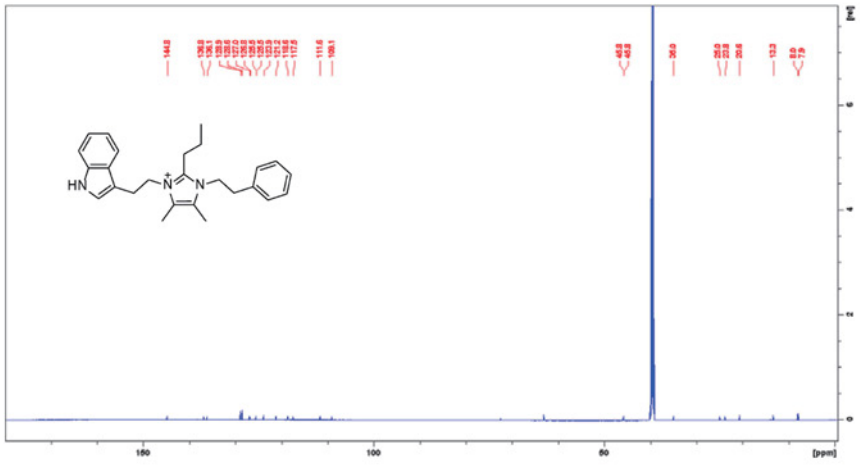

Figure S3. The ^{13}C-NMR (175 MHz, DMSO-d_6) spectrum of compound 1.

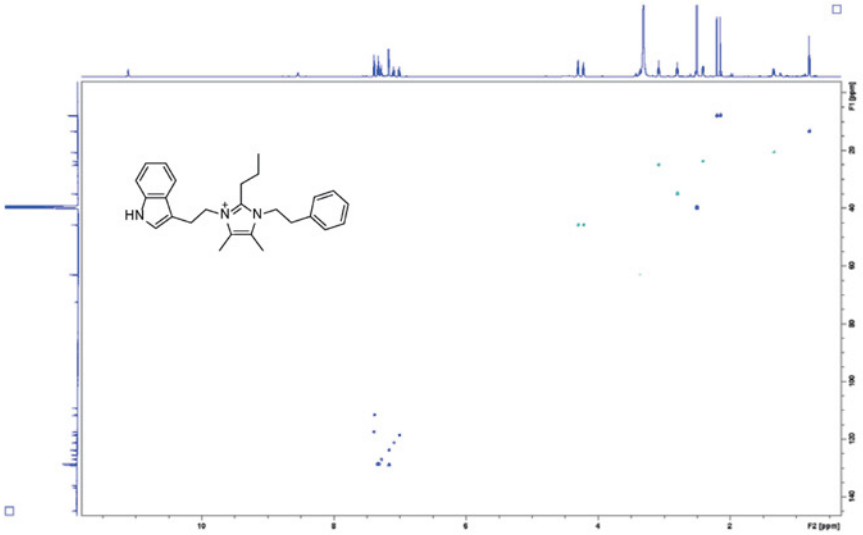

Figure S4. The HSQC (700 MHz, DMSO-d_6) spectrum of compound 1.

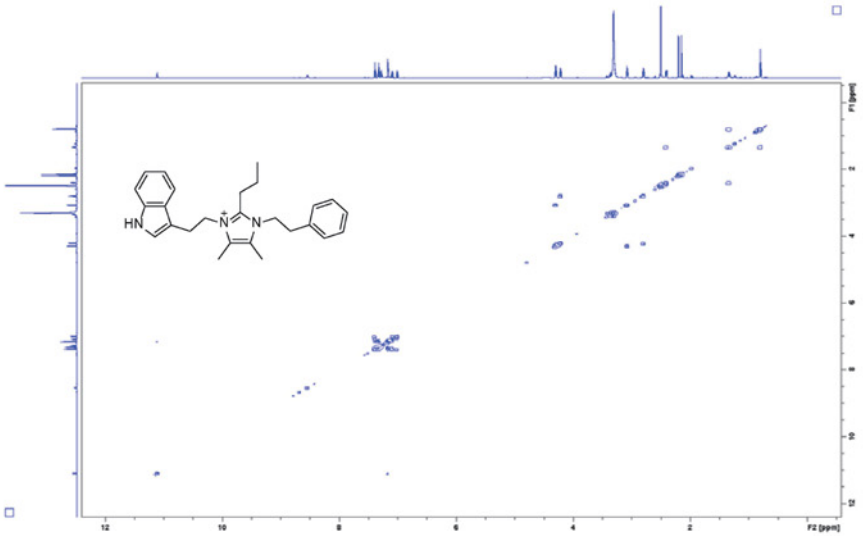

Figure S5. The ^{1}H-^{1}H COSY (700 MHz, DMSO-d_6) spectrum of compound 1.

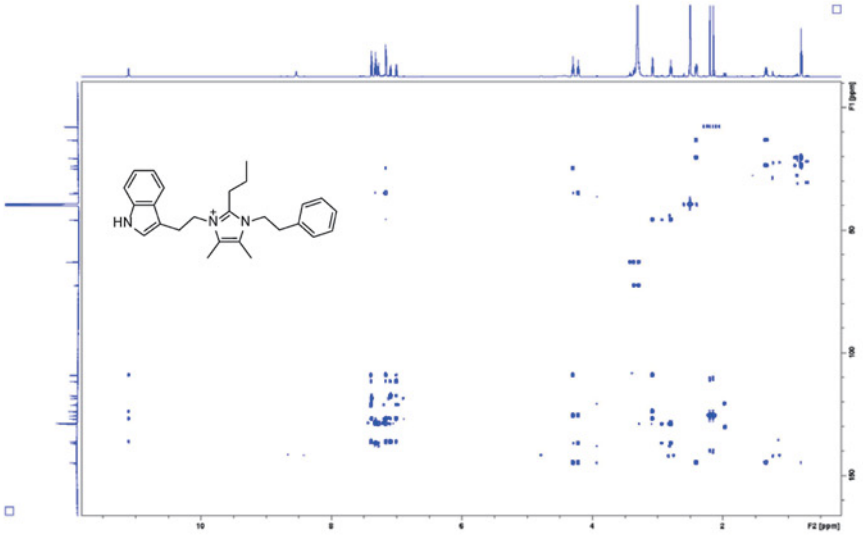

Figure S6. The ^{1}H-^{13}C HMBC (700 MHz, DMSO-d_6) spectrum of compound 1.

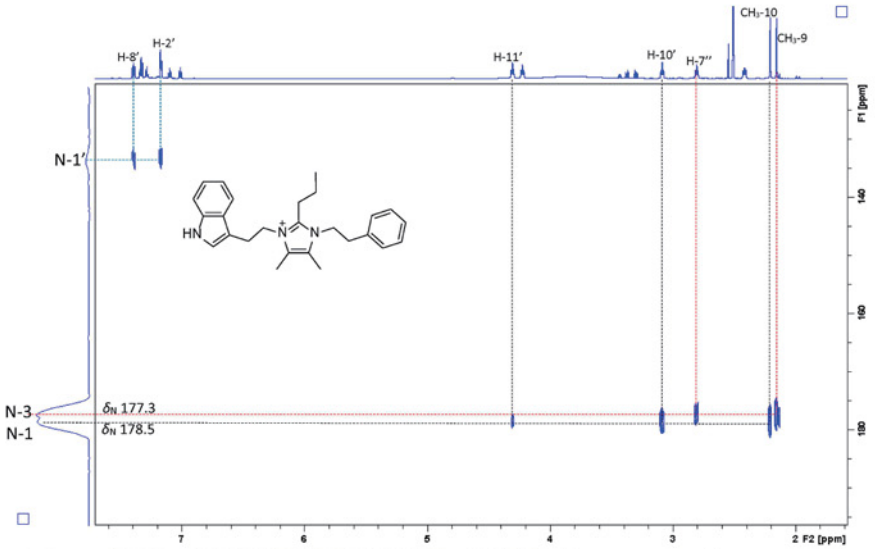

Figure S7. The ^{1}H-^{15}N HMBC (700 MHz, DMSO-d_6) spectrum of compound 1.

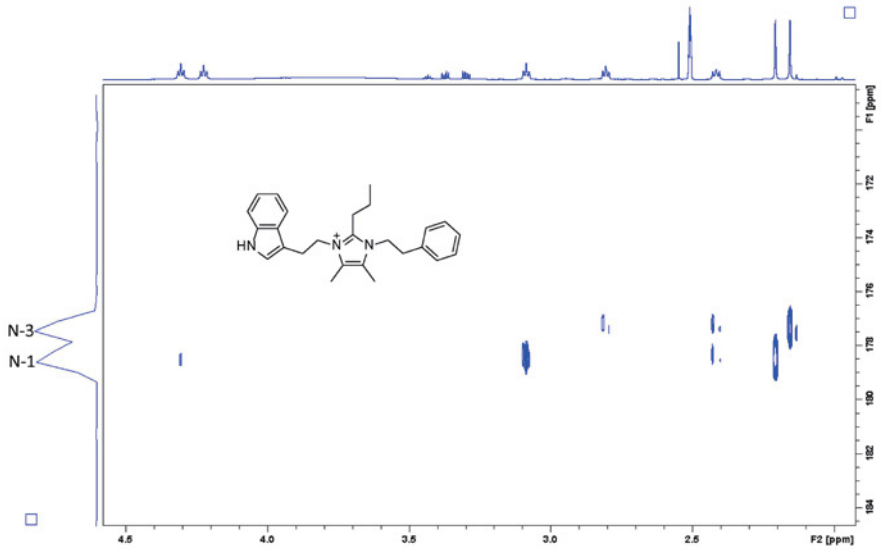

Figure S8. The ^{1}H-^{15}N HMBC (700 MHz, DMSO-d_6) spectrum of compound 1 (measured with non-uniform sampling).

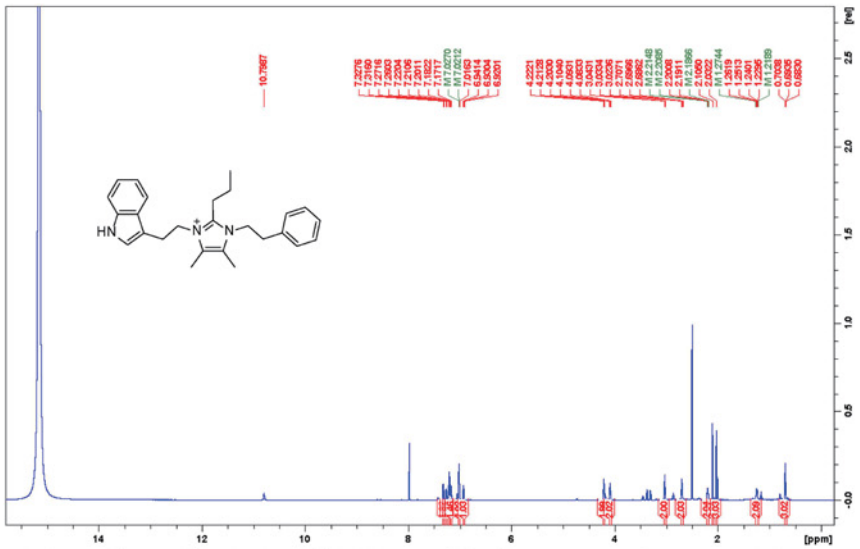

Figure S9. The ^{1}H-NMR (700 MHz, DMSO-d_6) spectrum of compound 1 with TFA added.

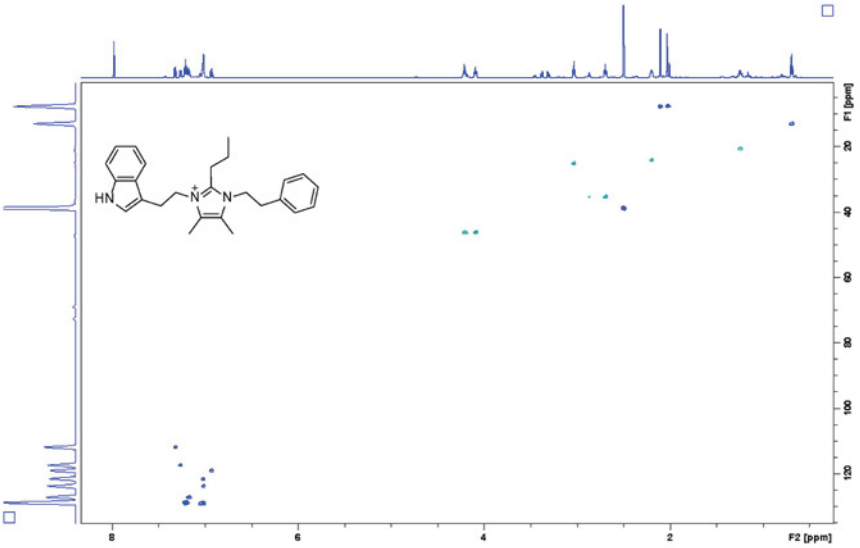

Figure S10. The HSQC (700 MHz, DMSO-*d*$_6$) spectrum of compound 1 with TFA added.

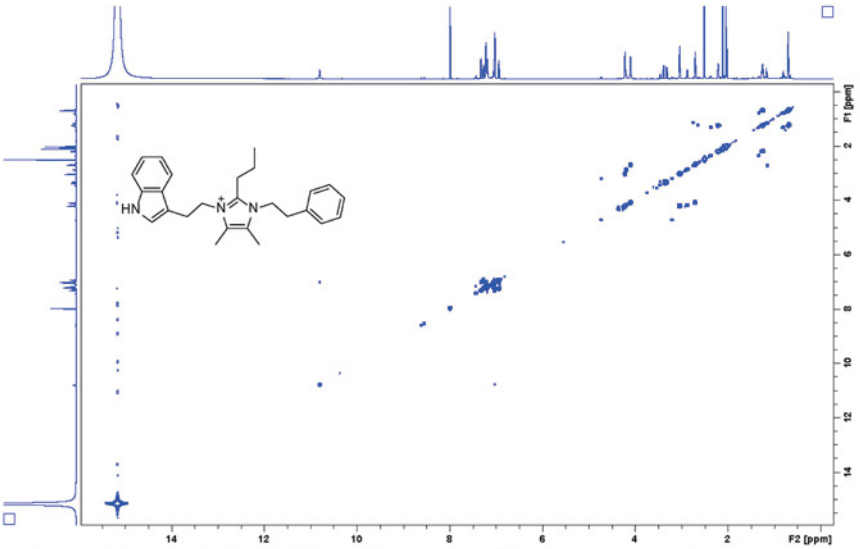

Figure S11. The ^{1}H-^{1}H COSY (700 MHz, DMSO-*d*$_6$) spectrum of compound 1 with TFA added.

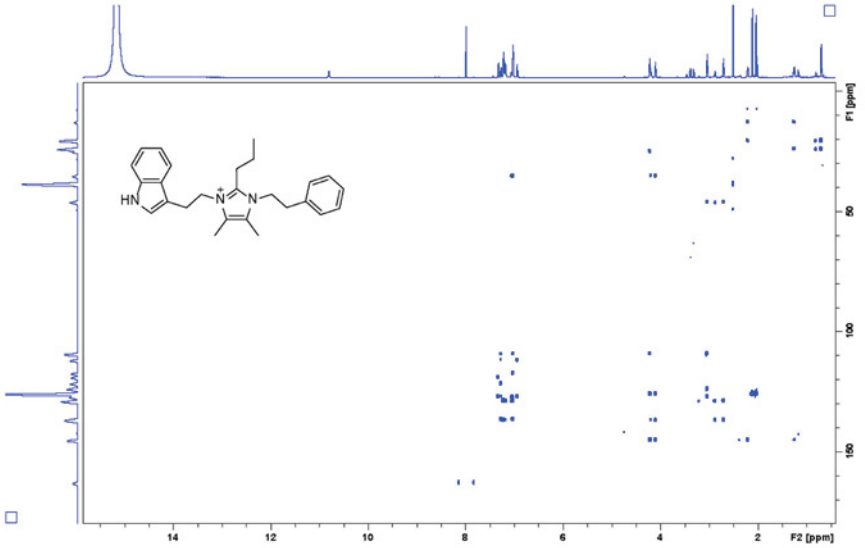

Figure S12. The ^{1}H-^{13}C HMBC (700 MHz, DMSO-d_6) spectrum of compound 1with TFA added.

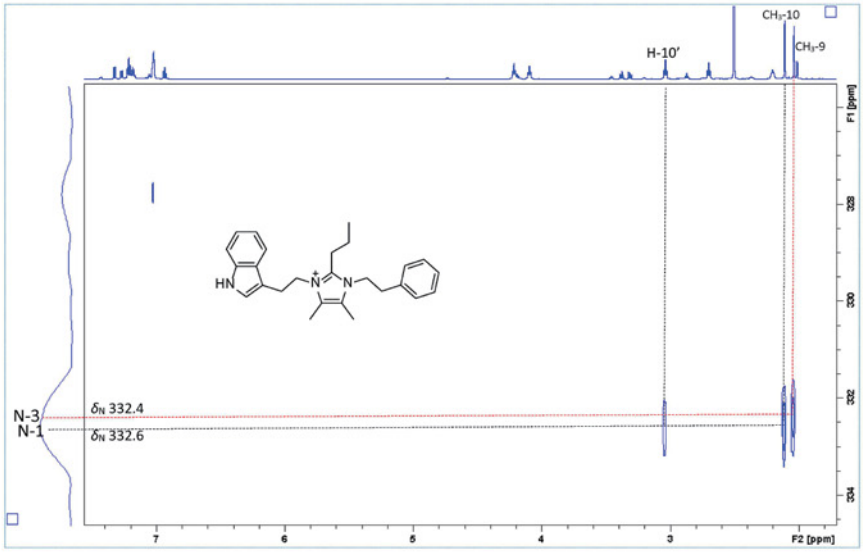

Figure S13. The ^{1}H-^{15}N HMBC (700 MHz, DMSO-d_6) spectrum of compound 1 with TFA added.

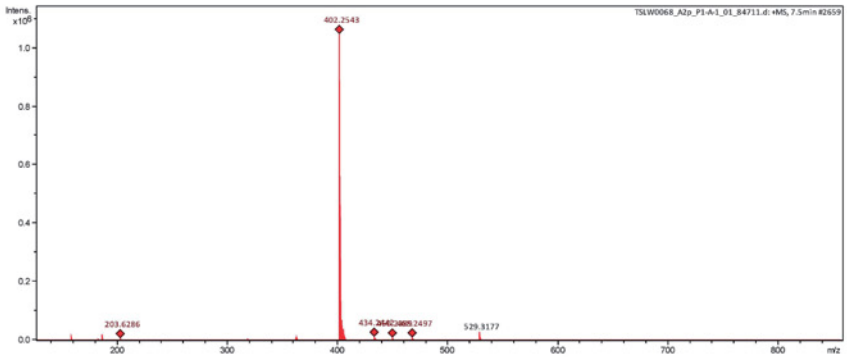

Meas. m/z	#	Ion Formula	m/z	err [ppm]	mSigma	# mSigma	Score	rdb	eÂ¯ Conf	N-Rule
402.2543	1	C26H32N3O	402.2540	-0.9	85.1	1	100.00	12.5	even	ok
402.2543	2	C14H36N5O8	402.2558	3.7	154.4	2	1.20	-0.5	even	ok
402.2543	3	C11H28N15O2	402.2545	0.4	154.9	3	2.40	5.5	even	ok

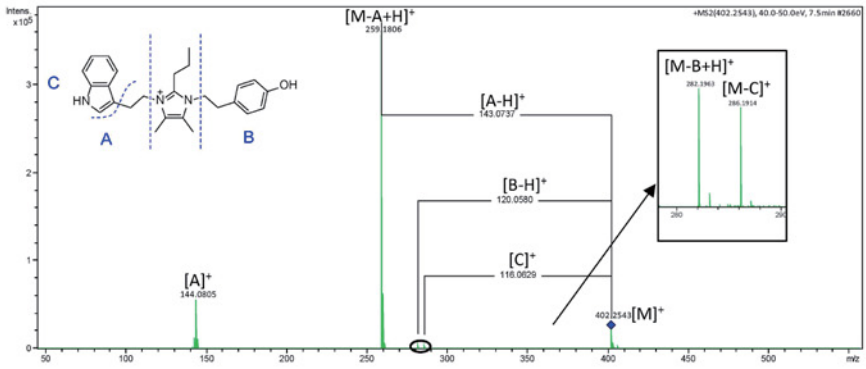

Figure S14. The HR-ESI-MS and HR-ESI-MS/MS of compound 2.

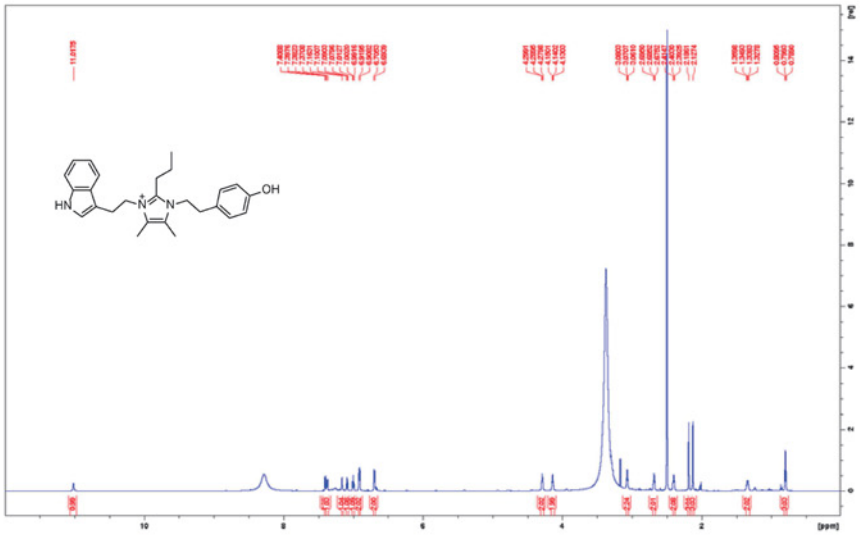

Figure S15. The ^{1}H-NMR (700 MHz, DMSO-d_6) spectrum of compound 2

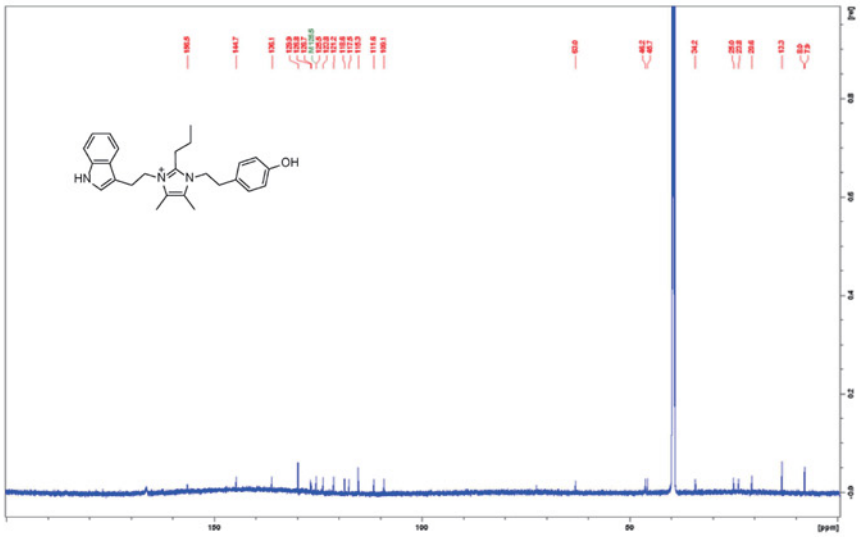

Figure S16. The ^{13}C-NMR (175 MHz, DMSO-d_6) spectrum of compound 2.

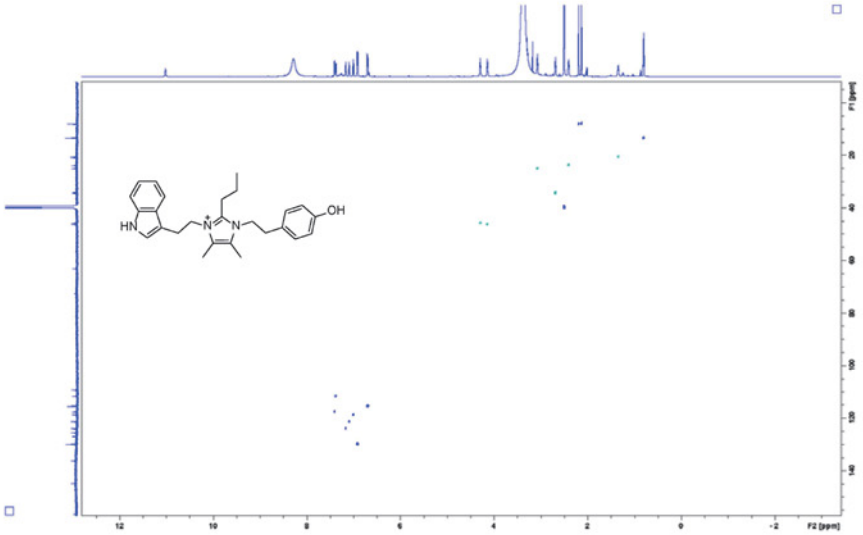

Figure S17. The HSQC (700 MHz, DMSO-d_6) spectrum of compound 2.

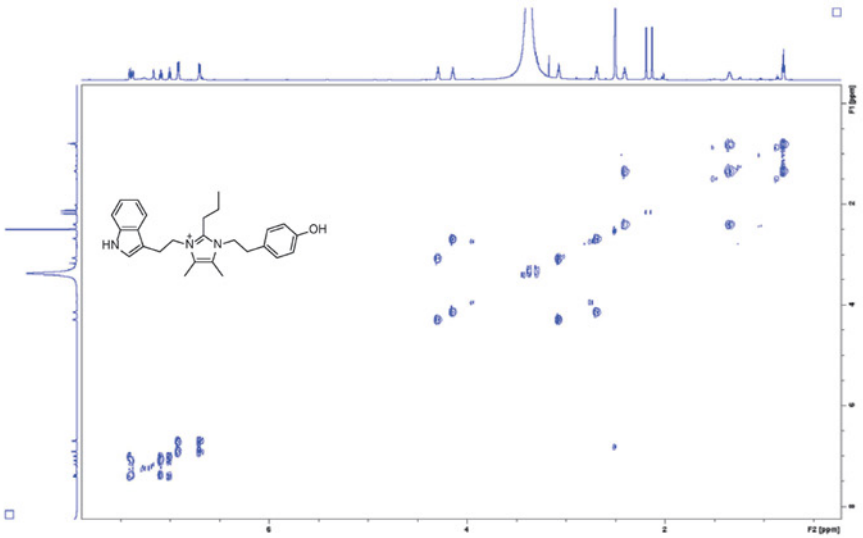

Figure S18. The ^{1}H-^{1}H COSY (700 MHz, DMSO-d_6) spectrum of compound 2.

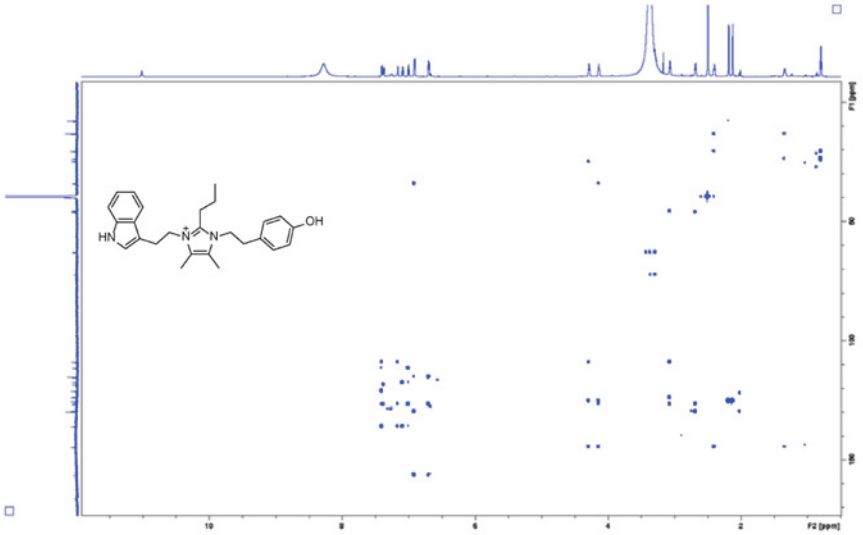

Figure S19. The ^{1}H-^{13}C HMBC (700 MHz, DMSO-d_6) spectrum of compound 2.

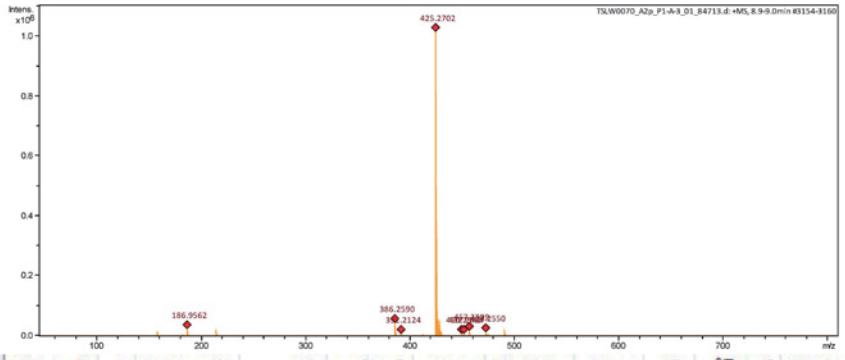

Meas. m/z	#	Ion Formula	m/z	err [ppm]	mSigma	# mSigma	Score	rdb	eÅ¯ Conf	N-Rule
425.2702	1	C28H33N4	425.2700	-0.6	29.0	1	100.00	14.5	even	ok
425.2702	2	C27H37O4	425.2686	-3.7	42.4	2	33.46	9.5	even	ok

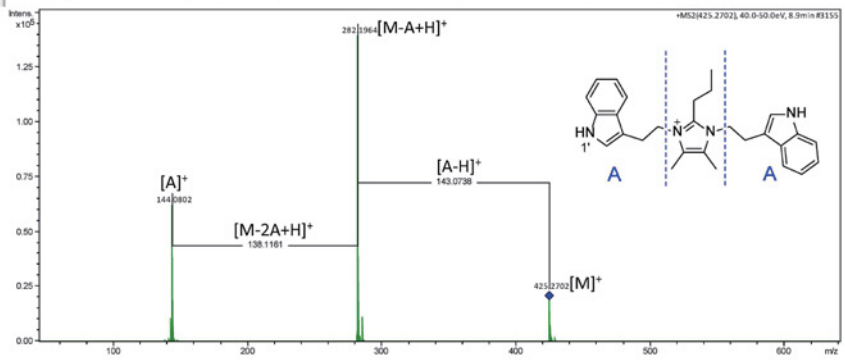

Figure S20. The HR-ESI-MS and HR-ESI-MS/MS of compound 3.

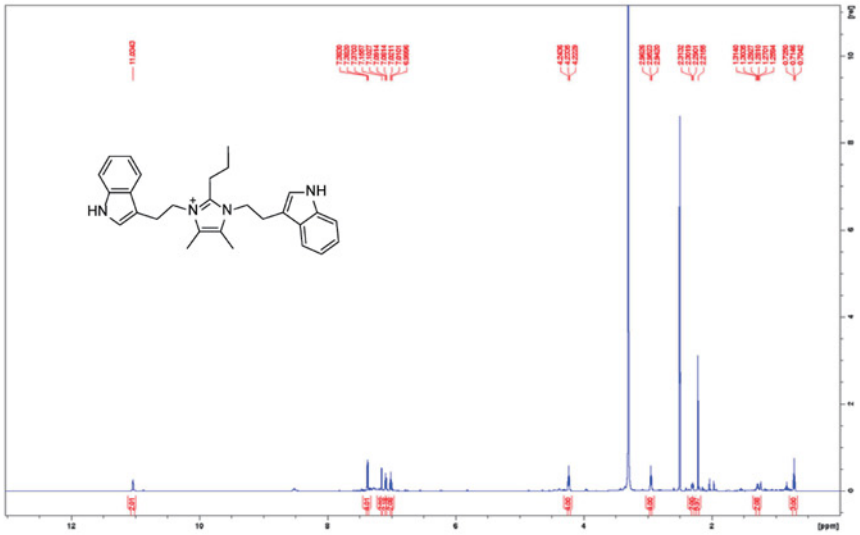

Figure S21. The ^{1}H-NMR (700 MHz, DMSO-d_6) spectrum of compound 3

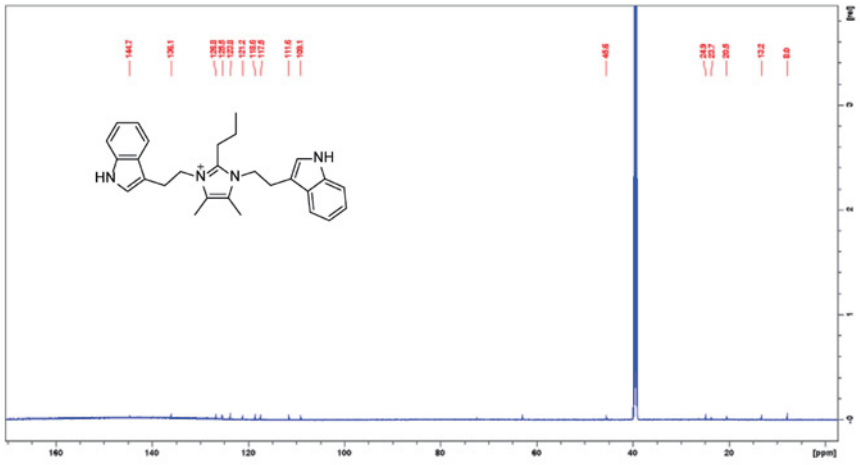

Figure S22. The ^{13}C-NMR (175 MHz, DMSO-d_6) spectrum of compound 3

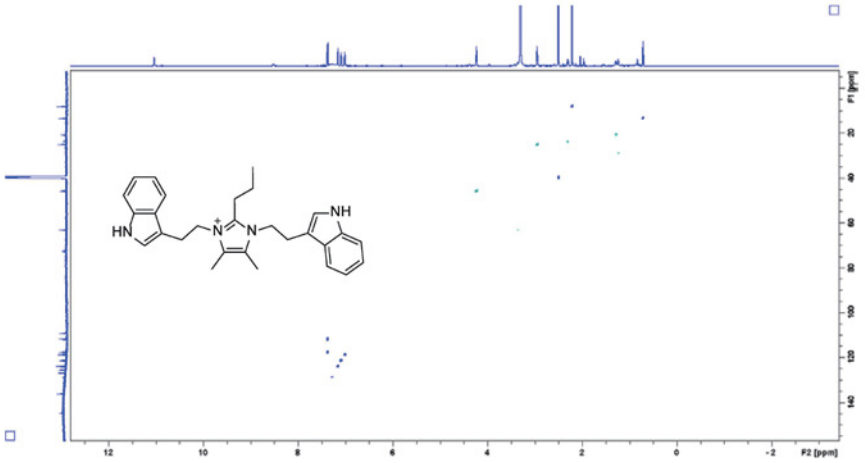

Figure S23. The HSQC (700 MHz, DMSO-d_6) spectrum of compound 3.

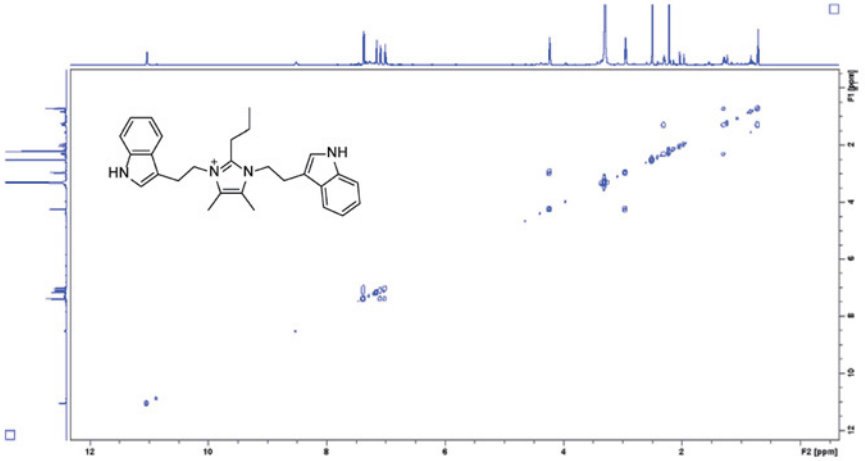

Figure S24. The ^{1}H-^{1}H COSY (700 MHz, DMSO-d_6) spectrum of compound 3.

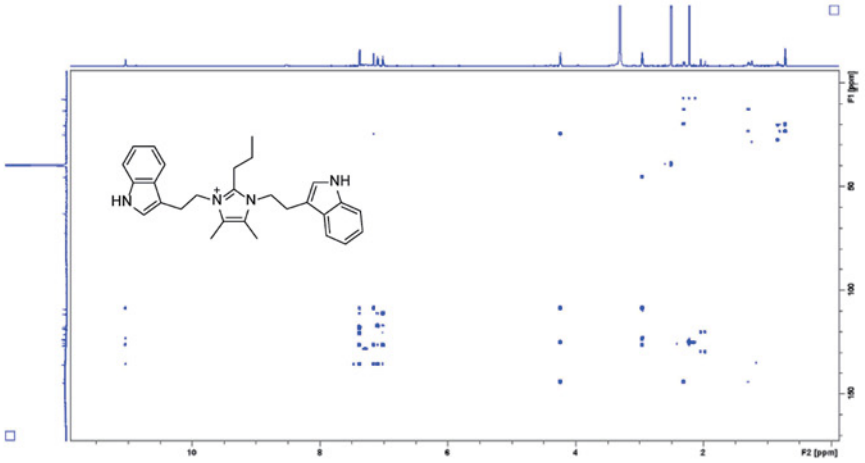

Figure S25. The ^{1}H-^{13}C HMBC (700 MHz, DMSO-d_6) spectrum of compound 3.

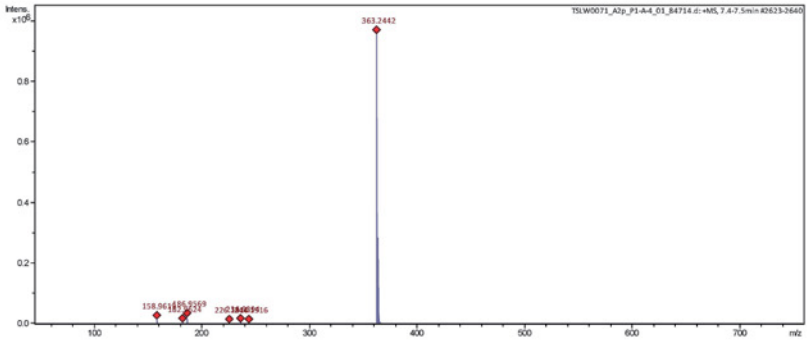

Meas. m/z	#	Ion Formula	m/z	err [ppm]	mSigma	# mSigma	Score	rdb	eÅ¯ Conf	N-Rule
363.2442	1	C24H31N2O	363.2431	-2.9	15.9	1	100.00	10.5	even	ok

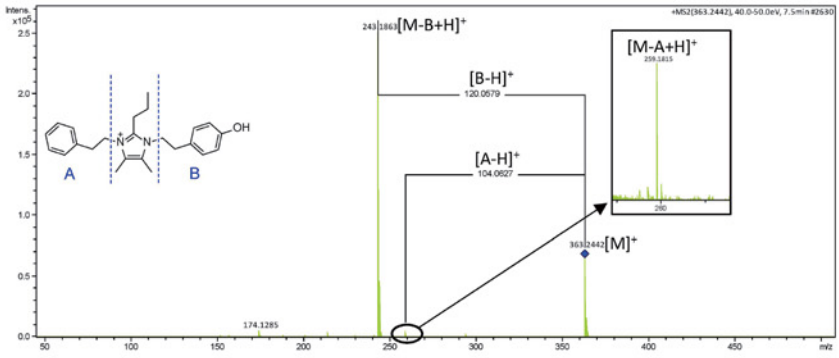

Figure S26. The HR-ESI-MS and HR-ESI-MS/MS of compound 4.

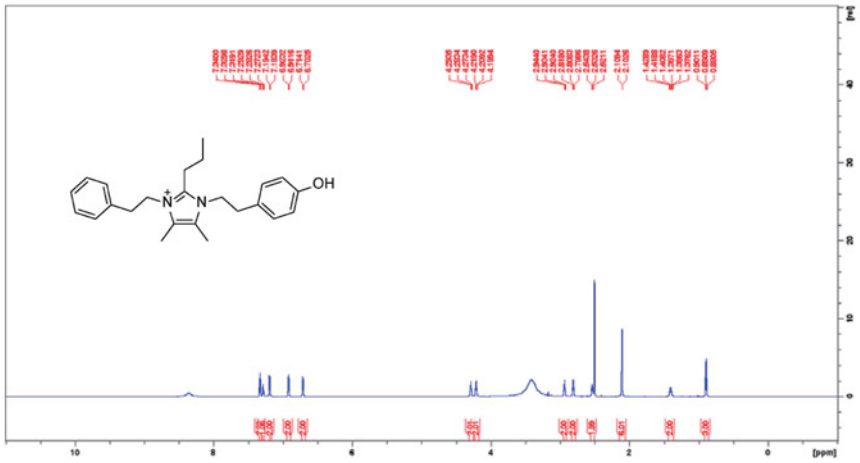

Figure S27. The ^{1}H-NMR (700 MHz, DMSO-d_6) spectrum of compound 4

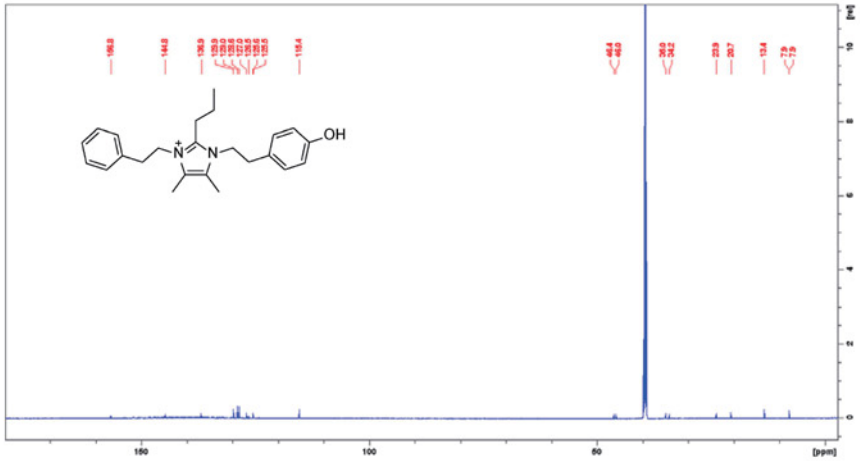

Figure S28. The ^{13}C-NMR (175 MHz, DMSO-d_6) spectrum of compound 4

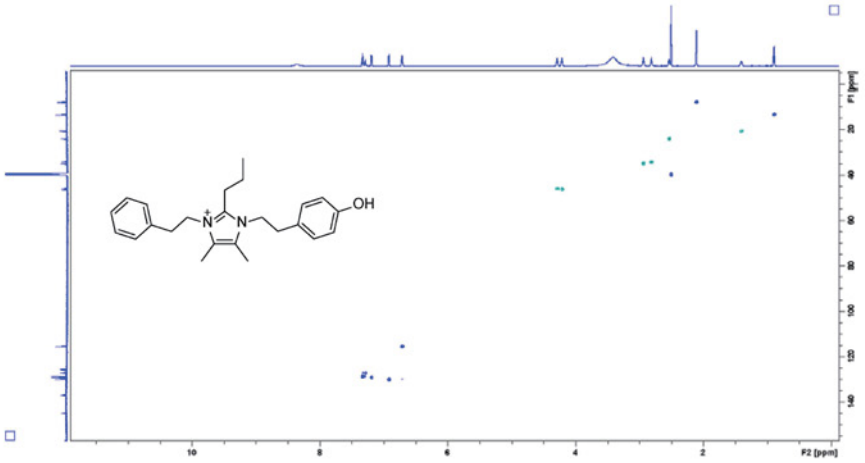

Figure S29. The HSQC (700 MHz, DMSO-d_6) spectrum of compound 4.

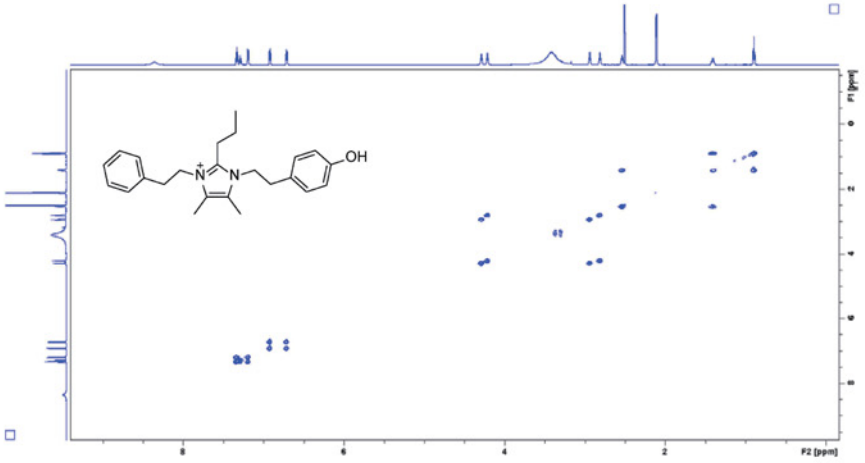

Figure S30. The ^{1}H-^{1}H COSY (700 MHz, DMSO-d_6) spectrum of compound 4.

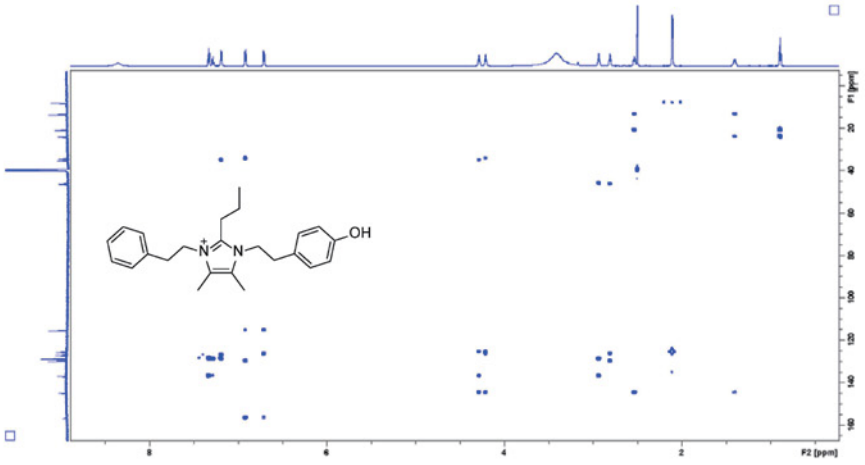

Figure S31. The ^{1}H-^{13}C HMBC (700 MHz, DMSO-d_6) spectrum of compound 4.

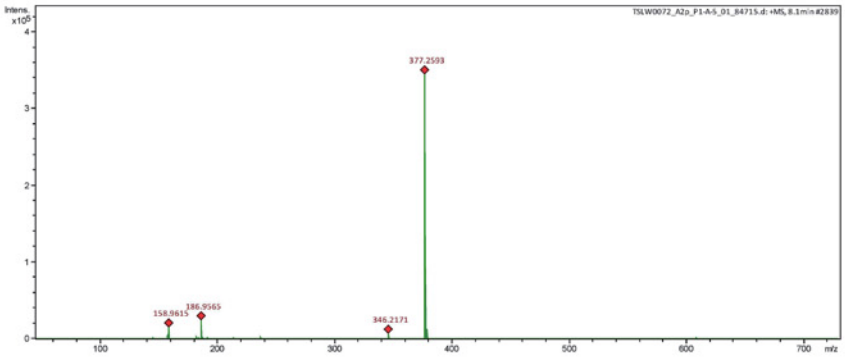

Meas. m/z	#	Ion Formula	m/z	err [ppm]	mSigma	# mSigma	Score	rdb	eÂ¯ Conf	N-Rule
377.2593	1	C25H33N2O	377.2587	-1.5	8.8	1	100.00	10.5	even	ok

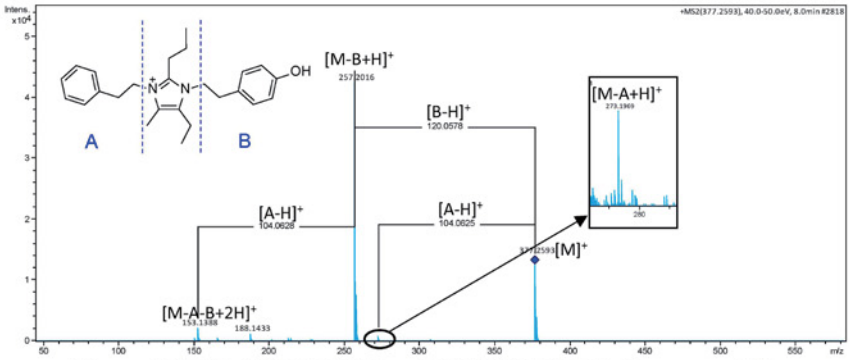

Figure S32. The HR-ESI-MS and HR-ESI-MS/MS of compound 5.

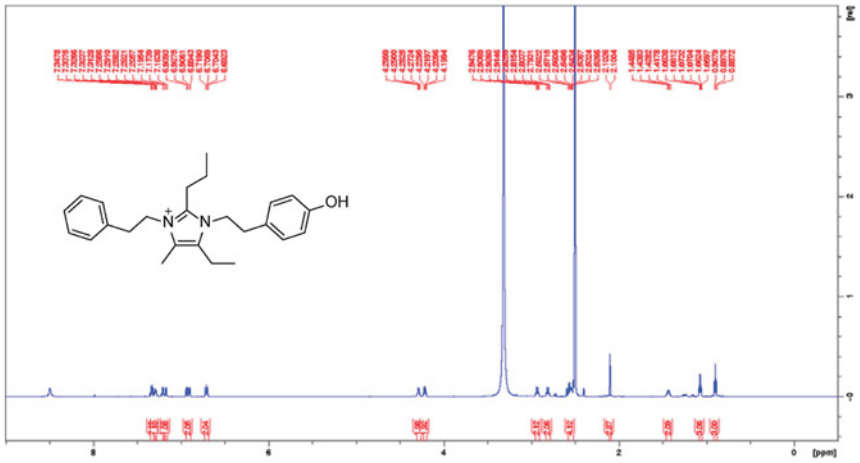

Figure S33. The ^{1}H-NMR (700 MHz, DMSO-d_6) spectrum of compound 5

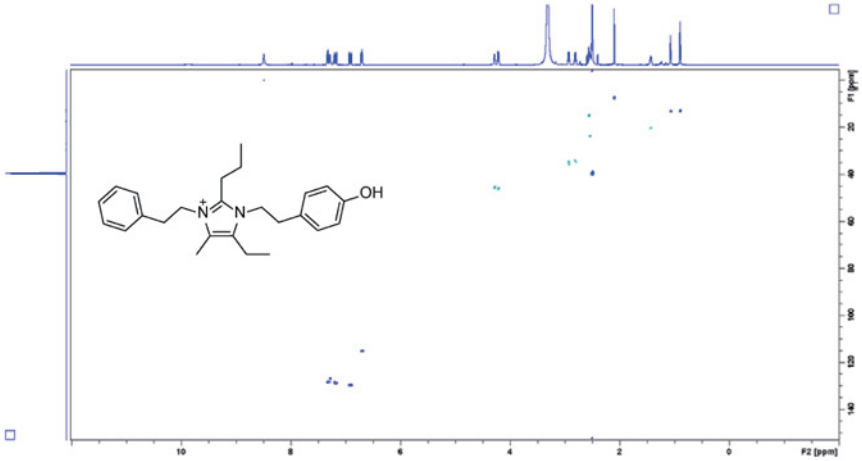

Figure S34. The HSQC (700 MHz, DMSO-d_6) spectrum of compound 5.

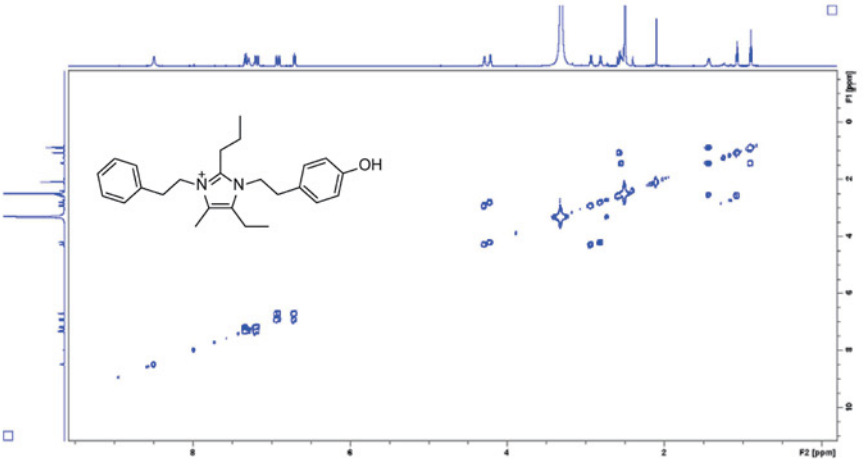

Figure S35. The ^{1}H-^{1}H COSY (700 MHz, DMSO-d_6) spectrum of compound 5.

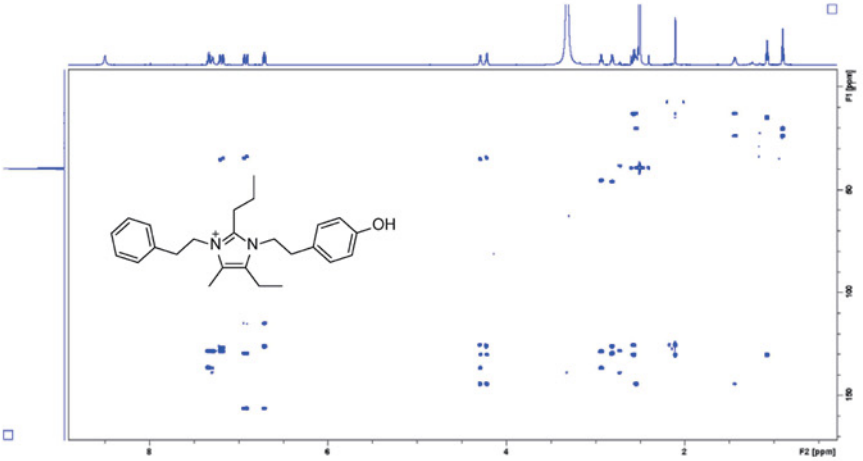

Figure S36. The ^{1}H-^{13}C HMBC (700 MHz, DMSO-d_6) spectrum of compound 5.

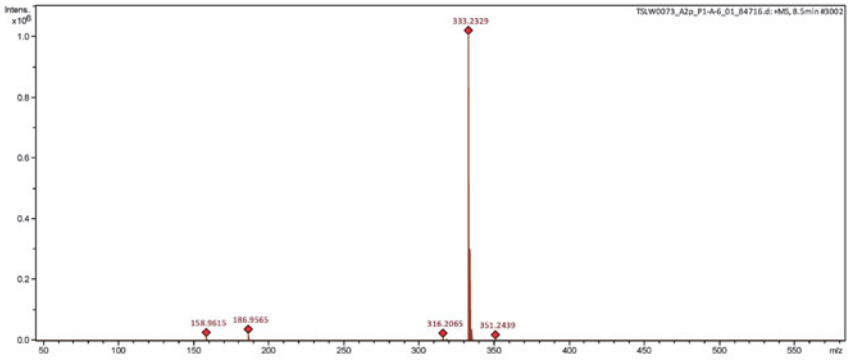

Meas. m/z	#	Ion Formula	m/z	err [ppm]	mSigma	# mSigma	Score	rdb	eÂ¯ Conf	N-Rule
333.2329	1	C23H29N2	333.2325	-1.2	23.6	1	100.00	10.5	even	ok

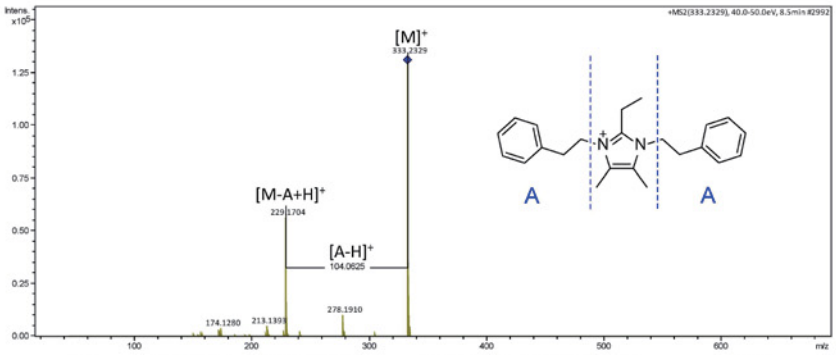

Figure S37. The HR-ESI-MS and HR-ESI-MS/MS of compound 6.

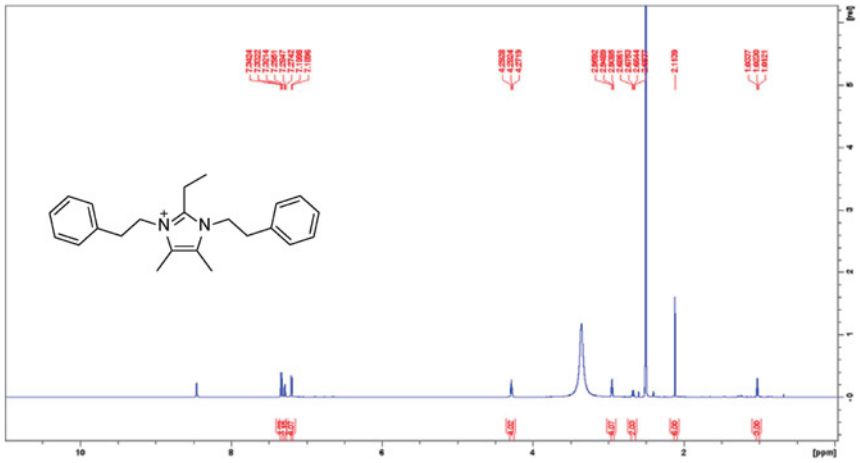

Figure S38. The ^{1}H-NMR (700 MHz, DMSO-d_6) spectrum of compound 6

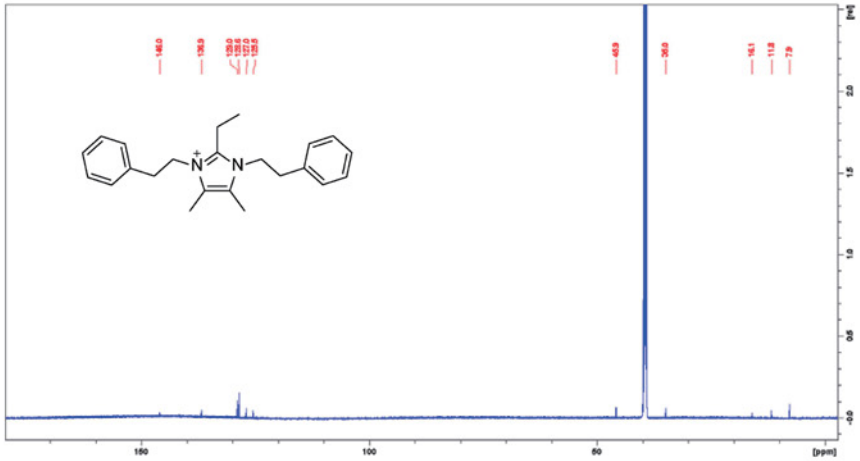

Figure S39. The ^{13}C-NMR (175 MHz, DMSO-d_6) spectrum of compound 6

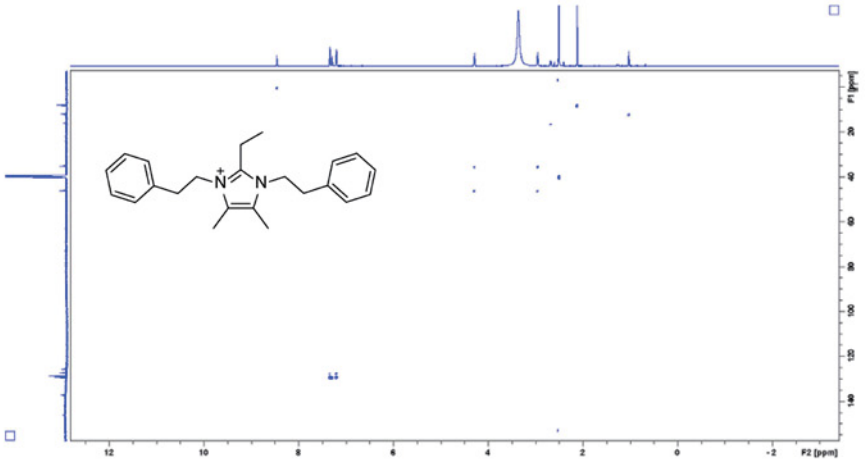

Figure S40. The HSQC (700 MHz, DMSO-d_6) spectrum of compound 6.

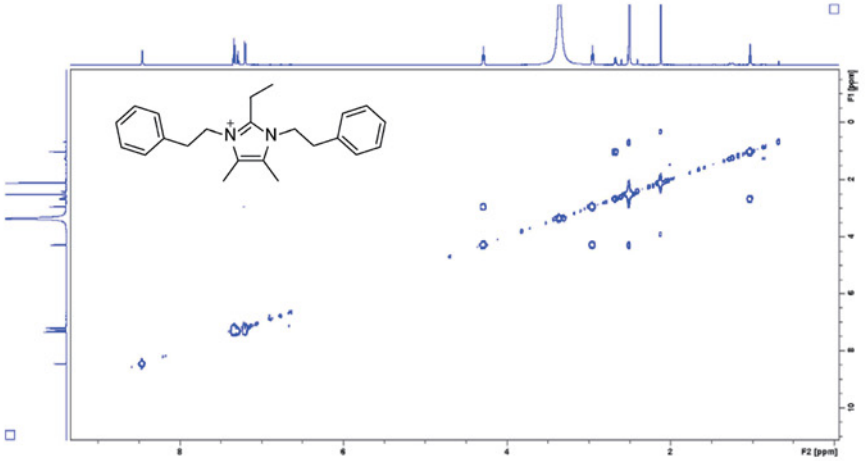

Figure S41. The ^{1}H-^{1}H COSY (700 MHz, DMSO-d_6) spectrum of compound 6.

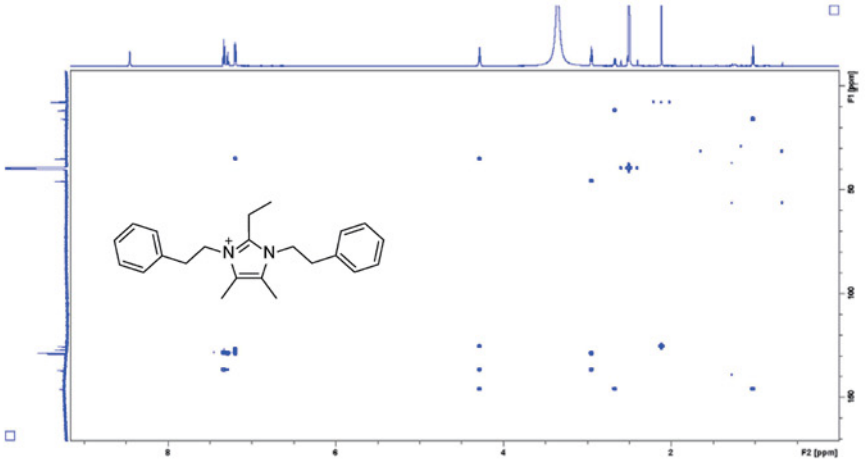

Figure S42. The ^{1}H-^{13}C HMBC (700 MHz, DMSO-d_6) spectrum of compound 6.

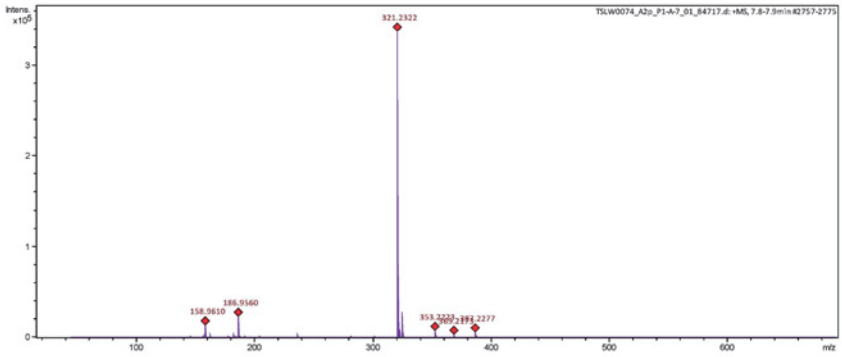

Meas. m/z	#	Ion Formula	m/z	err [ppm]	mSigma	# mSigma	Score	rdb	eÂ¯ Conf	N-Rule
321.2322	1	C22H29N2	321.2325	1.0	4.4	1	100.00	9.5	even	ok

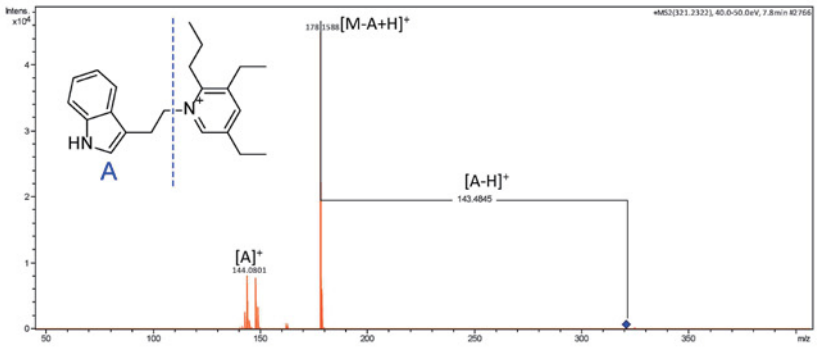

Figure S43. The HR-ESI-MS and HR-ESI-MS/MS of compound 7.

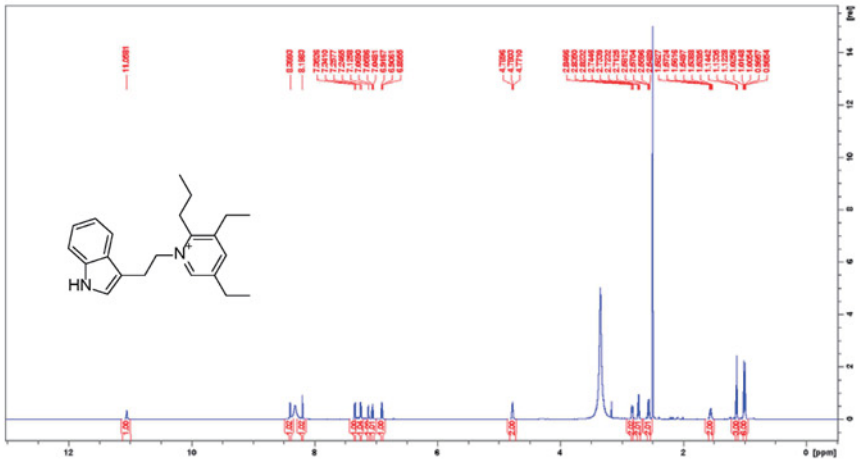

Figure S44. The ^{1}H-NMR (700 MHz, DMSO-d_6) spectrum of compound 7

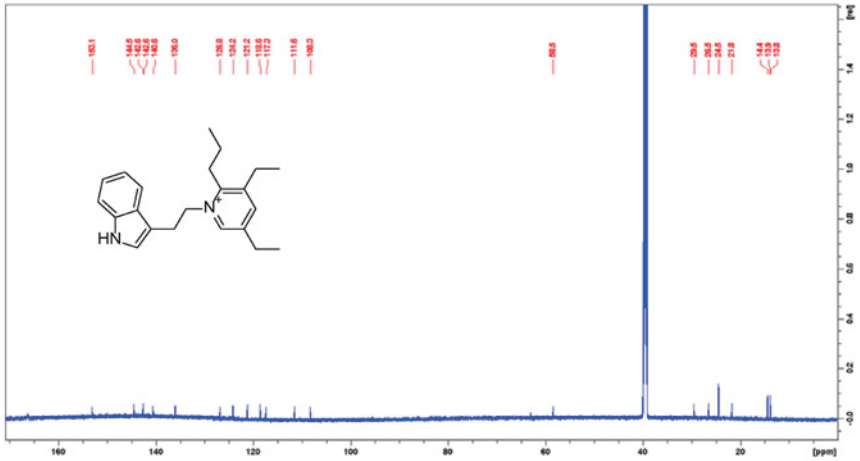

Figure S45. The ^{13}C-NMR (175 MHz, DMSO-d_6) spectrum of compound 7

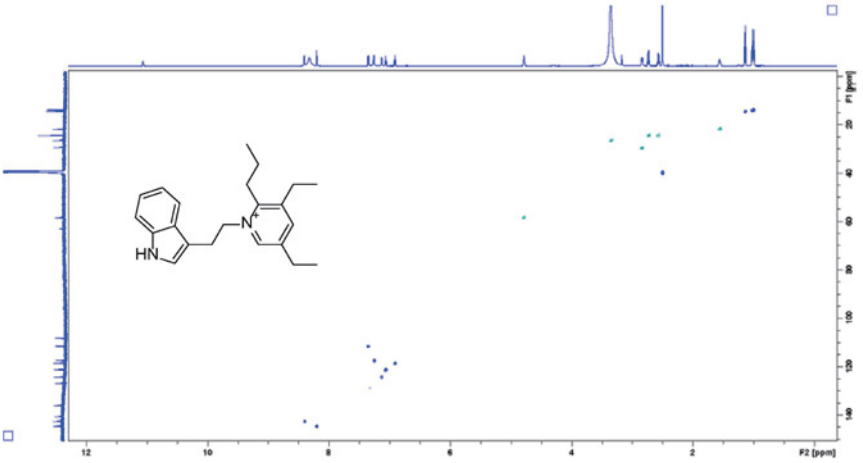

Figure S46. The HSQC (700 MHz, DMSO-d_6) spectrum of compound 7.

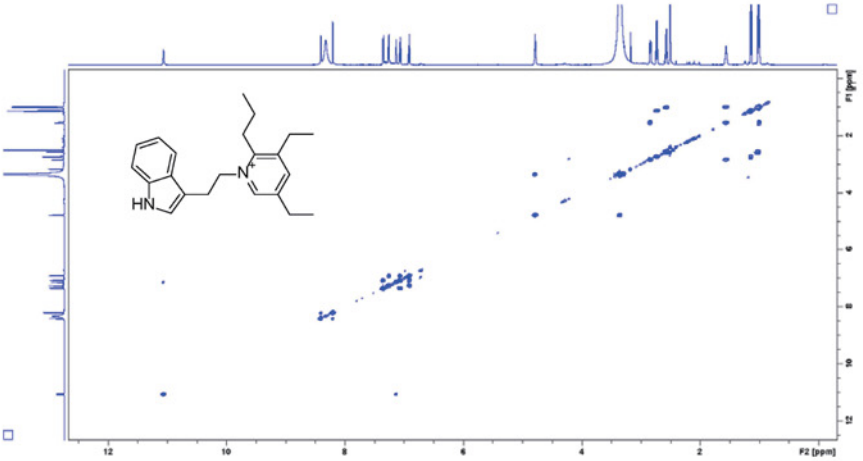

Figure S47. The ^{1}H-^{1}H COSY (700 MHz, DMSO-d_6) spectrum of compound 7.

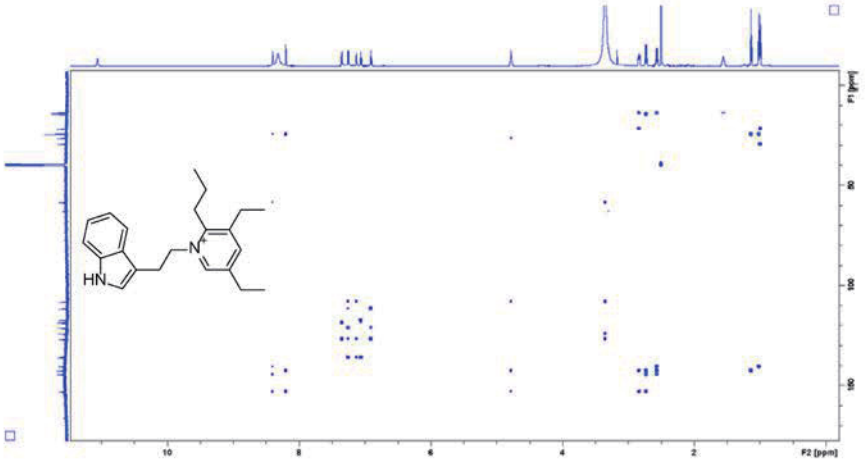

Figure S48. The ^{1}H-^{13}C HMBC (700 MHz, DMSO-d_6) spectrum of compound 7.

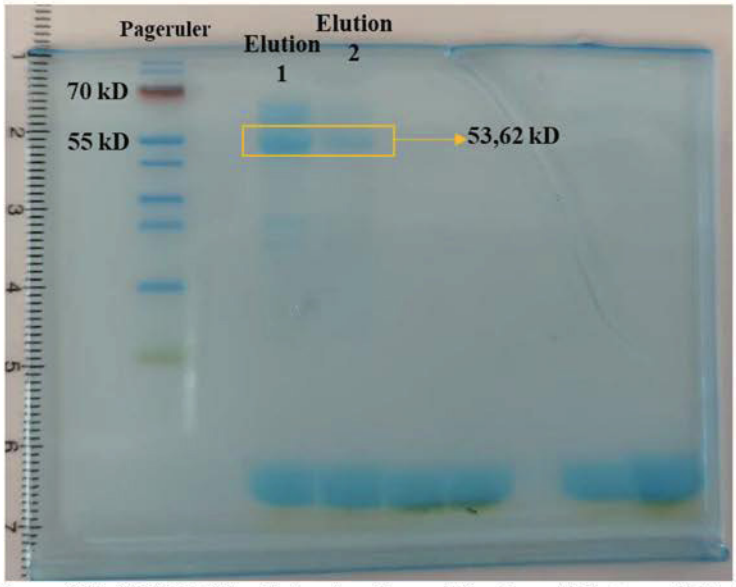

Figure S49. SDS-PAGE gel showing the purification of His-tagged DisA.

Chapter 4. Publication 3

Physiochemical interaction between osmotic stress and a bacterial exometabolite promotes plant disease

Felix Getzke[#], Lei Wang[#], Nienke Denissen, Fantin Mesny, Hidde Wesseler, Paul Schulze-Lefert, Till F. Schäberle[*], Stéphane Hacquard[*]. ([#]co-first author)

(under review, *Nature Communications***)**

The genome data of the strong competitor within the *Arabidopsis thaliana* root microbiome, i.e. *Pseudomonas brassicacearum* Root401, was scanned for putative biosynthetic gene clusters (BGCs). This genomic mining approach revealed a homologue to the syp-syr BGC that is responsible for syringopeptin and syringomycin biosynthesis. In combination with a molecular networking-guided survey this led to the identification of four new cyclic lipopeptides, which we named Brassicapeptins A to D from the culture broth of *P. brassicacearum* Root401. Their structures were determined using HR-ESI-MS, HR-ESI-MS/MS, 1D and 2D NMR data and Marfey's analysis. Comparison to the previously described syringopeptins, which are also produced by *Pseudomonas* strains, the discovered brassicapeptins revealed notable structural differences, including a different fatty acid starter unit and a smaller ring structure that is formed intramolecularly between the six C-terminal amino acid residues, thereby suggesting that brassicapaptins represent a novel sub-group of cyclic lipopeptides. Brassicapeptin A exhibited

strong activity against *Listeria monocytogenes* DSM20600 with MIC value of 2 μg/mL and moderate activity against *Mycobacterium smegmatis* ATCC607 with MIC value of 8 μg/mL.

The work of our collaborators revealed that brassicapeptin A is necessary and sufficient to promote disease on plants that are under salt stress. Their data support the hypothesis that brassicapeptin A-induced disruption of ion homeostasis at the root interface enhances salt stress and promotes bacterial colonization, thereby leading to plant disease.

Physiochemical interaction between osmotic stress and a bacterial exometabolite promotes plant disease

Felix Getzke[1,#], Lei Wang[2,#], Nienke Denissen[1], Fantin Mesny[1,6], Hidde Wesseler[1], Paul Schulze-Lefert[1,3], Till F. Schäberle[2,4,5,*], Stéphane Hacquard[1,3,*]

[1]Department of Plant Microbe Interactions, Max Planck Institute for Plant Breeding Research, 50829 Cologne, Germany

[2]Institute for Insect Biotechnology, Justus-Liebig-University Giessen, 35392 Giessen, Germany.

[3]Cluster of Excellence on Plant Sciences (CEPLAS), Max Planck Institute for Plant Breeding Research, 50829 Cologne, Germany

[4]German Center for Infection Research (DZIF), Partner Site Giessen-Marburg-Langen, 35392 Giessen, Germany

[5]Fraunhofer Institute for Molecular Biology and Applied Ecology (IME), Branch for Bioresources, 35392 Giessen, Germany

[6]Present address: Institute for Plant Sciences, University of Cologne, 50674 Cologne, Germany

[#]contributed equally to this work

*Correspondence: Stéphane Hacquard: hacquard@mpipz.mpg.de and Till F. Schäberle: Till.F.Schaeberle@agrar.uni-giessen.de

Abstract

Various microbes isolated from healthy plants are detrimental under laboratory conditions, indicating the existence of molecular mechanisms preventing disease in nature. Here, we demonstrated that application of sodium chloride (NaCl) in natural and gnotobiotic soil systems is needed to induce plant disease caused by an otherwise non-pathogenic root-derived

Pseudomonas brassicacearum isolate (R401). Disease caused by combinatorial treatment of NaCl and R401 triggered extensive, root-specific transcriptional reprogramming that did not involve down-regulation of host innate immune genes, nor dampening of ROS-mediated immunity. Instead, we identified and structurally characterized the R401 lipopeptide brassicapeptin A as necessary and sufficient to promote disease on salt-treated plants. Brassicapeptin A production transitions R401 from being beneficial to being detrimental on salt-treated plants by disturbing host ion homeostasis, thereby bolstering bacterial infection and susceptibility to osmolytes. We conclude that the interaction between a global change stressor and a bacterial exometabolite drives disease emergence in the plant microbiome.

Keywords

plant disease, root microbiome, opportunistic pathogens, non-ribosomal peptide, abiotic stress, biotic stress, immunity, microbiota, natural product

Introduction

Subterranean and aerial plant tissues are colonized by complex microbial communities that are referred to as the root and shoot microbiota, respectively[1, 2, 3, 4]. Recent efforts to systematically isolate and characterise the microbiota of healthy-looking *Arabidopsis thaliana* grown in natural soils revealed that few bacteria (< 5%) can cause disease under specific laboratory conditions[5, 6, 7]. These include for example *Pseudomonas brassicacearum* Root401 (referred to as R401), *Streptomyces spp.* Root107 (R107), *Xanthomonas spp.* Leaf131 and Leaf148 (L131, L148), or multiple *Pseudomonas viridiflava* isolates that were retrieved from symptomless plant tissues[2, 5, 8, 9, 10]. The identification of these so-called opportunistic pathogens suggests the existence of molecular mechanisms that suppress detrimental phenotypes in nature whilst facilitating virulence under laboratory conditions.

Stevens (1960)[11] advanced the concept of the 'disease triangle', by which environmental factors contribute to the establishment of plant diseases. In this triangle, abiotic conditions can influence the host, the microbiota, or the interaction between the two, facilitating or inhibiting pathogen progression[12, 13, 14]. Similar to pathogen perception, *e.g.*, the sensing of salt stress results in signalling cascades involving cytoplasmic Ca^{2+} influx, ROS production and the accumulation of plant hormones, primarily abscisic acid[15, 16, 17, 18] (ABA). ABA mediates closure of stomata to restrict transpirational water loss[18] and inhibits the expression of the salicylic acid (SA) biosynthetic gene *ISOCHORISMATE SYNTHASE1* (*ICS1/SID2*) in *A. thaliana*, thereby suppressing SA-dependent immunity[19, 20]. This ABA-SA cross-talk was recently shown to be leaf-age dependent and controlled by the SNAC-A transcription factor cascade[21]. Collectively, abiotic stress signalling and host innate immunity processes are tightly connected and likely contribute to disease emergence in nature[14, 22, 23].

Here, we focus on a dominant member of the bacterial root microbiota called *P. brassicacearum* R401 that was previously shown to be detrimental in mono-association experiments with *A. thaliana* in an agar matrix-based gnotobiotic system[6]. This strain was also recently shown to deploy unrelated inhibitory exometabolites that co-function to keep bacterial competitors at bay and promote strain colonization success in roots[24]. We report here that R401 is non-pathogenic on plants grown in natural or gnotobiotic peat-based soil systems and that NaCl treatment promotes R401 disease symptoms in these soil-grown plants, providing evidence for environmental conditions that conditionally promote plant disease. In R401, we identify a biosynthetic gene cluster (BGC) homologous to the *syp-syr* BGC that is responsible for syringopeptin biosynthesis in *P. syringae* B728a[25] and we demonstrate that 1) this locus is sufficient to transition R401 from being beneficial to being detrimental on salt-treated plants and 2) the produced exometabolite is sufficient to drive disease in salt-treated plants. We conclude that the physiochemical interaction between a bacterial exometabolite and an osmotic stress promotes plant disease in complex soil-microbiome systems.

Results

R401 is detrimental on soil-grown plants facing salt stress

Inoculation of R401 on *A. thaliana* plants grown on ½ Murashige-Skoog (½ MS) agar matrix plates was shown to cause extensive plant growth inhibition and anthocyanin accumulation in shoots[6] and we were able to reproduce similar phenotypes (**Fig. 1a**). However, in the sterile peat matrix of the gnotobiotic Flowpot system[26] or in natural, non-sterile Cologne agricultural soil (CAS), R401 inoculation did not cause disease (**Fig. 1b**,**c**). Salt stress has been shown to facilitate *Pseudomonas* infections in tomato[27] (*Solanum lycopersicum*, Solanaceae) and cucumber[28] (*Cucumis sativus*, Cucurbitaceae). We therefore speculated that salt stress may facilitate the detrimental effects of *P. brassicacearum* R401 on *A. thaliana* (Brassicaceae). In axenic conditions (**Fig. 1b**) and in the presence of a complex, natural soil microbiota (**Fig. 1c**), the application of 100 mM NaCl negatively affected plant growth (HK 0 mM NaCl vs. HK 100 mM NaCl; $p < 0.001$, Kruskal-Wallis followed by Dunn's post-hoc test, **Fig. 1b**,**c**). Co-inoculation of R401 and 100 mM NaCl further aggravated this effect in both soil systems, leading to highly stunted and chlorotic plants, reminiscent of R401 effects in ½ MS agar plates (**Fig. 1a-c**). Collectively, this indicates that in complex soil systems, the opportunistic pathogen R401 requires specific conditions to cause disease on *A. thaliana.*

Salt-treated plants down-regulate immune processes in shoots but not in roots

We hypothesized that salt stress response in *A. thaliana* comes at the cost of dampening immune sectors in roots, which in turn promotes R401 virulence. We sequenced the root and shoot transcriptome of *A. thaliana* 28 days post treatment with either heat-killed (HK) or live R401 wild-type (WT) strains mono-inoculated in absence or presence of NaCl (0 vs. 100 mM) in the Flowpot system (**Fig. 1b**, **Supplementary Table 1**). Inoculation of R401 in the absence of salt stress had marginal effects on both root and shoot transcriptomes compared to control samples (0 mM NaCl + R401 HK), with 2 and 14 differentially expressed genes identified (DEGs), respectively ($p < 0.05$, $-1 < \text{Log2FC} > 1$, **Fig. 2a**). Salt stress alone also triggered

109 subtle transcriptional reprogramming in roots (85 DEGs, **Fig. 2a** and **Supplementary Fig. 1a**),
110 but not in shoots (1,192 DEGs, **Fig. 2a** and **Supplementary Fig. 1b**). Based on PANTHER
111 functional annotation analyses[29, 30, 31], up-regulated genes in roots of salt-treated plants can
112 be categorized into the GO-terms 'response to abscisic acid', 'response to osmotic stress',
113 and 'response to water deprivation', while in shoots the most enriched GO-terms included
114 'anthocyanin-containing compound biosynthetic process', 'hyperosmotic salinity response'
115 and 'abscisic acid-activated signaling pathway'. Collectively, these data confirmed that salt
116 stress as applied in our experimental setup activated the stereotypical salt stress response
117 and interfered with plant photosynthesis[32, 33, 34, 35]. Notably, combinatorial treatment of R401
118 and salt had the most extensive effect on the host transcriptome, with 2,824 and 2,150 DEGs
119 identified in roots and shoots, respectively (**Fig. 2a** and **Supplementary Fig. 1a,b**). However,
120 only in roots did R401 cause major additive transcriptional reprogramming compared to salt
121 stress alone, with 1,922 newly identified DEGs (**Fig. 2a)**. Although this activation associate
122 with disease, no increased proliferation of R401 was noted compared to control plants
123 (**Supplementary Fig. 1c**). Functional annotation analysis of DEGs responding to salt stress
124 or combinatorial treatment of salt and R401 revealed 14 GO-term clusters involved in primary
125 metabolism (*e.g.*, 'photosynthesis' and 'response to carbohydrate') or biotic (*e.g.*, 'immune
126 system process' and 'regulation of response to biotic stimulus') and abiotic stress (*e.g.*,
127 'response to abiotic stimulus' and 'cellular response to abscisic acid stimulus'; **Fig. 2b**).
128 Notably, innate immune processes (see largest cluster in **Fig. 2b**) such as 'systemic acquired
129 resistance', 'response to molecule of bacterial origin' and 'regulation of jasmonic acid (JA)-
130 mediated signalling pathway' were down-regulated in shoots but not in roots in response salt
131 or salt and R401 combinatorial treatment.
132
133 **Mutation of host NADPH oxidase *RBOHD* does not promote R401 virulence**
134 We next tested whether salt stress-mediated suppression of immunity in shoots could facilitate
135 virulence of other opportunistic pathogens, such as *Streptomyces sp.* R107 and *Xanthomonas*
136 *sp.* L131[6, 7]. Resistance to *Xanthomonas* L131, but also another closely related L148

137 opportunistic pathogen was recently shown to fully depends on the host NADPH/respiratory
138 burst oxidase homologue D[7, 9, 10] (RBOHD), which was approx. 51-fold down-regulated by salt
139 stress in *A. thaliana* shoots in our dataset (*p.adj* < 0.05, **Supplementary Table 1**). Therefore,
140 we hypothesized that salt stress might bolster virulence of opportunistic pathogens by
141 dampening ROS-mediated immunity in *A. thaliana*. However, while R401 and R107 became
142 more detrimental on salt-treated *A. thaliana* than on control plants, this was not the case for
143 L131 (**Supplementary Fig. 2a**). In contrast – and consistent with previous work[7] - inoculation
144 of L131 on an immunocompromised A. *thaliana rbohD* mutant promoted disease. However,
145 this virulence facilitation phenotype was not observed for R401, indicating that R401 disease
146 emergence did not require impairment of RBOHD-dependent ROS production in *A. thaliana*
147 (**Supplementary Fig. 2b**). Taken together, our results suggest that disease caused by R401
148 on salt-treated plants is not associated with down-regulation of innate immune sectors in roots,
149 nor with dampening of RBOHD-dependent ROS-mediated protective immunity.
150
151 **R401 *sypC* is required for bacterial detrimental activity in salt-treated plants**
152 Given the lack of genes encoding the type-III secretion system in the genome of R401[36, 37, 38],
153 we hypothesized that this strain might use specialized metabolites as virulence factors.
154 AntiSMASH-based prediction[39] of BGCs revealed a >140 kb BGC with high similarity to the
155 *syp-syr* BGC of *Pseudomonas syringae* B728a involved in syringopeptin and syringomycin
156 biosynthesis[25] (**Fig. 3a**). The molecules were shown to be required for virulence of *syp-syr*-
157 enconding *Pseudomonas syringae* strains[40]. R401 has been phylogenetically assigned to the
158 *P. brassicacearum* species[24]; therefore, we termed the putatively produced specialized
159 metabolites 'brassicapeptin' and 'brassicamycin'. To test whether the *syp-syr* BGC contributes
160 to R401 disease symptoms on salt-treated *A. thaliana*, we generated a marker-free knockout
161 mutant (Δ*sypc*) lacking *sypC*, one of the core biosynthetic genes putatively involved in
162 brassicapeptin biosynthesis (**Fig. 3a**). We then mono-inoculated heat-killed (HK) or live R401
163 wild type (WT) or Δ*sypc* mutant cells into the gnotobiotic Flowpot system across a gradient of
164 NaCl concentrations (0–150 mM NaCl). R401 WT was again able to cause disease on salt-

165 treated plants and this effect was NaCl-concentration dependent (**Fig. 3b**), indicating a dose-
166 dependent relationship between increased salt concentrations and R401 detrimental activity
167 (**Fig. 3c**). Remarkably, the detrimental effect of R401 WT on salt-treated plants was fully
168 abolished in the Δ*sypc* mutant, which was even able to partly rescue salt stress-induced plant
169 growth inhibition (**Fig. 3b**). Therefore, mutation of a single bacterial gene involved in the
170 production of a specialized exometabolite was sufficient to turn this opportunistic pathogen
171 into a beneficial plant growth-promoting isolate under salt stress. Notably, *sypC*-dependent
172 detrimental activity of R401 under salt stress was retained in plants co-cultured with a
173 representative, yet simplified 15-member synthetic microbial community in the FlowPot
174 system (**Supplementary Fig. 3**, see methods). In salt-treated plants, *sypC* is therefore a R401
175 disease determinant that dominantly functions irrespective of the absence or presence of
176 microbial competitors. Consistently, we previously showed that R401 displayed broad
177 antagonistic activity towards various root microbiota members through production of iron-
178 chelating pyoverdine and DAPG antimicrobial[24]. Here, we generated a R401 triple mutant
179 impaired in the production of pyoverdine, DAPG, and brassicapeptin (Δ*pvdy*Δ*phld*Δ*sypc*) and
180 observed that *sypC* also contributed to inhibit the growth of some microbes based on
181 measurement of R401 inhibitory halos (**Supplementary Fig. 4**). Although the *syp-syr*
182 containing BGC is rare in genomes of plant-associated *Pseudomonas* isolates[2, 5, 41, 42]
183 (**Supplementary Fig. 5**), its acquisition is predicted to have broad implication for plant disease
184 emergence in complex soil systems colonized by highly diverse microbial communities.
185
186 **R401 *sypC* drives root colonization and promotes disease in salt-treated tomato**
187 We first tested whether detrimental activity of R401 WT also occurred in the context of other
188 abiotic stresses, such as drought or low photosynthetically active radiation (low PAR[43]). While
189 low PAR had more severe effects on shoot fresh weight compared to drought, this treatment
190 did not facilitate R401-mediated disease emergence. In contrast, drought stress mimicked by
191 the application of 5% polyethylene glycol (PEG8000) promoted R401 virulence, demonstrating
192 that the detrimental activity of R401 is potentiated by hyperosmotic stresses (**Supplementary**

193 **Fig. 6**). Next, we assessed whether *A. thaliana* disease symptoms observed upon inoculation
194 of R401 under salt also occurred in other plant species. Notably, salt- and *sypC*-dependent
195 detrimental activity of R401 was recapitulated in *Solanum lycopersicum cv.* Micro-Tom (Micro-
196 Tom), but not in *Lotus japonicus* Gifu (Gifu) (**Supplementary Fig. 7a**,**b**). This is potentially
197 explained by the fact that the latter plant exhibited high tolerance to the applied salt conditions
198 (**Supplementary Fig. 7b**). We next harvested roots and shoots of both Micro-Tom and Gifu
199 seedlings and quantified colonisation capability of R401 WT and Δ*sypc* mutant in the presence
200 or absence of NaCl. While colonisation of R401 WT remained stable, irrespective of the salt
201 treatment or the host plant, the Δ*sypc* mutant showed impaired root colonization in salt-treated
202 vs. control Micro-Tom plants, which was not observed in salt-resistant Gifu plants
203 (**Supplementary Fig. 7c,d**). In axenic liquid medium, growth of R401 WT and Δ*sypc* was
204 identical irrespective of the NaCl concentration (**Fig. 3d**), indicating that R401 was insensitive
205 to 100 mM NaCl and required *sypC* to proliferate in roots of salt-treated Micro-Tom.
206 Collectively, these data suggest a conserved functioning of brassicapeptin in salt-stressed *A.*
207 *thaliana* and Micro-Tom roots, irrespective of the 112 million years of reproductive isolation
208 between these plants[44].
209
210 **Isolation and structural characterisation of R401 brassicapeptin**
211 Next, we aimed to isolate the R401 brassicapeptin and elucidate its structure. Therefore, a
212 70L fermentation of R401 was performed and extracted using ethyl acetate. The therefrom-
213 resulting organic crude extract was further fractionated and purified using column
214 chromatography (*e.g.*, medium pressure (flash) and high-performance liquid chromatography
215 (HPLC) to finally yield the natural products brassicapeptin A as the major compound of this
216 class, and brassicapeptin B in minor amounts. Additionally, the high-resolution electro spray
217 ionization (HR-ESI)-MS/MS data analysis indicated two further minor derivatives,
218 brassicapeptin C and D (**Supplementary Note 1** and **Supplementary Fig. 8**). Brassicapeptin
219 A and B were obtained as white amorphous powders and subsequently analysed by mass
220 spectrometry (MS). The HR-ESI-MS spectrum of brassicapeptin A indicated a molecular

221 weight of 2052.2004, suggesting a molecular formula of $C_{96}H_{161}N_{23}O_{26}$ (**Supplementary Fig.**
222 **8a**) and of $C_{94}H_{157}N_{23}O_{26}$ for brassicapeptin B ($[M+2H]^{2+}$ *m/z* 1027.1080 and *m/z* 1005.0940,
223 respectively) (**Supplementary Fig. 8b**). Comparison of the HR-ESI-MS/MS fragmentation
224 patterns of brassicapeptin A and B gave first insights into the amino acid composition and
225 revealed a high similarity between the molecules (*i.e.*, from b_1-b_7 and from y_1-y_{10}, except for
226 differences from b_8-b_{11} and from y_{11}-y_{14}) (**Fig. 4a,b**). To fully resolve their structures, nuclear
227 magnetic resonance (NMR) experiments and Marfey's analysis were performed (for details
228 about structure elucidation see **Supplementary Note 1** and **Supplementary Fig. 8**). A
229 combination of 1D and 2D experiments (^{1}H, ^{13}C, HMBC, HSQC, COSY, TOCSY and ROESY)
230 revealed the brassicapeptins to consist of 22 amino acid residues plus a fatty acid chain (**Fig.**
231 **4c,d**). The latter is six carbons in length, including a carbonyl group; the amino acid chain is
232 cyclized by an intramolecular connection between threonine (Thr_{17}) and isoleucine (Ile_{22}) (**Fig.**
233 **4c**). Brassicapeptin A and B differ only by one amino acid, which is a homoserine (Hse_9) in
234 brassicapeptin A and a glycine (Gly_9) in B, respectively (**Fig. 4c**). The here discovered
235 brassicapeptins represent large cyclic lipopeptides. Comparison to the previously described
236 syringopeptins[45, 46, 47], which are also produced by *Pseudomonas* strains, revealed notable
237 structural differences, including a different fatty acid starter unit and a smaller ring structure
238 that is formed intramolecularly between the six C-terminal amino acid residues
239 (**Supplementary Fig. 9**); thereby suggesting that brassicapaptins represent a novel sub-
240 group of cyclic lipopeptides.
241
242 **Brassicapeptin A and NaCl additively contribute to plant disease**
243 Because R401 is detrimental on *A. thaliana* grown on ½ Murashige-Skoog (½ MS) agar plates
244 (**Fig. 1a**), we assessed the putative phytotoxic activity of brassicapeptin A in this reductionist
245 system. We transplanted seven-day-old *A. thaliana* seedlings to ½ MS agar plates containing
246 increasing concentrations of purified brassicapeptin A solubilized in dimethyl sulfoxide
247 (DMSO), in the presence or absence of 100 mM NaCl. After 14 days, brassicapeptin A showed
248 a dosage-dependent effect on root and shoot growth, suggesting that the molecule alone is

sufficient to induce a stunted growth phenotype that is reminiscent of the effect of R401 in this gnotobiotic system (**Fig. 5a-c**). Note that beyond its phytotoxic effect, brassicapeptin A also displayed broad spectrum inhibitory activity towards various bacterial and fungal isolates based on minimal inhibitory concentration assay (**Supplementary Table 2**). Notably, plants exposed to 1 µg/mL brassicapeptin A and 100 mM NaCl died immediately after transfer, whereas those exposed to 1 µg/mL brassicapeptin A alone remained alive and did not show leaf bleaching and severely inhibited root growth phenotypes (**Fig. 5a-c**). Furthermore, brassicapeptin A induced ion leakage in *A. thaliana* leaf discs after 16 h of incubation (**Fig. 5d**), corroborating earlier report showing that syringomycin, a structurally-related lipodepsipeptide, likely function as a pore-forming molecule that insert into host plasma membranes[48], thereby resulting in uncontrolled ion fluxes. Therefore, brassicapeptin A-induced disruption of ion homeostasis, combined with increased osmotic pressure in the root environment, likely contribute to R401-induced disease symptoms in salt-stressed plants. Taken together, our data support the hypothesis that brassicapeptin A-induced disruption of ion homeostasis at the root interface enhances salt stress and promotes bacterial colonization, thereby leading to disease.

Discussion

Here, we report that salt-mediated dampening of host innate immunity likely contributes little to R401-mediated disease in soil-grown plants. Instead, we identify a bacterial exometabolite - with predicted pore-forming activity - that is sufficient to drive disease in salt-treated plants and that dominantly functions, irrespective of the presence or absence microbial competitors in soil.

After 28 days of chronic salt treatment, the response of *A. thaliana* to salt stress was largely shoot-specific with photosynthesis-related genes being extensively downregulated, likely due to accumulation of Cl^- and Na^+ ions in leaves that disrupt photosynthetic machinery[32, 49, 50]. In

276 roots, only subtle transcriptional reprogramming was observed after 28 days of continuous
277 salt stress, which can be explained by previous observation reporting a gradual decline of salt
278 stress response over time in *A. thaliana*[34]. The effect of R401 in the absence of salt stress was
279 also minor in both shoots and roots, while in the presence of hyperosmotic NaCl
280 concentrations and of R401, extensive and root-specific transcriptional reprogramming was
281 observed. This suggests that host response to disease induced by the combinatorial presence
282 of salt and R401 primarily occurs in roots. Given that salt stress-induced dampening of
283 immunity occurs in leaves, but not in roots, we propose that R401-induced stunted plant
284 phenotypes under salt stress is largely immunity-independent. This is corroborated by our
285 observation that R401 does not become detrimental on an immunocompromised *rbohD A.*
286 *thaliana* mutant and by the fact that purified brassicapeptin A and salt are sufficient to induce
287 disease-like symptoms in R401-free plant growth assays. Furthermore, low PAR treatment
288 was shown to dampen SA- and JA-dependent immunity sectors in *A. thaliana* roots and
289 shoots, which promotes infection by *Botrytis cinearea* and *Pseudomonas syringae pv. tomato*
290 DC3000[43]. However, R401 did not cause disease under such conditions. Although we cannot
291 fully exclude the possibility that salt-induced dampening of immunity still contributes to R401
292 virulence, our results suggest that this effect remains marginal.
293
294 R401 encodes a 140 kb BGC that is responsible for the production of the non-ribosomal
295 peptides brassicapeptin A and B. A R401 mutant lacking *sypC*, one of the core biosynthetic
296 genes required for the production of brasscapeptin, lost its ability to cause disease *in planta*,
297 demonstrating a requirement of brassicapeptin production for the detrimental activity of R401
298 in salt-treated plants. Structurally related compounds have been demonstrated to intercalate
299 plasma membranes, thereby destabilising them and causing pore formation disrupting cell
300 integrity, eventually leading to uncontrolled diffusion of cell solutes into the surrounding
301 medium[46, 51, 52]. We observed leakage of cellular solutes from *A. thaliana* leaf discs that were
302 treated with brassicapeptin A, supporting the assumption that the molecule inserts into plant
303 plasma membranes. R401 showed *sypC*-dependent detrimental activity under salt but also

304 drought stress, confirming that hyperosmotic conditions and R401 brassicapeptin are required
305 for disease emergence in soil-grown plants. This is supported by a linear dose-response
306 relationship between applied NaCl concentrations and the detrimental effect of R401 on *A.*
307 *thaliana*. In ½ MS agar plates, purified brassicapeptin A was sufficient to negatively impact
308 shoot and root phenotypes already in the absence of salt stress, but this phenotype was
309 aggravated by the supplementation of 100 mM NaCl to the culture medium. Nutrient
310 concentrations in ½ MS agar medium are therefore likely sufficient to impose hyperosmotic
311 stress on brassicapeptin A-treated plants. Collectively, this indicates that the direct interaction
312 of a bacterial specialized metabolite and high osmotic concentrations in the environment is
313 sufficient to explain R401 detrimental activity on salt-sensitive plants, as shown here for *A.*
314 *thaliana* and Micro-Tom. Root-specific transcriptional reprogramming to R401 and NaCl
315 treatment, together with NaCl-specific benefits of brassicapeptin production on R401
316 proliferation, likely *via* nutrient leaching from the root endosphere, further indicate a root-
317 specific interaction of NaCl and brassicapeptin. While R401 likely fulfils extensive biocontrol
318 activities due to its diverse repertoire of antibacterial and antifungal specialized
319 exometabolites[24], favourable abiotic conditions allow for disease development by
320 brassicapeptin-producing R401.
321
322 R401, R131 and R107 have been isolated from healthy *A. thaliana* plants; however, under
323 favourable conditions they can become detrimental to plant health – in the case of R401 even
324 in the context of natural or synthetic microbial communities. Groundwater-derived
325 *Pseudomonas sp.* N2C3 (N2C3) also contains the *syp-syr* BGC and has been demonstrated
326 to cause *syp*-dependent stunting of *A. thaliana* root and shoot growth in ½ MS agar medium[53].
327 In natural soil, N2C3 does not cause any detrimental phenotypes, even after inoculation of
328 high bacterial titres[54] (1×10^6 cells per gram soil, a phenotype that is reminiscent of the herein
329 described effects of R401. Using computational analyses, convergent gain and loss of the
330 *syp-syr* BGC has been demonstrated for the *Pseudomonas fluorescence*-clade, which
331 comprises *P. brassicacearum*[53]. Loss of *sypC* in R401 was sufficient to turn this detrimental

strain into a plant growth-promoting strain under salt stress. While the mechanisms of growth promotion of the Δ*sypc* R401 mutant remain elusive, it is conceivable that the acquisition of the *syp-syr* BGC in this strain – and likely in other *Pseudomonas* spp. isolates - might overwrite their growth-promoting capabilities.

High soil salinity is one of the main constraints for agricultural performance worldwide and arises through frequent irrigation and fertilisation, which results in the accumulation of nutrient salts in agricultural soils. This accumulation will become more problematic due to an increasing demand for field irrigation owing to climate change[33, 35, 55, 56, 57]. Our data provide first line of evidence indicating that the interplay between the host, its microbiota, and the osmotic environment can conditionally lead to disease due to the presence of specific bacterial taxa that employed exometabolites that likely disrupt ion homeostasis and promote nutrient leakage at the host interface. Given that the disease phenotype conferred by R401 under salt stress is retained in a microbial community context, it reflects an important phenomenon that has physiological relevance for plant disease emergence in natural environment. It is also plausible that membrane-intercalating exometabolites outside of the genus *Pseudomonas*, such as surfactin produced by *Bacillus spp.* may cause similar detrimental activity as R401 brassicapeptin A[58, 59, 60, 61, 62]. Taken together, our data provides a mechanistic explanation for the emergence of a disease in the plant microbiome that require a single bacterial exometabolite and adequate abiotic stress conditions. Our work also defines an ecological framework to understand the conditional detrimental activity of R401 and likely other *Pseudomonas spp.* isolates in complex soil environments.

Methods

Primers

All primers used in this study can be found in **Supplementary Table 3**.

359 *Microorganisms*

360 The bacterial and fungal strains used in this study have been initially isolated from unplanted
361 soil, *A. thaliana* roots or shoots[2, 3] and are summarized in **Supplementary Table 4.** The R401
362 Δ*sypc* mutant has been deposited in the bacterial culture collection of the Department of Plant
363 Microbe Interactions at the Max Planck Institute for Plant Breeding Research in Cologne,
364 Germany, and are available upon request from Stéphane Hacquard
365 (hacquard@mpipz.mpg.de).

366

367 *Plant species*

368 *A. thaliana* ecotype Columbia-0 (Col-0), *Lotus japonicus* ecotype Gifu B-129, and *Solanum*
369 *lycopersicum cv.* Micro-Tom were used as wild-types. *A. thaliana rbohd* contains a *dSpm*
370 transposon in the fifth exon of *AtrbohD*[63] (AT5G47910;

371

372 *Microbial culture conditions*

373 Bacteria were streaked from glycerol stocks (25% glycerol) on TSA plates (15 g/L Tryptic Soy
374 Broth, Sigma Aldrich; with 10g/l Bacto Agar, Duchefa Biochemie) and grown at 25 °C. Single
375 colonies were inoculated in liquid 50% TSB (15 g/L Tryptic Soy broth, Sigma Aldrich) and
376 grown until dense at 25 °C with 180 rpm agitation. Dense cultures were then stored at 4 °C
377 and diluted 1 to 10 in TSB the day before the experiment and cultured at 25 °C with 180 rpm
378 agitation overnight to ensure sufficient cell densities for slow- and rapidly-growing bacteria.
379 Glycerol stocks were stored at -80 °C and kept on dry ice when transported. Individual pieces
380 of fungal mycelium were transferred to potato dextrose agar (PDA; Sigma-Aldrich) Petri dishes
381 from glycerol stocks (approx. 30 pieces of fungal mycelium in 25% sterile glycerol, stored at -
382 80 °C). Fungi were grown at 25 °C in the dark for 14 days.

383

384 *Seed sterilisation*

385 *A. thaliana* and *S. lycopersicum* Micro-Tom seeds were sterilized using 70% ethanol and
386 bleach. Seeds were submerged in 70% ethanol and left shaking at 40 rpm for 14 minutes.

387 Ethanol was removed before the seeds were submerged in 8.3% sodium hypochlorite (Roth)
388 containing 1 µL of Tween 20 (Sigma-Aldrich) and left shaking at 40 rpm for 4 minutes. Under
389 sterile conditions, the seeds were washed 7 times and finally taken up with sterile 10 mM
390 $MgCl_2$. Seeds were left for stratification at 4 °C for 3 days. Seed sterility was confirmed by
391 plating approx. 100 seeds on a 50% TSA plate.
392 The seed coat of *L. japonicus* Gifu seeds was first abraded using sanding paper, then seeds
393 were incubated for 20 min in diluted bleach, followed by five-times washing in sterile water.
394 Sterilized Gifu seeds were pregerminated on sterile, water-soaked Whatman paper for 7 days.
395
396 *Gnotobiotic Flowpot experiments*
397 Peat sterilisation and Flowpot assembly were performed as described before[24]. For Micro-
398 Tom and Gifu, big Flowpots fitting 50 mL soil were used, as described before[41]. Microbes were
399 grown and inocula were prepared as described above. Each Flowpot was inoculated with 50
400 mL half strength Murashige and Skoog medium with vitamins (½ MS; 2.2 g/L, Duchefa
401 Biochemie, 0.5 g/L MES, pH 5.7). For bacteria, a final OD_{600} of 0.0025 in 50 ml ½ MS were
402 inoculated per Flowpot. For salt stress treatment ½ MS contained 50, 100 or 150 mM NaCl.
403 For drought treatment, ½ MS contained 5% polyethylene glycol (PEG8000; Sigma-Aldrich).
404 Per Flowpot, five or three surface-sterilized and stratified *A. thaliana* or Micro-Tom seeds were
405 inoculated, respectively. For Gifu, 7 days old, pregerminated seedlings with similar
406 developmental stages were carefully transferred to the Flowpots. Microboxes were then
407 incubated in a light cabinet under short day conditions (10 h light at 21 °C, 14 h dark at 19 °C)
408 for 28 days and randomized every 2–3 days. For low PAR treatments, microboxes were partly
409 covered in cardboard boxes, as described in Hou et al. 2021[43].
410
411 *Natural soil experiments*
412 Cologne agricultural soil (CAS) was obtained from the Max Planck Institute for Plant Breeding
413 Research in Cologne, Germany. R401 WT was cultured as described above. CAS was placed
414 in squared pots with an edge length of 9 cm and flush inoculated with 100 mL sterile water or

100 mM NaCl containing either live or heat-killed R401 WT cells at an OD_{600} of 0.0025. Four surface-sterilized and stratified Col-0 seeds were placed per pot. Pots where then placed in trays in the greenhouse for 28 days. The temperature was set at 22 °C during day and 18 °C during night, with a relative humidity at 65% and 16 h of light.

Agar plate experiments

For the experiment depicted in **Fig. 1a**, 24 surface-sterilized and stratified *A. thaliana* seeds were placed in two rows per 12 cm square plate containing ½ MS medium with 10 g/L Bacto-Agar (Duchefa Biochemie). Plants were grown for 14 days and then flushed with 15 mL 10 mM $MgCl_2$ containing either live or heat-killed R401 WT cells at an OD_{600} of 0.0005 for 5 mins. Plants were transferred to new plates and grown for another 5 days lates for 19 dpi.

RNA Seq Experiments

Total RNA was extracted from *A. thaliana* roots and shoots by RNeasy Plant Mini Kit (Qiagen). RNA-Seq libraries were prepared by the Max Planck Genome-centre Cologne with NEBNext® Ultra™ II Directional RNA Library Prep Kit for Illumina® and then sequenced on a NextSeq 2000 in 2 x 150 paired-end read mode. RNA-Seq read quality was observed with FastQC v0.11.9, then reads were trimmed with Trimmomatic PE v0.38[64] using parameters TRAILING:20 AVGQUAL:20 MINLEN:100. Trimmed reads were then mapped on the reference *A. thaliana* genome TAIR10 using Hisat2 v2.2.1[65], taking into consideration exon and splicing sites locations (according to annotation file TAIR10_GFF3_genes.gff downloaded from arabidopsis.org in October 2022). The number of fragments (pair of reads) mapped on each gene was then quantified using featureCounts v2.0.0[66] (parameter -p, default settings). Resulting data were used to calculate FPKM (fragments per kilobase of transcript per million fragments mapped) values for each gene in each sample: (1) Scaling factor: SF=Total number of mapped reads / 1e6; (2) Fragments per million: FPM=Number of reads mapped on one gene / SF; (3) FPKM= FPM / (Gene length / 1000). Numbers of mapped reads on each gene were also used to perform

differential gene expression analysis with DESeq2 v1.24.0[67] and functions estimateSizeFactor, estimateDispersions and nbinomWaldTest. log2FoldChanges values were then corrected with shrinkage algorithm apeglm v1.6.0[68]. One R401 WT and 100 mM NaCl-treated shoot sample (sample ID: 5642.W) was highly contaminated with brown trout (*Salmo trutta*) reads, likely arising during library preparation. This sample was therefore excluded from the analysis.

antiSMASH

antiSMASH[39] predictions are derived from Getzke et al. 2023[24].

Δsypc mutant generation

R401 Δ*sypc* mutant generation was conducted as described in Getzke et al. 2023[24]. All utilized primers can be found in **Supplementary Table 3**.

Quantification of R401 load on plant roots and shoots

Col-0, Gifu and Micro-Tom roots and shoots were carefully cleaned, dried and collected in pre-weighed, sterile 2 mL tubes containing 1 steel bead (3 mm diameter). Tubes were weighed again to assess the root or shoot fresh weight. Subsequently, samples were ground in a Precellys 24 TissueLyser (Bertin Technologies) for 2 x 30 s at 6,200 rpm with 15 s intervals. Then, 150 µL of sterile 10 mM $MgCl_2$ were added to each tube and roots were ground again under the same conditions. Each sample was subsequently dilute five times 1:10 in sterile 10 mM $MgCl_2$. Undiluted samples and each dilution were plated on 50% TSA square plates, dried and left to grow at 25 °C until single colonies appeared. Pictures were taken and single colonies were counted blinded.

468 *Microbial growth rates validation*

469 Assessment of microbial growth rates was conducted as described before[24]. Either artificial
470 root exudates (ARE) or ARE supplemented with 100 mM NaCl were inoculated with R401 WT
471 or Δ*sypc* cells to a final OD_{600} 0.01.

472

473 *Modified Burkholder assays*

474 Modified Burkholder assays to determine the antagonistic potential of R401 and its mutants
475 was carried out as described in Getzke et al. 2023[24]. For *Fusarium oxysporum* F212, pieces
476 of 14 days old mycelium were transferred to pre-weighed sterile 2 mL screw cap tubes
477 containing one and approx. 15 steel beads of 3 mm and 1 mm diameter, respectively. Per 50
478 mg harvested fungal mycelium, 500 µL of sterile 10 mM $MgCl_2$ were added. The mycelium
479 was subsequently grinded in a paint shaker at approx. 600 rpm for at least 10 min until
480 homogeneous. The resulting slurry was used to inoculate 25% TSA medium to a final
481 concentration of 100 µg/mL.

482

483 *Isolation of R401 brassicapeptin*

484 R401 was precultured in 300 mL flasks containing 100 mL TSB medium for 2 days at 30 °C
485 and 160 rpm. 80 mL preculture were added to 1 L M19 medium (casein peptone 20 g/l, D-
486 mannitol 20 g/L) in 5 L flasks. This procedure was carried out 70-times. All flasks were
487 incubated at 30 °C and 160 rpm for 24 hours, followed by an extraction using EtOAc (volume
488 ratio 1:1) for three times, yielding 16.24 g crude extract. Twenty-one fractions were collected
489 from reversed phase flash chromatography (Interchim Puriflash 4125 chromatography system
490 with Puriflash C18-AQ30 µm F0120 column) with an elution gradient starting from 10%
491 MeOH/H_2O to 100% MeOH over 4 h. Fraction 19 (143.8 mg) was further subjected to semi-
492 preparative HPLC (semipreparative purification column: VP 250/10 Nucleodur C18 Gravity-
493 SB, 5 µm; Macherey-Nagel, Flow: 3 mL/min; Gradient: 0–20 min, gradient increased from 40%
494 to 100% MeOH; 20–32 min, 100% MeOH) to give two subfractions (fractions 19.1 and 19.2).
495 Fraction 20 (96.7 mg) was also subjected to semi-preparative HPLC (semipreparative

purification column: VP 250/10 Nucleodur C18 Gravity-SB, 5 µm; Macherey-Nagel; Flow: 3 mL/min; Gradient: 0–20 min, gradient increased from 40% to 100% MeOH; 20–32 min, 100% MeOH) to give two subfractions (fractions 20.1 and 20.2). Subfraction 19.2 (6.7 mg) and 20.2 (6.7 mg) were further purified by semi-preparative HPLC (analysis column: EC 250/4.6 Nucleodur C18 Gravity-SB, 5 µm; Macherey-Nagel; Flow: 1 mL/min; Gradient: 0 – 40 min, gradient increased from 40% to 100% MeOH; 40–50 min, 100% MeOH) to yield brassicapeptin A (6.1 mg, t_R = 38.4 min). Fraction 18 (108.6 mg) was subjected to semi-preparative HPLC (semipreparative purification column: VP 250/10 Nucleodur C18 Gravity-SB, 5 µm; Macherey-Nagel; Flow: 3 mL/min; Gradient: 0–20 min, gradient increased from 40% to 100% MeOH; 20–32 min, 100% MeOH) to give three subfractions (fractions 18.1–18.3). Subfraction 18.3 (8 mg) was further purified by semi-preparative HPLC (analysis column: EC 250/4.6 Nucleodur C18 Gravity-SB, 5 µm; Macherey-Nagel; Flow: 1 mL/min; Gradient: 0–3 min, 10% MeCN; 3–58 min, gradient increased from 10% to 92.5% MeCN; 58–65 min, 100% MeCN) to yield brassicapeptin A (3 mg, t_R = 56.4 min) and B (0.9 mg, t_R = 52.3 min).

Structure elucidation of R401 brassicapeptin

The planar structure of the isolated compounds was elucidated by analysis of NMR data, LC-HR-MS and LC-HR-MS/MS data. The 1D and 2D NMR spectra were recorded in CD_3OD or DMSO-d_6 using Bruker Avance II 600 MHz spectrometers equipped with a Prodigy cryoprobe (Bruker, Ettlingen, Germany) and Bruker Avance Neo 700 MHz spectrometer equipped with a 5 mm CryoProbe Prodigy TCI (^1H,^{15}N,^{13}C Z-GRD) (Bruker). The NMR data can be found in **Supplementary Table 5**, all 1D and 2D NMR spectra can be found in **Supplementary Fig. 8c-i**. The LC-HR-MS and MS/MS data were recorded on a quadrupole time-of-flight spectrometer (LC-QTOF maXis II, Bruker Daltonik) equipped with an electrospray ionization source in line with an Agilent 1290 infinity LC system (Agilent). C18 RP-UHPLC (ACQUITY UPLC BEH C18 column; 130 Å, 1.7 µm, 2.1 × 100 mm) was performed at 45°C with the following linear gradient: 0 min: 95% A; 0.30 min: 95% A; 18.00 min: 4.75% A; 18.10 min: 0% A; 22.50 min: 0% A; 22.60 min: 95% A; 25.00 min: 95% A (A: H2O, 0.1% HCOOH; B: CH3CN,

524 0.1% HCOOH; flow rate: 0.6 mL/min). Mass spectral data were acquired using a 50 to 2,000
525 *m/z* scan range at 1 Hz scan rate. MS/MS experiments were performed with 6 Hz and the top
526 five most intense ions in each full MS spectrum were targeted for fragmentation by higher-
527 energy collisional dissociation at 25 eV or 55 eV using N2 at 10–2 mbar. Precursors were
528 excluded after two spectra, released after 0.5 min, and reconsidered if the intensity of an
529 excluded precursor increased by factor 1.5 or more. The HR-ESI-MS data can be found in
530 **Supplementary Fig. 8a,b,k,l,** the HR-ESI-MS/MS data can be found in **Supplementary**
531 **Table 6**. The absolute configuration of isolated compounds was elucidated by Marfey assay.
532 A 5 mM stock solution in H_2O was prepared from the reference amino acids. 20 µL 1 M
533 $NaHCO_3$ and 50 µL 7 mM L FDVA (Sigma Aldrich) in acetone was added to 50 µL stock
534 solution of the reference amino acids. The mixture was stirred at 40 °C for 3 h and then
535 quenched by adding 20 µL of 1 M HCl. After evaporation, the residue was dissolved in 40 µl
536 DMSO and analysed by UPLC HRMS (maXis II). brassicapeptin A (0.5 mg) and B (0.3 mg)
537 were dissolved in 200 µL of 6 M DCl in D_2O and stirred at 160 °C for 7 h. After concentrating
538 the solution under reduced pressure, the residue was dissolved in 200 µl H_2O and 100 µL of
539 1 M $NaHCO_3$ and 200 µL of 7 mM L FDVA in acetone were added. After stirring for 3 h at
540 40 °C, the solution was quenched by adding 100 µL of 1 M HCl. After evaporation to dryness,
541 the residue was dissolved in 50 µL DMSO and analysed by UPLC HRMS (maXis II). The
542 results of the Marfey analysis can be found in **Supplementary Fig. 8j**.
543
544 *In planta activity test of R401 brassicapeptin A*
545 Surface sterilized and stratified *A. thaliana* seeds were pregerminated on ½ MS agar plates.
546 After seven days, seedlings were transferred to ½ MS agar plates supplemented with either
547 1 ng/µL, 1 µg/µL brassicapeptin A solubilized in DMSO or DMSO as negative control and
548 either 0 mM or 100 mM NaCl. After 14 days agar plates for seven days and then transferred
549 to new plates containing NaCl and/or brassicapeptin A. Agar plates were incubated in a light
550 cabinet under short day conditions (10 h light at 21 °C, 14 h dark at 19 °C) for additional 14
551 days and randomized every 2–3 days.

552

553 *Minimal inhibitory concentration assay*

554 Determination of the minimum inhibitory concentration (MIC) of brassicapeptin A was carried
555 out by micro broth dilution assays in 96 well plates as literature[69]. brassicapeptin A was
556 dissolved in dimethyl sulfoxide (DMSO, Carl Roth GmbH + Co.) with a concentration of 6.4
557 mg/mL and tested in triplicate. Dilution series (64−0.03 µg/mL) of rifampicin, tetracycline, and
558 gentamicin (all Sigma -Aldrich) were prepared as positive controls for *Escherichia coli*
559 ATCC25922, *Staphylococcus aureus* ATCC25923 and *Listeria monocytogenes* DSM20600.
560 Same dilution series of rifampicin, tetracycline, and isoniazid for *Mycobacterium smegmatis*
561 ATCC607. For *Septoria tritici* MUCL45408, *Botrytis cinerea* HAG001286 and *Colletotrichum*
562 *coccodes* DSM62126, tebuconazole (Cayman Chemical Company), amphotericin B (Sigma-
563 Aldrich) and nystatin (Sigma Aldrich) were used as the positive control with same dilution
564 series. The MIC values for brassicapeptin A can be found in **Supplementary Table 2**.

565

566 *Ion leakage assay*

567 Five discs with 3 mm diameter of approx. 28 days old *A. thaliana* Col-0 leaves were transferred
568 to wells of a 24-well plate, filled with sterile MiliQ water supplemented with either 1 ng/µl,
569 1 µg/µL brassicapeptin A solubilized in DMSO or DMSO as negative control. Before the
570 transfer of leaf discs and after 16 h, ion leakage measurements were taken using the Twin
571 Cond conductivity meter B-173 (HORIBA).

572

573 *Statistical analyses*

574 All statistical analyses were conducted in R 4.1.2. Data visualisation was conducted using the
575 ggplot2 package (as part of the Tidyverse) or the ComplexHeatmap package. As
576 nonparametric tests, Kruskal-Wallis followed by Dunn's post-hoc test and Benjamini-Hochberg
577 (BH) adjustment for multiple comparisons from the PMCMRplus package (Pohlert, 2022) were
578 used. The respective statistical tests are indicated in each figure description. Significance was
579 indicated by significance group ($p \leq 0.05$). No statistical methods were used to pre-determine

580 sample sizes. Halo size quantification in modified Burkholder experiments, and root length
581 measurements were performed blinded using the Fiji package of ImageJ. Colony counts of
582 R401 were performed blinded. RNA sequencing data processed as described above and
583 further analysed and visualized as previously described[6]. GO Term enrichment was conducted
584 as indicted in the respective figure description or results section. Figures were assembled in
585 Adobe Illustrator.
586

587 **Author contributions**

588 F.G., S.H., T.F.S. and P.S.L. initiated the project. F.G. designed the experiments. L.W. and
589 T.F.S. isolated and elucidated brassicapeptins. F.G. and N.D. performed Flowpot
590 experiments. N.D. determined R401 load on roots and shoots. F.G. and H.W. performed CAS
591 and the initial agar plate experiment. F.M. performed initial RNA sequencing data analysis
592 including differential gene expression analysis. F.G. performed all further RNA sequencing
593 analyses. F.G. performed all brassicapeptin A experiments. S.H. and T.F.S. supervised the
594 project. F.G., L.W. and S.H. generated the figures. L.W. provided the original draft on
595 brassicapeptin structure elucidation. F.G. and S. H. wrote the manuscript, with inputs from all
596 co-authors.
597

598 **Acknowledgements**

599 This work was supported by funds to S.H. from European Research Council starting and
600 consolidator grants (MICRORULES 758003 and MICROBIOSIS 101089198). It includes also
601 funds to S.H. and P.S.-L. from the Max Planck Society, the Cluster of Excellence on Plant
602 Sciences (CEPLAS) and the Priority Programme: Deconstruction and Reconstruction of the
603 Plant Microbiota (SPP DECRyPT 2125; project P.S.-L.: SCHU 799/8-1; project S.H.: HA
604 8169/2-2), both funded by the Deutsche Forschungsgemeinschaft. Work in the Schäberle lab
605 was supported by the German Federal Ministry of Education and Research (BMBF). L.W. was
606 funded by the China Scholarship Council (CSC NO. 201908080177). We thank the Max

607 Planck-Genome-Centre Cologne for advising and performing the RNA sequencing. We also
608 thank Brigitte Pickel for her support in halo size quantifications and Flowpot harvest and Maria
609 Patras for her support in Marfey´s analysis. Finally, thanks to Neysan Donnelly for editing this
610 manuscript.

611

612 **Data availability**

613 RNAseq read data are available at GEO accession: GSE242479
614 (token for private access: whqfuiyqthkpxur). All supplementary tables have been deposited at
615 EDMOND and can be accessed *via* the following link: https://doi.org/10.17617/3.I1ABIM

616

617 **Code availability**

618 All code generated for this study are available at https://github.com/scriptsFG/Getzke-Wang-
619 et-al-2023.git

620

621 **References**

622 1. Agler MT, *et al.* Microbial Hub Taxa Link Host and Abiotic Factors to Plant
623 Microbiome Variation. *PLoS Biol* **14**, e1002352 (2016).
624 2. Bai Y, *et al.* Functional overlap of the Arabidopsis leaf and root microbiota.
625 *Nature* **528**, 364-+ (2015).
626 3. Duran P, *et al.* Microbial Interkingdom Interactions in Roots Promote
627 Arabidopsis Survival. *Cell* **175**, 973-+ (2018).
628 4. Thiergart T, *et al.* Root microbiota assembly and adaptive differentiation among
629 European Arabidopsis populations. *Nat Ecol Evol* **4**, 122-+ (2020).
630 5. Karasov TL, *et al.* Arabidopsis thaliana and Pseudomonas Pathogens Exhibit
631 Stable Associations over Evolutionary Timescales. *Cell Host Microbe* **24**, 168-
632 + (2018).

633 6. Ma KW, *et al.* Coordination of microbe-host homeostasis by crosstalk with plant
634 innate immunity. *Nat Plants* **7**, 814-+ (2021).
635 7. Pfeilmeier S, *et al.* The plant NADPH oxidase RBOHD is required for microbiota
636 homeostasis in leaves. *Nat Microbiol* **6**, 852-+ (2021).
637 8. Shalev O, Karasov TL, Lundberg DS, Ashkenazy H, Ayutthaya PPN, Weigel D.
638 Commensal Pseudomonas strains facilitate protective response against
639 pathogens in the host plant. *Nat Ecol Evol* **6**, 383-+ (2022).
640 9. Pfeilmeier S, Werz A, Ote M, Bortfeld-Miller M, Kirner P, Keppler A, Hemmerle
641 L, Gäbelein CG, Pestalozzi CM, Vorholt, JA. Dysbiosis of a leaf microbiome is
642 caused by enzyme secretion of opportunistic Xanthomonas strains. *biorxiv*,
643 (2023).
644 10. Entila F, Han X, Mine A, Schulze-Lefert P, Tsuda K. Commensal lifestyle
645 regulated by a negative feedback loop between Arabidopsis ROS and the
646 bacterial T2SS. *Biorxiv*, (2023).
647 11. Stevens RB. in: Plant Pathology, an Advanced Treatise, Vol. 3. J.G. Horsfall
648 and A.E. Dimond, eds. Academic Press, NY., 357-429 (1960).
649 12. Cheng YT, Zhang L, He SY. Plant-Microbe Interactions Facing Environmental
650 Challenge. *Cell Host Microbe* **26**, 183-192 (2019).
651 13. Arnault G, Mony C, Vandenkoornhuyse P. Plant microbiota dysbiosis and the
652 Anna Karenina Principle. *Trends Plant Sci* **28**, 18-30 (2023).
653 14. Mesny F, Hacquard S, Thomma BP. Co-evolution within the plant holobiont
654 drives host performance. *Embo Rep*, (2023).
655 15. Hua DP, *et al.* A Plasma Membrane Receptor Kinase, GHR1, Mediates
656 Abscisic Acid- and Hydrogen Peroxide-Regulated Stomatal Movement in
657 Arabidopsis. *Plant Cell* **24**, 2546-2561 (2012).

658 16. Zhang YY, *et al.* Phospholipase D alpha 1 and Phosphatidic Acid Regulate
659 NADPH Oxidase Activity and Production of Reactive Oxygen Species in ABA-
660 Mediated Stomatal Closure in Arabidopsis. *Plant Cell* **21**, 2357-2377 (2009).
661 17. Zhu JK. Salt and drought stress signal transduction in plants. *Annu Rev Plant*
662 *Biol* **53**, 247-273 (2002).
663 18. Zhu JK. Abiotic Stress Signaling and Responses in Plants. *Cell* **167**, 313-324
664 (2016).
665 19. Pieterse CMJ, Van der Does D, Zamioudis C, Leon-Reyes A, Van Wees SCM.
666 Hormonal Modulation of Plant Immunity. *Annu Rev Cell Dev Bi* **28**, 489-521
667 (2012).
668 20. Yasuda M, *et al.* Antagonistic interaction between systemic acquired resistance
669 and the abscisic acid-mediated abiotic stress response in Arabidopsis. *Plant*
670 *Cell* **20**, 1678-1692 (2008).
671 21. Berens ML, *et al.* Balancing trade-offs between biotic and abiotic stress
672 responses through leaf age-dependent variation in stress hormone cross-talk.
673 *P Natl Acad Sci USA* **116**, 2364-2373 (2019).
674 22. Fan J, Hill L, Crooks C, Doerner P, Lamb C. Abscisic Acid Has a Key Role in
675 Modulating Diverse Plant-Pathogen Interactions. *Plant Physiol* **150**, 1750-1761
676 (2009).
677 23. Jiang CJ, *et al.* Abscisic Acid Interacts Antagonistically with Salicylic Acid
678 Signaling Pathway in Rice-Magnaporthe grisea Interaction. *Mol Plant Microbe*
679 *In* **23**, 791-798 (2010).
680 24. Getzke F, *et al.* Cofunctioning of bacterial exometabolites drives root microbiota
681 establishment. *P Natl Acad Sci USA* **120**, (2023).

682 25. Feil H, *et al.* Comparison of the complete genome sequences of Pseudomonas
683 syringae pv. syringae B728a and pv. tomato DC3000. *P Natl Acad Sci USA*
684 **102**, 11064-11069 (2005).
685 26. Kremer JM, *et al.* Peat-based gnotobiotic plant growth systems for Arabidopsis
686 microbiome research. *Nat Protoc* **16**, (2021).
687 27. Dimartino M, *et al.* Occurrence and Pathogenicity of Pseudomonas
688 Fluorescens and P. Putida on Tomato Plants in Italy. *J Plant Pathol* **93**, 79-87
689 (2011).
690 28. Chojak-Kozniewska J, Linkiewicz A, Sowa S, Radzioch MA, Kuzniak E.
691 Interactive effects of salt stress and Pseudomonas syringae pv. lachrymans
692 infection in cucumber: Involvement of antioxidant enzymes, abscisic acid and
693 salicylic acid. *Environ Exp Bot* **136**, 9-20 (2017).
694 29. Mi HY, Muruganujan A, Casagrande JT, Thomas PD. Large-scale gene
695 function analysis with the PANTHER classification system. *Nat Protoc* **8**, 1551-
696 1566 (2013).
697 30. Mi HY, Muruganujan A, Ebert D, Huang XS, Thomas PD. PANTHER version
698 14: more genomes, a new PANTHER GO-slim and improvements in
699 enrichment analysis tools. *Nucleic Acids Res* **47**, D419-D426 (2019).
700 31. Carbon S, *et al.* Expansion of the Gene Ontology knowledgebase and
701 resources. *Nucleic Acids Res* **45**, D331-D338 (2017).
702 32. Chaves MM, Flexas J, Pinheiro C. Photosynthesis under drought and salt
703 stress: regulation mechanisms from whole plant to cell. *Ann Bot-London* **103**,
704 551-560 (2009).
705 33. Eynard A, Lal R, Wiebe K. Crop response in salt-affected soils. *J Sustain Agr*
706 **27**, 5-50 (2005).

34. Geng Y, *et al.* A Spatio-Temporal Understanding of Growth Regulation during the Salt Stress Response in Arabidopsis. *Plant Cell* **25**, 2132-2154 (2013).

35. Hanin M, Ebel C, Ngom M, Laplaze L, Masmoudi K. New Insights on Plant Salt Tolerance Mechanisms and Their Potential Use for Breeding. *Front Plant Sci* **7**, (2016).

36. Cunnac S, Lindeberg M, Collmer A. Pseudomonas syringae type III secretion system effectors: repertoires in search of functions. *Curr Opin Microbiol* **12**, 53-60 (2009).

37. Guo M, Tian F, Wamboldt Y, Alfano JR. The Majority of the Type III Effector Inventory of Pseudomonas syringae pv. tomato DC3000 Can Suppress Plant Immunity. *Mol Plant Microbe In* **22**, 1069-1080 (2009).

38. Wagner S, Grin I, Malmsheimer S, Singh N, Torres-Vargas CE, Westerhausen S. Bacterial type III secretion systems: a complex device for the delivery of bacterial effector proteins into eukaryotic host cells. *Fems Microbiol Lett* **365**, (2018).

39. Blin K, *et al.* antiSMASH 6.0: improving cluster detection and comparison capabilities. *Nucleic Acids Res* **49**, W29-W35 (2021).

40. Scholz-Schroeder BK, Hutchison ML, Grgurina I, Gross DC. The contribution of syringopeptin and syringomycin to virulence of Pseudomonas syringae pv. syringae strain B301D on the basis of sypA and syrB1 biosynthesis mutant analysis. *Mol Plant Microbe In* **14**, 336-348 (2001).

41. Wippel K, *et al.* Host preference and invasiveness of commensal bacteria in the Lotus and Arabidopsis root microbiota. *Nat Microbiol* **6**, 1150-+ (2021).

42. Levy A, *et al.* Genomic features of bacterial adaptation to plants. *Nat Genet* **50**, 138-+ (2018).

732 43. Hou S, *et al.* A microbiota-root-shoot circuit favours Arabidopsis growth over
733 defence under suboptimal light. *Nat Plants* **7**, 1078-+ (2021).
734 44. Ku HM, Vision T, Liu JP, Tanksley SD. Comparing sequenced segments of the
735 tomato and Arabidopsis genomes: Large-scale duplication followed by
736 selective gene loss creates a network of synteny. *P Natl Acad Sci USA* **97**,
737 9121-9126 (2000).
738 45. Grgurina I, *et al.* A new syringopeptin produced by bean strains of
739 Pseudomonas syringae pv. syringae. *Bba-Protein Struct M* **1597**, 81-89 (2002).
740 46. Grgurina I, *et al.* Novel cyclic lipodepsipeptide from Pseudomonas syringae pv.
741 lachrymans strain 508 and syringopeptin antimicrobial activities. *Antimicrob*
742 *Agents Ch* **49**, 5037-5045 (2005).
743 47. Isogai A, Iguchi H, Nakayama J, Kusai A, Takemoto JY, Suzuki A. Structural-
744 Analysis of New Syringopeptins by Tandem Mass-Spectrometry. *Biosci Biotech*
745 *Bioch* **59**, 1374-1376 (1995).
746 48. Bender CL, Alarcon-Chaidez F, Gross DC. Pseudomonas syringae
747 phytotoxins: Mode of action, regulation, and biosynthesis by peptide and
748 polyketide synthetases. *Microbiol Mol Biol R* **63**, 266-+ (1999).
749 49. Acosta-Motos JR, Ortuno MF, Bernal-Vicente A, Diaz-Vivancos P, Sanchez-
750 Blanco MJ, Hernandez JA. Plant Responses to Salt Stress: Adaptive
751 Mechanisms. *Agronomy-Basel* **7**, (2017).
752 50. Ashraf M, Harris PJC. Potential biochemical indicators of salinity tolerance in
753 plants. *Plant Sci* **166**, 3-16 (2004).
754 51. Dalla Serra M, *et al.* The interaction of lipodepsipeptide toxins from
755 Pseudomonas syringae pv. syringae with biological and model membranes: A

comparison of syringotoxin, syringomycin, and two syringopeptins. *Mol Plant Microbe In* **12**, 391-400 (1999).

52. Hutchison ML, Gross DC. Lipopeptide phytotoxins produced by Pseudomonas syringae pv syringae: Comparison of the biosurfactant and ion channel-forming activities of syringopeptin and syringomycin. *Mol Plant Microbe In* **10**, 347-354 (1997).

53. Melnyk RA, Hossain SS, Haney CH. Convergent gain and loss of genomic islands drive lifestyle changes in plant-associated Pseudomonas. *Isme J* **13**, 1575-1588 (2019).

54. Song Y, *et al.* FERONIA restricts Pseudomonas in the rhizosphere microbiome via regulation of reactive oxygen species. *Nat Plants* **7**, 644-+ (2021).

55. Corwin DL. Climate change impacts on soil salinity in agricultural areas. *Eur J Soil Sci* **72**, 842-862 (2021).

56. Eswar D, Karuppusamy R, Chellamuthu S. Drivers of soil salinity and their correlation with climate change. *Curr Opin Env Sust* **50**, 310-318 (2021).

57. Mukhopadhyay R, Sarkar B, Jat HS, Sharma PC, Bolan NS. Soil salinity under climate change: Challenges for sustainable agriculture and food security. *J Environ Manage* **280**, (2021).

58. Bionda N, Pitteloud JP, Cudic P. Cyclic lipodepsipeptides: a new class of antibacterial agents in the battle against resistant bacteria. *Future Med Chem* **5**, 1311-1330 (2013).

59. Kuiper I, *et al.* Characterization of two Pseudomonas putida lipopeptide biosurfactants, putisolvin I and II, which inhibit biofilm formation and break down existing biofilms. *Mol Microbiol* **51**, 97-113 (2004).

780 60. Neu TR, Hartner T, Poralla K. Surface-Active Properties of Viscosin - a
781 Peptidolipid Antibiotic. *Appl Microbiol Biot* **32**, 518-520 (1990).
782 61. Peypoux F, Bonmatin JM, Wallach J. Recent trends in the biochemistry of
783 surfactin. *Appl Microbiol Biot* **51**, 553-563 (1999).
784 62. Raaijmakers JM, de Bruijn I, Nybroe O, Ongena M. Natural functions of
785 lipopeptides from Bacillus and Pseudomonas: more than surfactants and
786 antibiotics. *Fems Microbiol Rev* **34**, 1037-1062 (2010).
787 63. Torres MA, Dangl JL, Jones JDG. Arabidopsis gp91(phox) homologues
788 AtrbohD and AtrbohF are required for accumulation of reactive oxygen
789 intermediates in the plant defense response. *P Natl Acad Sci USA* **99**, 517-522
790 (2002).
791 64. Bolger AM, Lohse M, Usadel B. Trimmomatic: a flexible trimmer for Illumina
792 sequence data. *Bioinformatics* **30**, 2114-2120 (2014).
793 65. Kim D, Paggi JM, Park C, Bennett C, Salzberg SL. Graph-based genome
794 alignment and genotyping with HISAT2 and HISAT-genotype. *Nat Biotechnol*
795 **37**, 907-+ (2019).
796 66. Liao Y, Smyth GK, Shi W. featureCounts: an efficient general purpose program
797 for assigning sequence reads to genomic features. *Bioinformatics* **30**, 923-930
798 (2014).
799 67. Love MI, Huber W, Anders S. Moderated estimation of fold change and
800 dispersion for RNA-seq data with DESeq2. *Genome Biol* **15**, (2014).
801 68. Zhu AQ, Ibrahim JG, Love MI. Heavy-tailed prior distributions for sequence
802 count data: removing the noise and preserving large differences. *Bioinformatics*
803 **35**, 2084-2092 (2019).

69. Wang L, *et al.* Discovery and Biosynthesis of Antimicrobial Phenethylamine Alkaloids from the Marine Flavobacterium Tenacibaculum discolor sv11. *J Nat Prod* **85**, 1039-1051 (2022).

70. Zhou YY, *et al.* Metascape provides a biologist-oriented resource for the analysis of systems-level datasets. *Nat Commun* **10**, (2019).

Figures

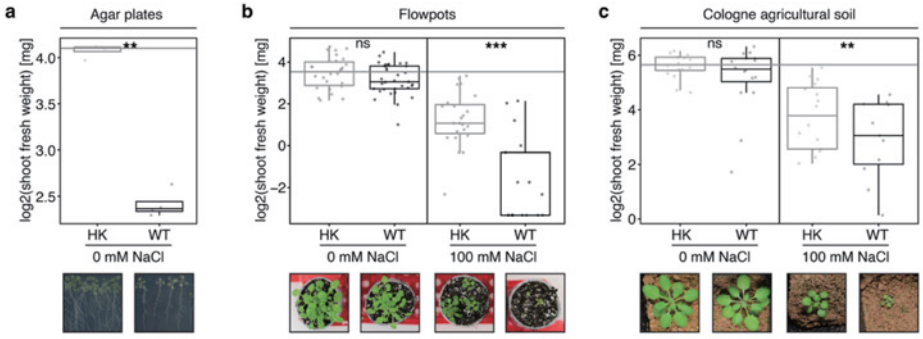

Fig. 1: Detrimental activity of *P. brassicacearum* R401 is facilitated by salt stress in soil. (**a**) log2-transformed shoot fresh weight of *A. thaliana* plants grown axenically on ½ MS agar plates for 19 dpi. At 14 dpi plants were flushed with either heat-killed (HK) or live wild-type (WT) R401 cells. Five minutes after flushing plants were transferred to new sterile plates and grown for five days (n = 5). (**b**) log2-transformed shoot fresh weight of *A. thaliana* plants grown in the gnotobiotic Flowpot system for 28 dpi in the presence or absence of 100 mM NaCl and either heat-killed (HK) or live wild-type (WT) R401 cells (n = 30). **(c)** log2-transformed shoot fresh weight of *A. thaliana* plants grown in the non-sterile Cologne agricultural soil (CAS) in the greenhouse for 28 dpi in the presence or absence of 100 mM NaCl and either heat-killed (HK) or live wild-type (WT) R401 (n = 16). (**a**-**c**) Representative images illustrating the respective plant phenotypes are shown below each plot. Within each figure panel, all images are to scale. Statistical significance was determined by Kruskal-Wallis followed by Dunn's post-hoc test and Benjamini-Hochberg adjustment. Significance compared to HK is indicated by black asterisks (** and *** indicate $p < 0.01$, and 0.001, respectively; ns, not significant). Statistical comparisons were conducted between WT and HK samples for each NaCl treatment separately.

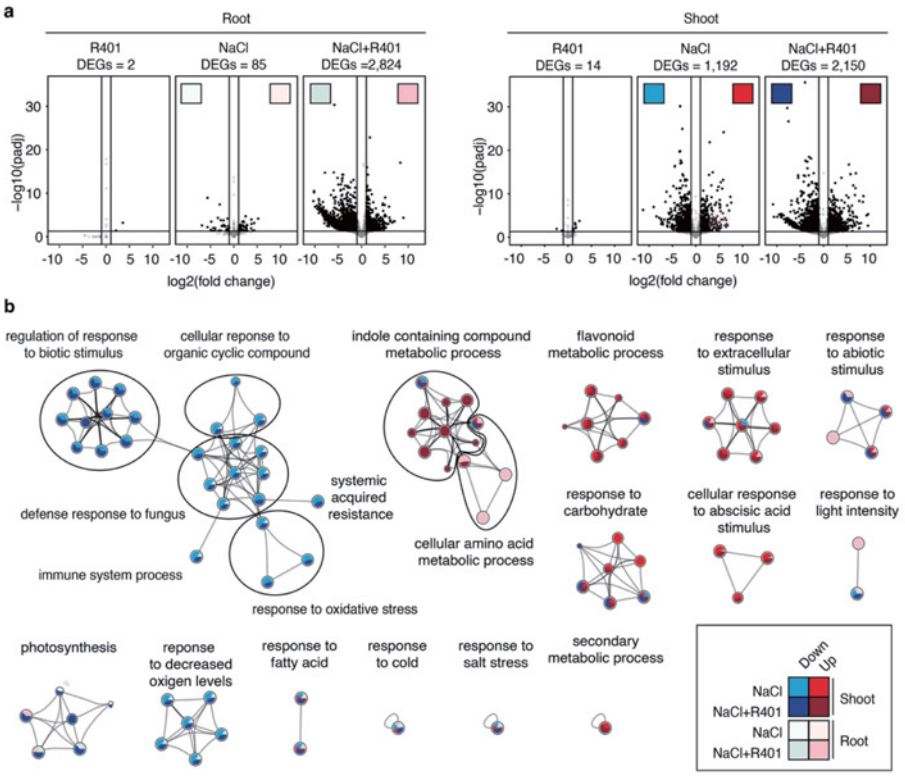

852

853 **Fig. 2: Interaction between R401 and NaCl triggers extensive transcriptional**
854 **reprogramming in roots.** (**a**) Transcriptomic analysis of *A. thaliana* shoots and roots (28 dpi)
855 grown in the gnotobiotic Flowpot system in the presence of R401, 100 mM NaCl or 100 mM
856 NaCl and R401 compared to the control condition (0 mM NaCl with Heat-Killed R401), n =
857 three biological replicates. The number of differentially-enriched genes (DEGs) as compared
858 to the control condition is indicated above the graphs and are shown in black in the volcano
859 plots. The coloured squares highlight the conditions shown in panel (b). (**b**) Network of
860 significantly enriched GO terms with NaCl or NaCl + R401-treated shoots and roots. All
861 significantly up- and downregulated genes as compared to control conditions (0 mM NaCl +
862 HK R401) were selected for the analysis. GO term enrichment analysis and clustering was
863 performed by Metascape[70] (Zhou et al., 2019). Unfilled spheres indicate subclusters.

864

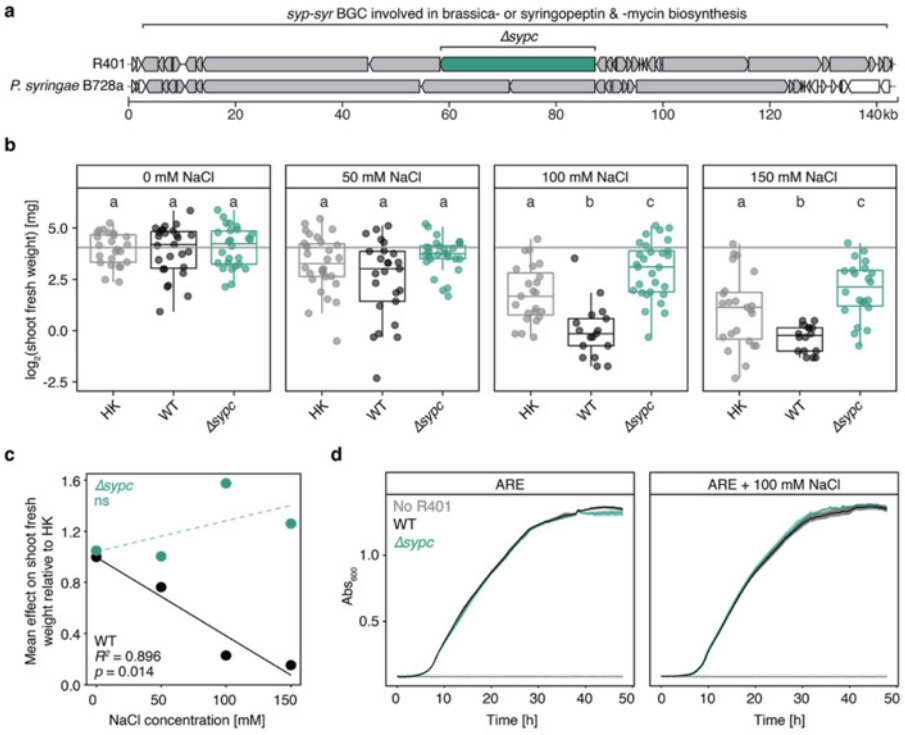

Fig. 3: Brassicapeptin production is required for R401 detrimental activity on salt-treated plants. (**a**) Schematic overview of the genomic context of the fragmented *syp-syr*-operon which encodes genes for syringopeptin and syringomycin biosynthesis in *Pseudomonas syringae* B728a and likely for related specialized metabolites in *Pseudomonas brassicacearum* R401, thereby termed brassicapeptin and brassicamycin. Genes within the biosynthetic gene cluster (BGC) are colored in grey, R401 *sypc* is highlighted in green. *sypc* is likely involved in brassicapeptin biosynthesis in R401. A Δ*sypc* knockout mutant has been generated in R401, lacking the full-length *sypc* coding region. (**b**) log2-transformed shoot fresh weight of *A. thaliana* plants grown in the gnotobiotic Flowpot system for 28 dpi in the presence of increasing concentrations of NaCl (0, 50, 100, or 150 mM NaCl) and either heat-killed (HK), live wild-type (WT) or live Δ*sypc* R401 cells. Letters indicate statistically significant differences as determined by Kruskal-Wallis followed by Dunn's post-hoc test and Benjamini-Hochberg adjustment with $p < 0.05$ (n = 30). Statistical comparisons were conducted for each salt

879 treatment separately. (**c**) Correlation analysis of the mean effect of either R401 WT or Δ*sypc*
880 on *A. thaliana* shoot fresh weight, normalized by the respective HK control and the applied
881 salt concentrations. Data derives from (b). *p*-values and R^2 derive from a linear model; ns, not
882 significant. (**d**) Growth curves of R401 WT and Δ*sypc* mutant in artificial root exudate (ARE)
883 liquid medium or ARE medium supplemented with 100 mM NaCl; n = 10.
884
885
886
887
888
889
890
891
892
893
894
895
896
897
898
899
900
901
902
903
904
905
906

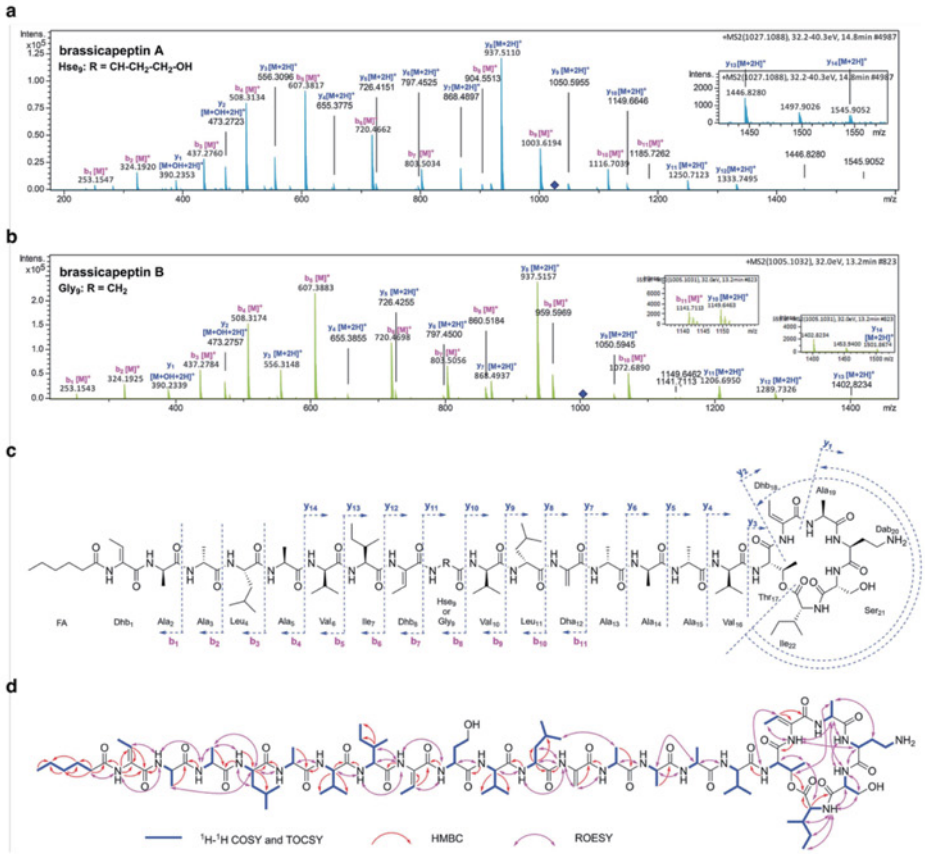

907

908 **Fig. 4: Structure elucidation of R401 brassicapeptin A and B.** (**a**,**b**) HR-ESI-MS/MS
909 fragments of brassicapeptin A (**a**) and brassicapeptin B (**b**). (**c**) Chemical structures of
910 brassicapeptin A and B detected from ESI-MS/MS fragmentations and nuclear magnetic
911 resonance (NMR) analysis. Brassicapeptin A and B differ only by one amino acid, which is a
912 homoserine (Hse_9) in brassicapeptin A and a glycine (Gly_9) in B, respectively. (**d**) ^1H-^1H
913 Correlated Spectroscopy (COSY; blue), Total Correlation Spectroscopy (TOCSY; blue),
914 Heteronuclear Multiple Bond Correlation (HMBC; red) and Rotating-frame Nuclear
915 Overhauser Effect Spectroscopy (ROESY; pink) revealed the complete structure of
916 brassicapeptin A.

917

918

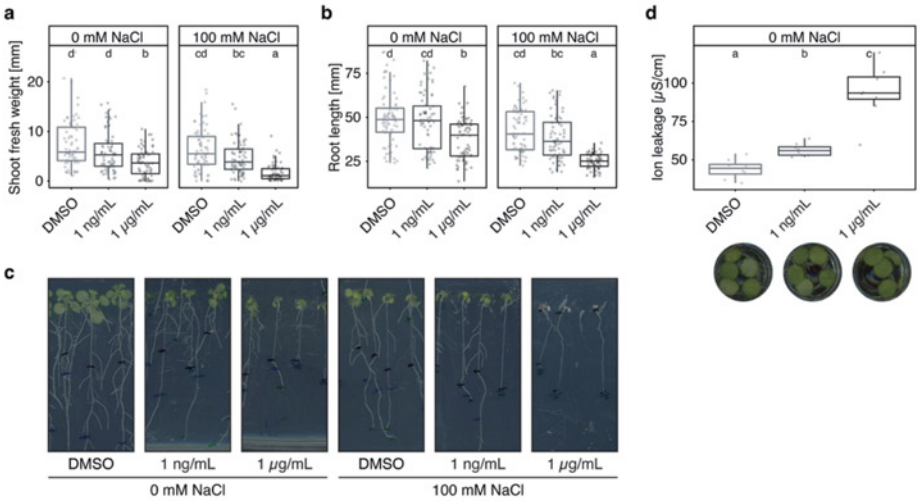

Fig. 5: Brassicapeptin A interaction with NaCl is sufficient to cause disease. (**a**-**c**) Shoot fresh weight (**a**), root length (**b**) and images of representative phenotypes **(c)** of *A. thaliana* plants grown axenically on ½ MS agar plates supplemented with increasing concentration of brassicapeptin A and either 0 or 100 mM NaCl (n = 72). Sterile *A. thaliana* seeds were pre-germinated on ½ MS agar plates for seven days and then transferred to new plates containing NaCl and/or brassicapeptin A for another 14 days; black, blue, and green markings in (c) indicate root length after seedling transfer or 7 and 14 days of growth, respectively. (**d**) Ion leakage assay of *A. thaliana* leaf discs, 16 h after treatment with increasing concentrations of brassicapeptin A. Circular images depict exemplary phenotypes, indicating the lack of cell death (n = 8). DMSO or brassicapeptin A was taken up in sterile miliQ water. All solutions were measured before the experiment resulting in measurements of 2 µS/cm. (**a**-**d**) Brassicapeptin was solubilized in DMSO. Concentrations in red indicate final brassicapeptin A concentrations in the agar or miliQ water. (**a**,**b**,**d**) Letters indicate statistically significant differences as determined by Kruskal-Wallis followed by Dunn's post-hoc test and Benjamini-Hochberg adjustment with $p < 0.05$. Statistical comparisons were conducted for each salt treatment separately.

Supporting Information of Publication 3

937 **Supplementary figures**

938

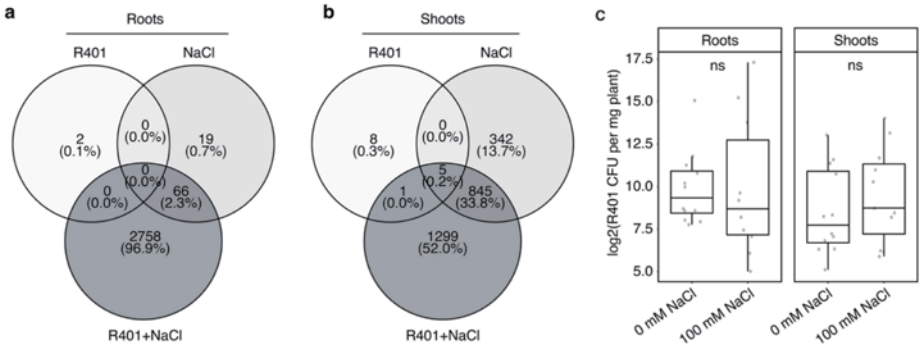

939

940 **Supplementary Fig. 1: R401 colonisation and transcriptome modulation are not linked.**
941 (**a**,**b**) Venn diagram of DEGs (from **Fig. 2a**) in roots (**a**) and shoots (**b**) of *A. thaliana* plants co-
942 inoculated with R401, 100 mM NaCl or both in the gnotobiotic Flowpot system. DEGs derive
943 from a pairwise comparison to control (HK and 0 mM NaCl)-treated plants. Percentages
944 indicate the total number of DEGs of all three comparisons. (**c**) Colonization capability of R401
945 on roots and shoots of *A. thaliana* seedlings grown in the gnotobiotic Flowpot system for 28
946 dpi in the presence or absence of 100 mM NaCl. Colony forming units have been normalized
947 to tissue fresh weight; n = 12. No statistically significant differences were determined by
948 Kruskal-Wallis followed by Dunn's post-hoc test and Benjamini-Hochberg adjustment as
949 indicated by "ns", not significant.

950

951

952

953

954

955

956

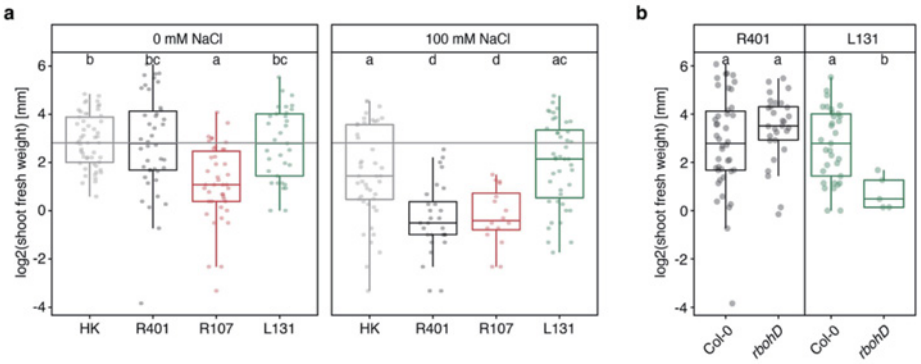

957

958 **Supplementary Fig. 2: R401 does not become detrimental in an immunocompromised**
959 ***rbohD A. thaliana* mutant.** (**a**) log2-transformed shoot fresh weight of *A. thaliana* plants
960 grown in the gnotobiotic Flowpot system for 28 dpi in the presence or absence of 100 mM
961 NaCl and either heat-killed (HK) R401 cells or live R401, *Streptomyces sp.* R107 or
962 *Xanthomonas sp.* L131 cells. (**b**) log2-transformed shoot fresh weight of *A. thaliana* wildtype
963 (Columbia-0, Col-0) or *rbohD* mutant plants grown in the gnotobiotic Flowpot system for 28 dpi
964 in the presence of either live R401 or *Xanthomonas sp.* L131 cells. Col-0 data are identical
965 with (a). (**a**,**b**) Letters indicate statistically significant differences as determined by Kruskal-
966 Wallis followed by Dunn's post-hoc test and Benjamini-Hochberg adjustment with $p < 0.05$ (n
967 = 30).

968

969

970

971

972

973

974

975

976

977

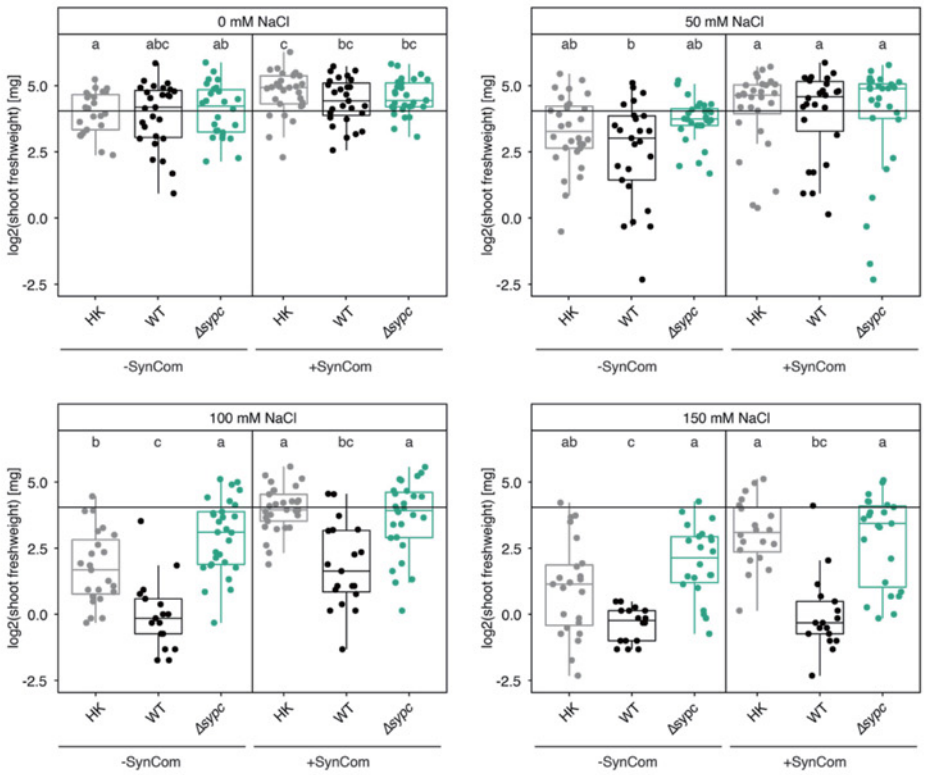

978

979 **Supplementary Fig. 3: *SypC*-dependent detrimental activity of R401 is retained in a**
980 **microbial community context.** Log2-transformed shoot fresh weight of *A. thaliana* plants
981 grown in the gnotobiotic Flowpot system for 28 dpi in the presence of increasing
982 concentrations of NaCl (0, 50, 100, or 150 mM NaCl) and either heat-killed (HK), live wild-type
983 (WT) or live Δ*sypc* R401 cells co-inoculated in the absence (-SynCom) or presence
984 (+SynCom) of a 15-member microbial synthetic community. Letters indicate statistically
985 significant differences as determined by Kruskal-Wallis followed by Dunn's post-hoc test and
986 Benjamini-Hochberg adjustment with $p < 0.05$ (n = 60). Statistical comparisons were
987 conducted for each salt treatment separately.

988

989

990

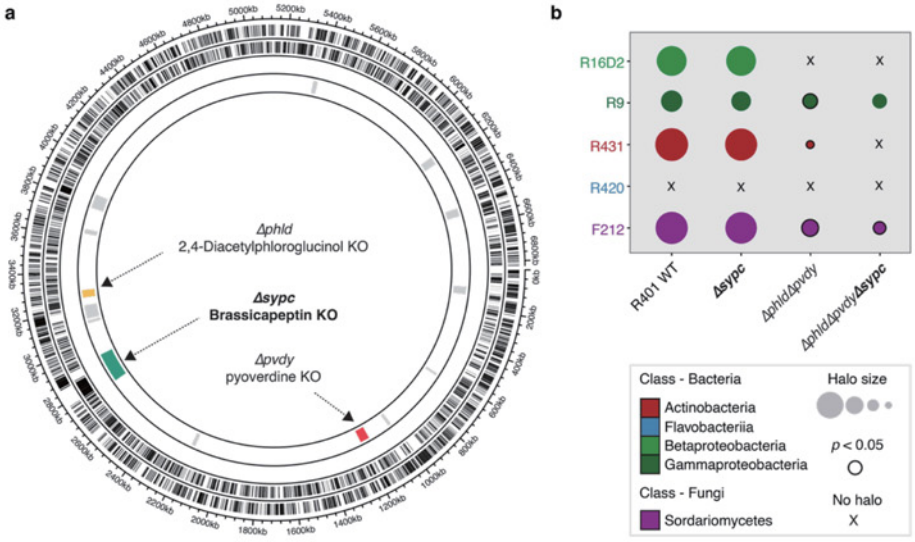

Supplementary Fig. 4: *SypC* contributes to R401 inhibitory activity against root microbiota members. (**a**) Genomic map of the main chromosome of R401, illustrating the locations of three biosynthetic gene clusters (BGC) involved in brassicapeptin A (green), 2,4-Diacetylphloroglucinol (DAPG, yellow) and pyoverdine (red) production in R401. Further indicated are respective mutants for each BGC (Δ*sypc*, Δ*phld*, Δ*pvdy*, respectively). R401 Δ*phld* and Δ*pvdy* have been previously characterized[24]. (**b**) Balloon plot depicting the inhibitory activity of R401 WT, Δ*sypc* (single), Δ*phld*Δ*pvdy* (double), or Δ*phld*Δ*pvdy*Δ*sypc* (triple) mutants, against four taxonomically diverse bacteria and one fungus. Inhibitory activity was measured as halo of inhibition size by a modified Burkholder assay as described before[24]. Statistical significance was determined by Kruskal-Wallis followed by Dunn's post-hoc test and Benjamini-Hochberg adjustment in comparison to the respective lower-order mutant or the wild-type in the case of the single mutant. Black circles indicate $p < 0.05$ (n = 5). 'x' indicates no detectable halo formation. Target strains are coloured based on the bacterial or fungal classes.

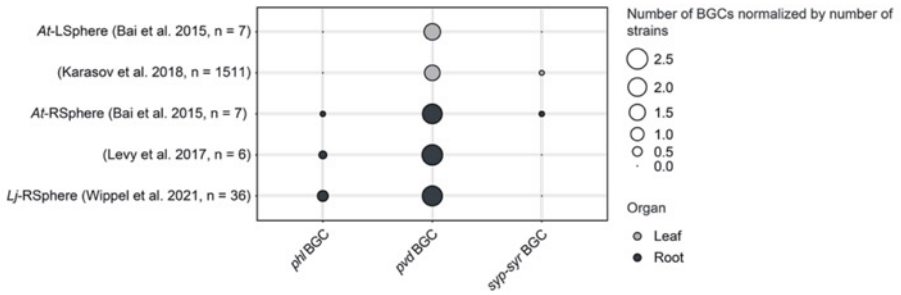

Supplementary Fig. 5: *Syp-syr* BGC is rare in genomes of plant-derived *Pseudomonas sp.* isolates. Using antiSMASH, we predicted BGCs for the genomes of *Pseudomonas sp.* isolates from different root and leaf derived culture collections. For each culture collection, the normalized number of *phl* BGCs (DAPG), *pvd* BGCs (pyoverdine), and syp-syr BGCs (syringo/brassica-peptin) are depicted. Dot size indicates the number of detected BGCs normalized by the number of tested strains.

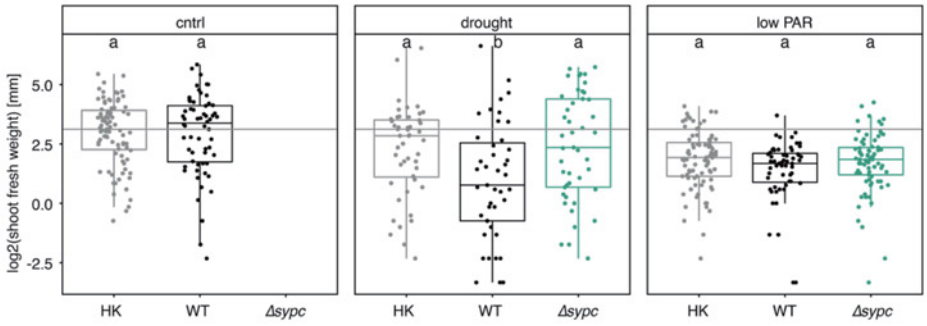

Supplementary Fig. 6: *SypC*-dependent detrimental activity of R401 on *A. thaliana* is osmotic-stress dependent. Log2-transformed shoot fresh weight of *A. thaliana* plants grown in the gnotobiotic Flowpot system for 28 dpi in the presence or absence of drought stress (5% PEG8000) or low photosynthetically active radiation (low PAR, induced by shading; Hou et al., 2021) and either heat-killed (HK), live wild-type (WT) or live Δ*sypc* R401 cells (n = 30).

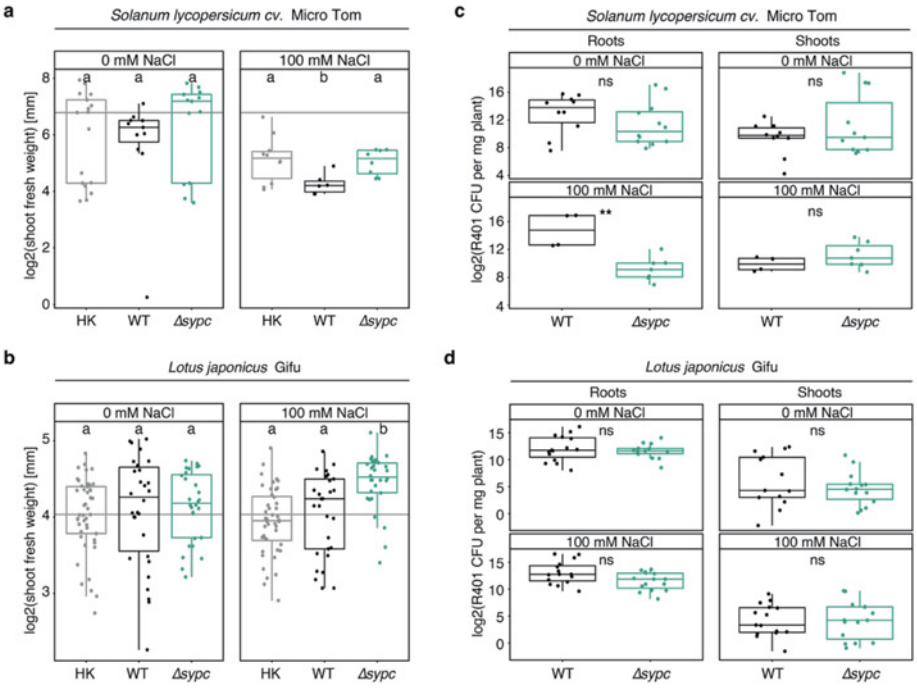

Supplementary Fig. 7: *SypC*-dependent detrimental activity of R401 is retained in salt-treated *S. lycopersicum*. (**a**,**b**) log2-transformed shoot fresh weight of *Solanum lycopersicum cv.* Micro-Tom (**a**; n = 15) and *Lotus japonicus* Gifu (**b**; n = 45) plants grown in the gnotobiotic Flowpot system for 28 dpi in the presence or absence of 100 mM NaCl and either heat-killed (HK), live wild-type (WT) or live Δ*sypc* R401 cells. (**a**,**b**) Letters indicate statistically significant differences as determined by Kruskal-Wallis followed by Dunn's post-hoc test and Benjamini-Hochberg adjustment with $p < 0.05$. Statistical comparisons were conducted for each abiotic stress treatment separately. (**c**,**d**) Colonization capability of R401 on roots and shoots of *Solanum lycopersicum cv.* Micro-Tom (**c**) and *Lotus japonicus* Gifu (**d**) plants grown in the gnotobiotic Flowpot system for 28 dpi in the presence or absence of 100 mM NaCl. Colony forming units have been normalized to tissue fresh weight; n = 15. Statistical significance was determined by Kruskal-Wallis followed by Dunn's post-hoc test and Benjamini-Hochberg adjustment. Significance between WT and Δ*sypc* is indicated by black asterisks (** indicates

1067 $p < 0.01$; ns, not significant). Statistical comparisons were conducted for each NaCl treatment
1068 and compartment separately.
1069
1070
1071
1072
1073
1074
1075
1076
1077
1078
1079
1080
1081
1082
1083
1084
1085
1086
1087
1088
1089
1090
1091
1092
1093
1094

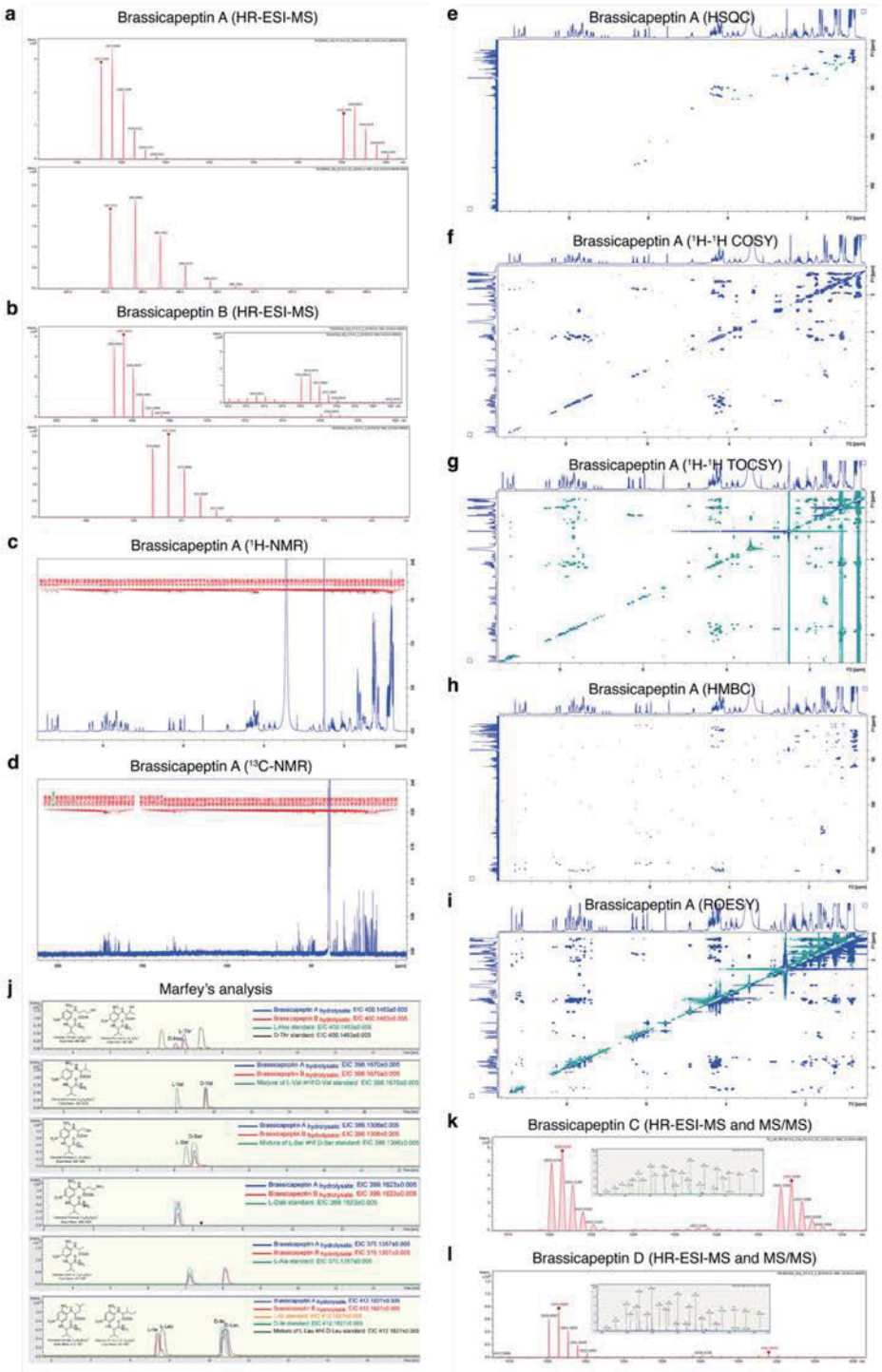
a
Brassicapeptin A (HR-ESI-MS)
b
Brassicapeptin B (HR-ESI-MS)
c
Brassicapeptin A (¹H-NMR)
d
Brassicapeptin A (¹³C-NMR)
e
Brassicapeptin A (HSQC)
f
Brassicapeptin A (¹H-¹H COSY)
g
Brassicapeptin A (¹H-¹H TOCSY)
h
Brassicapeptin A (HMBC)
i
Brassicapeptin A (ROESY)
j
Marfey's analysis
k
Brassicapeptin C (HR-ESI-MS and MS/MS)
l
Brassicapeptin D (HR-ESI-MS and MS/MS)

1095

46

Supplementary Fig. 8: Structure elucidation of brassicapeptins. (**a,b**) HR-ESI-MS of brassicapeptin A (**a**) and brassicapeptin B (**b**). (**c**) ^{1}H-NMR (600 MHz, DMSO-d_6) spectrum of brassicapeptin A. (**d**) ^{13}C-NMR (150 MHz, DMSO-d_6) spectrum of brassicapeptin A. (**e**) HSQC (600 MHz, DMSO-d_6) spectrum of brassicapeptin A. (**f**) ^{1}H-^{1}H COSY (600 MHz, DMSO-d_6) spectrum of brassicapeptin A. (**g**) ^{1}H-^{1}H TOCSY (600 MHz, DMSO-d_6) spectrum of brassicapeptin A. (**h**) HMBC (600 MHz, DMSO-d_6) spectrum of brassicapeptin A. (**i**) ROESY (600 MHz, DMSO-d_6) spectrum of brassicapeptin A. (**j**) Comparison of the Marfey derivatization products of brassicapeptin A and B DCl hydrolysate and amino acid standards. (**k**) HR-ESI-MS and HR-ESI-MS/MS (insert) of brassicapeptin C. (**l**) HR-ESI-MS and HR-ESI-MS/MS (insert) of brassicapeptin D

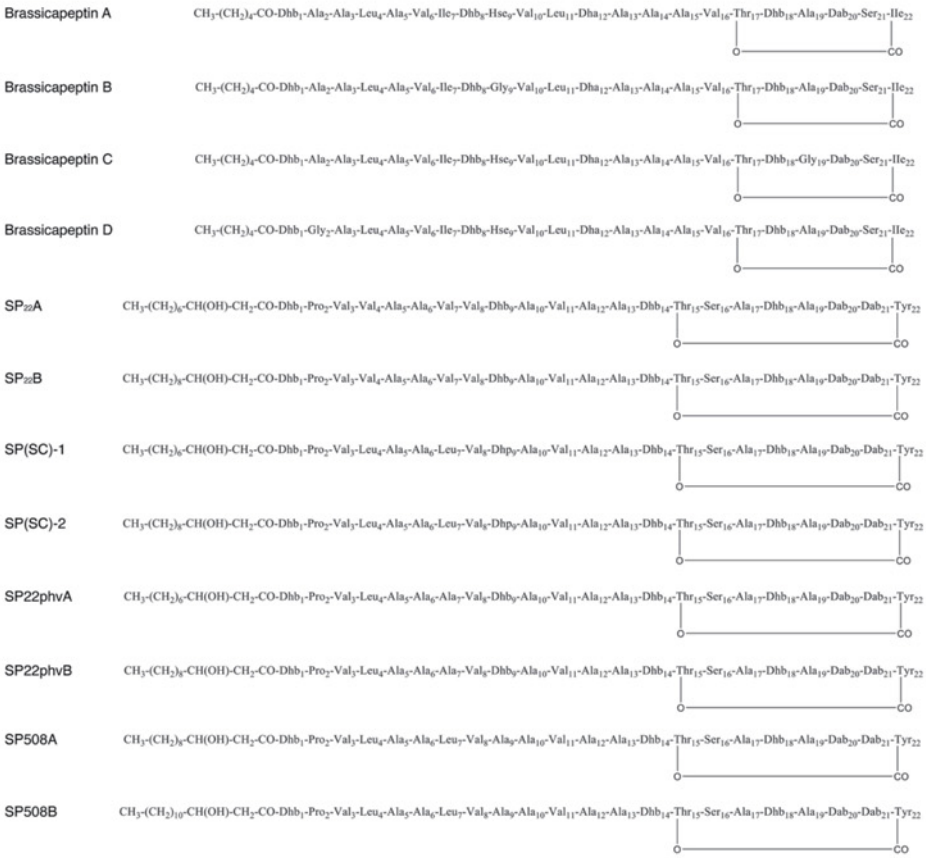

Supplementary Fig. 9: Structural comparison between R401 brassicapeptins and previously identified syringopeptins. Structures of R401 brassicapeptins A-D and other syringopeptins containing 22-amino-acid residues[45, 46, 47]. Note that the proposed structures of the minor variants brassicapeptin C and D are putative and based on MS/MS fragmentation patterns.

Supplementary Notes

Supplementary Note 1: Structural characterisation of R401 brassicapeptins.

Structural characterisation of R401 brassicapeptins was achieved by cultivating 70 liters of axenically grown R401. The fermentation broth was extracted using the organic solvent ethyl acetate (EtOAc) extraction, which yielded 16.24 g. This crude extract was subjected to chromatographic purification, using reversed phase C18 column chromatography, followed by semipreparative high-performance liquid chromatography (HPLC). In that way, brassicapeptins A and B were isolated, both as a white amorphous powder. The molecular formula of brassicapeptins A and B were predicted using high-resolution electrospray ionization mass spectrometry (HR-ESI-MS). In the HR-ESI-MS spectrum of brassicapeptin A, two double-charged ion peaks, *i.e.*, $[M+2H]^{2+}$ at *m/z* 1027.1080 and $[M+Na+H]^{2+}$ at *m/z* 1038.0990, as well as a triple-charged ion peak $[M+3H]^{3+}$ at *m/z* 685.0747 (**Supplementary Fig. 8a**), suggesting a molecular formula of $C_{96}H_{161}N_{23}O_{26}$ and requiring 28 degrees of unsaturation. For brassicapeptin B, the molecular formula was suggested as $C_{94}H_{157}N_{23}O_{25}$ based on the two double-charged ion peaks $[M+2H]^{2+}$ at *m/z* 1005.0940 and $[M+Na+H]^{2+}$ at *m/z* 1016.0852, together with a triple-charged ion peak $[M+3H]^{3+}$ at *m/z* 670.4000 in the HR-ESI-MS spectrum (**Supplementary Fig. 8b**).

To fully resolve the structures, we performed nuclear magnetic resonance (NMR)-experiments of brassicapeptin A and Marfey's analysis of both derivatives, *i.e.*, brassicapeptin A and B. The ^{1}H NMR and Heteronuclear Single Quantum Coherence (HSQC) spectrum displayed 22 amide protons, which resonated from δ_H 7.30 to δ_H 9.40 and 18 α protons that resonated from δ_H 3.70 to δ_H 4.50 (**Supplementary Table 5**). A correlation from a methylene group at δ_H 2.85 and 2.77 (Dab-Hγ) to amide protons at δ_H 7.68 (Dab-NH_2, 2H, overlapped) from the ^{1}H-^{1}H Correlated Spectroscopy (COSY) spectrum indicated a terminal amide group (Dab-γ) belonging to a diaminobutyric acid (Dab) residue, which was confirmed by Total Correlation

Spectroscopy (TOCSY) correlation from Dab-NH (δ_H 9.20) to Dab-Hα (δ_H 3.82), Dab-Hβ (δ_H 2.32 and 2.02), Dab-Hγ, and Dab-NH_2 (**Fig. 4d** and **Supplementary Table 5**). A dehydroalanine (Dha) residue was assigned based on the Heteronuclear Multiple Bond Correlation (HMBC) correlations from δ_H 5.97 and 5.52 (Dha-Hβ) to δ_C 135.32 (Dha-Cα) and δ_C 163.74 (Dha-CO) (**Fig. 4d** and **Supplementary Table 5**). Three 2,3-dehydroaminobutyric acid (Dhb) residues were assigned based on clear COSY correlations between three olefinic protons (Dhb-Hβ) and three methyl groups (Dhb-Hγ) (i.e., δ_H 6.35/δ_H 1.61, δ_H 6.25/δ_H 1.67, and δ_H 6.07/δ_H 1.66), as well as HMBC correlations from the olefinic proton of Dhb-Hβ to carbon of Dhb-Cα and Dhb carbonyl (*i.e.*, from δ_H 6.35 to δ_C 130.47 and 164.11, from δ_H 6.25 to δ_C 130.89 and 164.15, and from δ_H 6.07 to δ_C 131.51 and δ_C 165.93), and from the methyl group of Dhb-Hγ to carbon of Dhb-Cβ and Dhb-Cα (*i.e.*, from δ_H 1.61 to δ_C 127.82 and δ_C 130.47; from δ_H 1.67 to δ_C 127.02 and δ_C 130.89; from δ_H 1.66 to δ_C 124.14 and δ_C 131.51) (**Fig. 4d** and **Supplementary Table 5**). A threonine (Thr) residue was identified from the TOCSY correlations between Thr-NH (δ_H 7.84)/Thr-Hα (δ_H 4.16), Thr-NH/Thr-Hβ (δ_H 4.90) and Thr-Hβ/Thr-Hγ (δ_H 1.16) (**Fig. 4d** and **Supplementary Table 5**). The presence of a serine (Ser) residue was verified based on the COSY correlations between Ser-Hβ (δ_H 3.73 and 3.87)/Ser-Hα (δ_H 4.23), together with the TOCSY correlations between Ser-NH (δ_H 7.45)/Ser-Hα and Ser-NH/Ser-Hβ (**Fig. 4d** and **Supplementary Table 5**). In addition, we also clarified the presence of a homoserine (Hse) residue from the COSY correlations between Hse-Hα (δ_H 4.39)/Hse-Hβ (δ_H 1.73 and 1.84) and Hse-Hβ/Hse-Hγ (δ_H 3.41), as well as TOCSY correlations from Hse-NH (δ_H 7.56) to Hse-Hα, Hse-Hβ and Hse-Hγ (**Fig. 4d** and **Supplementary Table 5**). Two leucine (Leu) residues were verified based on the TOCSY correlations between Leu-NH/Leu-Hα and Leu-NH/Leu-Hβ (*i.e.*, δ_H 7.54/δ_H 4.15, δ_H 7.54/δ_H 1.49, δ_H 7.90/δ_H 4.36 and δ_H 7.90/δ_H 1.13), together with HMBC correlations from Leu-Hβ to Leu-Cγ, Leu-Cδ and Leu-Cδ' (*i.e.*, from δ_H 1.49 to δ_C 24.05, 21.22, 22.89, and from δ_H 1.32 and 1.13 to δ_C 36.25, 11.43 and 14.44) (**Fig. 4d** and **Supplementary Table 5**). Two isoleucine (Ile) residues were identified based on the TOCSY correlations from Ile-NH to Ile-Hα, Ile-Hβ and Ile-Hγ' (*i.e.*, from δ_H 7.75 to δ_H 4.28, δ_H 1.86 and δ_H 0.86 and from δ_H 7.39 to δ_H 4.42, δ_H 1.89 and 0.80), as well as

COSY correlations from Ile-Hγ to Ile-Hβ and Ile-Hδ (i.e., from δ_H 1.41 and 1.13 to δ_H 1.86 and δ_H 0.89, and from δ_H 1.47 and 1.05 to δ_H 1.89 and δ_H 0.84) (**Fig. 4d** and **Supplementary Table 5**). Three valine (Val) residues were assigned based on TOCSY correlations from Val-NH to Val-Hα and Val-Hβ (*i.e.*, from δ_H 7.66 to δ_H 4.19 and δ_H 1.99, from δ_H 7.71 to δ_H 4.25 and δ_H 2.03, and from δ_H 7.83 to δ_H 4.16 and δ_H 2.06), together with HMBC correlations from Val-Hγ and Val-Hγ' to Val-Cβ (*i.e.*, from δ_H 0.79 and 0.83 to δ_C 29.77, from δ_H 0.81 and 0.83 to δ_C 30.22, and from δ_H 0.91 and 0.93 to δ_C 30.05) (**Fig. 4d** and **Supplementary Table 5**). In addition, we also clarified the presence of seven alanine (Ala) residues from the TOCSY correlations from Ala-NH to Ala-Hα and Ala-Hβ (*i.e.*, from δ_H 8.34 to δ_H 4.32 and δ_H 1.28, from δ_H 8.26 to δ_H 4.20 and δ_H 1.27, from δ_H 8.02 to δ_H 4.24 and δ_H 1.23, from δ_H 7.96 to δ_H 3.99 and δ_H 1.24, from δ_H 7.95 to δ_H 4.33 and δ_H 1.22, from δ_H 7.91 to δ_H 4.13 and δ_H 1.29, and from δ_H 7.65 to δ_H 4.24 and δ_H 1.23) (**Fig. 4d** and **Supplementary Table 5**). The above 1D and 2D NMR data revealed 22 amino acid residues of Brassicapeptin A, including one diaminobutyric acid (Dab), one dehydroalanine (Dha), three 2,3-dehydroaminobutyric acids (Dhb), one threonine (Thr), one serine (Ser), one homoserine (Hse), two leucines (Leu), two isoleucines (Ile), three valines (Val), and seven alanines (Ala). Additionally, four methylene groups at δ_C 34.82 (δ_H 2.30 and 2.26), δ_C 30.77 (δ_H 1.27), δ_C 24.49 (δ_H 1.53) and δ_C 21.83 (δ_H 1.28) and one methyl at δ_C 13.78 (δ_H 0.86) were observed from the HSQC spectrum, together with another carbonyl group at δ_C 172.58 detected from the ^{13}C NMR spectrum (**Fig. 4d** and **Supplementary Table 5**). These signals were attributed to a fatty acid (FA) chain consisting of six carbons, thereby including a carbonyl group. This was based on TOCSY correlations from FA-H_2 (δ_H 2.30 and δ_H 2.26) to FA-H_3 (δ_H 1.53), FA-H_4 (δ_H 1.27), FA-H_5 (δ_H 1.28) and FA-H_6 (δ_H 0.86), as well as HMBC correlations from FA-H_2 to FA-CO (δ_C 172.58), FA-C_4 (δ_C 30.77) and FA-C_3 (δ_C 24.49), from FA-H_4 to FA-C_3 and FA-C_5 (δ_C 21.83), and from both FA-H_3 and FA-H_6 (δ_H 0.86) to FA-C_5 (**Fig. 4d** and **Supplementary Table 5**). The fatty acid chain and the amino acid residues accounted for 27 of the 28 degrees of unsaturation indicated by the molecular formula. Therefore, it was concluded that brassicapeptin A possesses an additional ring.

1219 The connectivity and the sequence of the amino acids for Brassicapeptin A was established
1220 by HMBC and Rotating-frame Nuclear Overhauser Effect Spectroscopy (ROESY) NMR data,
1221 along with the high-resolution electrospray ionization tandem mass spectrometry (HR-ESI-
1222 MS/MS) data. The fatty acid chain was assigned to be linked with a Dhb residue (Dhb_1) based
1223 on HMBC correlation from Dhb_1-NH (δ_H 9.38) to FA-CO, which can be confirmed by the
1224 ROESY correlation between Dhb_1-NH and FA-H_2 (**Fig. 4d** and **Supplementary Table 5**). The
1225 Dhb_1 residue was further supported to be linked with a peptide fragment of Ala_2-Ala_3-Leu_4-Ala_5
1226 by ROESY correlations between Dhb_1-NH/Ala_2-NH (δ_H 8.26), Dhb_1-Hβ (δ_H 6.07)/Ala_2-NH, Ala_2-
1227 NH/Ala_3-NH (δ_H 7.91), Ala_3-Hβ (δ_H 1.29)/Leu_4-NH (δ_H 7.54), Leu_4-Hα (δ_H 4.15)/Ala_5-NH (δ_H
1228 7.65), as well as by HMBC correlation from Ala_2-NH to Dhb_1-CO (δ_C 165.93), from Ala_3-NH to
1229 Ala_2-CO (δ_C 172.96), from Leu_4-NH to Ala_3-CO (δ_C 172.25), and from Ala_5-NH to Leu_4-CO (δ_C
1230 171.68) (**Fig. 4d** and **Supplementary Table 5**). Thus, a FA-Dhb_1-Ala_2-Ala_3-Leu_4-Ala_5 part was
1231 elucidated, which was also supported by the MS/MS fragments b_1-b_4 (**Fig. 4a)**. Key ROESY
1232 correlations were observed between Ala_5-Hα (δ_H 4.24)/Val_6-NH (δ_H 7.66), Val_6-Hα (δ_H
1233 4.19)/Ile_7-NH (δ_H 7.75), Ile_7-NH/Dhb_8-NH (δ_H 9.14), Dhb_8-NH/Hse_9-NH (δ_H 7.56), Hse_9-Hα (δ_H
1234 4.39)/Val_{10}-NH (δ_H 7.71), Val_{10}-Hα (δ_H 4.25)/Leu_{11}-NH (δ_H 7.90), and Leu_{11}-NH/Dha_{12}-NH (δ_H
1235 9.12), as well as key HMBC correlations of NH signals of Val_6, Ile_7, Dhb_8, Hse_9, Val_{10}, Leu_{11}
1236 and Dha_{12}, respectively, to their neighboring carbonyls of Ala_5 (δ_C 172.21), Val_6 (δ_C 171.32),
1237 Ile_7 (δ_C 170.46), Dhb_8 (δ_C 164.11), Hse_9 (δ_C 171.38), Val_{10} (δ_C 171.42), and Leu_{11} (δ_C 170.68),
1238 which correspond to the peptide fragment of Val_6-Ile_7-Dhb_8-Hse_9-Val_{10}-Leu_{11}-Dha_{12} (**Fig. 4d**
1239 and **Supplementary Table 5**). This assignment was also evident from the MS/MS fragments
1240 b_5-b_{11} and y_7-y_{14} (**Fig. 4a**). Further ROESY correlations between Dha_{12}-Hβ (δ_H 5.97 and
1241 5.52)/Ala_{13}-NH (δ_H 8.34), Ala_{13}-Hα (δ_H 4.32)/Ala_{14}-NH (δ_H 8.02), Ala_{14}-Hα (δ_H 4.24)/Ala_{15}-NH
1242 (δ_H 7.95), and Ala_{15}-Hα (δ_H 4.33)/Val_{16}-NH (δ_H 7.83), in association with the HMBC correlations
1243 from Val_{16}-NH to Ala_{15}-CO (δ_C 172.89), from Ala_{15}-NH to Ala_{14}-CO (δ_C 172.04), from Ala_{14}-NH
1244 to Ala_{13}-CO (δ_C 171.94), and from Ala_{13}-NH to Dha_{12}-CO (δ_C 163.74), established another
1245 partial peptide sequence of Dha_{12}-Ala_{13}-Ala_{14}-Ala_{15}-Val_{16}, which was in agreement with the
1246 MS/MS fragments y_3-y_8 (**Fig. 4a,d** and **Supplementary Table 5**). These data corroborated

the linear chain of brassicapeptin A as FA-Dhb$_1$-Ala$_2$-Ala$_3$-Leu$_4$-Ala$_5$-Val$_6$-Ile$_7$-Dhb$_8$-Hse$_9$-Val$_{10}$-Leu$_{11}$-Dha$_{12}$-Ala$_{13}$-Ala$_{14}$-Ala$_{15}$-Val$_{16}$. Similarly, the observed ROESY correlation of Ile$_{22}$-NH (δ_H 7.39)/Ser$_{21}$-Hα (δ_H 4.23), Ser$_{21}$-NH (δ_H 7.45)/Dab$_{20}$-Hα (δ_H 3.82) and Dab$_{20}$-NH (δ_H 9.20)/Ala$_{19}$-Hα (δ_H 3.99) suggested the fragment of Ala$_{19}$-Dab$_{20}$-Ser$_{21}$-Ile$_{22}$, which was evident from the MS/MS fragment y_1 (**Fig. 4a,d** and **Supplementary Table 5**). Further ROESY correlations between Dhb$_{18}$-NH (δ_H 9.27)/Ala$_{19}$-Hα, and Dhb$_{18}$-NH/Thr$_{17}$-NH (δ_H 7.84), along with the HMBC correlations from Dhb$_{18}$-NH to Thr$_{17}$-CO (δ_C 170.53), established the partial structure of Thr$_{17}$-Dhb$_{18}$-Ala$_{19}$, which was confirmed by the fragments y_2 and y_3 (**Fig. 4a,d** and **Supplementary Table 5**). Moreover, the ROESY correlation observed for Ile$_{22}$-Hα (δ_H 4.42)/Thr$_{17}$-Hγ (δ_H 1.16), in addition to the HMBC correlation from Thr$_{17}$-Hβ (δ_H 4.90) to Ile$_{22}$-CO (δ_C 169.45), established the nature of the cyclization of brassicapeptin A via the connection of the Thr$_{17}$ unit with Ile$_{22}$, fulfilling the degrees of unsaturation and further supported by the detected MS/MS fragment y_3 (**Fig. 4a,d** and **Supplementary Table 5**). Thus, the cyclic substructure was established as *cyclo*(Thr$_{17}$-Dhb$_{18}$-Ala$_{19}$-Dab$_{20}$-Ser$_{21}$-Ile$_{22}$). Finally, the connectivity of the cyclic part and the linear chain was established through the HMBC correlation from Thr$_{17}$-NH to Val$_{16}$-CO (δ_C 172.86), which was further corroborated by the fragments y_3 and y_4 from the MS/MS data (**Fig. 4a,d** and **Supplementary Table 5**). Hence, the planar structure of brassicapeptin A was elucidated. Comparison of the HR-ESI-MS/MS fragments of brassicapeptins A and B revealed the high similarity from b_1 to b_7 and from y_1-y_{10}, except for the differences from b_7 to b_{11} and from y_{11}-y_{14} (**Fig. 4a,b**). These differences indicated that the Hse$_9$ residue present in brassicapeptin A was replaced by a Gly residue (**Fig. 4c**). Thus, the planar structure of brassicapeptin B was elucidated as FA-Dhb$_1$-Ala$_2$-Ala$_3$-Leu$_4$-Ala$_5$-Val$_6$-Ile$_7$-Dhb$_8$-Gly$_9$-Val$_{10}$-Leu$_{11}$-Dha$_{12}$-Ala$_{13}$-Ala$_{14}$-Ala$_{15}$-Val$_{16}$-*cyclo*(Thr$_{17}$-Dhb$_{18}$-Ala$_{19}$-Dab$_{20}$-Ser$_{21}$-Ile$_{22}$). We were not able to get the NMR data of brassicapeptin B due to the limited amount of sample.

Marfey's analysis and ROESY data was used to determine the absolute configuration. Brassicapeptins A and B were first hydrolyzed, followed by chemical derivatization with N_α-(2,4-dinitro-5-fluorophenyl)-L-valinamide ($_L$-FDVA, Marfey's reagent), then comparing the

retention time with the reference substrates using UPLC-MS analysis (**Supplementary Fig. 8j**). Marfey's analysis revealed that the homoserine residue (Hse_9), serine residue (Ser_{21}) and valine residues (Val_6, Val_{10}, and Val_{16}) were present in $_D$-configuration, whereas the diaminobutyric acid residue (Dab_{20}) and threonine residue (Thr_{17}) were present in $_L$-configuration (**Supplementary Fig. 8j**). The observed ROESY correlation for Thr_{17}-Hα/Thr_{17}-Hγ and Ile_{22}-Hα /Thr_{17}-Hγ indicated the $_R$-configuration for Thr_{17}-Cβ and $_D$-configuration for Ile_{22} (**Fig. 4d** and **Supplementary Table 5**). The Ile_7 was further assigned as $_L$-configuration due to the fact that a mixture of both, $_D$- and $_L$-configuration of isoleucines were observed from Marfey's analysis (**Supplementary Fig. 8j**). Further detected ROESY correlations between Ala_{19}-Hβ/Thr_{17}-Hβ and Ala_{19}-Hβ/Dab_{20}-Hγ allowed the assignment of $_L$-configuration for Ala_{19} (**Fig. 4d** and **Supplementary Table 5**). The ROESY correlations between Ala_{14}-Hα/Ala_{15}-Hα, Ala_2-Hβ/Leu_4-Hα and Ala_3-Hβ/Leu_4-Hα suggested the same configuration for Ala_{14} and Ala_{15}, same configuration for Ala_2 and Ala_3 and different configuration for Ala_3 and Leu_4. Additionally, a 2:5 ratio of $_L$- and $_D$-alanine was observed, indicating the $_D$-configuration of Ala_2, Ala_3, Ala_{14} and Ala_{15} and $_L$-configuration of Leu_4 (**Fig. 4d**, **Supplementary Table 5** and **Supplementary Fig. 8j**). Marfey's analysis also indicated the presence of both, $_L$- and $_D$-leucine, which allowed us to assign the $_D$-configuration for Leu_{11} (**Supplementary Fig. 8j**). Additional ROESY correlations observed between Ala_{13}-Hα/Leu_{11}-Hδ' allowed the assignment of a $_L$-configuration for Ala_{13} (**Fig. 4d** and **Supplementary Table 5**). The Ala_5 was then deduced as $_D$-configuration from the observed 2:5 ratio of $_L$- and $_D$-alanine. The same absolute configuration of brassicapeptin B was established based on the same results of the Marfey's analysis, except the Hse_9 residue was replaced by a glycine (Gly) residue (**Fig. 4d** and **Supplementary Fig. 8j**). Thus, the structure of brassicapeptins A and B were elucidated as shown (**Fig. 4c)**.

Besides brassicapeptin A and B, another two minor derivatives (*i.e.*, brassicapeptins C and D) were also elucidated based on the HR-ESI-MS/MS data. In the HR-ESI-MS spectrum of brassicapeptin C, two double-charged ion peaks at at *m*/*z* 1020.1176 $[M+2H]^{2+}$ and 1031.1058 $[M+Na+H]^{2+}$ were observed (**Supplementary Fig. 8k**), suggesting a molecular formula of $C_{95}H_{159}N_{23}O_{26}$. The HR-ESI-MS/MS data of brassicapeptin C revealed high similarity to

brassicapeptin A (**Supplementary Fig. 8k** and **Supplementary Table 6**). The fragments b_1-b_{10} were similar, while the fragments y_1-y_{11} exhibited a 14 Da difference to brassicapeptin A. These differences suggested that the amino acid residues from position 19 to 22 of the cyclic substructure in brassicapeptin C were different. A proposed sequence of Gly_{19}-Dab_{20}-Ser_{21}-Ile_{22} was supposed based on the 14 Da difference. The molecular formula of brassicapeptin D was suggested to be $C_{95}H_{159}N_{23}O_{26}$, which is identical to brassicapeptin C, based on the two double-charged ion peaks $[M+2H]^{2+}$ at *m/z* 1020.0997 and $[M+Na+H]^{2+}$ at *m/z* 1031.0908 (**Supplementary Fig. 8l**). However, the fragments y_1-y_{11} of brassicapeptin D were similar, while the fragments b_1-b_{10} exhibited a 14 Da difference, when compared the HR-ESI-MS/MS data of brassicapeptin A (**Supplementary Fig. 8l** and **Supplementary Table 6**). This suggests the same amino acid residues from position 3 to 22 (Ala_3-Leu_4-Ala_5-Val_6-Ile_7-Dhb_8-Gly_9-Val_{10}-Leu_{11}-Dha_{12}-Ala_{13}-Ala_{14}-Ala_{15}-Val_{16}-*cyclo*(Thr_{17}-Dhb_{18}-Ala_{19}-Dab_{20}-Ser_{21}-Ile_{22}) except for the fatty acid chain and the first two amino acid residues, which supposed to be $C_6H_{11}O$-Dhb_1-Gly_2 based on the 14 Da difference. We were not able to assign the substructure of the amino acid residues from position 19 to 22 and the first two amino acid residues for brassicapeptin D based on NMR data or Marfey's analysis, since we could not isolate these minor variants. Brassicapeptins A-D are new cyclic lipopeptides containing 22 amino acid residues, which show similarity to previously described syringopeptins (**Supplementary Fig. 9**)

Chapter 5. Publication 4

Mono- and Dimeric chromone derivatives isolated from fungus *Palmiascoma qujingense* ST006189.

Lei Wang, Sergei Ivlev, Yang Liu and Till F. Schäberle

(in preparation)

In this project it was aimed to isolate and identify new chromone derivatives from the culture of *Palmiascoma qujingense* ST006189. Preliminary data suggested the presence of new natural products in ths strain. Therefore, an OSMAC approach was used, aiming at enhancing the chemical diversity of *P. qujingense* ST006189. The structures of the isolated secondary metabolites were elucidated by 1D, 2D NMR spectroscopy and by HR-ESI-MS, as well as by X-ray crystallographic analyses. In summary, HR-ESI-MS-guided isolation yielded four new monomeric chromone derivatives and three new dimeric chromone derivatives, together with 3 known compounds.

Chromone derivatives are a group of oxygen-containing heterocyclic compounds bearing a benzo-γ-pyrone skeleton (Mohsin et al., 2020). Chromone containing natural and synthetic molecules are well known for their diversity of pharmacological properties, such as anticancer, antiviral, antibacterial, antifungal, anti-inflammatory, antiallergenic, antioxidant, antimalarial and neuroprotective (Mohsin et al., 2020). These derivatives play an important role in medicinal chemistry and can be considered a privileged structure for drug discovery due to their synthetic accessibility and structural diversity (Reis et al., 2017).

The genus *Palmiascoma* was first introduced by Liu et al. in 2015 (Liu et al., 2015). A species of this genus, i.e. *P. qujingense*, was reported as a pathogenic fungi, which can cause branch blight on Juglans regia (Wang et al., 2022). Up to now, there is no report about natural products produced by this genus. In a continuous effort to search for new bioactive molecules, we first studied the secondary metabolites from *P. qujingense*. LC-MS analysis revealed that *P. qujingense* ST006189 contains a variety of chromone derivatives. Herein, we present the isolation and structure elucidation of chromone derivatives from *P. qujingense* ST006189.

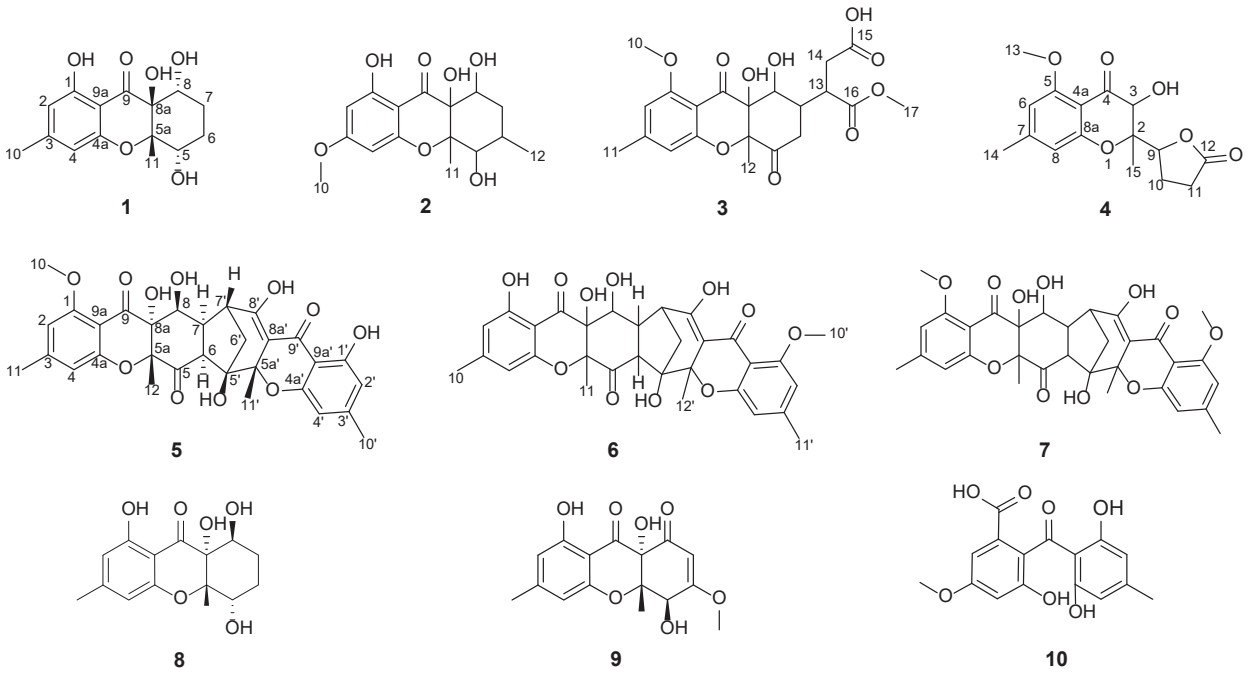

Figure 5A. Structures of compounds **1**–**10**.

Results

Palmiascoma qujingense ST006189 was cultivated at 28 °C and 140 rpm for 26 days. It was subsequently extracted with EtOAc to yield 29.89 g of crude extract. The crude extract was subjected to chromatographic purification, using reversed phase flash, followed by semipreparative high-performance liquid chromatography (HPLC) to yield four new monomeric chromone derivatives (**1**-**4**) and three new dimeric chromone derivatives (**5**-**7**), together with 3 known compounds (**8**-**10**).

Compound **1** was obtained as s a white amorphous powder. The HRESIMS spectrum exhibited a prominent ion peak at *m/z* 295.1179 $[M+H]^+$ consistent with the molecular formula $C_{15}H_{18}O_6$, accounting for 7 degrees of unsaturation. The ^{13}C NMR spectrum of 1 (**Table 5A**) displayed signals for one carbonyl carbon at δ_C 202.2, six aromatic carbons at δ_C 160.5, 160.2, 149.65, 108.9, 108.1 and 107.2 of which two were oxygenated (δ_C 160.5 and 160.2), four oxygenated carbons at δ_C 83.2, 76.6, 71.7 and 70.9, two methylene carbons at δ_C 28.1 and 24.6, and two methyl carbons at δ_C 22.0 and 17.0. The ^1H NMR spectroscopic data showed the presence of four hydroxy protons at δ_H 11.53 (1H, s), 5.73 (1H, s), 4.75 (1H, s) and 4.70 (1H, s), two aromatic protons at δ_H 6.23 (1H, s) and 6.22 (1H, s), two oxymethine protons at δ_H 3.64 (1H, s) and 3.59 (1H, dd), four methylene protons at δ_H 2.14 (1H, q), δ_H 1.90 (1H, t), δ_H 1.57 (1H, dd) and δ_H 1.49 (1H, dd), and two methyl groups at δ_H 2.22 (3H, s) and 1.26 (3H, s) (**Table 5A**). In HMBC spectrum, one hydroxy proton (δ_H 11.53) was assigned to be linked to C-1 based on its correlations to C-1 (δ_C 160.2), C-2 (δ_C 108.1) and C-9a (δ_C 107.2) (**Figure 5B**). One methyl group (δ_H 2.22) was located at C-3 in the aromatic ring due to the HMBC correlations from H-10 to C-3 (δ_C 149.5), C-2 and C-4 (**Figure 5B**). The above NMR data established a 1,2,3,5-tetrasubstitued benzene moiety (ring A). the HMBC correlations from H-2 and H-4 to C-9, and the chemical shift of C-4a at δ_C 160.5 established a γ -pyrone ring (ring B) in the structure (**Figure 5B**). The above spectroscopic data accounted for six degrees of unsaturation, and the remaining one degree of unsaturation were represented by a bicyclic carbon skeleton. Further COSY correlations between OH-8 (δ_H 4.70)/H-8 (δ_H 3.64), H-8/H-7 (δ_H 1.90 and 1.57), H-7/H-6 (δ_H 2.14 and 1.49), H-6/H-5 (δ_H 3.59), and H-5/OH-5 (δ_H 4.75), together with the HMBC correlations from H-11 (δ_H 1.26) to C-5 (δ_C 70.9), C-5a (δ_C 83.2) and C-8a (δ_C 76.6), from H-5 to C-11 (δ_C 17.0), C-6 (δ_C 24.6), C-7 (δ_C 28.1) and C-5a (δ_C 83.2), from H-8 to C-5a, C-8a and C-6, and from both H-6b (δ_H 1.49) and H-7b (δ_H 1.57) to C-5 and C-8 (δ_C 71.7) (**Figure 5B**), established a 1,2,3,4-tetrasubstitued cyclohexane moiety (ring

C) with one methyl substituent at C-5a and three hydroxy groups at C-5, C-8 and C-8a, respectively. Rings A and C were further determined to be linked via the ketone C-9 and an ether linkage between C-4a and C-5a (ring B), as deduced by HMBC correlations from H-8 to C-9 (**Figure 5B**). The relative configuration of **1** was established on the basis of the NOESY spectrum. The NOESY correlations between OH-8a (δ_H 5.73)/H-5, H-11/H-5 and H-11/H-8 suggested that H-5, H-8, H-11 and OH-8a were on the same face of the ring, while OH-5 and OH-8 were on the opposite side (**Figure 5C**). The absolute configuration of **1** was determined as a (5*S*,5a*S*,8*R*,8a*S*) configuration by single-crystal X-ray diffraction analysis (**Figure 5D**). Thus, the structure of **1** was elucidated, representing a new chromone derivative, and named as palmiachromone A.

Table 5A. ^{1}H (700 MHz) and ^{13}C NMR (175 MHz) data of compounds **1** and **2**.

Position	1		2	
	δ_C	δ_H, multi (*J* in Hz)	δ_C	δ_H, multi (*J* in Hz)
1	160.2, C		163.5, C	
2	108.1, CH	6.23, s	93.8, CH	6.01, d (2.27)
3	149.5, C		167.1, C	
4	108.9, CH	6.22, s	94.2, CH	5.94, d (2.76)
4a	160.5, C		160.0, C	
5	70.9, CH	3.59, dd (11.7, 3.5)	68.9, CH	4.35, t (4.70)
5a	83.2, C		85.5, C	
6	24.6, CH_2	2.14, q (12.0); 1.49, dd (12.3, 3.4)	33.2, CH	2.13 [a], m
7	28.1, CH_2	1.90, t (13.9); 1.57, dd (13.9, 2.2)	32.2, CH_2	2.13 [a], m 1.55, dd (12.6, 2.1);
8	71.7, CH	3.64, s	67.1, CH	4.27, d (2.1)
8a	76.6, C		74.9, C	
9	202.2, C		195.3, C	
9a	107.2, C		101.4, C	
10	22.0, CH_3	2.22, s	55.6, OCH_3	3.78, s
11	17.0, CH_3	1.26, s	15.5, CH_3	1.45, s
12			15.1, CH_3	1.13, d (7.4)
13				
14				
15				
1-OH		11.53, s		11.73, s
3-OH				
5-OH		4.75, s		4.90, d (4.5)
8-OH		4.70, s		4.84, d (4.7)
8a-OH		5.73, s		5.95, s

Compound **2** was obtained as s a white amorphous powder. The HR-ESI-MS spectrum exhibited a prominent peak $[M+H]^+$ at *m/z* 325.1284 consistent with the molecular formula $C_{16}H_{20}O_7$. Detailed analysis of the 1D and 2D NMR spectra revealed a same molecular skeleton as compound **1** (**Table 5A**), except a methoxy group (δ_C 55.6) instead of methyl group at C-3, and the appearance of an additional methyl group (δ_C 15.1) at C-6 in compound **2**. These differences were confirmed

by HMBC correlations from H-10 (δ_H 3.78) to C-3 (δ_C 167.1), from H-12 (δ_H 1.13) to C-5 (δ_C 68.9), C-6 (δ_C 33.2) and C-7 (δ_C 32.2), as well as by COSY correlations between H-12/H-6 (δ_H 2.13), H-6/H-5 (δ_H 4.35), and H-6/H-7 (δ_H 1.55) (**Figure 5B**). The relative configuration of **2** was established on the basis of the NOESY spectrum, the NOESY correlations observed between H-11 (δ_H 1.45)/H-12, OH-8a (δ_H 5.95)/H-11, OH-8a /H-5 and OH-8/H-8 ((δ_H 4.27) suggested that H-5, H-8, H-11, H-12 and OH-8a were on the same face of the ring, while H-6, OH-5 and OH-8 were on the opposite side (**Figure 5C**), therefore compound **2** was named as palmiachromone B.

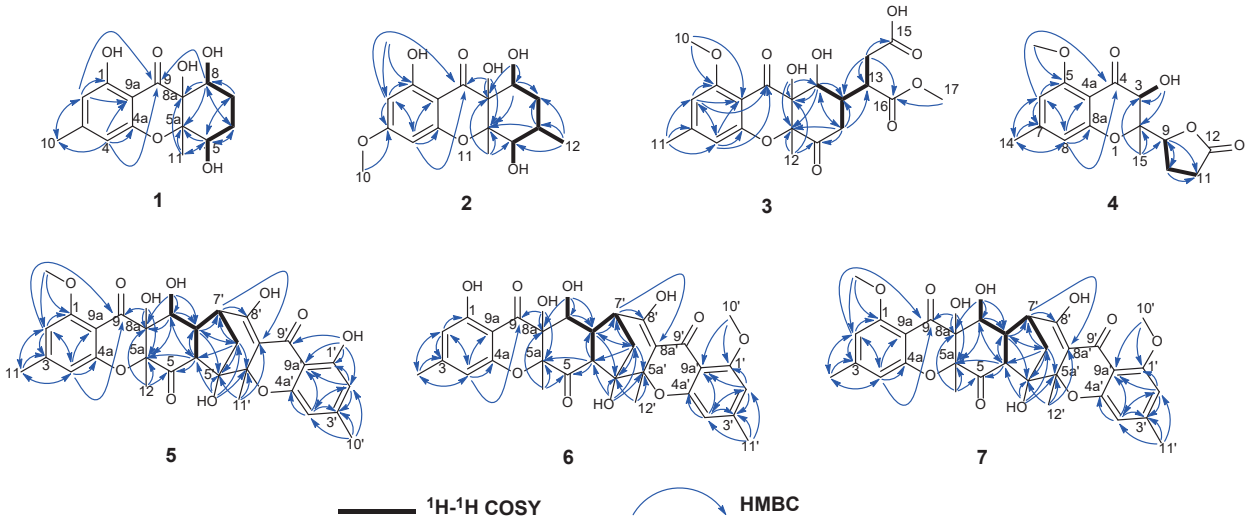

Figure 5B. Key ^{1}H-^{1}H COSY and HMBC correlations of compounds **1**–**7**.

Compound **3** was obtained as a yellow amorphous powder. The molecular formula of **3** was determined as $C_{21}H_{24}O_{10}$ on the basis of HR-ESI-MS data (*m/z* 437.1444 $[M+H]^+$). The ^{13}C NMR spectrum (**Table 5B**) displayed four carbonyl carbons at δ_C 204.9,186.6, 172.4, and 175.0, six aromatic carbons at δ_C 160.8, 158.7, 147.1, 110.4, 106.6 and 105.2, two oxygenated sp^3 quaternary carbons at δ_C 85.7 and 77.4, one oxymethine at δ_C 68.4, two methoxy carbons at δ_C 55.6 and 51.3, and two methyl carbons at δ_C 21.8 and 19.2, as well as two methylene carbons at δ_C 36.4 and 33.2, and two methine carbons δ_C 37.7 and 42.9. The ^{1}H NMR spectra (**Table 5B**) showed signals of two aromatic protons at δ_H 6.50 (1H, s) and 6.42 (1H, s), one hydroxy proton at δ_H 6.26 (1H, s), one oxymethine proton at δ_H 4.40, two methoxy protons at δ_H 3.79 and 3.58, two methyl protons at δ_H 2.28 and 1.53, two sets of methylene protons at δ_H 2.77, 2.08, 2.73, 2.57, and two sets of methine protons at δ_H 2.91 and 2.62. The above spectroscopic data revealed a similar core structure

to compound **1**. However, a methoxy group (δ_H 3.79) instead of a hydroxy group located at C-1 (δ_C 160.8) in compound **3**, which was confirmed by HMBC correlations from H-10 (δ_H 3.79) to C-1 (δ_C 160.8) and C-9a (δ_H δ_C 106.6) (**Figure 5B**), and a carbonyl group in compound **3** was formed at C-5 instead of a hydroxy group based on the HMBC correlations from both H-12 and H-6 to C-5 (δ_C 204.9) (**Figure 5B**). The remaining signals were assigned to a 2-monosubstituted monomethyl succinate moiety based on HMBC correlations from H-17 (δ_H 3.58) to C-16 (δ_C 172.4), from H-14b (δ_H 2.57) to C-13 (δ_C 42.9), C-15 (δ_C 175.0) and C-16, and from H-6a to C-13, this monomethyl succinate moiety located at C-7 based on the HMBC correlation from H-14b (δ_H 2.57) to C-7, as well as COSY correlations between H-7/H-13 (**Figure 5B**). The relative configuration of **3** was established on the basis of $^1H/^1H$ coupling constant analysis and NOESY spectrum, the observation that H-6b had a 3.6 Hz coupling with H-7 suggested that H-6b and H-7 were on the same side of the ring C, further NOESY correlations observed between H-6a/H-12, H-8/H-13, H-8/OH-8a, and between OH-8a/H-7 suggested that H-7, H-8, H-13 and OH-8a were on the same side of the ring, while H-12 and OH-8 were on the opposite side (**Figure 5C**). Thus, a name as palmiachromone C was given to compound **3**.

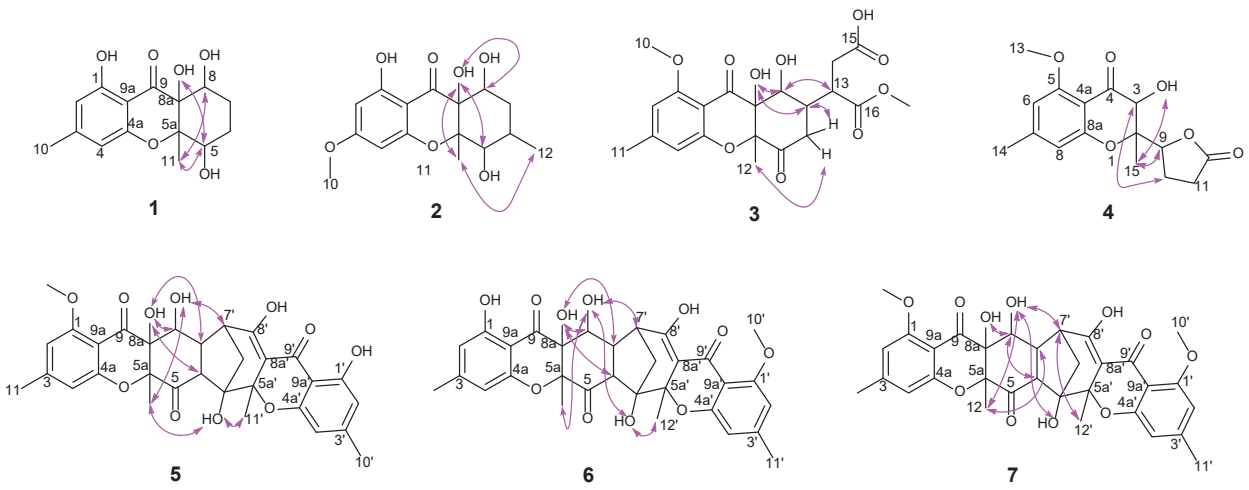

Figure 5C. Key ^1H-^1H NOESY correlations of compounds **1**–**7**.

Table 5B. ^{1}H (700 MHz) and ^{13}C NMR (175 MHz) data of compounds **3** and **4**.

Position	3		4	
	δ_C	δ_H, multi (*J* in Hz)	δ_C	δ_H, multi (*J* in Hz)
1	160.8, C			
2	105.2, CH	6.50, s	82.9, C	
3	147.1, C		71.6, CH	4.42, s
4	110.4, CH	6.42, s	190.3, C	
4a	158.7, C		106.5, C	
5	204.9, C		159.4, C	
5a	85.7, C			
6	36.4, CH_2	2.77, t (14.0) 2.08, dd (14.2, 3.6)	105.3, CH	6.51, s
7	37.7, CH	2.62, m	147.7, C	
8	68.4, CH	4.40, d (1.2)	110.1, CH	6.38, s
8a	77.4, C		159.0, C	
9	186.6, C		82.2, CH	4.70, t (7.27)
9a	106.6, C			
10	55.6, OCH_3	3.79, s	21.4, CH_2	2.45, m; 2.24, m
11	21.8, CH_3	2.28, s	27.9, CH_2	2.57, m
12	19.2, CH_3	1.53, s	176.9, C	
13	42.9, CH	2.91, m	55.8, OCH_3	3.79, s
14	33.2, CH_2	2.73, dd (16.7, 3.5) 2.57, dd (16.5, 10.2)	21.7, CH_3	2.27, s
15	175.0, C		13.5, CH_3	1.20, s
16	172.4, C			
17	51.3, OCH_3	3.58, s		
3-OH				5.72, s
8-OH		n.d.		
8a-OH		6.26, s		

Compound **4** was obtained as s a white amorphous powder. The molecular formula was deduced to be $C_{16}H_{18}O_6$ on the basis of HR-ESI-MS (*m/z* 307.1173 $[M+H]^+$). The ^{1}H NMR spectra (**Table 5B**) showed signals of two aromatic protons at δ_H 6.51 (1H, s) and 6.38 (1H, s), one hydroxy proton at δ_H 5.72 (1H, s), two oxymethine protons at δ_H 4.70 (1H, t) and 4.42 (1H, s), one methoxy group at δ_H 3.79 (3H, s), two methylene groups at δ_H 2.57 (2H, m), δ_H 2.45 (1H, m) and δ_H 2.24 (1H, m), and two methyl groups at δ_H 2.27 (3H, s) and 1.20 (3H, s). The ^{13}C NMR, HSQC and DEPT spectra (**Table 5B**) displayed 16 carbon signals including two carbonyl carbons at δ_C 190.3 and 176.9, six aromatic carbons at δ_C 159.4, 159.0, 147.7, 110.1, 106.5 and 105.3 with two oxygenated (δ_C 159.4 and 159.0), three oxygenated carbons at δ_C 82.9, 82.2 and 71.6, one methoxy carbon at δ_C 55.8, two methylene carbons at δ_C 27.9 and 21.4, and two methyl carbons at δ_C 21.7 and 13.5. Comparing the above NMR data with those of ascherlactone B from from *Aschersonia confluens* BCC53152 suggested that compound **4** was also a chromone derivative (Sadorn et al., 2020). The main differences between them were the presence of an additional hydroxy group (δ_H 5.72) at C-3 and the absence of a methoxy group at C-10 in compound **4**. These differences can be confirmed by COSY correlations between OH-3 (δ_H 5.72)/H-3 (δ_H 4.42), H-9 (δ_H 4.70)/H-10 (δ_H 2.45 and 2.24)

and H-10/H-11(δ_H 2.57), as well as by HMBC correlations from OH-3 to C-2 (δ_C 82.9) and C-3 (δ_C 71.6), from H-9 and H-11 to C-10 (δ_C 21.4), and from H-10 to C-9 (δ_C 82.2) and C-11 (δ_C 27.9) (**Figure 5B**). The ROESY correlations between H-15 (δ_H 1.20)/H-9, OH-3 (δ_H 5.72)/H-15 and between H-3/H-10 (δ_H 2.45 and 2.24) suggested that H-15, H-9 and OH-3 were on the same side, while H-3 was on the opposite side (**Figure 5B**). Thus, the structure of **4** was elucidated and named as palmiachromone D.

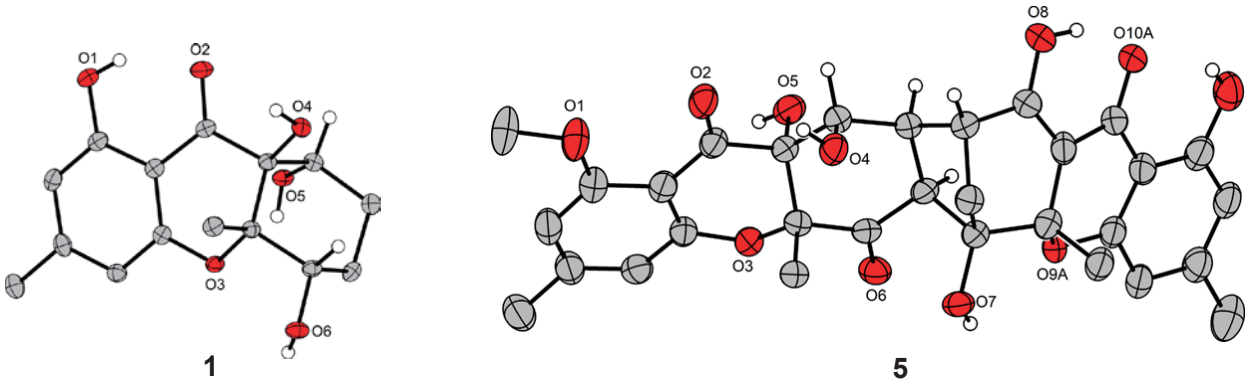

Figure 5D. X-ray structures of compounds **1** and **5**.

Compound **5** was obtained as s a colourless crystal, and its molecular formula ($C_{31}H_{30}O_{11}$) was determined by HR-ESI-MS (*m/z* 579.1860 $[M+H]^+$), requiring 17 degrees of unsaturation. The ^1H NMR and HSQC spectra of **5** exhibited one chelated enol proton at δ_H 13.22 (1H, br s), one phenolic proton at 11.22 (1H, s), three hydroxyl protons at 6.31 (1H, s), 5.65 (1H, s) and 5.14 (1H, s), four aromatic protons at δ_H 6.50 (1H, s), 6.46 (1H, s), 6.33 (1H, s) and 6.32 (1H, s), one oxymethine proton at δ_H 4.64 (1H, t), one methoxy group at δ_H 3.79 (3H, s), three methine protons at δ_H 3.65 (1H, d), 2.80 (1H, dd) and 2.77 (1H, d), one methylene group at δ_H 2.48 (1H, dd) and 2.17 (1H, d), and four methyl groups at δ_H 2.29 (3H, s), 2.26 (3H, s), 1.50 (3H, s) and 1.39 (3H, s) (**Table 5C**). The ^{13}C NMR, HSQC and DEPT spectra of **5** displayed 31 signals including four aromatic methine carbons at δ_C 110.7, 109.9, 109.3 and 105.3, one oxymethine carbon at δ_C 65.9, one methoxy carbon at δ_C 55.8, three methine carbons at δ_C 51.3, 45.5 and 42.3, one methylene carbon at δ_C 38.1, four methyl carbons at δ_C 22.0, 21.9, 20.7 and 17.8. The remaining 17 carbons were non-protonated, of which were assigned as four carbonyl carbons at δ_C 202.8, 186.5, 186.1 and 180.1, four oxygenated aromatic carbons at δ_C 160.9, 160.9, 159.1 and 158.8, five sp^2 tertiary carbons at δ_C 149.5, 147.5, 106.3, 104.5 and 104.2, and four oxygenated sp^3 quaternary carbons at

δ_C 85.0, 84.7, 82.2 and 76.6 (**Table 5C**). Comparing the above NMR data with those of compounds **1**-**4** indicated that compound **5** was also a chromone derivative, of which rings A and B showed identical chromone core structure with compound **3**, and rings F and G were identical with compound **1**, except the oxygenated sp^3 quaternary carbon at δ_C 76.6 shift to downfield at δ_C 104.2 (**Figure 5B**). Comparing the NMR data of ring C with **3**, the only difference is the methylene group at δ_H 2.77 and 2.08 changed to methine group at δ_H 3.65 in compound **5**, which is confirmed by COSY correlations between H-6 (δ_H 3.65)/H-7 (δ_H 2.80), H-7/H-8 (δ_H 4.64), and H-8/OH-8 (δ_H 5.65), together with HMBC correlations from H-6 to C-5, C-5a, C-7 (δ_C 45.5) and C-8 (δ_C 65.9), from H-8 to C-5a, C-6 (δ_C 51.3), C-7 and C-8a. The remaining two COSY correlations between H-6'a (δ_H 2.48)/H-7' (δ_H 2.77) and H-7'/H-7, together with HMBC correlations from H-7 to C-5' (δ_C 82.2), C-6' (δ_C 38.1) and C-7' (δ_C 42.3), from H-6'a to C-7'and C-5', from H-6'b (δ_H 2.17) to C-6 and C-7, and from OH-5' (δ_H 5.14) to C-5', C-6' and C-6 recommendeda five membered ring D fused with ring C in the structure. The remaining HMBC correlations from H-7' to C-8' (δ_C 180.1) and C-8a', from H-6' to C-5a', C-8' and C-8a', from OH-5' to C-5a', and from H-11' to C-5' suggested the formation of ring E.

The relative configuration of 5 was determined based on NOESY spectrum. The NOE correlations between OH-8a/H-6, OH-8a/H-7, OH-8a/H-8, OH-8/H-7', OH-8/H-12, OH-5'/H-12 and OH-5'/H-11' revealed that H-6, H-7, H-8 and OH-8a were on the same side of the ring, while OH-8, OH-5', H-7', H-12 and H-11' were on the opposite side (**Figure 5C**). These NOESY data also revealed that there is a *cis*-ring fusion between rings C and D. Moreover, the absolute configuration of compound **5** was determined as 5a*R*, 6*S*, 7*S*, 8*S*, 8a*R*, 5'*R*, 5a'*S* and 7'*R* by single-crystal X-ray diffraction analysis (**Figure 5D**). Therefore, compound **5** was elucidated as a new dimeric chromone derivative, and named as Palmiadimericchromone A.

Table 5C. ^{1}H (700 MHz) and ^{13}C NMR (175 MHz) data of compounds **5-7**.

Position	5		6		7	
	δ_C	δ_H, multi (*J* in Hz)	δ_C	δ_H, multi (*J* in Hz)	δ_C	δ_H, multi (*J* in Hz)
1	160.9, C		161.6, C		160.8, C	
2	105.3, CH	6.50, s	109.3, CH	6.36, s	105.2, CH	6.50, s
3	147.5, C		150.6, C		147.4, C	
4	110.7, CH	6.46, s	109.1, CH	6.40, s	110.6, CH	6.45, s
4a	159.1, C		157.7, C		159.1, C	
5	202.8, C		201.9, C		202.9, C	
5a	85.0, C		85.8, C		84.9, C	
6	51.3, CH	3.65, d (9.9)	51.5, CH	3.71, d (10.0)	51.2, CH	3.65, d (10.0)
7	45.5, CH	2.80, dd (9.2, 7.5)	44.6, CH	2.66, dd (9.6, 7.1)	44.7, CH	2.65, dd (9.5, 7.2)
8	65.9, CH	4.64, t (6.6)	65.4, CH	4.70, t (6.8)	66.0, CH	4.63, t (6.2)
8a	76.6, C		76.3, C		76.5, C	
9	186.5, C		194.3, C		186.5, C	
9a	106.3, C		103.7, C		106.3, C	
10	55.8, OCH_3	3.79, s	22.0, CH_3	2.27, s	55.9, OCH_3	3.81, s
11	21.9, CH_3	2.29, s	17.9, CH_3	1.42, s	21.8, CH_3	2.29, s
12	17.8, CH_3	1.39, s			17.8, CH_3	1.38, s
1-OH				11.43, br s		
8-OH		5.65, d (6.5)		6.00, d (6.9)		5.64, d (6.2)
8a-OH		6.31, s		6.70, s		6.29, br s
1’	160.9, C		159.9, C		159.9, C	
2’	109.9, CH	6.32, s	106.1, CH	6.55, s	106.1, CH	6.54, s
3’	149.5, C		147.2, C		147.2, C	
4’	109.3, CH	6.33, s	110.8, CH	6.45, s	110.8, CH	6.45, s
4a’	158.8, C		159.2, C		159.2, C	
5’	82.2, C		82.4, C		82.3, C	
5a’	84.7, C		83.7, C		83.8, C	
6’	38.1, CH_2	2.48, dd (12.3, 4.2) 2.17, d (12.3)	37.5, CH_2	2.46, dd (12.5, 4.2) 2.18, d (12.3)	37.5, CH_2	2.45, dd (12.4, 4.1) 2.16, d (12.4)
7’	42.3, CH	2.77, d (4.1)	45.2, CH	2.76, d (4.1)	45.3, CH	2.74, d (4.0)
8’	180.1, C		191.9, C		192.2, C	
8a’	104.2, C		104.2, C		104.2, C	
9’	186.1, C		175.7, C		175.6, C	
9a’	104.5, C		105.7, C		105.8, C	
10’	21.9, CH_3	2.26, s	55.9, OCH_3	3.81, s	55.7, OCH_3	3.79, s
11’	20.7, CH_3	1.50, s	21.9, CH_3	2.32, s	21.9, CH_3	2.32, s
12’			19.4, CH_3	1.44, s	19.5, CH_3	1.44, s
1’-OH		11.22, s				
5’-OH		5.14, s		5.19, s		5.07, br s
8’-OH		13.22, br s		15.62		n.d.

The molecular formula of compound **6**, $C_{31}H_{30}O_{11}$, which was determined by HR-ESI-MS (*m/z* 579.1863 $[M+H]^+$), was identical with compound **5**. The ^{1}H and ^{13}C NMR data of compound **6** were close similar to those of compound **5** (**Table 5C**), suggesting a dimeric chromone derivative skeleton for **6**. The main difference of the NMR data between them was that the methoxy group (OCH_3-1, δ_H 3.79) and the aromatic hydroxy group (OH-1’, δ_H 11.22) in **5** was replaced by an aromatic hydroxy group (OH-1, δ_H 11.43) and a methoxy group (OCH_3-1’, δ_H 3.81) in **6**, respectively. This difference can be confirmed by the HMBC correlations from H-10’ to C-1’ (δ_C 159.9) and C-9a’ (δ_C 105.7) (**Figure 5B**). The NOESY correlations between OH-8/H-7’, OH-8/OH-5’, OH-8/H-11, OH-5’/H-12’, OH-8a/H-6 and OH-8a/H-8 revealed that H-6, H-7, H-8 and

OH-8a were on the same side of the ring, while OH-8, OH-5', H-7', H-12 and H-11' were on the opposite side (**Figure 5B**), suggesting the same or opposite absolute configuration for compound **6**. Thus, compound **6** was elucidated and named as Palmiadimericchromone B.

Compound **7** was obtained as a white amorphous powder. The HR-ESI-MS spectrum (*m/z* 593.2016 $[M+H]^+$) indicated a 14 Da more compared to compound **5**, supporting the molecular formula of $C_{32}H_{32}O_{11}$. The NMR data of **7** revealed a close similarity to those of **5**, except for one additional methoxy group at δ_H 3.79 (OCH_3-1') linked to C-1' (**Table 5C**), which is confirmed by HMBC correlations from H-10' to C-1' (δ_C 159.9) and C-9a' (δ_C 105.8) (**Figure 5B**). The relative configuration of **7** was established on the basis of the NOESYspectrum, the NOESY correlations between OH-8/H-12, OH-8/OH-5', OH-8/H-7', H-7/H-12, H-7'/H-12', OH-8a/H-8 and H-6/H-8 suggested that H-6, H-8 and OH-8a were on the same side of the ring, while H-7, OH-8, OH-5', H-7', H-12 and H-11' were on the opposite side (**Figure 5B**). Therefore, compound **7** was also elucidated as a new dimeric chromone derivative, and named as Palmiadimericchromone C.

The known compounds (**8**–**10**) were identified as diversonol (**8**) (Siddiqui et al., 2011), blennolides L (**9**) (Maha et al., 2018) and 14-*O*-demethylsulochrin (**10**) (Du et al., 2018) by comparing their NMR data.

Compounds **1**, **2**, **4**, **5** and **7**-**10** were tested for their bioactivity against bacteria (*Escherichia coli* ATCC35218, *Staphylococcus aureus* ATCC25923, *Mycobacterium smegmatis* ATCC607 and *Mycobacterium tuberculosis* ATCC 9431") and fungi (*Candida albicans* FH2173 and *Septoria tritici* MUCL45408). Among them, only compound **5** exhibited moderate activity against *S. aureus* ATCC25923, *M. smegmatis* ATCC607 and *M. tuberculosis* ATCC 9431" with minimum inhibitory concentration (MIC) value of 32 μg/mL.

Experimental section

General Experimental Procedures

The 1D and 2D NMR spectra were recorded in DMSO-d_6 using a Bruker Avance Neo 700 MHz spectrometer equipped with a 5 mm CryoProbe Prodigy TCI (^1H,^{13}C Z-GRD) (Bruker, Ettlingen, Germany). The LC-HRMS data for all compounds were recorded on a micrOTOF-QII mass spectrometer (Bruker, Billerica, MA, USA) equipped with an ESI-source coupled to an Agilent Infinity 1290 UHPLC system using an ACQUITY UPLC BEH C18 Column, 130 Å, 1.7 μm, 2.1 mm×100 mm (Waters, Eschborn, Germany) with an ACQUITY UPLC BEH C18 VanGuard Pre-

column, 130 Å, 1.7 µm, 2.1 mm × 5 mm (Waters, Eschborn, Germany). The LC-HR-MS and MS/MS data were recorded on a quadrupole time-of-flight spectrometer (LC-QTOF maXis II, Bruker Daltonik) equipped with an electrospray ionization source in line with an Agilent 1290 infinity LC system (Agilent). C18 RP-UHPLC (ACQUITY UPLC BEH C18 column [130 Å, 1.7 µm, 2.1 × 100 mm]) was performed at 45°C with the following linear gradient: 0 min: 95% A; 0.30 min: 95% A; 18.00 min: 4.75% A; 18.10 min: 0% A; 22.50 min: 0% A; 22.60 min: 95% A; 25.00 min: 95% A (A: H2O, 0.1% HCOOH; B: CH3CN, 0.1% HCOOH; flow rate: 0.6 mL/min). Mass spectral data were acquired using a 50 to 2,000 m/z scan range at 1 Hz scan rate. MS/MS experiments were performed with 6 Hz and the top five most intense ions in each full MS spectrum were targeted for fragmentation by higher-energy collisional dissociation at 25 eV or 55 eV using N2 at 10–2 mbar. Precursors were excluded after two spectra, released after 0.5 min and reconsidered if the intensity of an excluded precursor increased by factor 1.5 or more. Shimadzu LC-20A HPLC system (Shimadzu Deutschland GmbH, Duisburg, Germany) was used for HPLC analysis. The analytical column (250×4.6 mm) employed was prefilled with EC Nucleodur C18 (Gravity-SB, 5 μm; Macherey-Nagel, Düren, Germany), and the following gradient was used (0.1% formic acid in ACN, 0.1% formic acid in H_2O): 0 min (10% ACN); 10 min (10% ACN); 40 min (100% ACN); 50 min (100% ACN). The Semi-preparative HPLC was performed using Shimadzu LC-20A HPLC system (Shimadzu Deutschland GmbH, Duisburg, Germany) or Hewlett-Packard Agilent 1100 HPLC System (Agilent Technologies, CA, USA), The semi-preparative column (VP 250/10 Nucleodur C18 Gravity-SB, 5 μm; Macherey-Nagel, Düren, Germany) was used with a mixture of CAN (0.1% formic acid) and H_2O (0.1% formic acid) as mobile phases. MPLC was performed on the Interchim Puriflash 4125 chromatography system (Interchim, Montluçon, France).

OSMAC Approach

The medium used for preculture of strain *P. qujingense* ST006189 was Medium 5189 (20 g malt extract, 2 g yeast extract, 10 g glucose, 0.5 g $(NH_4)_2HPO_4$, 20 g agar, 1 L of distilled water, PH 6.0). The media used for one strain many compounds (OSMAC) approach were Medium 5189A (20 g malt extract, 2 g yeast extract, 10 g glucose, 0.5g $(NH_4)_2HPO_4$, 1 L of distilled water, PH 6.0), Medium 5189B (100 g rice in 110 mL Medium 5189A), Medium 5367A (24 g potato dextrose broth, 2 g yeast extract, 1 L of distilled water, PH 5.1), Medium 5367B (100 g rice in 110 mL

Medium 5367A), Medium 5332A (5 g soluble starch, 5 g corn starch, 10 g glucose, 5 g yeast extract, 7.5 g cornsteep liquid, 2 g $CaCO_3$, 1 L of distilled water, PH 6.0) and Medium 5332B (100 g rice in 110 mL Medium 5332A). The pre-culture was incubated at 28 ºC for 7 days, a volume of 1 m^3 of this preculture was used to inoculate in 300 mL flasks that contained 100 mL media for OSMAC approach at 28 ºC and 140 rpm. An amount of 5 mL of medium was harvested and extracted with EtOAc every 3 days after the sixth day of cultivation and analysed by UPLC−HR-MS/MS. The results of the OSMAC approach showed that most chromone derivatives was observed from the extract of 26 days fermentation in Medium 5367A.

Fermentation, Extraction and Isolation

A total volume of 38 L of fermentation was performed in 220 flasks (300 mL) that contained 100 mL Medium 5367A and 20 flasks (2 L) that contained 800 mL Medium 5367A and 28 ºC and 140 rpm. The fermentation was harvested after 26 days and extracted with EtOAc with the volume ratio of 1:1 three times, thereby generating 29.89 g of crude extract. The EtOAc crude extract was fractionated by reversed-phase flash chromatography (Interchim Puriflash 4125 chromatography system with a Puriflash C18-AQ30 μm F0120 column) with an elution gradient starting from 10% MeOH/H_2O to 100% MeOH over 1.5 h and yielded 30 fractions (Fr. 1−30). Fractions 8-10 (Fr. 8−10) was further subjected to reversed-phase flash chromatography (Interchim Puriflash 4125 chromatography system with a Puriflash C18-HP30 μm F0080 flash column) using an elution gradient from 10%ACN/H_2O to 100% ACN over 2 h and yielded 30 subfractions (Frr. (8-10)-1-30). Subfraction Frr. (8-10)-4 was further purified by semipreparative HPLC (0−1 min, 20% ACN; 1−18 min, gradient increased from 20% to 37% ACN; 18−20 min, gradient increased from 37% to 95% ACN; 20−28 min, 95% ACN) to yield compound **1** (9.7 mg, t_R = 15.5 min). Subfraction Frr. (8-10)-5 was purified by semipreparative HPLC (0−1 min, 15% ACN; 1−41 min, gradient increased from 15% to 42% ACN; 41−42 min, gradient increased from 42% to 95% ACN; 42−50 min, 95% ACN) to yield compound **2** (13.5 mg, t_R = 18.9 min), compound **3** (2 mg, t_R = 21.8 min), compound **9** (10.0 mg, t_R = 17.2 min) and compound **10** (7.0 mg, t_R = 19.8 min). Subfraction Frr. (8-10)-7 was purified by semipreparative HPLC (0−1 min, 17% ACN; 1−45 min, gradient increased from 17% to 35% ACN; 45−46 min, gradient increased from 35% to 95% ACN; 46−42 min, 95% ACN) to yield compound **4** (3.5 mg, t_R = 44.5 min) and compound **8** (3 mg, t_R = 39.1 min). Fractions 16-19 (Fr. 16−19) was further subjected to reversed-phase flash chromatography

(Interchim Puriflash 4125 chromatography system with a Puriflash C18-HP30 μm F0080 flash column) using an elution gradient from 10%ACN/H_2O to 100% ACN over 2 h and yielded 20 subfractions (Frr. (16-19)-1-20). Subfraction Frr. (16-19)-6 was purified by semipreparative HPLC (0−1 min, 35% ACN; 1−30 min, gradient increased from 35% to 64% ACN; 30−31 min, gradient increased from 64% to 95% ACN; 31−38 min, 95% ACN) to yield compound **5** (32.0 mg, t_R = 28.6 min), compound **6** (1.5 mg, t_R = 26.2 min) and compound **7** (1.1 mg, t_R = 21.6 min).

Palmiachromone A (**1**): white amorphous powder; the ^{1}H NMR (DMSO-*d*$_6$, 700 MHz) and ^{13}C NMR (DMSO-*d*$_6$, 175 MHz) data are given in **Table 4A**; HR-ESI-MS m/z 295.1176 $[M+H]^+$ (calculated for $C_{15}H_{19}O_6$, 295.1176, Figure S1).

Palmiachromone B (**2**): white amorphous powder; the ^{1}H NMR (DMSO-*d*$_6$, 700 MHz) and ^{13}C NMR (DMSO-*d*$_6$, 175 MHz) data are given in **Table 4A**; HR-ESI-MS m/z 325.1284 $[M+H]^+$ (calculated for $C_{16}H_{21}O_7$, 325.1282, Figure S8).

Palmiachromone C (**3**): yellow amorphous powder; the ^{1}H NMR (DMSO-*d*$_6$, 700 MHz) and ^{13}C NMR (DMSO-*d*$_6$, 175 MHz) data are given in **Table 4B**; HR-ESI-MS m/z 437.1444 $[M+H]^+$ (calculated for $C_{21}H_{25}O_{10}$, 437.1442, Figure S16).

Palmiachromone D (**4**): white amorphous powder; the ^{1}H NMR (DMSO-*d*$_6$, 700 MHz) and ^{13}C NMR (DMSO-*d*$_6$, 175 MHz) data are given in **Table 4B**; HR-ESI-MS m/z 307.1173 $[M+H]^+$ (calculated for $C_{16}H_{19}O_6$, 307.1176, Figure S24).

Palmiadimericchromone A (**5**): colourless crystal; the ^{1}H NMR (DMSO-*d*$_6$, 700 MHz) and ^{13}C NMR (DMSO-*d*$_6$, 175 MHz) data are given in **Table 4C**; HR-ESI-MS m/z 579.1860 $[M+H]^+$ (calculated for $C_{31}H_{31}O_{11}$, 579.1861, Figure S32).

Palmiadimericchromone B (**6**): white amorphous powder; the ^{1}H NMR (DMSO-*d*$_6$, 700 MHz) and ^{13}C NMR (DMSO-*d*$_6$, 175 MHz) data are given in **Table 4C**; HR-ESI-MS m/z 579.1863 $[M+H]^+$ (calculated for $C_{31}H_{31}O_{11}$, 579.1861, Figure S40).

Palmiadimericchromone C (**7**): white amorphous powder; the ^{1}H NMR (DMSO-*d*$_6$, 700 MHz) and ^{13}C NMR (DMSO-*d*$_6$, 175 MHz) data are given in **Table 4C**; HR-ESI-MS m/z 593.2016 $[M+H]^+$ (calculated for $C_{32}H_{33}O_{11}$, 593.2017, Figure S48).

X-ray crystallographic analysis

Compound **1**: A suitable crystal of $C_{15}H_{18}O_6$ was selected under inert oil and mounted using a MiTeGen loop. Intensity data of the crystal were recorded with a STADIVARI diffractometer. The

diffractometer was operated with Cu-Kα radiation (1.54186 Å, microfocus source) and equipped with a Dectris PILATUS 300K detector. Evaluation, integration and reduction of the diffraction data was carried out using the X-Area software suite. Multi-scan and numerical absorption corrections were applied with the LANA and X-RED32 modules of the X-Area software suite. The structure was solved using dual-space methods (SHELXT-2018/2) and refined against F^2 (SHELXL-2019/1 using ShelXle interface) (Hübschle et al., 2011; Sheldrick, 2015a, 2015b). All non-hydrogen atoms were refined with anisotropic displacement parameters. The hydrogen atoms were refined using the "riding model" approach with isotropic displacement parameters 1.2 times (1.5 times for the methyl groups) of that of the preceding carbon atom. These data can be obtained free of charge from The Cambridge Crystallographic Data Centre via www.ccdc.cam.ac.uk/structures.

Compound **5**: A suitable crystal of C31H30O11 was selected under inert oil and mounted using a MiTeGen loop. Intensity data of the crystal were recorded with a STADIVARI diffractometer. The diffractometer was operated with Cu-Kα radiation (1.54186 Å, microfocus source) and equipped with a Dectris PILATUS 300K detector. Evaluation, integration and reduction of the diffraction data was carried out using the X-Area software suite. Multi-scan and numerical absorption corrections were applied with the LANA and X-RED32 modules of the X-Area software suite. The structure was solved using dual-space methods (SHELXT-2018/2) and refined against F^2 (SHELXL-2019/1 using ShelXle interface) (Hübschle et al., 2011; Sheldrick, 2015a, 2015b). All non-hydrogen atoms were refined with anisotropic displacement parameters. The hydrogen atoms were refined using the "riding model" approach with isotropic displacement parameters 1.2 times (1.5 times for the methyl groups) of that of the preceding carbon atom. A few parts of the molecules were refined disordered. The residual electron density in the solvent accessible voids could not be satisfactorily modelled and was eliminated using the SQUEEZE algorithm in the PLATON software (Spek, 2015; Spek, 2019). These data can be obtained free of charge from The Cambridge Crystallographic Data Centre via www.ccdc.cam.ac.uk/structures.

References

Du, X., Liu, D., Huang, J., Zhang, C., Proksch, P., & Lin, W. (**2018**). Polyketide derivatives from the sponge associated fungus Aspergillus europaeus with antioxidant and NO inhibitory activities. *Fitoterapia,* 130, 190-197.

Hübschle, C. B., Sheldrick, G. M., & Dittrich, B. (**2011**). ShelXle: a Qt graphical user interface for SHELXL. *Journal of applied crystallography,* 44, 1281-1284.

Liu, J. K., Hyde, K. D., Jones, E. G., Ariyawansa, H. A., Bhat, D. J., Boonmee, S., Maharachchikumbura, S. S., McKenzie, E. H., Phookamsak, R., & Phukhamsakda, C. (**2015**). Fungal diversity notes 1–110: taxonomic and phylogenetic contributions to fungal species. *Fungal diversity,* 72, 1-197.

Maha, A., Phainuphong, P., Rukachaisirikul, V., Saithong, S., Phongpaichit, S., Hadsadee, S., Jungsuttiwong, S., Preedanon, S., & Sakayaroj, J. (**2018**). Blennolide derivatives from the soil-derived fungus Trichoderma asperellum PSU-PSF14. *Tetrahedron,* 74, 5659-5664.

Mohsin, N. u. A., Irfan, M., Hassan, S. u., & Saleem, U. (**2020**). Current strategies in development of new chromone derivatives with diversified pharmacological activities: a review. *Pharmaceutical chemistry journal,* 54, 241-257.

Reis, J., Gaspar, A., Milhazes, N., & Borges, F. (**2017**). Chromone as a privileged scaffold in drug discovery: recent advances: miniperspective. *Journal of medicinal chemistry,* 60, 7941-7957.

Sadorn, K., Saepua, S., Punyain, W., Saortep, W., Choowong, W., Rachtawee, P., & Pittayakhajonwut, P. (**2020**). Chromanones and aryl glucoside analogs from the entomopathogenic fungus Aschersonia confluens BCC53152. *Fitoterapia,* 144, 104606.

Sheldrick, G. M. (**2015a**). Crystal structure refinement with SHELXL. *Acta Crystallographica Section C: Structural Chemistry,* 71, 3-8.

Sheldrick, G. M. (**2015b**). SHELXT–Integrated space-group and crystal-structure determination. *Acta Crystallographica Section A: Foundations and Advances,* 71, 3-8.

Siddiqui, I. N., Zahoor, A., Hussain, H., Ahmed, I., Ahmad, V. U., Padula, D., Draeger, S., Schulz, B., Meier, K., & Steinert, M. (**2011**). Diversonol and blennolide derivatives from the endophytic fungus Microdiplodia sp.: absolute configuration of diversonol. *Journal of natural products,* 74, 365-373.

Spek, A. L. (**2015**). PLATON SQUEEZE: a tool for the calculation of the disordered solvent contribution to the calculated structure factors. *Acta Crystallographica Section C: Structural Chemistry,* 71, 9-18.

Spek, A. L. (2019). PLATON. A Multipurpose Crystallographic Tool. Utrecht University, The Netherlands. In.

Wang, F., Zeng, Q., Lv, Y., Xu, X., Han, S., Yang, H., Li, S., Lin, T., Yang, H., & Liu, Y. (**2022**). Branch blight of Juglans regia caused by Palmiascoma qujingense in China. *Plant Disease,* 106, 2992.

Supporting Information of Publication 4

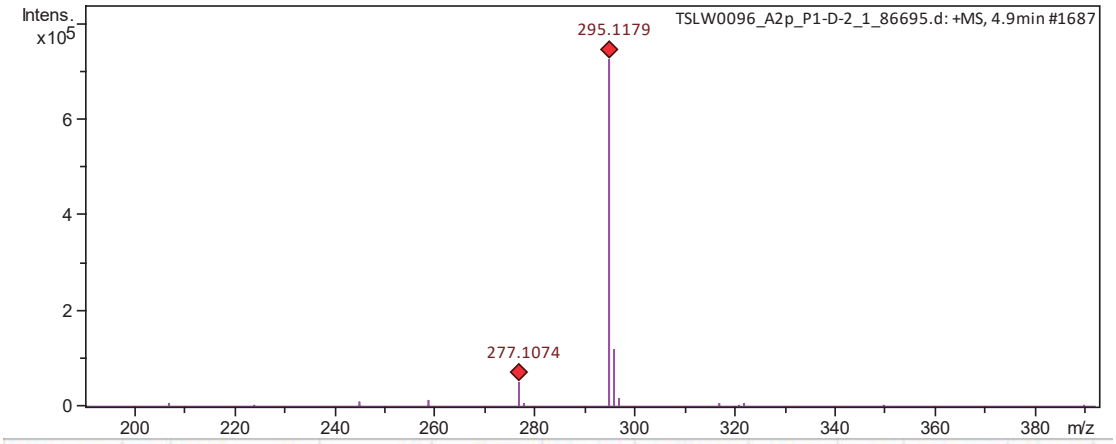

Meas. m/z	#	Ion Formula	m/z	err [ppm]	mSigma	# mSigma	Score	rdb	ei¥ Conf	N-Rule
295.1179	1	C15H19O6	295.1176	-1.1	1.5	1	100.00	6.5	even	ok
295.1179	2	C12H11N10	295.1163	-5.7	6.3	2	42.57	12.5	even	ok
295.1179	3	C16H15N4O2	295.1190	3.4	12.4	3	58.19	11.5	even	ok

Fig. S1. The HR-ESI-MS of compound **1**.

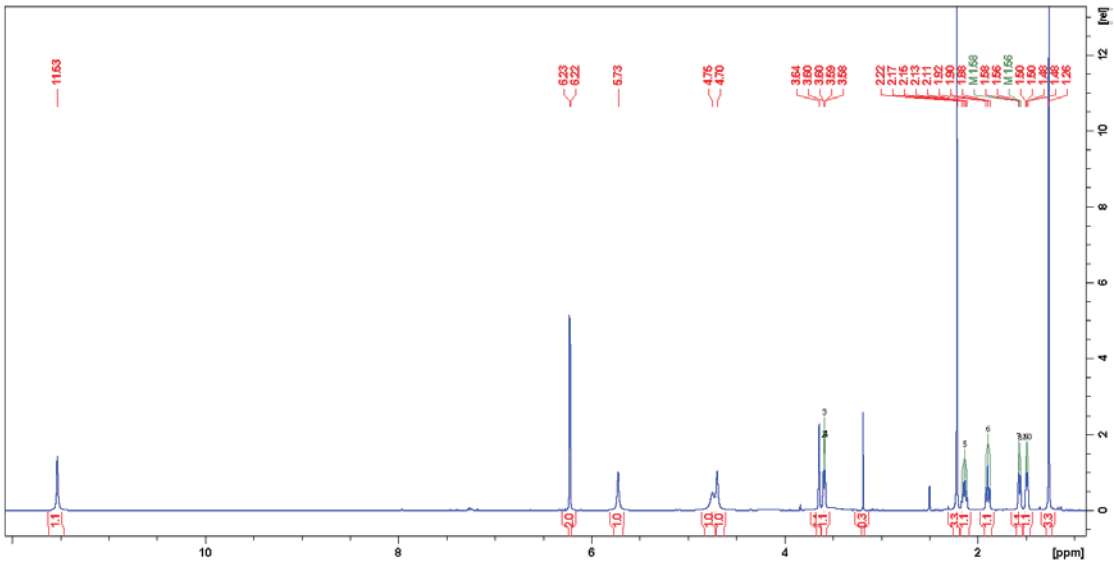

Fig. S2. ^{1}H-NMR (700 MHz, DMSO-d_6) spectrum of compound **1**.

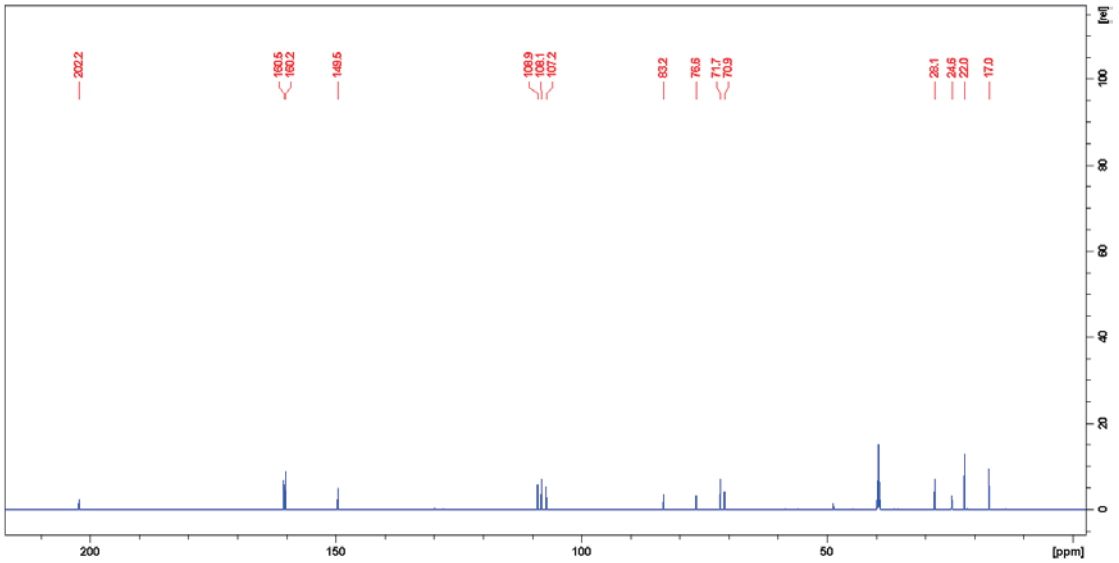

Fig. S3. The ^{13}C-NMR (175 MHz, DMSO-*d*$_6$) spectrum of compound **1**.

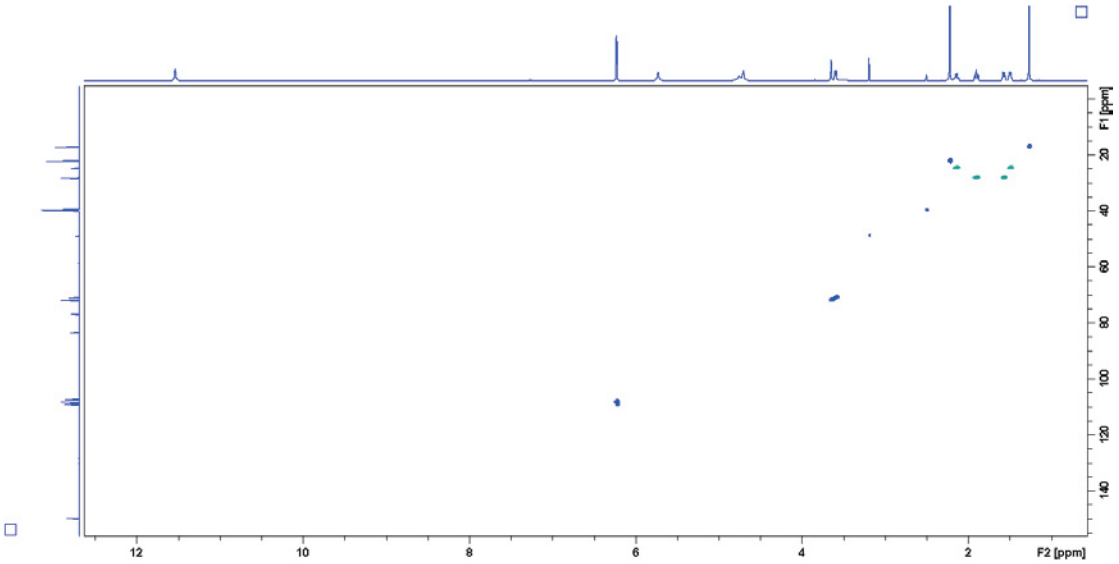

Fig. S4. The HSQC (700 MHz, DMSO-*d*$_6$) spectrum of compound **1**.

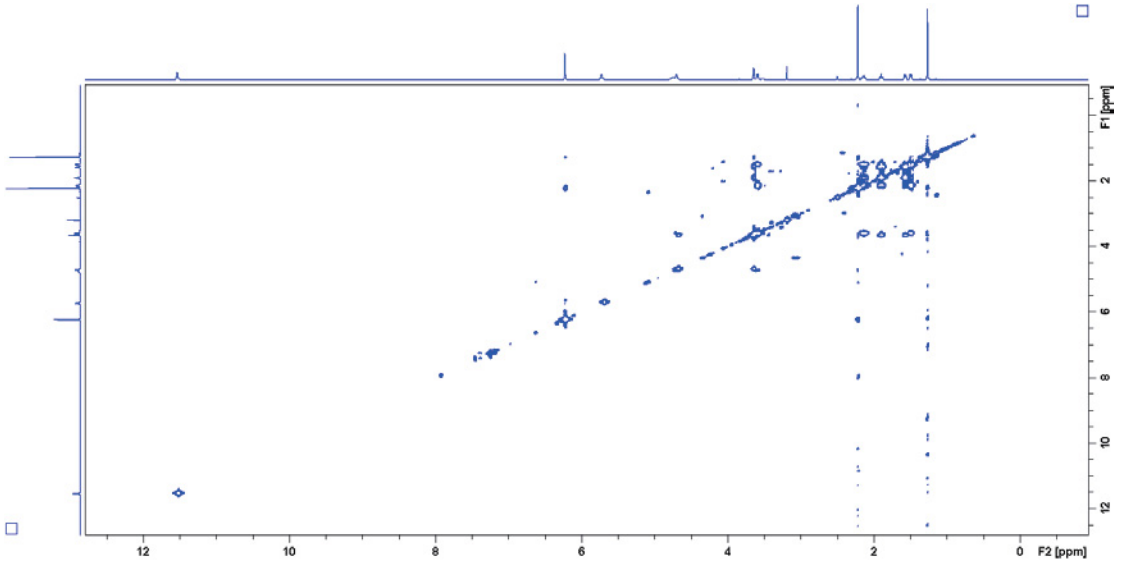

Fig. S5. The COSY (700 MHz, DMSO-d_6) spectrum of compound **1**.

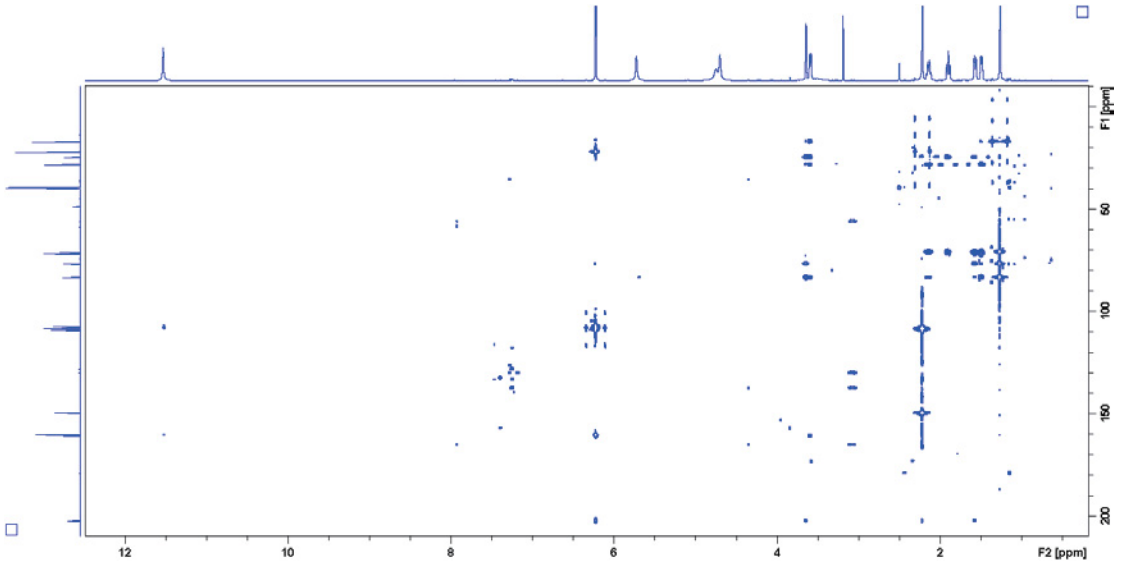

Fig. S6. The HMBC (700 MHz, DMSO-d_6) spectrum of compound **1**.

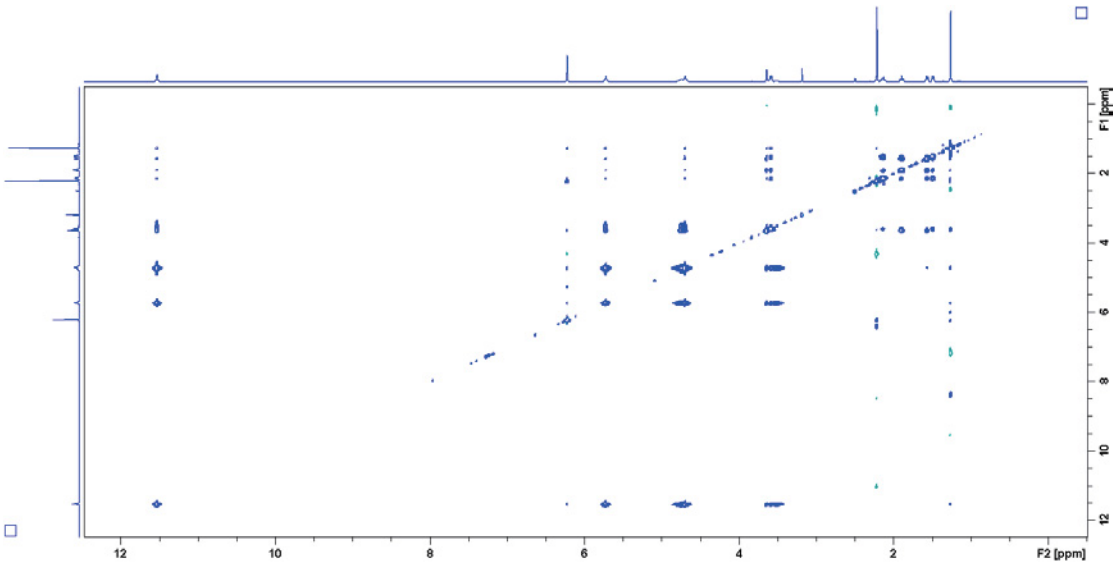

Fig. S7. The NOESY (600 MHz, DMSO-d_6) spectrum of compound **1**.

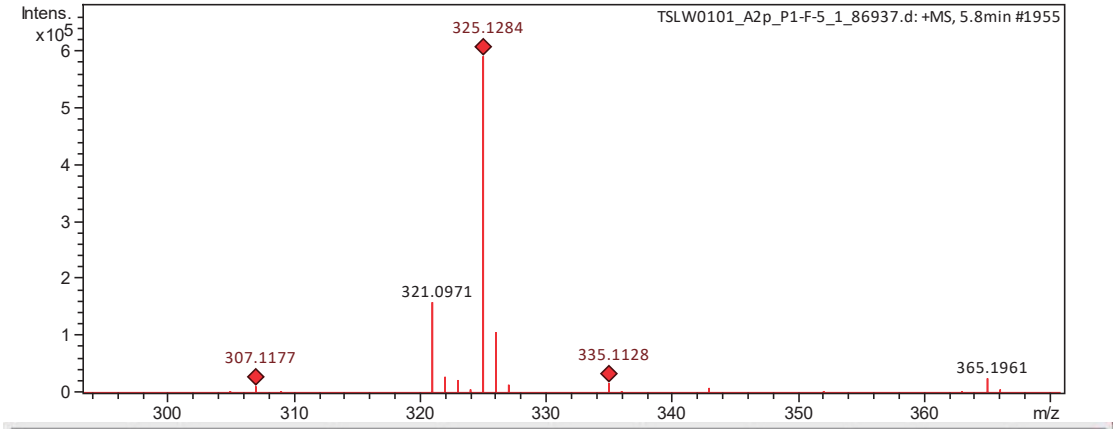

Meas. m/z	#	Ion Formula	m/z	err [ppm]	mSigma	# mSigma	Score	rdb	ei¥ Conf	N-Rule
325.1284	1	C16H21O7	325.1282	-0.7	1.1	1	100.00	6.5	even	ok
325.1284	2	C13H13N10O	325.1268	-4.9	6.1	2	43.45	12.5	even	ok
325.1284	3	C17H17N4O3	325.1295	3.4	12.9	3	52.09	11.5	even	ok
325.1284	4	C12H17N6O5	325.1255	-9.0	14.1	4	12.57	7.5	even	ok

Fig. S8. The HR-ESI-MS of compound **2**.

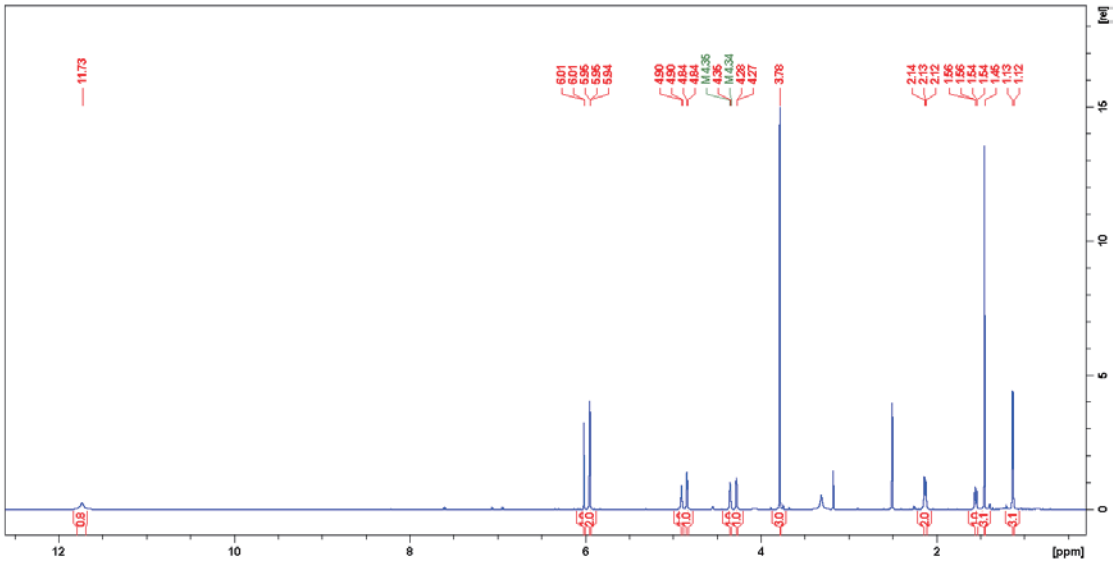

Fig. S9. ^{1}H-NMR (700 MHz, DMSO-*d*$_6$) spectrum of compound **2**.

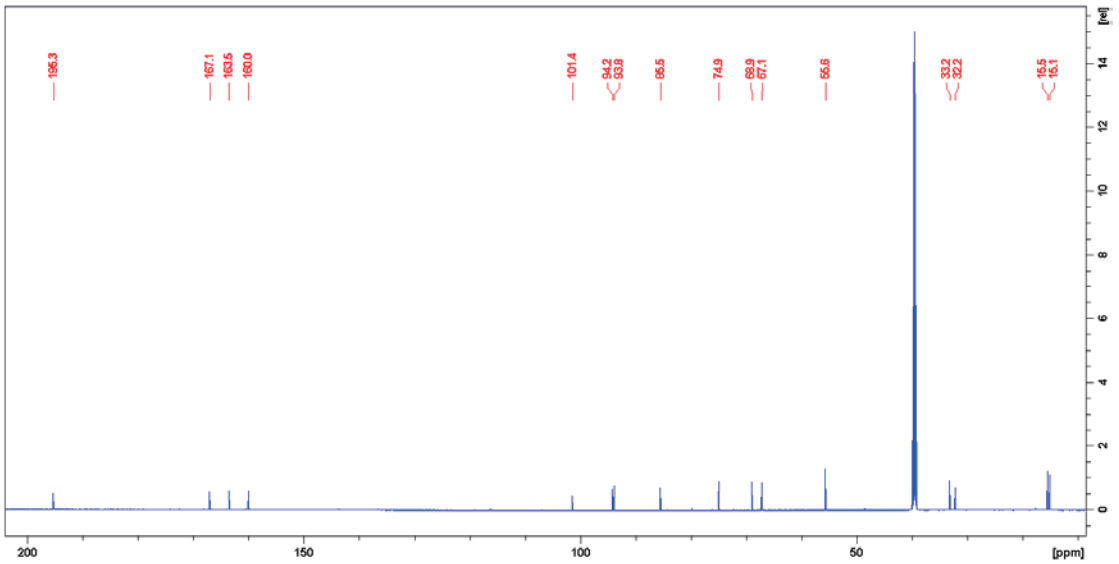

Fig. S10. The ^{13}C-NMR (175 MHz, DMSO-*d*$_6$) spectrum of compound **2**.

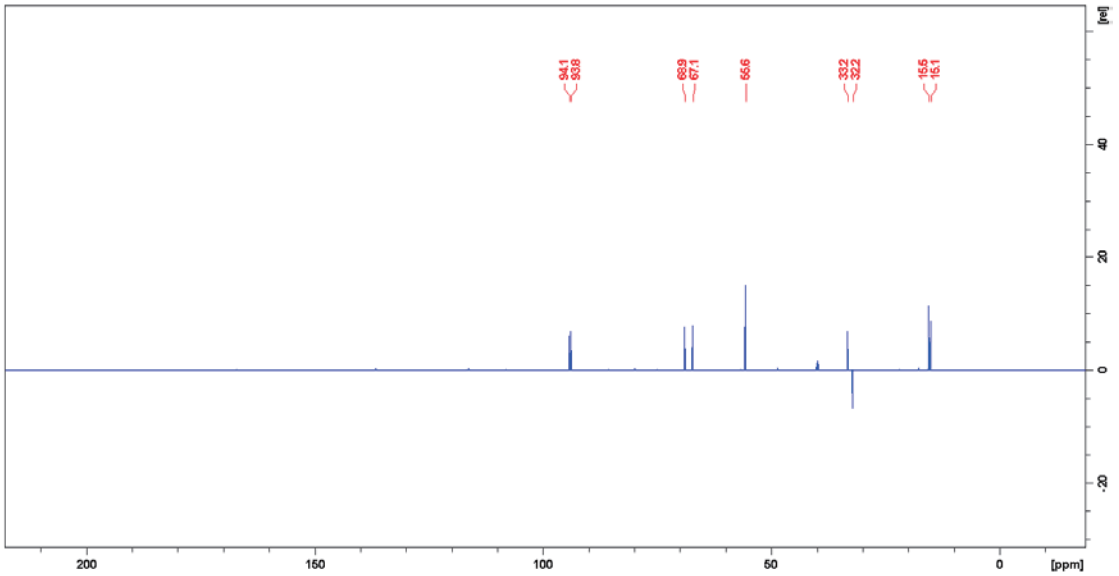

Fig. S11. The DEPT135 (175 MHz, DMSO-d_6) spectrum of compound **2**.

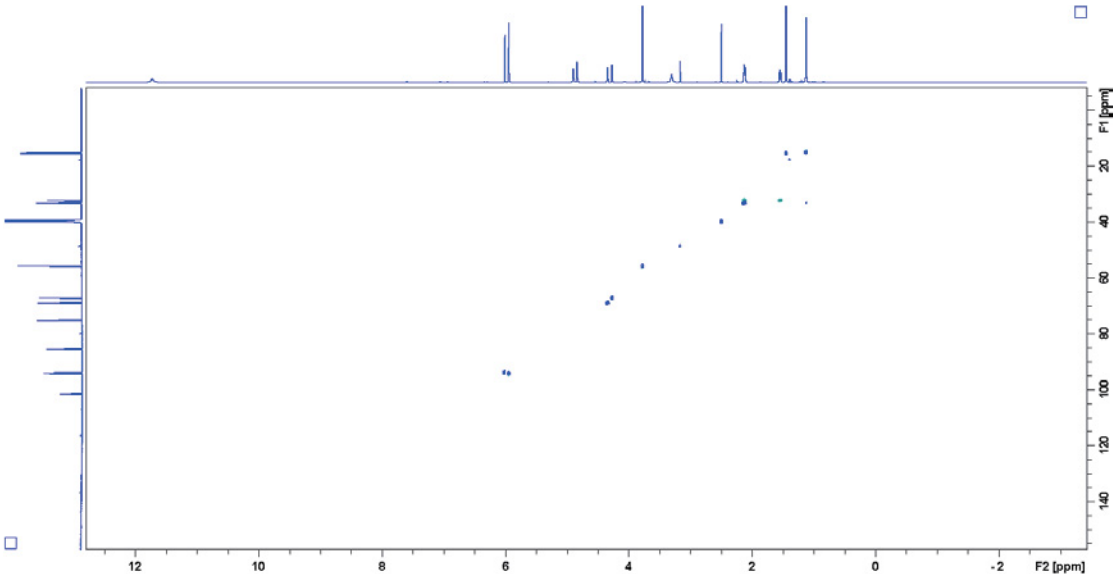

Fig. S12. The HSQC (700 MHz, DMSO-d_6) spectrum of compound **2**.

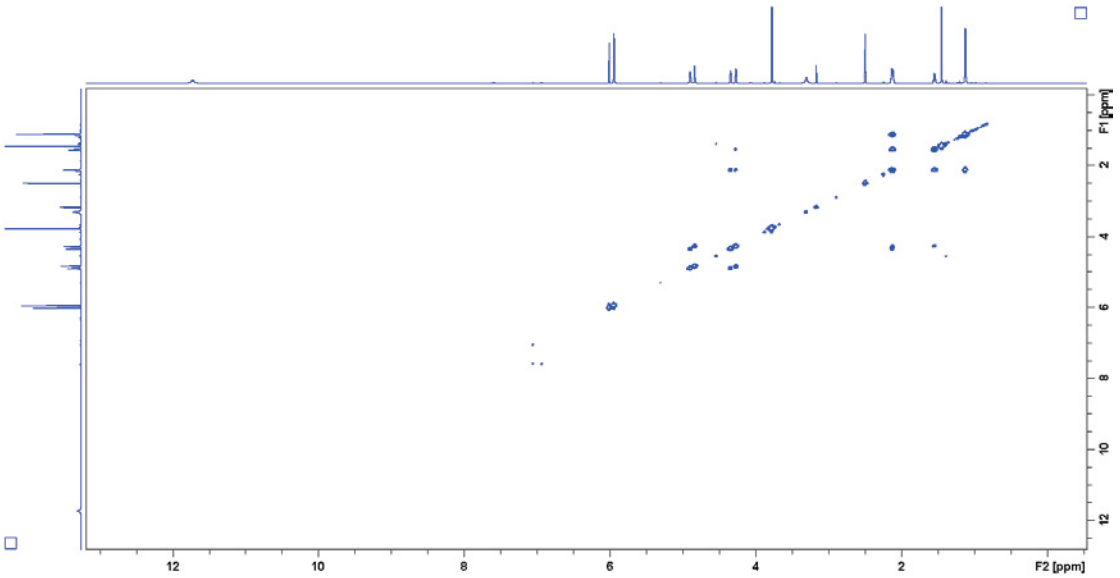

Fig. S13. The COSY (700 MHz, DMSO-d_6) spectrum of compound **2**.

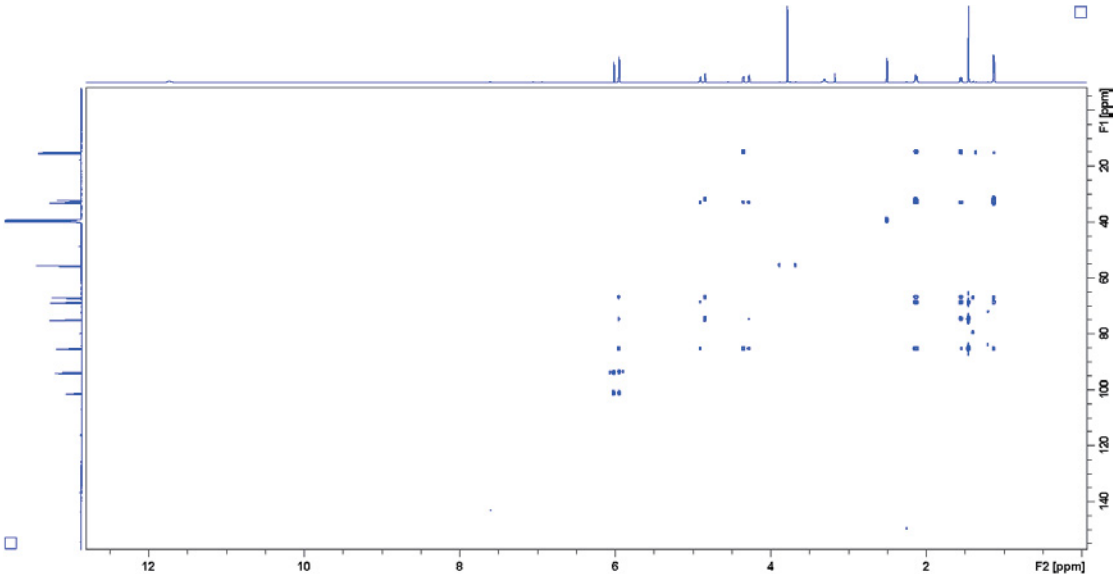

Fig. S14. The HMBC (700 MHz, DMSO-d_6) spectrum of compound **2**.

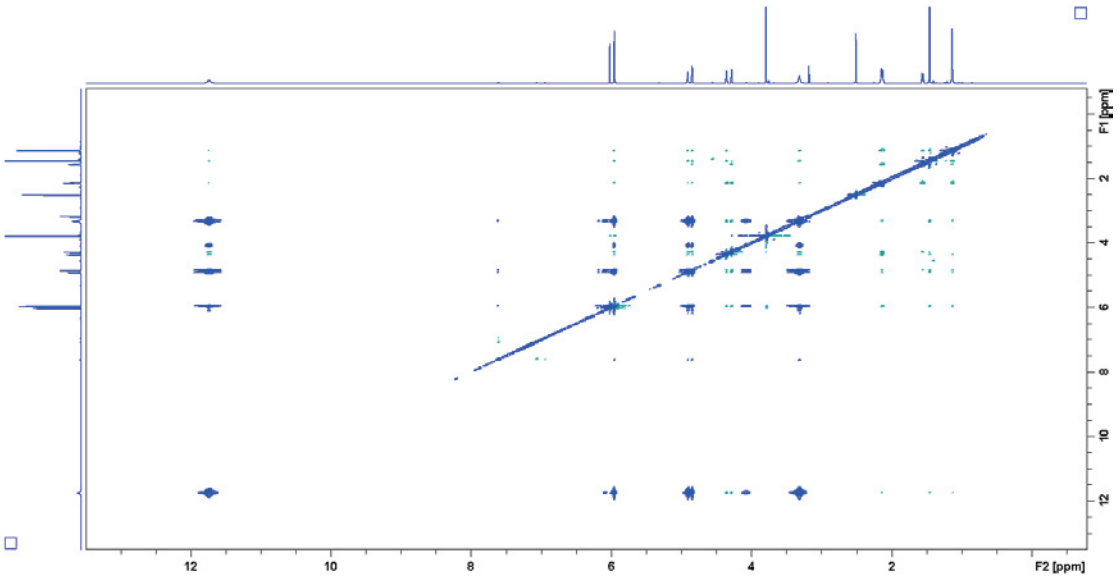

Fig. S15. The NOESY (600 MHz, DMSO-d_6) spectrum of compound **2**.

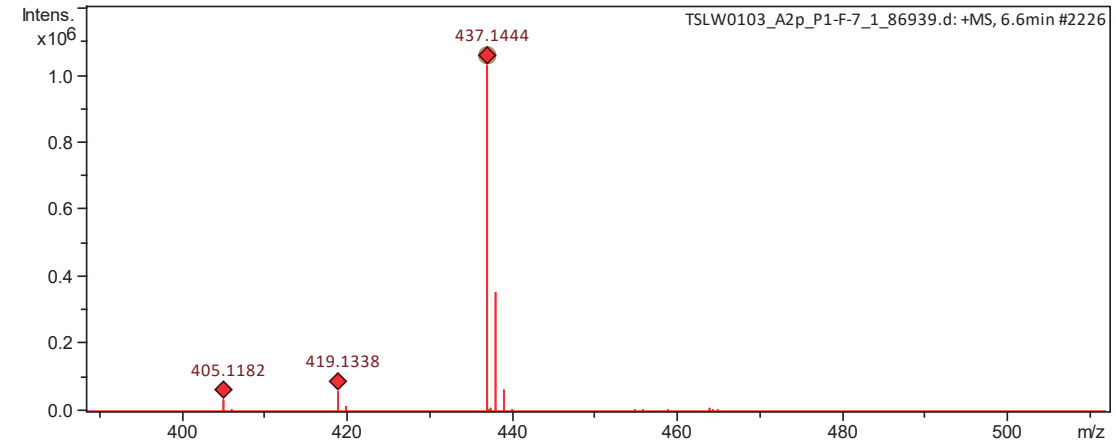

Meas. m/z	#	Ion Formula	m/z	err [ppm]	mSigma	# mSigma	Score	rdb	ei¥ Conf	N-Rule
437.1444	1	C21H25O10	437.1442	-0.5	56.7	1	100.00	9.5	even	ok
437.1444	2	C17H21N6O8	437.1415	-6.6	79.2	2	5.31	10.5	even	ok

Fig. S16. The HR-ESI-MS of compound **3**.

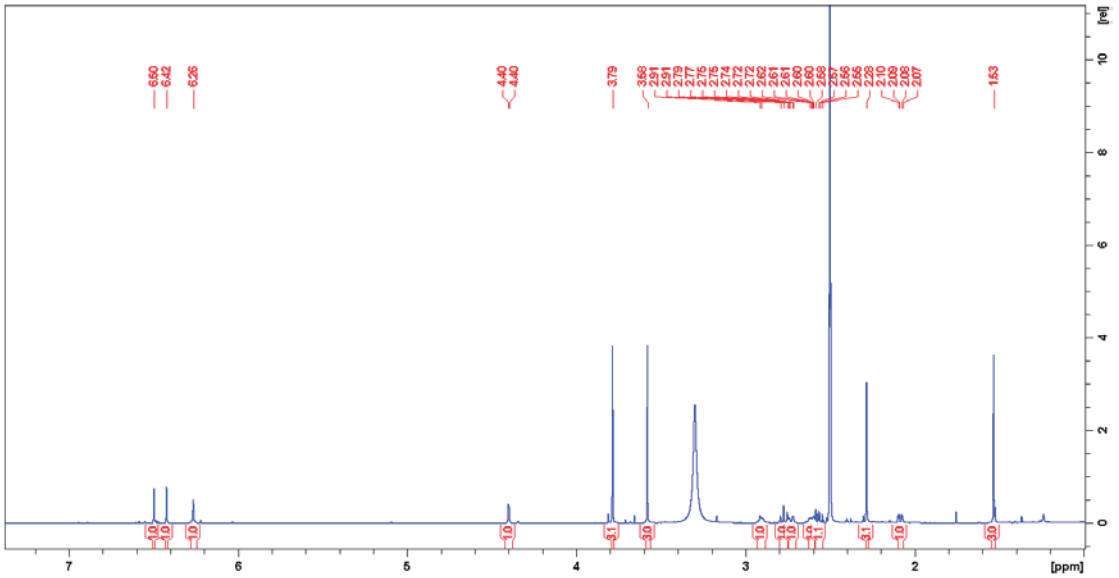

Fig. S17. ^{1}H-NMR (700 MHz, DMSO-*d*$_6$) spectrum of compound **3**.

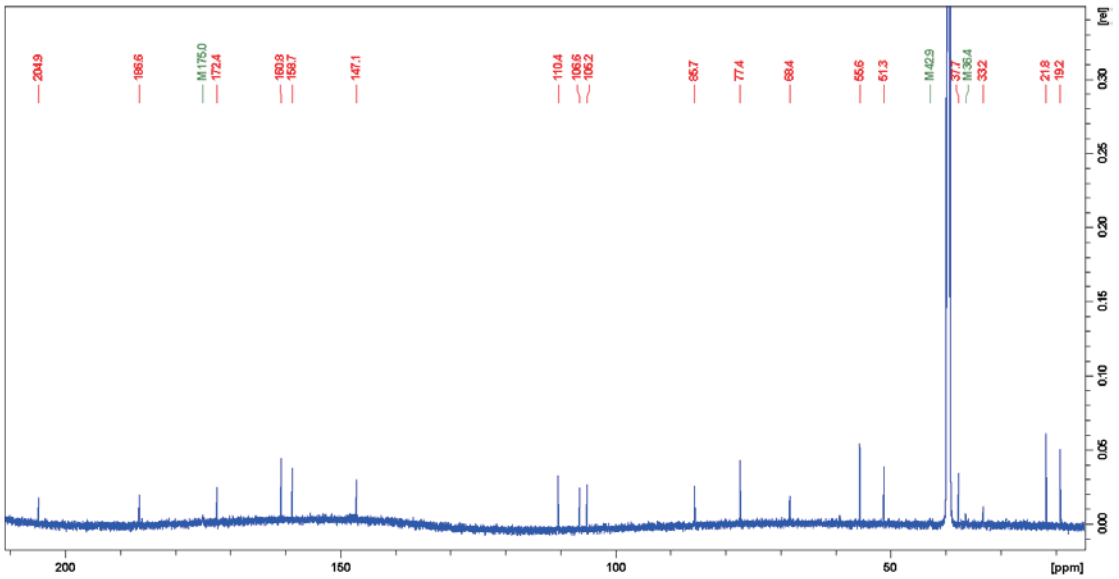

Fig. S18. The ^{13}C-NMR (175 MHz, DMSO-*d*$_6$) spectrum of compound **3**.

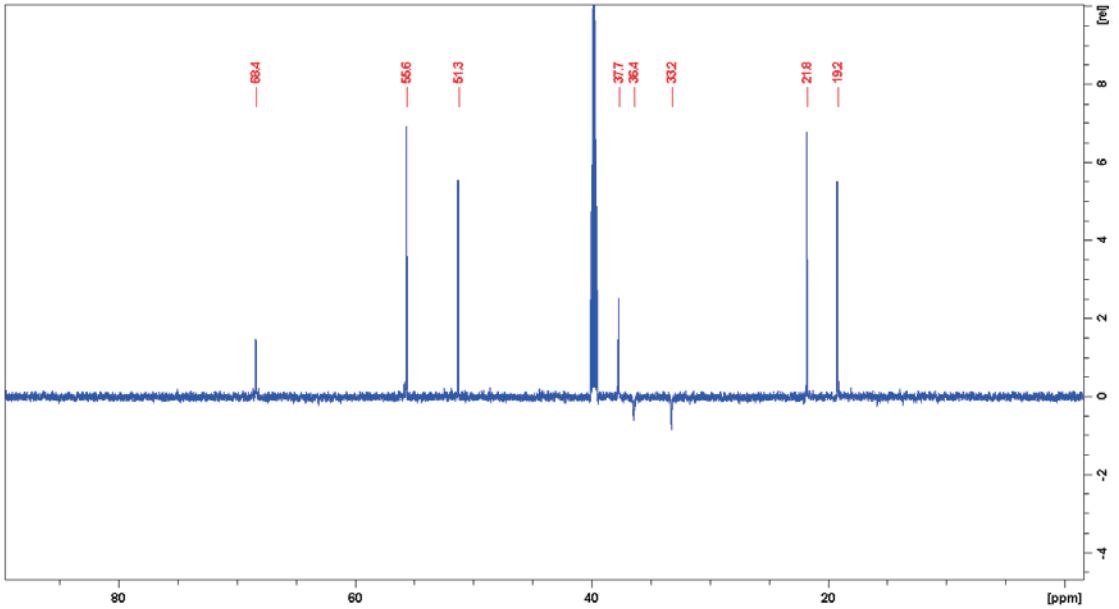

Fig. S19. The DEPT135 (175 MHz, DMSO-d_6) spectrum of compound **3**.

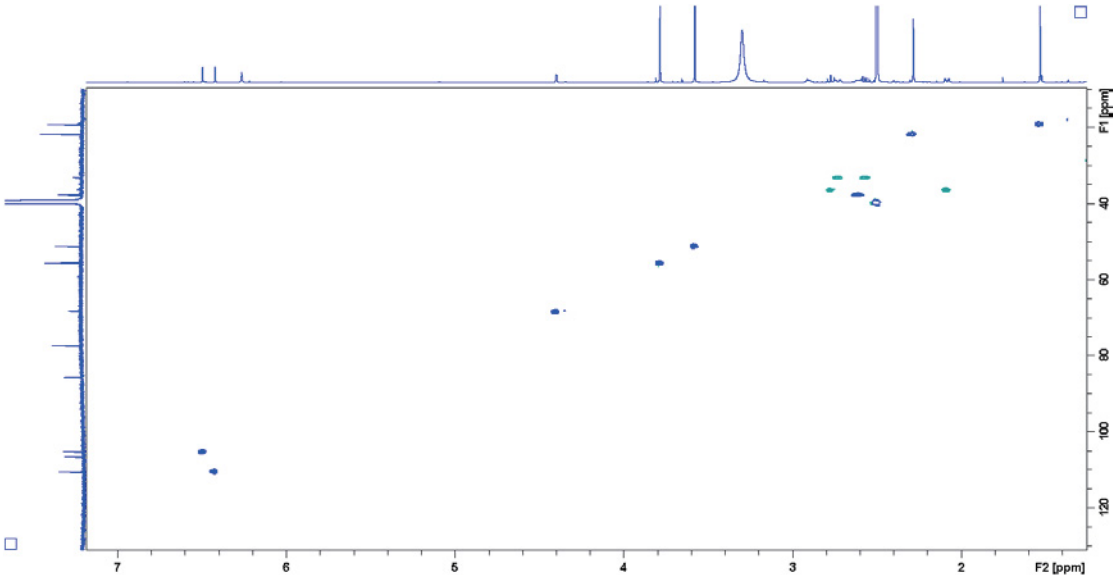

Fig. S20. The HSQC (700 MHz, DMSO-d_6) spectrum of compound **3**.

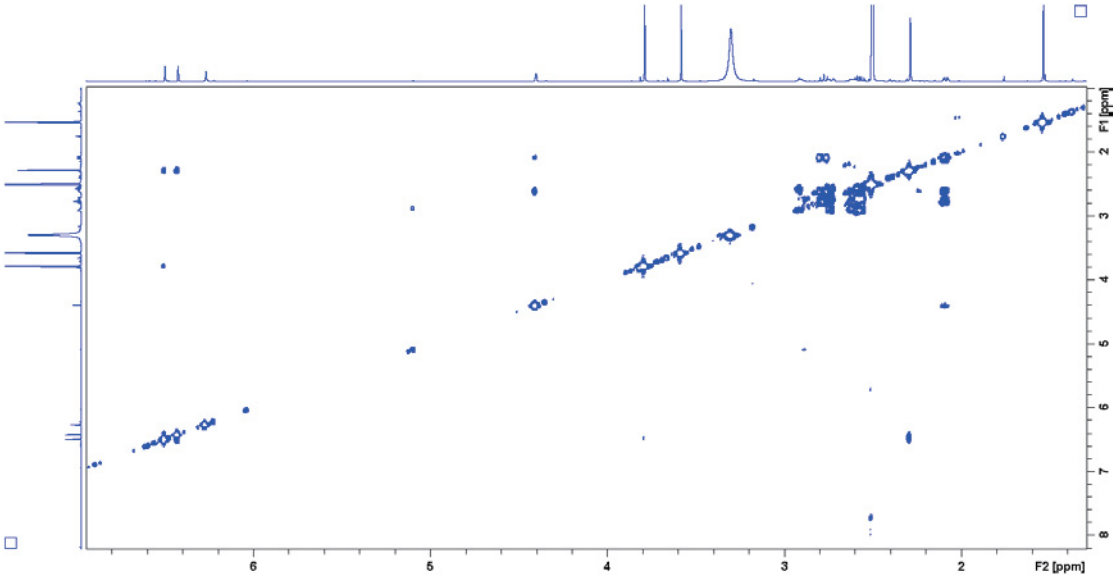

Fig. S21. The COSY (700 MHz, DMSO-d_6) spectrum of compound **3**.

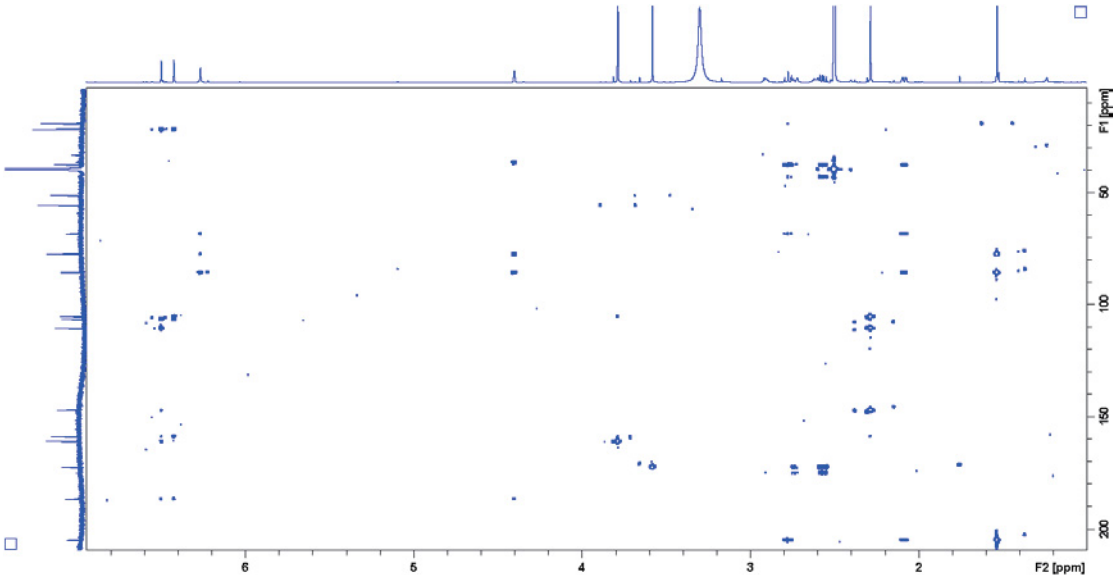

Fig. S22. The HMBC (700 MHz, DMSO-d_6) spectrum of compound **3**.

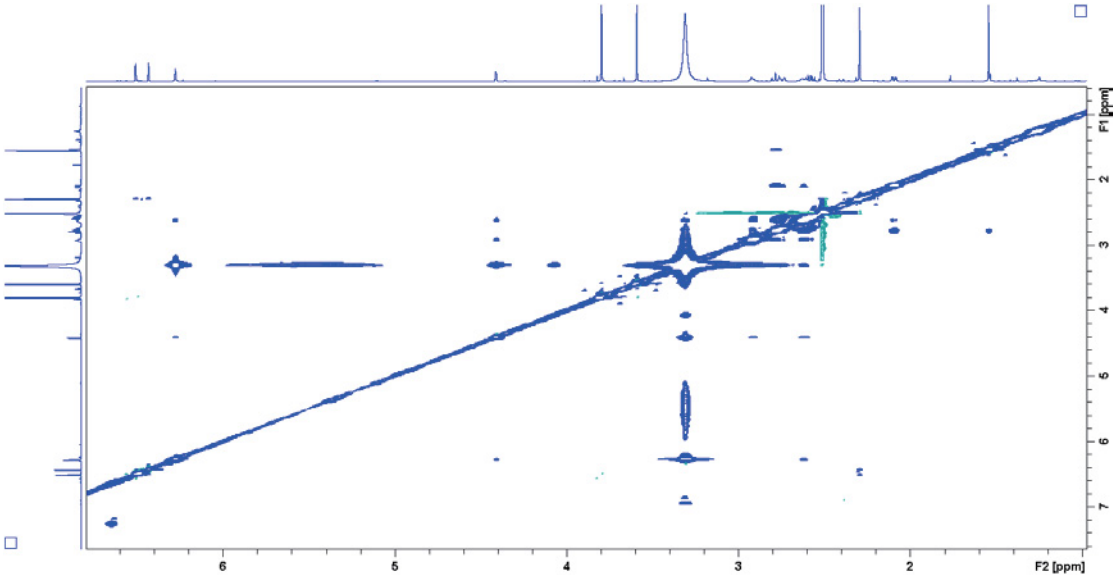

Fig. S23. The NOESY (600 MHz, DMSO-d_6) spectrum of compound **3**.

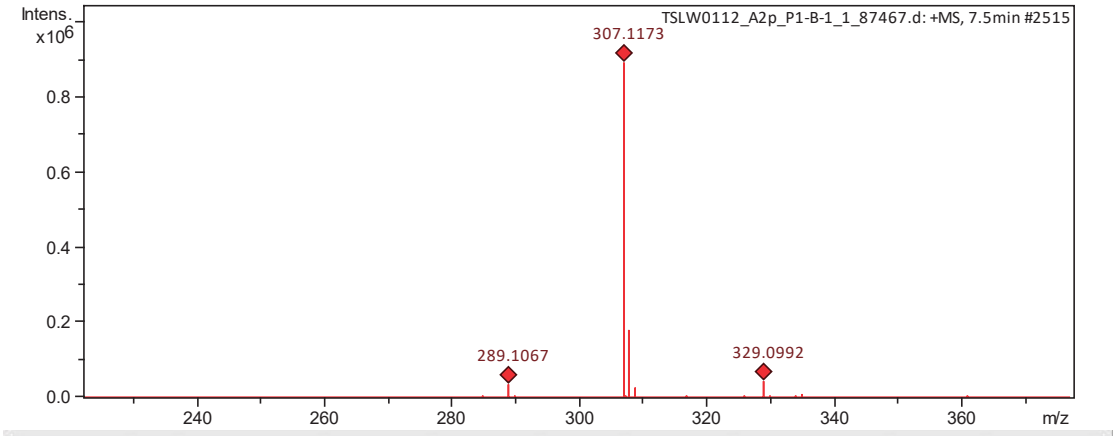

Meas. m/z	#	Ion Formula	m/z	err [ppm]	mSigma	# mSigma	Score	rdb	ei¥ Conf	N-Rule
307.1173	1	C16H19O6	307.1176	1.0	13.6	1	100.00	7.5	even	ok
307.1173	2	C13H11N10	307.1163	-3.4	15.7	2	65.01	13.5	even	ok
307.1173	3	C12H15N6O4	307.1149	-7.8	27.3	3	19.58	8.5	even	ok

Fig. S24. The HR-ESI-MS of compound **4**.

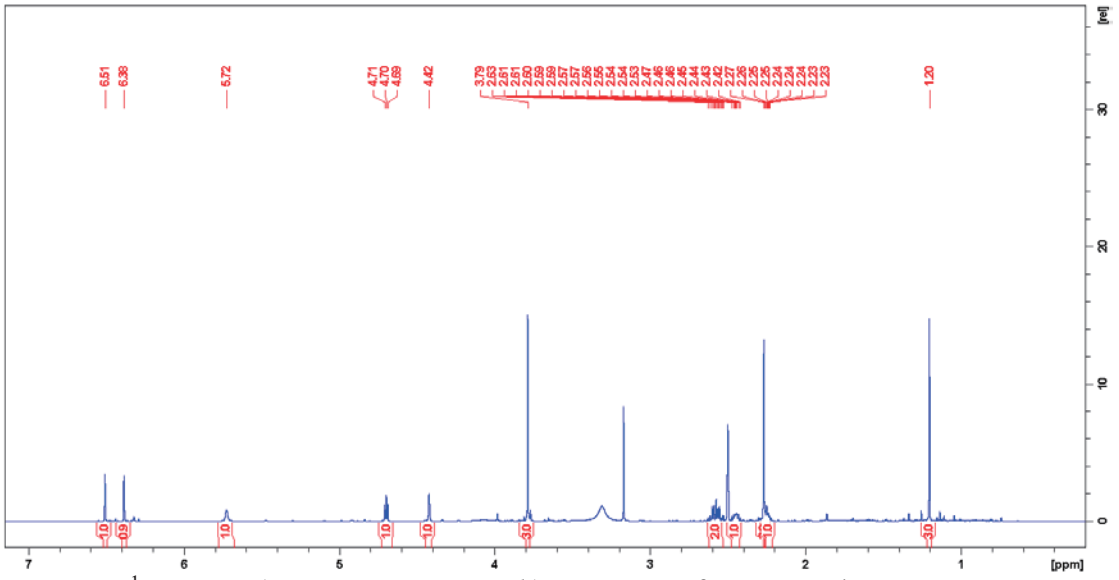

Fig. S25. ^{1}H-NMR (700 MHz, DMSO-d_6) spectrum of compound **4**.

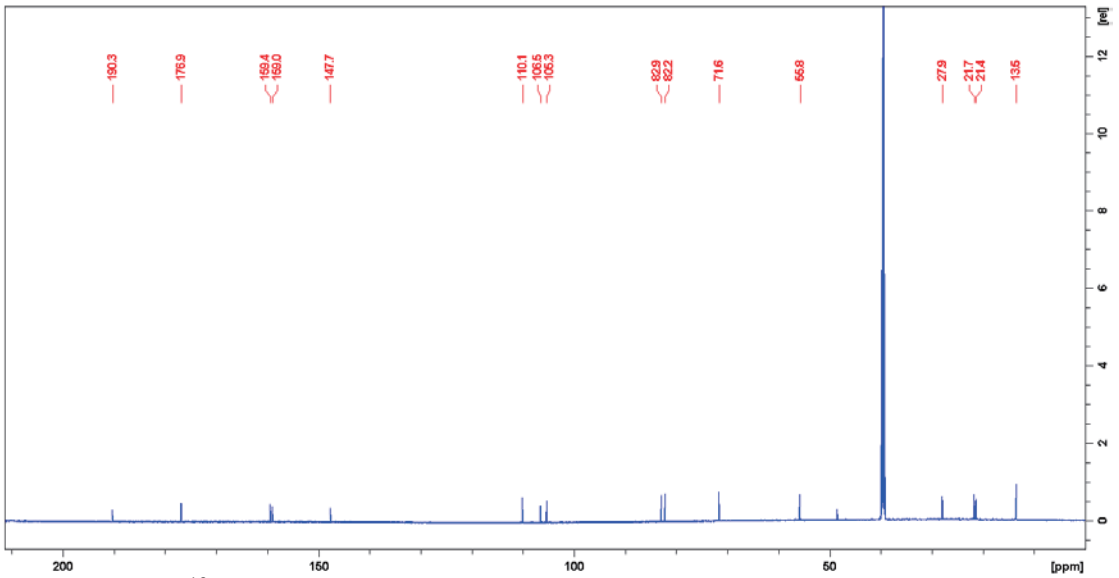

Fig. S26. The ^{13}C-NMR (175 MHz, DMSO-d_6) spectrum of compound **4**.

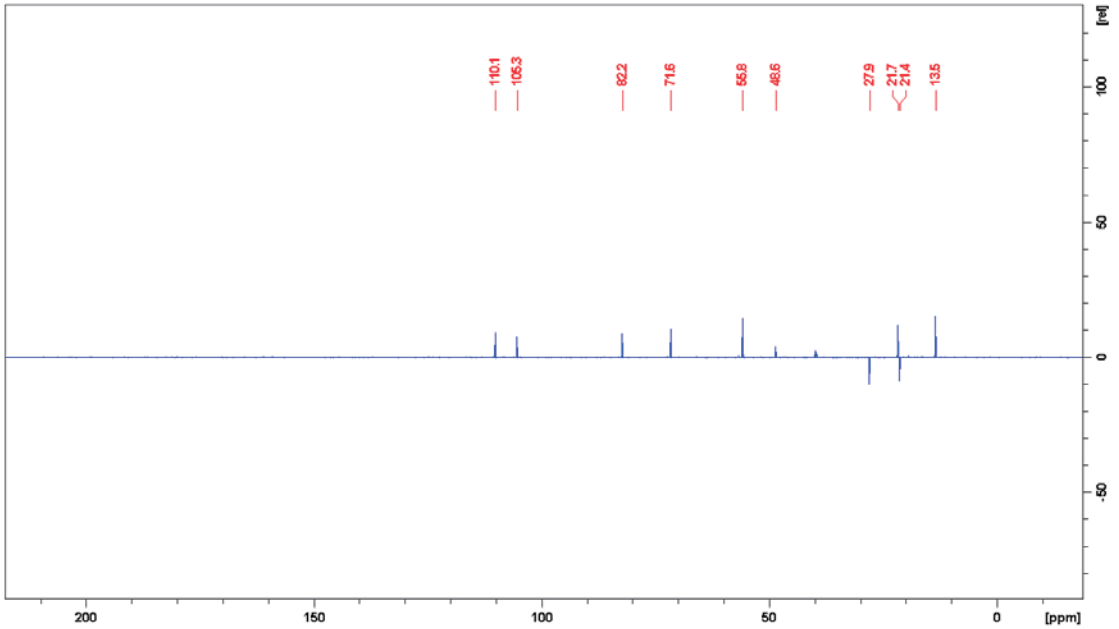

Fig. S27. The DEPT135 (175 MHz, DMSO-d_6) spectrum of compound **4**.

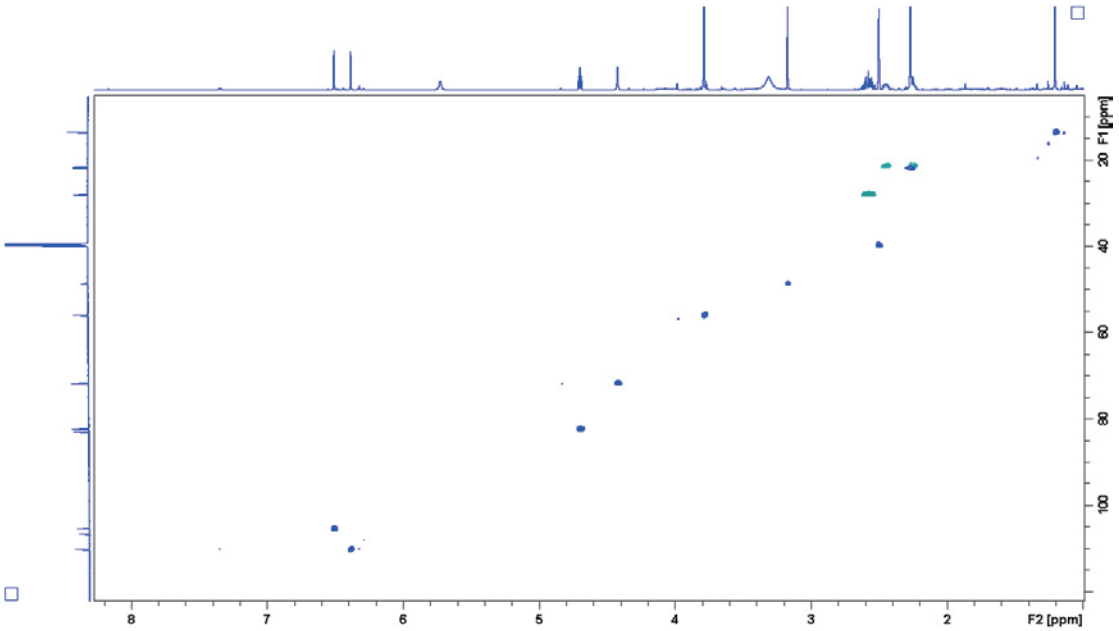

Fig. S28. The HSQC (700 MHz, DMSO-d_6) spectrum of compound **4**.

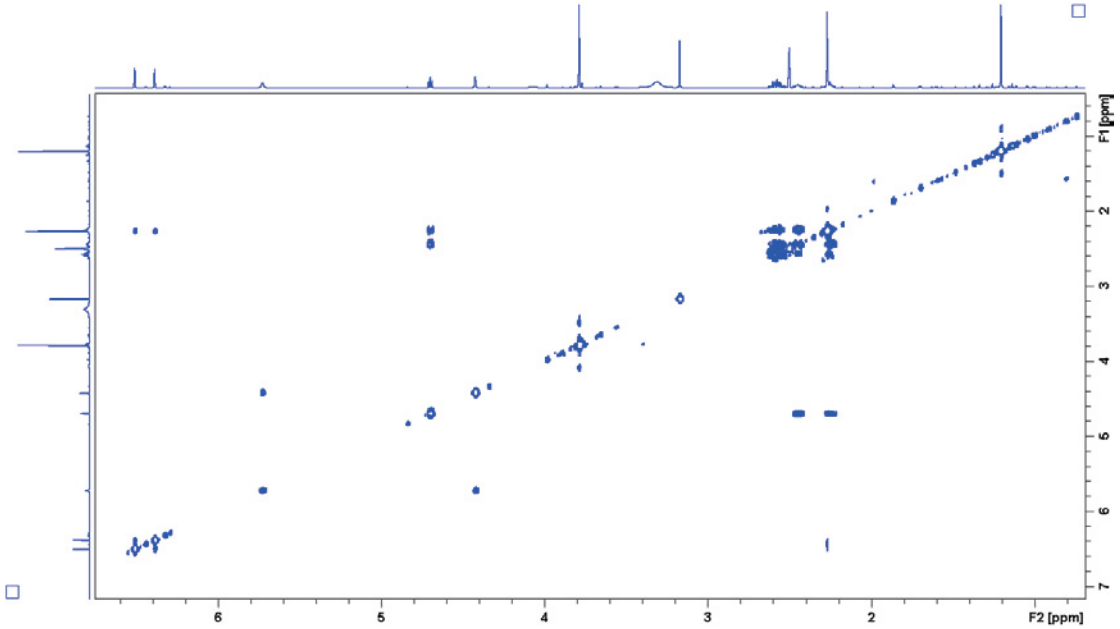

Fig. S29. The COSY (700 MHz, DMSO-*d*6) spectrum of compound **4**.

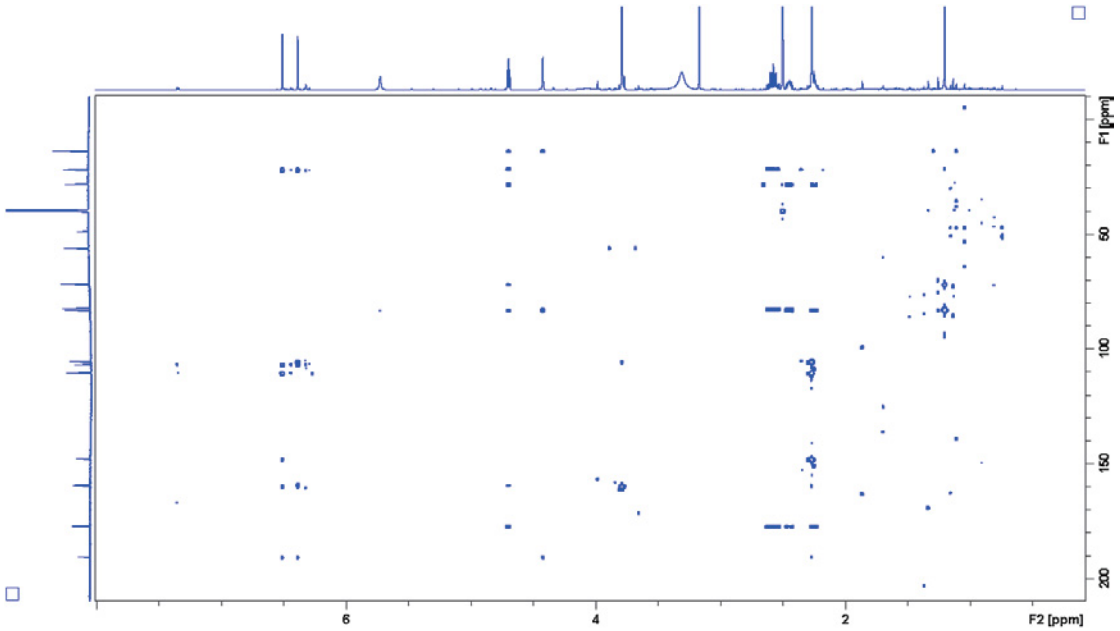

Fig. S30. The HMBC (700 MHz, DMSO-*d*6) spectrum of compound **4**.

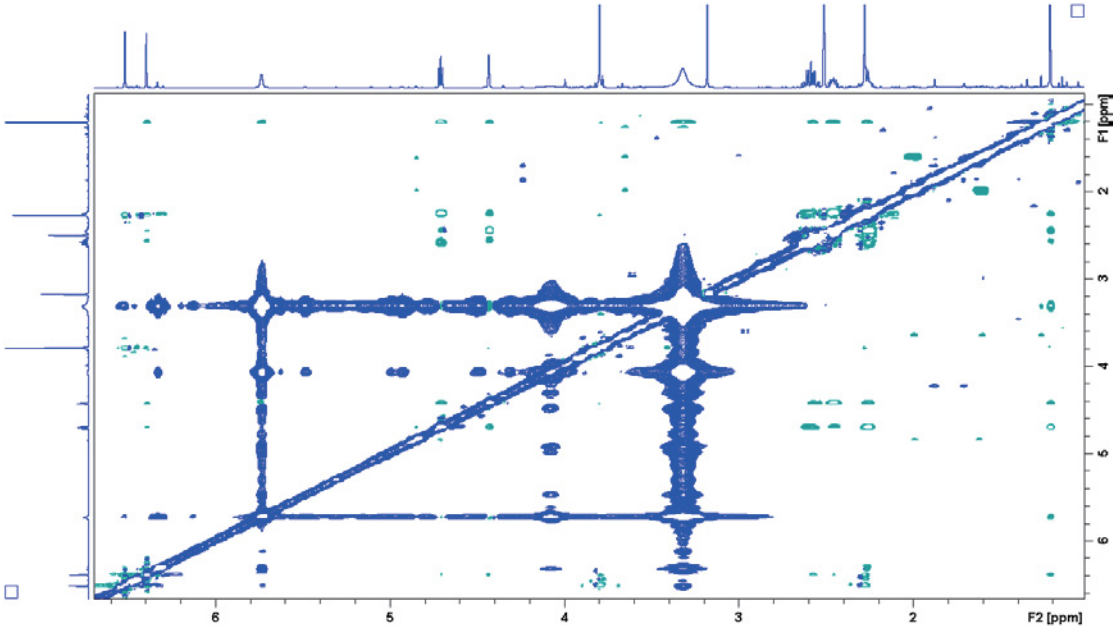

Fig. S31. The NOESY (600 MHz, DMSO-d_6) spectrum of compound **4**.

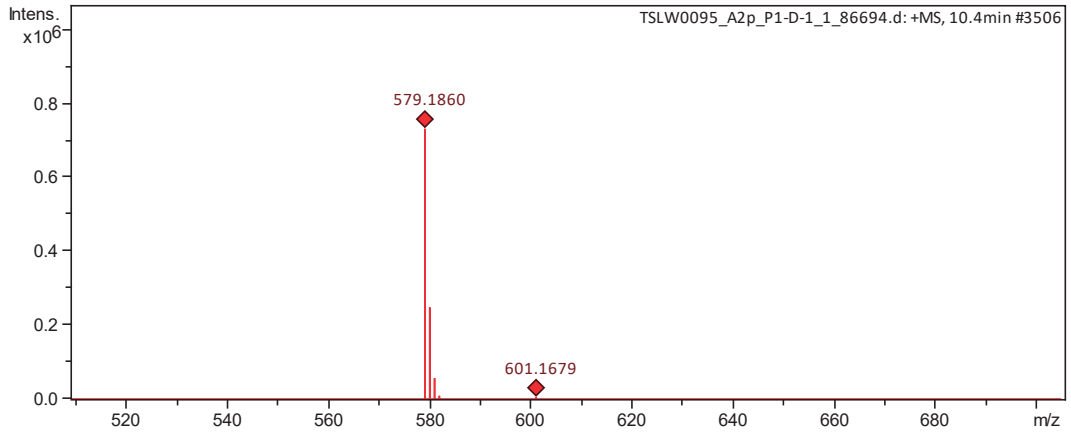

579.1860	1	C31H31O11	579.1861	0.2	2.1	1	100.00	16.5	even	ok
579.1860	2	C28H23N10O5	579.1847	-2.2	5.9	2	52.10	22.5	even	ok
579.1860	3	C32H27N4O7	579.1874	2.5	13.6	3	39.96	21.5	even	ok
579.1860	4	C29H19N14O	579.1861	0.2	15.1	4	79.23	27.5	even	ok
579.1860	5	C44H23N2	579.1856	-0.7	75.6	5	11.76	34.5	even	ok

Fig. S32. The HR-ESI-MS of compound **5**.

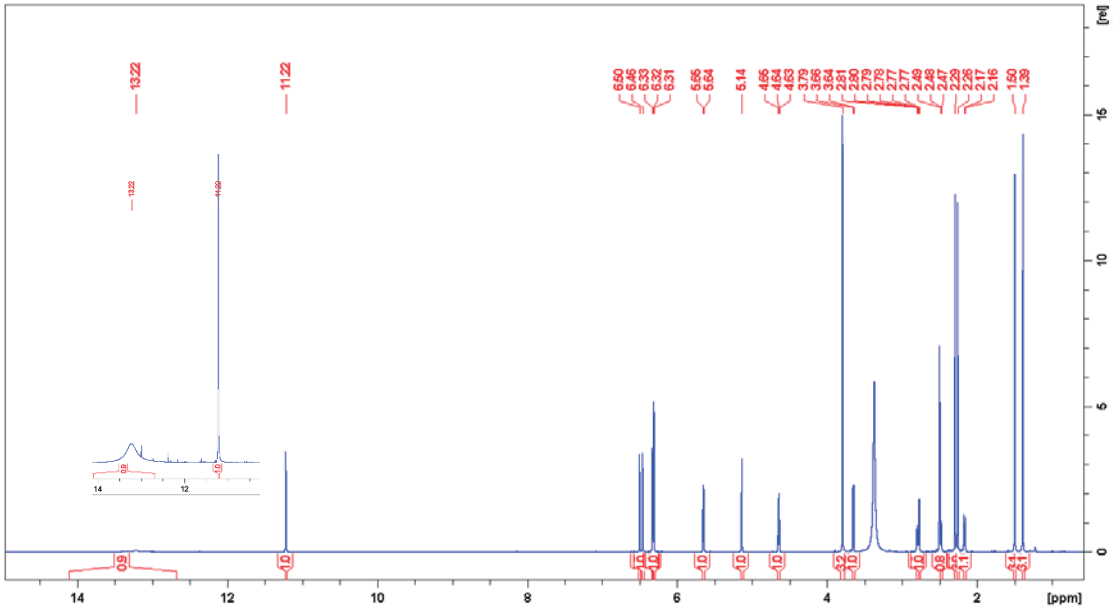

Fig. S33. ^{1}H-NMR (700 MHz, DMSO-d_6) spectrum of compound **5**.

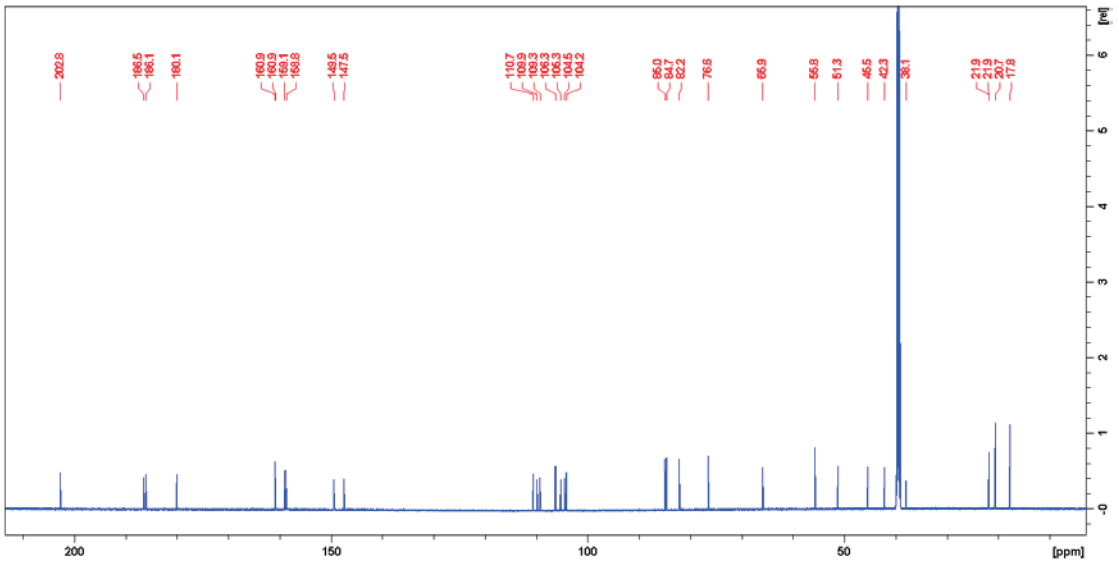

Fig. S34. The ^{13}C-NMR (175 MHz, DMSO-d_6) spectrum of compound **5**.

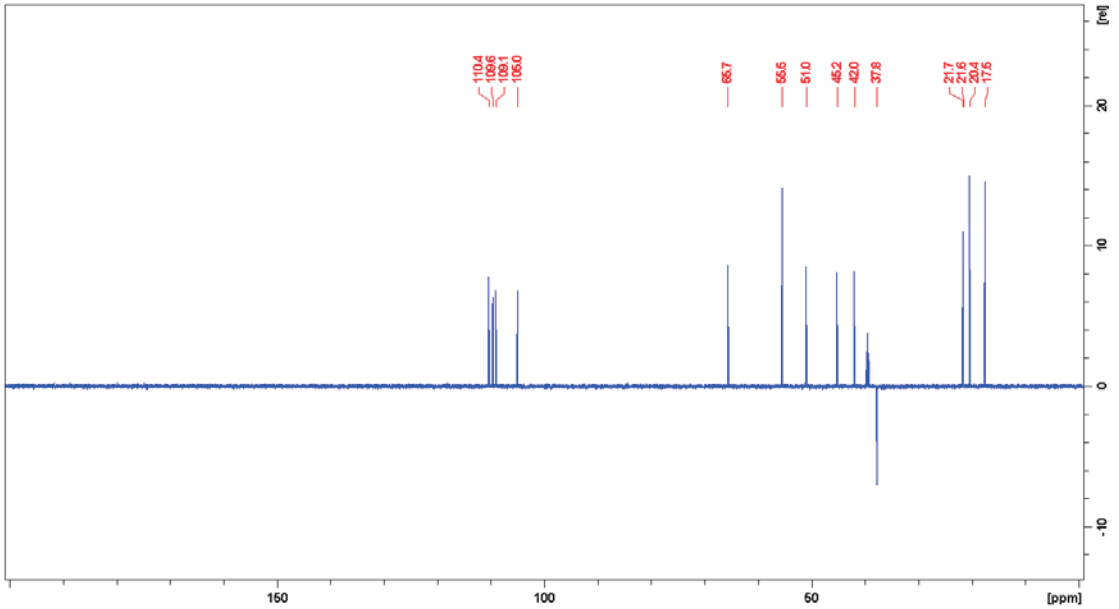

Fig. S35. The DEPT135 (175 MHz, DMSO-d_6) spectrum of compound **5**.

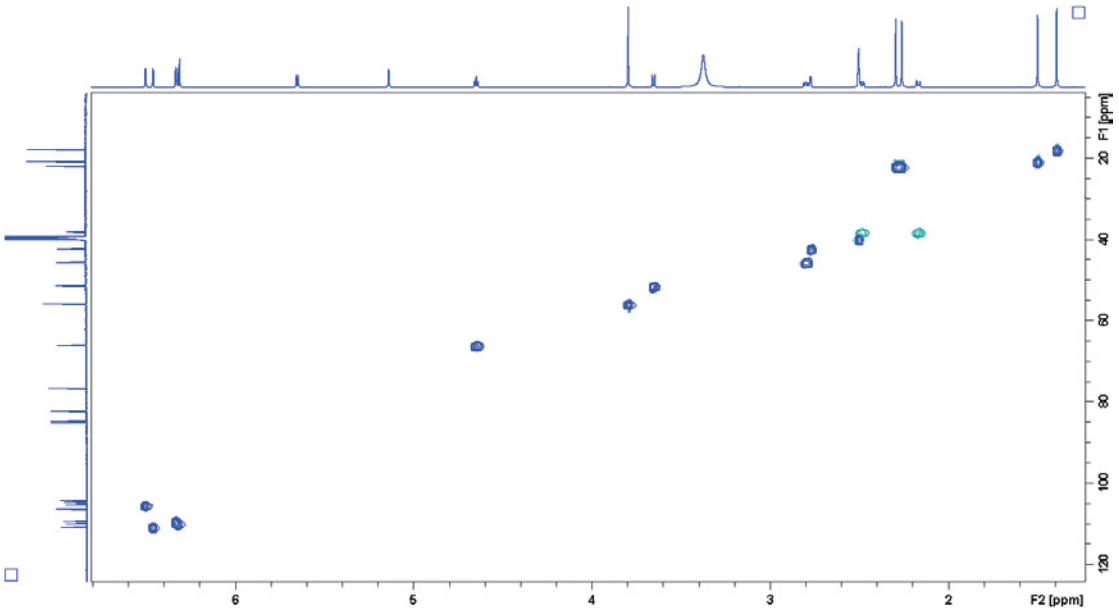

Fig. S36. The HSQC (700 MHz, DMSO-d_6) spectrum of compound **5**.

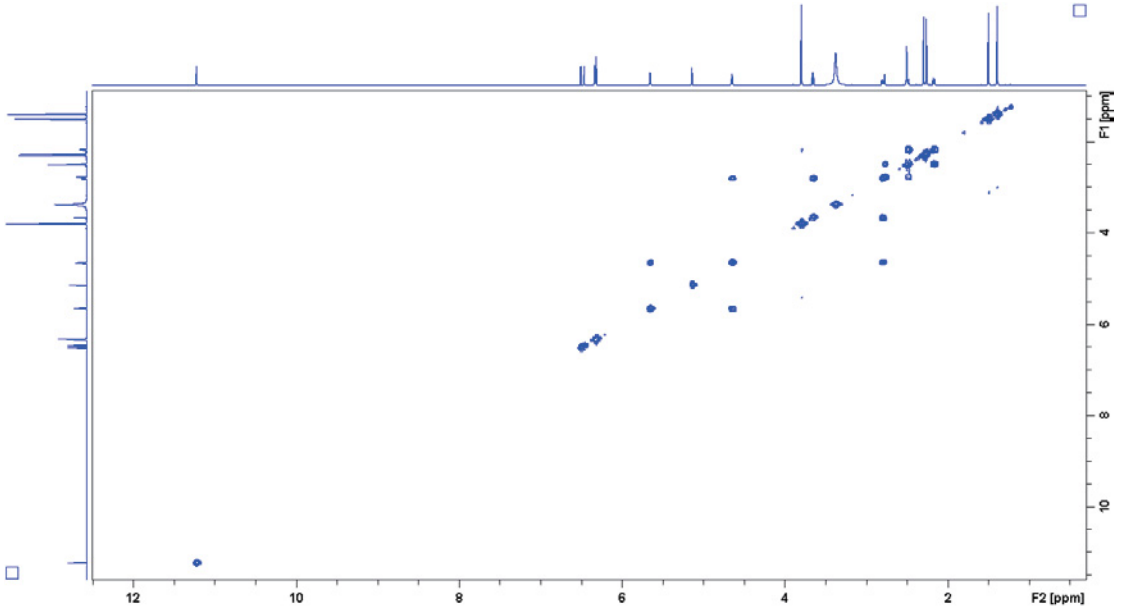

Fig. S37. The COSY (700 MHz, DMSO-d_6) spectrum of compound **5**.

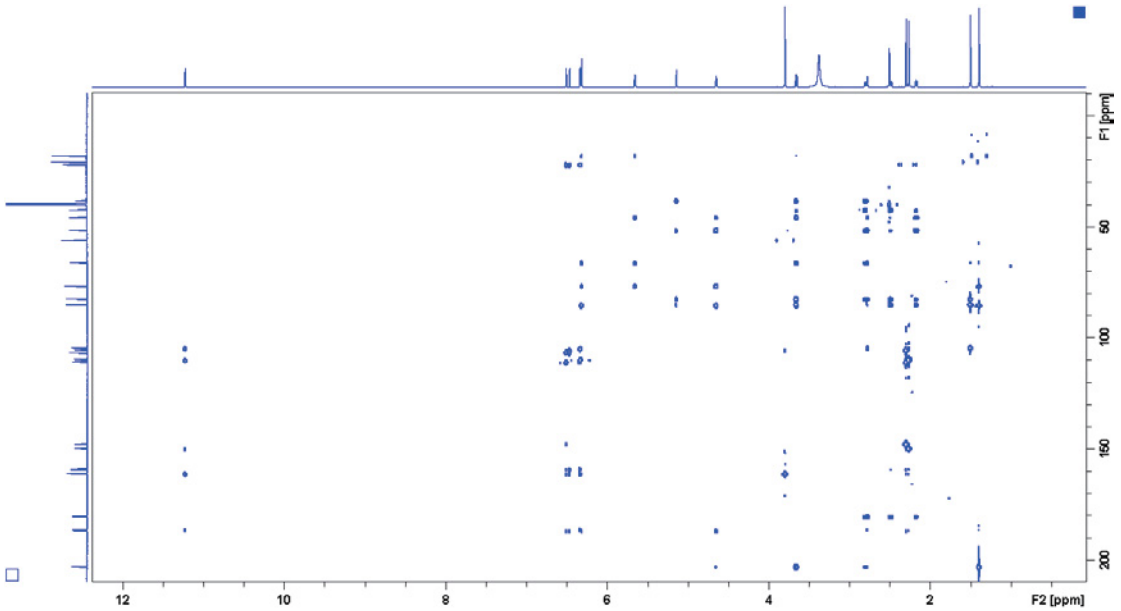

Fig. S38. The HMBC (700 MHz, DMSO-d_6) spectrum of compound **5**.

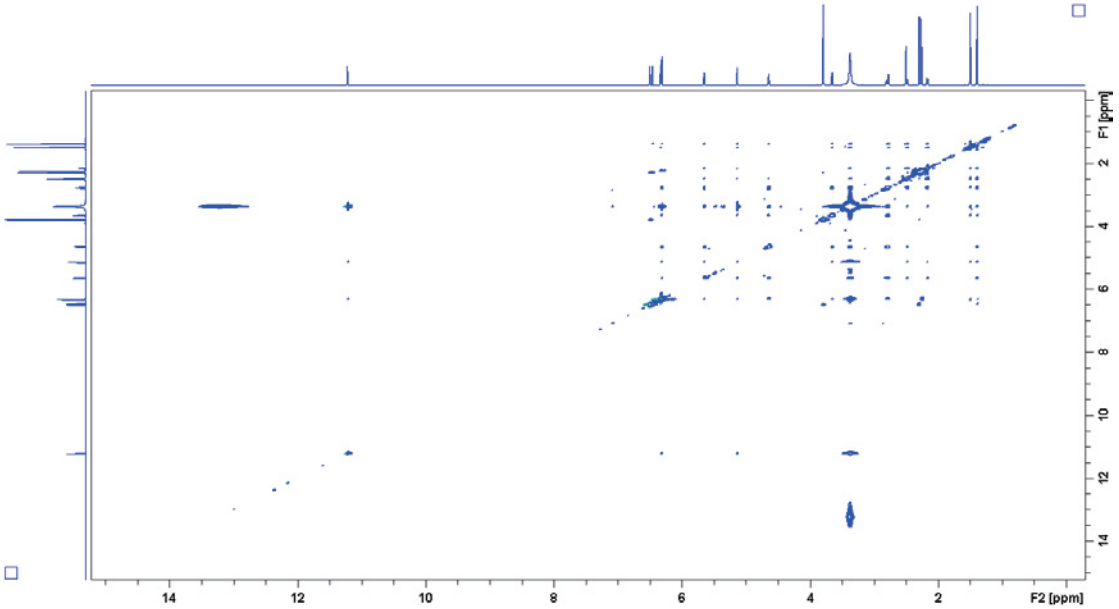

Fig. S39. The NOESY (600 MHz, DMSO-*d*$_6$) spectrum of compound **5**.

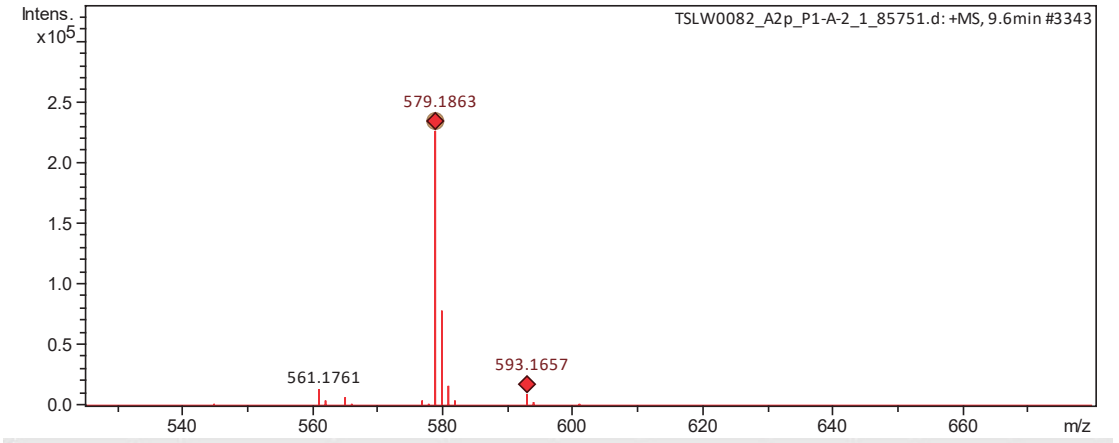

Meas. m/z	#	Ion Formula	m/z	err [ppm]	mSigma	# mSigma	Score	rdb	ei¥ Conf	N-Rule
579.1863	1	C31H31O11	579.1861	-0.4	4.6	1	100.00	16.5	even	ok
579.1863	2	C32H27N4O7	579.1874	1.9	9.1	2	58.31	21.5	even	ok
579.1863	3	C44H23N2	579.1856	-1.3	71.0	3	13.14	34.5	even	ok

Fig. S40. The HR-ESI-MS of compound **6**.

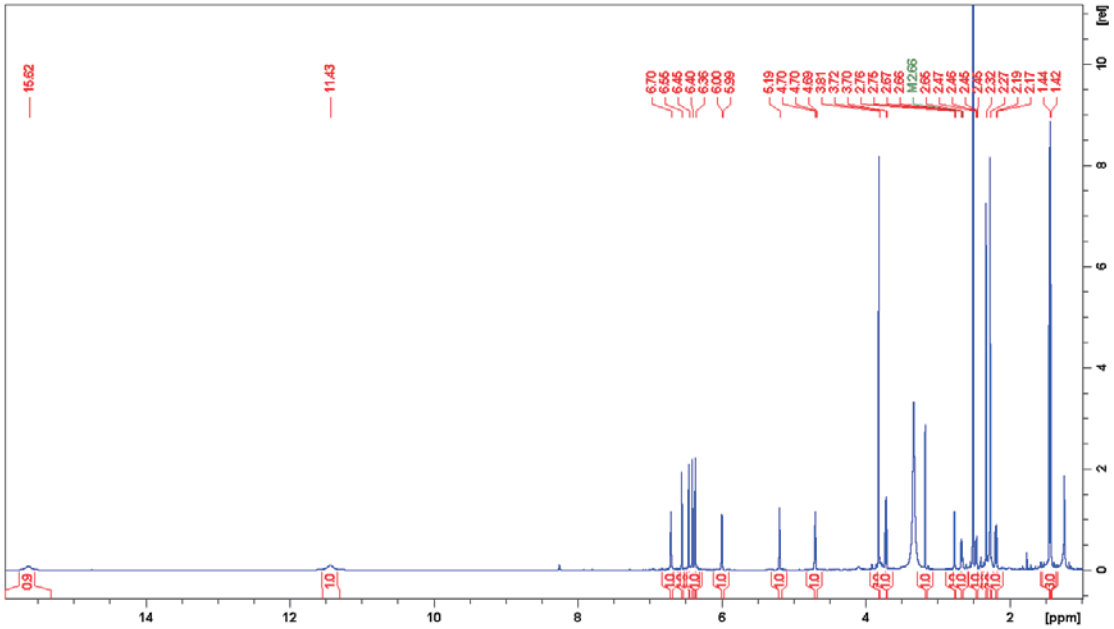

Fig. S41. ^{1}H-NMR (700 MHz, DMSO-*d*$_6$) spectrum of compound **6**.

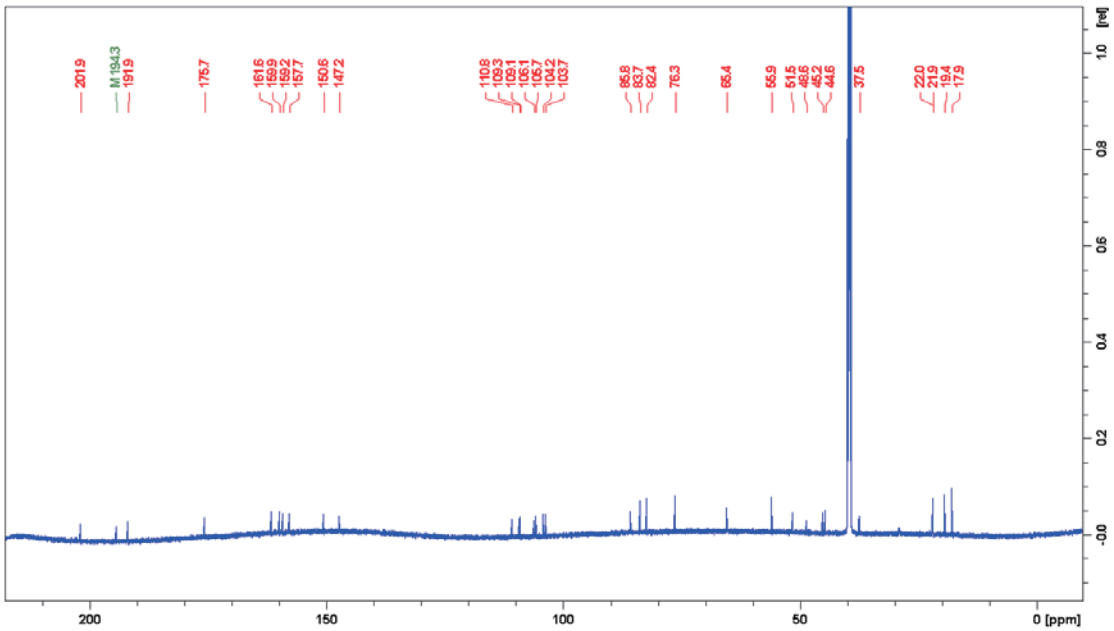

Fig. S42. The ^{13}C-NMR (175 MHz, DMSO-*d*$_6$) spectrum of compound **6**.

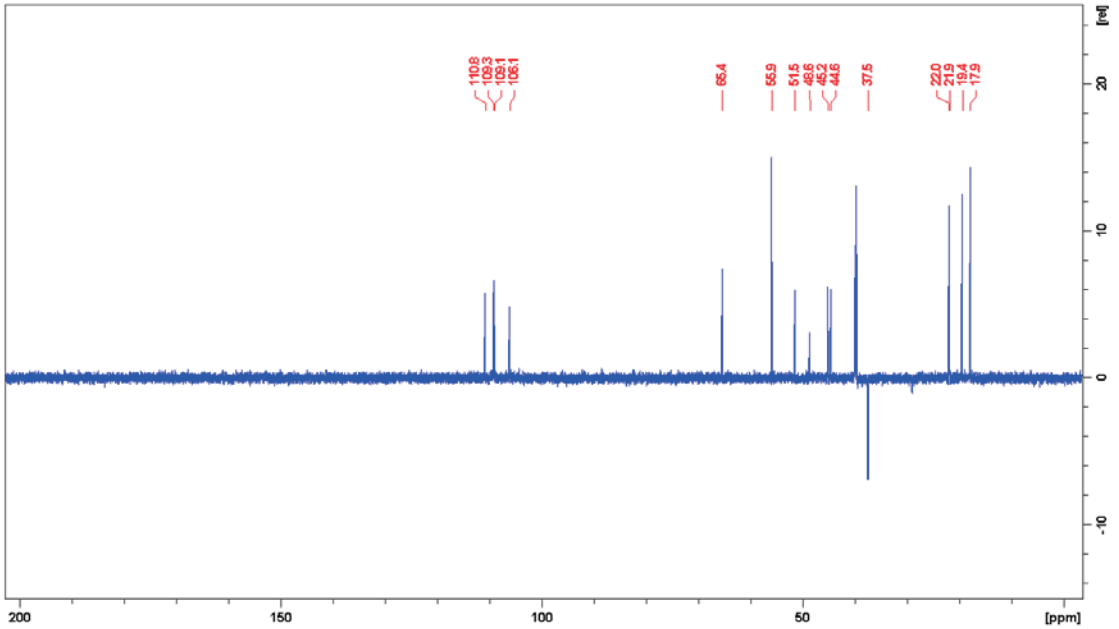

Fig. S43. The DEPT135 (175 MHz, DMSO-*d*$_6$) spectrum of compound **6**.

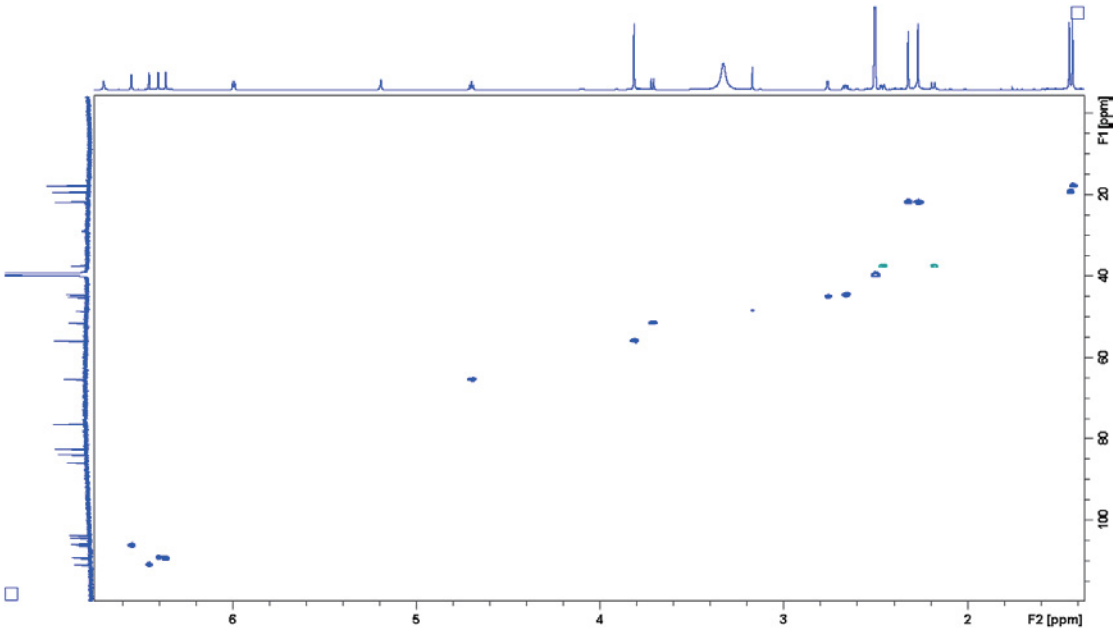

Fig. S44. The HSQC (700 MHz, DMSO-*d*$_6$) spectrum of compound **6**.

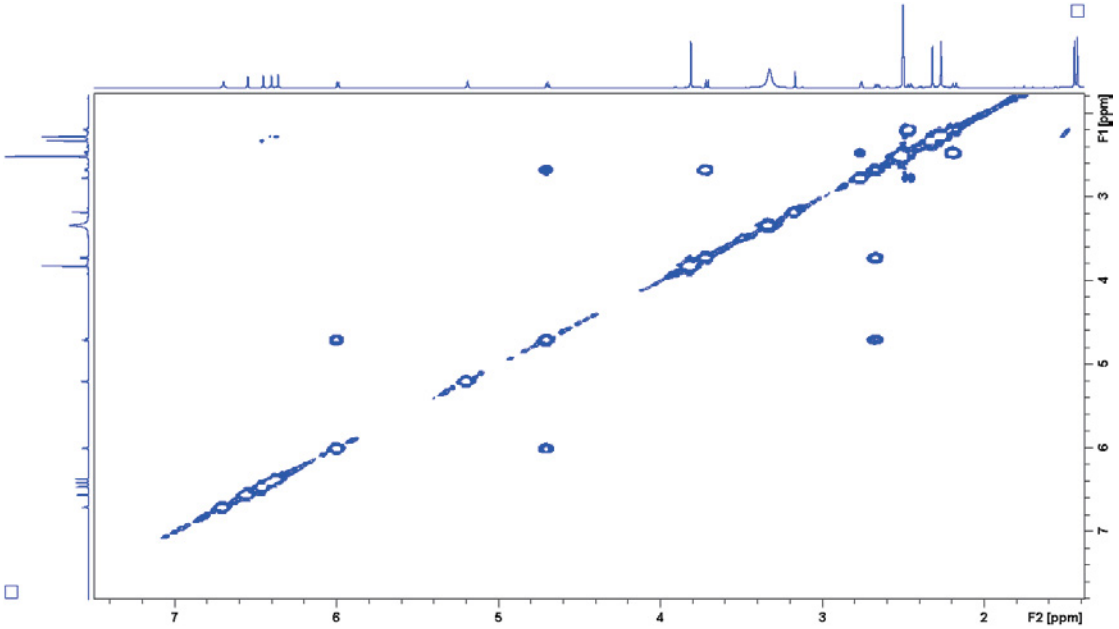

Fig. S45. The COSY (700 MHz, DMSO-*d*$_6$) spectrum of compound **6**.

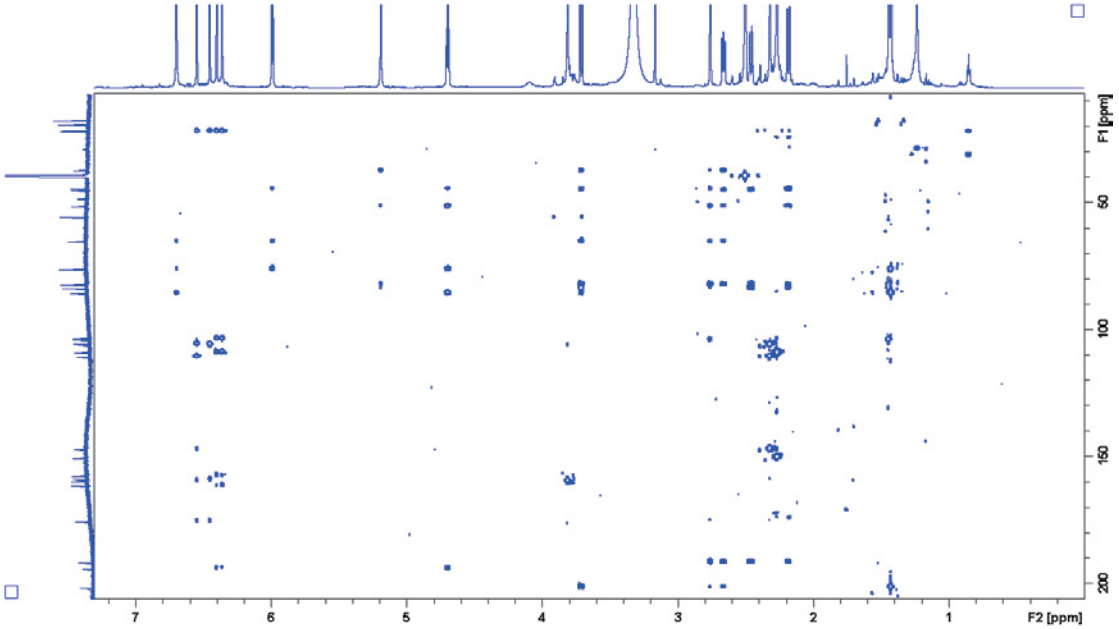

Fig. S46. The HMBC (700 MHz, DMSO-*d*$_6$) spectrum of compound **6**.

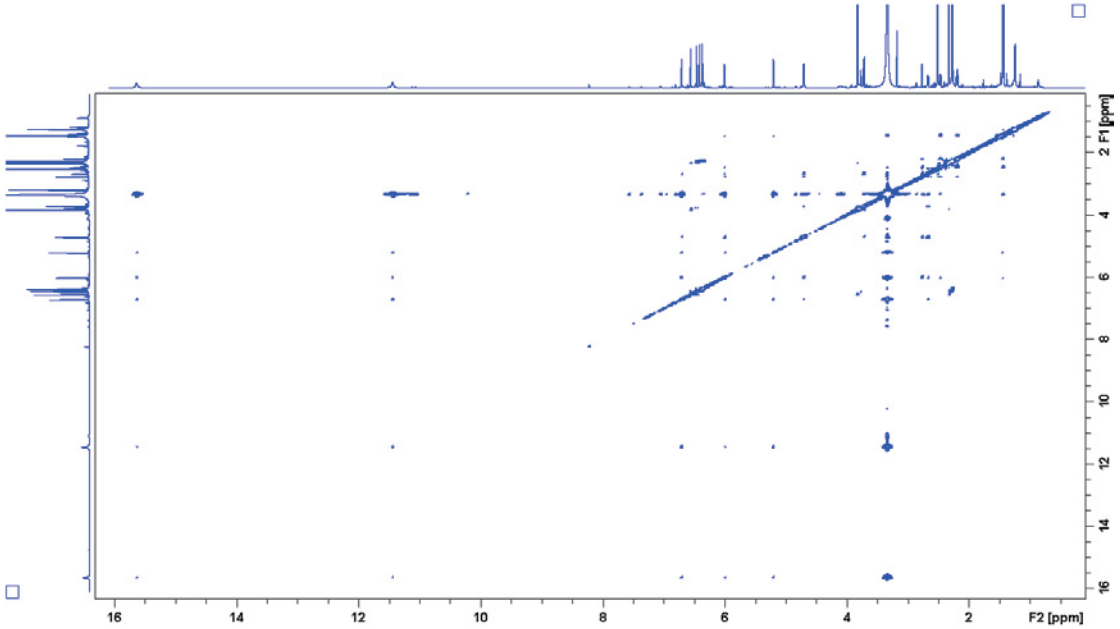

Fig. S47. The NOESY (600 MHz, DMSO-d_6) spectrum of compound **6**.

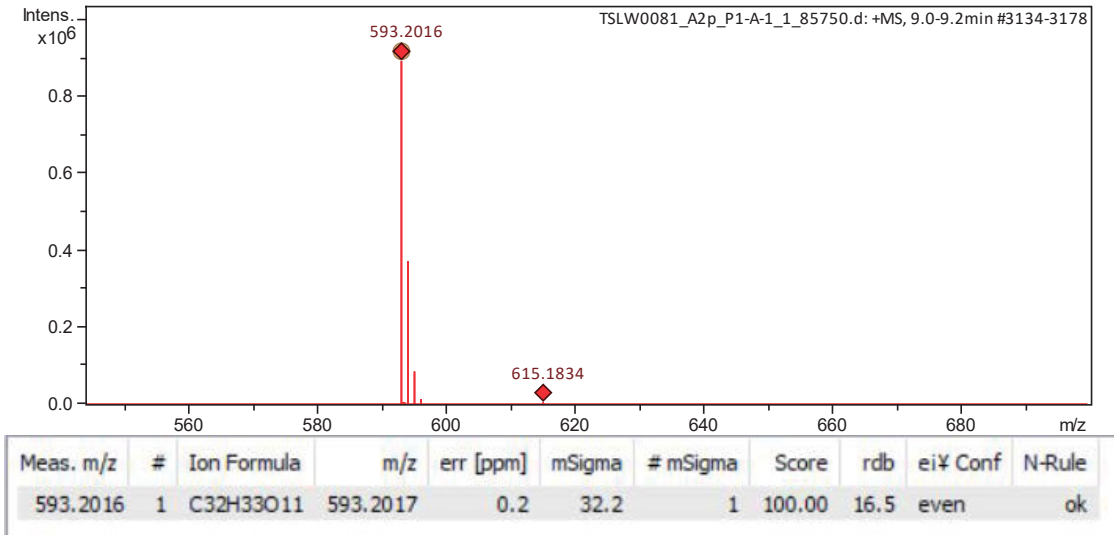

Meas. m/z	#	Ion Formula	m/z	err [ppm]	mSigma	# mSigma	Score	rdb	ei¥ Conf	N-Rule
593.2016	1	C32H33O11	593.2017	0.2	32.2	1	100.00	16.5	even	ok

Fig. S48. The HR-ESI-MS of compound **7**.

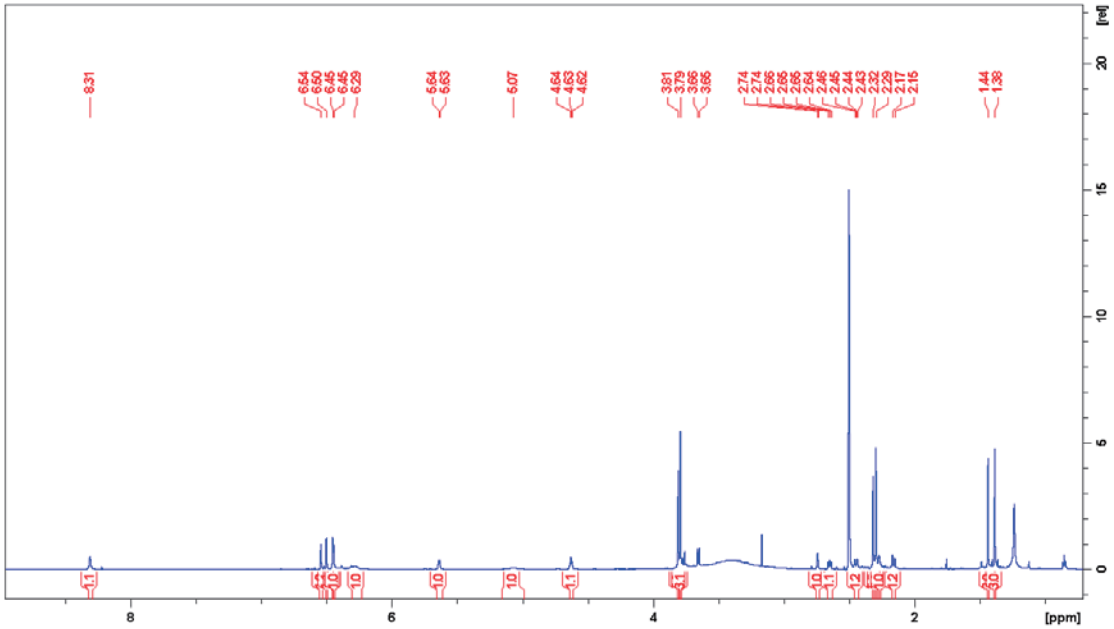

Fig. S49. ^{1}H-NMR (700 MHz, DMSO-*d*$_6$) spectrum of compound **7**.

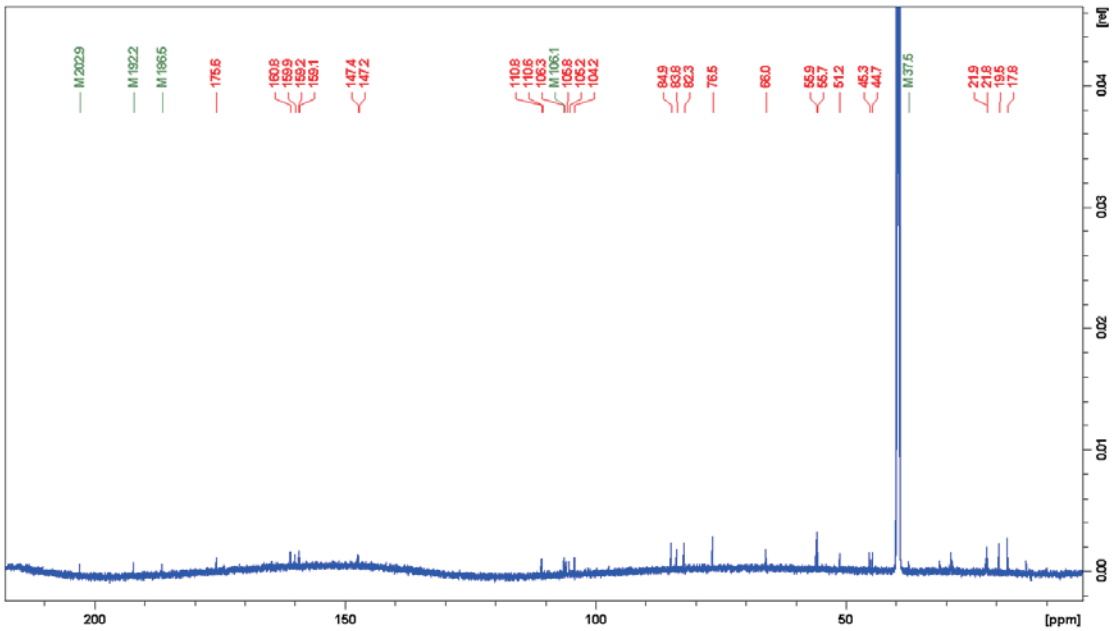

Fig. S50. The ^{13}C-NMR (175 MHz, DMSO-*d*$_6$) spectrum of compound **7**.

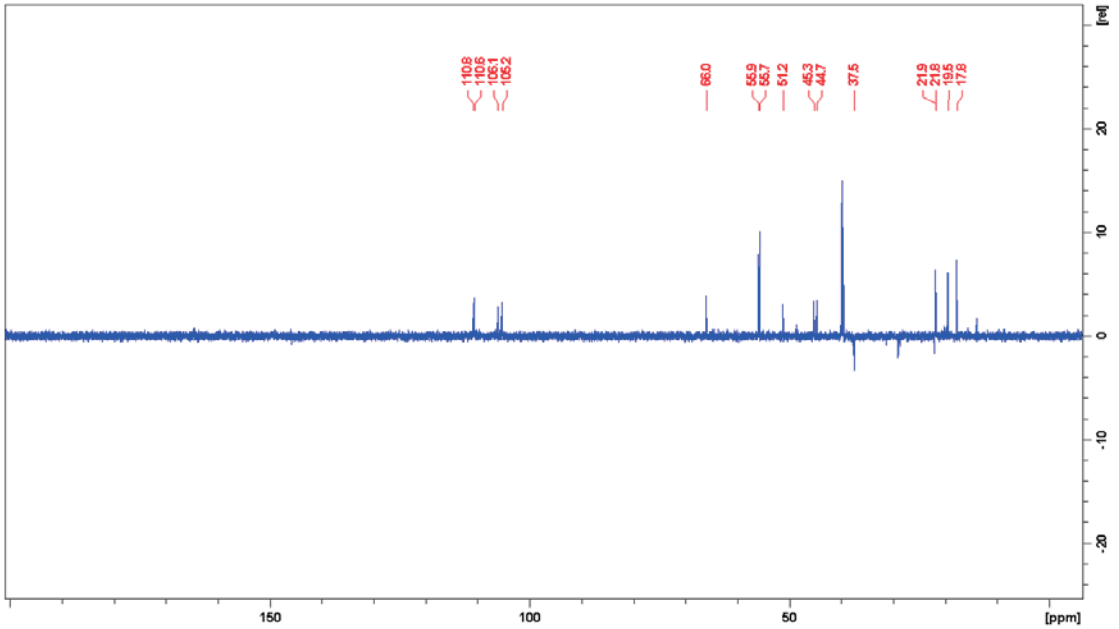

Fig. S51. The DEPT135 (175 MHz, DMSO-*d*$_6$) spectrum of compound **7**.

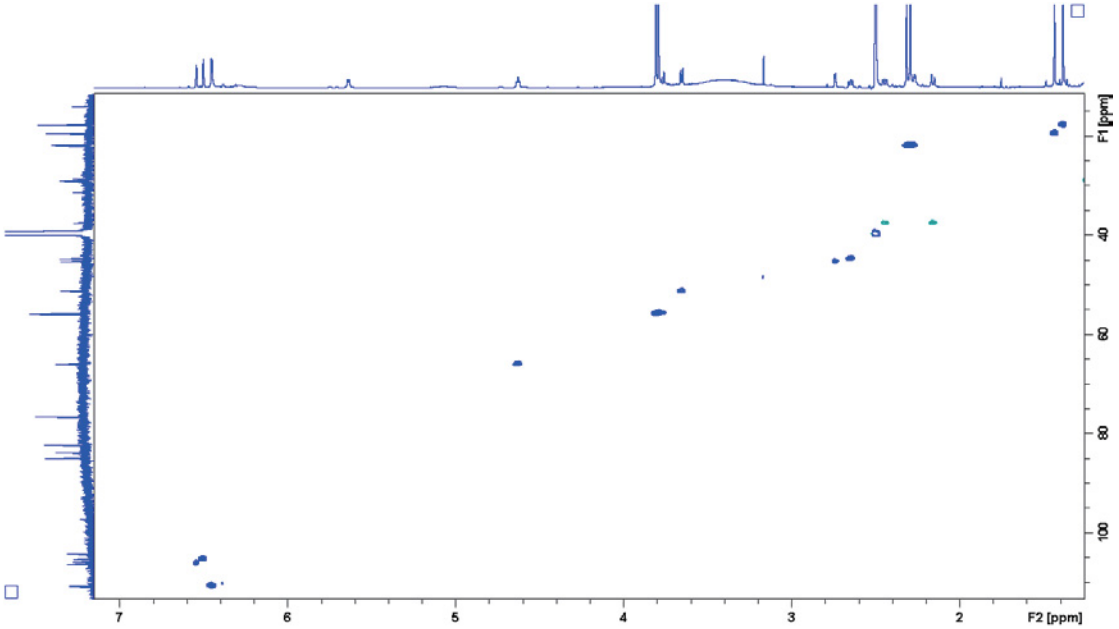

Fig. S52. The HSQC (700 MHz, DMSO-*d*$_6$) spectrum of compound **7**.

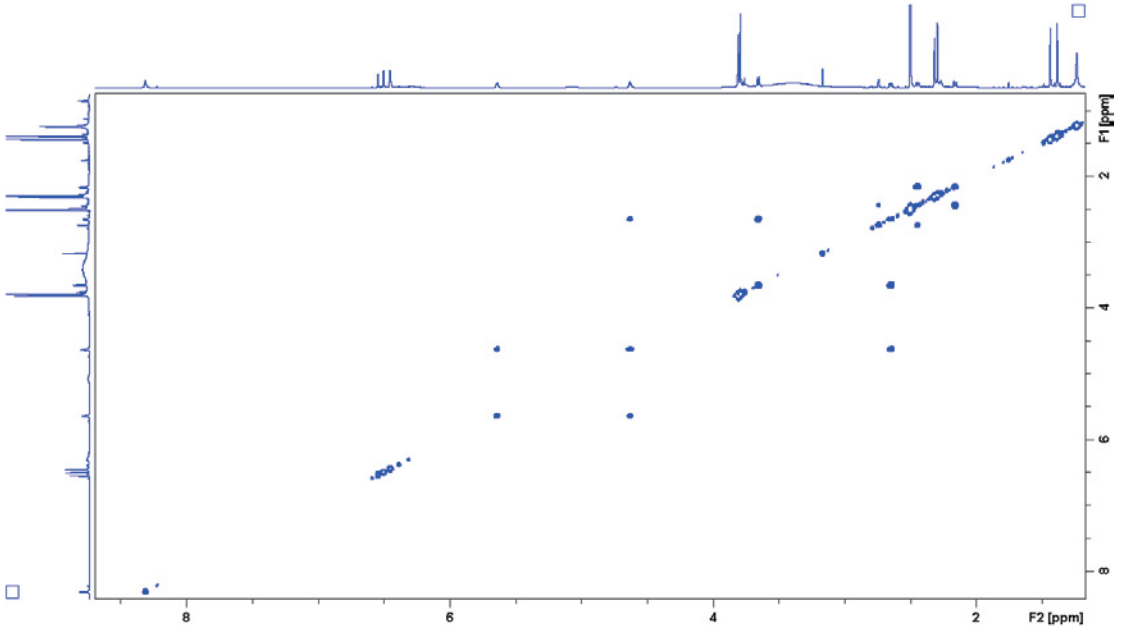

Fig. S53. The COSY (700 MHz, DMSO-*d*6) spectrum of compound **7**.

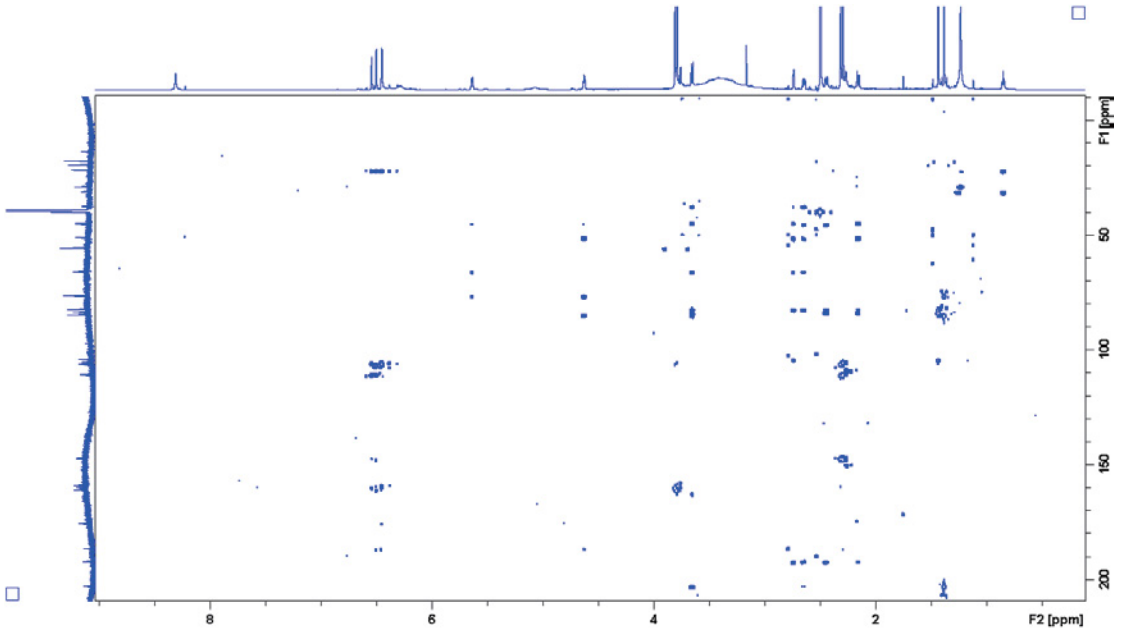

Fig. S54. The HMBC (700 MHz, DMSO-*d*6) spectrum of compound **7**.

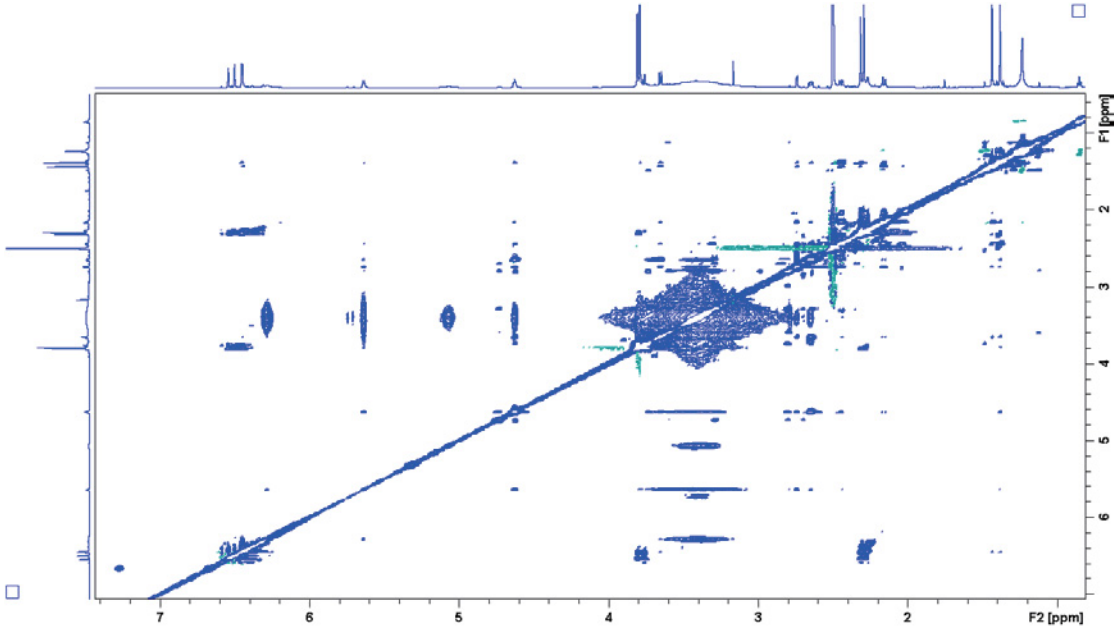

Fig. S55. The NOESY (600 MHz, DMSO-d_6) spectrum of compound **7**.

Chapter 6. Results and Discussion

The marine flavobacteria revealed a rich biosynthetic potential to produce arylamine-containing alkaloids

The genus *Tenacibaculum* is mainly obtained from marine environments, such as sea water, tidal flat, and aquaculture systems, as well as from marine organisms like bryozoan, sea anemone, oyster, sponge and green algae. Except for the isolation of several siderophores, research about natural products produced by these bacteria is rare. In our ongoing efforts to discover new bioactive natural products from bacteria, thirteen novel alkaloids with four different skeletons were isolated from the marine flavobacterium *T. discolor* sv11. The isolated compounds are the imidazolium-containing alkaloids discolins A–H, the pyrrolopyridine alkaloids dispyrrolopyridine A and B, the pyridinium-containing alkaloids dispyridine and dispyridine A and the pyrrolium-containing alkaloid dispyrrole (**Figure 6A**). Our work indicated that the genus *Tenacibaculum* holds a tremendous potential to produce diverse nitrogen-containing heterocycles with different skeletons, which are mainly obtained through chemical synthesis until now.

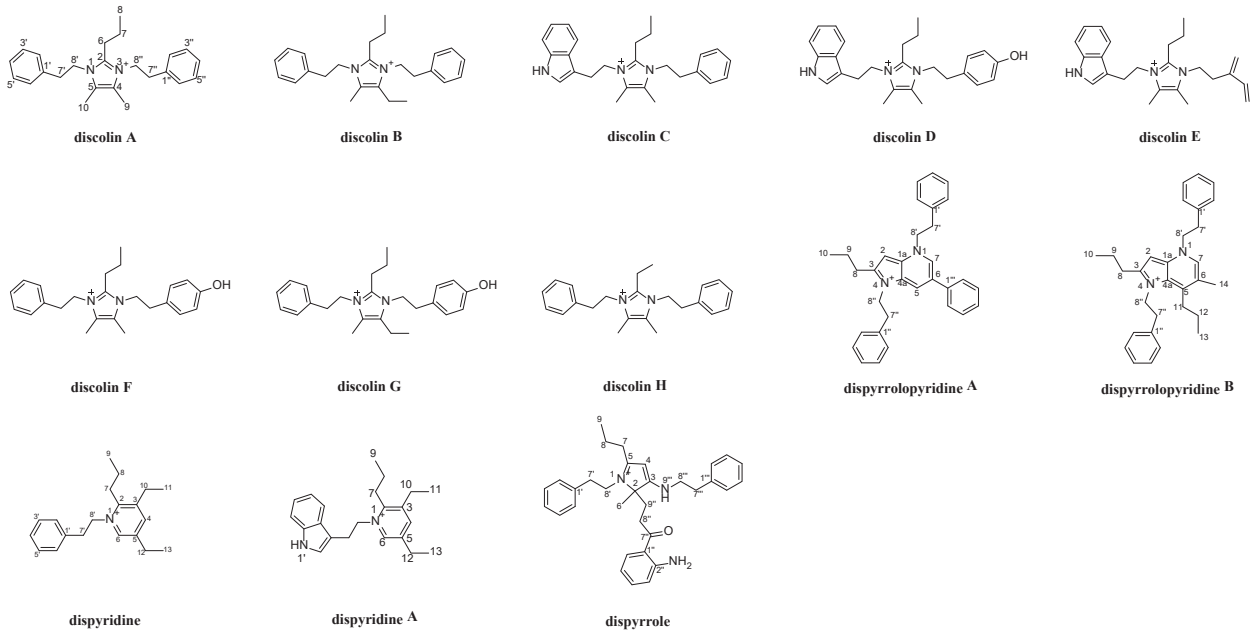

Figure 6A. Compounds isolated from *T. discolor* sv11.

Imidazolium-containing alkaloids are mainly reported as secondary metabolites of some sponges or products of chemical synthesis. Their reported bioactivities are mostly focused on the cytotoxic activity. Eight alkaloids with the same imidazole nucleus were obtained from our project, of which, the aromatic diamine (*i.e.* phenethylamine, tryptamine and tyramine) located at position 1 and 3 of the central imidazolium ring are different with each other, and the length of the carbon chains linked to position 2 and 4 are also different. These structural differences result indifferent bioactivities: discolins A–C and H exhibited stronger inhibitory activity against the tested Gram-positive bacteria than the discolins D-G. These structural differences and changes in the bioactivity give us some insights into the structure-activity relationship of the discolins: the length of the carbon chain at position 2 can be altered without affecting the activity, while the substructures at position 1 and 3 of the central ring instead play an important role concerning antibacterial activity. Comparable evidence of some chemical synthesized imidazolium salts indicated that their

bioactivity is highly dependent upon the substituents on the nitrogen atoms of the imidazolium cation, which is in agreement with our observation.

Despite that an antimicrobial, antifungal, and nematicidal activity could be assigned to aromatic diamine-containing alkaloids, their real ecological role in the marine ecosystems is still unknown. Further studies, for instance, associating the expression of DisA homologues with several environmental conditions using transcriptomics or metabolomics, could provide additional insights about the ecological role of these natural products.

A novel sub group of cyclic lipopeptides was identified from *Pseudomonas brassicacearum* Root401

Pseudomonas brassicacearum Root401 was previously shown to be detrimental in mono-association experiment with *Arabidopsis thaliana* in an agar-based gnotobiotic system (Ma et al., 2021). This strain was also recently shown to produce exometabolites which can inhibit its bacterial competitors at bay and promote strain colonization success in roots (Getzke et al., 2023). Getzke's work indicated that *P. brassicacearum* Root401 is non-pathogenic on plants grown in natural or gnotobiotic peat-based soil systems and that NaCl treatment promotes *P. brassicacearum* Root401 disease symptoms in these soil-grown plants, providing evidence for environmental conditions that conditionally promote plant disease. Sequencing of the A. thaliana root and shoot transcriptomes reveals a root-specific response to combinatorial treatment of *P. brassicacearum* Root401 and NaCl that associate with disease emergence. In *P. brassicacearum* Root401, we identified a homologous biosynthetic gene cluster (BGC) to the syp-syr BGC that is responsible for syringopeptin biosynthesis in *P. syringae* B728a (Feil et al., 2005). Using targeted

mutagenesis, we demonstrate that this locus is sufficient to transition *P. brassicacearum* Root401 from being beneficial to being detrimental on salt-treated plants. Subsequently, a mass spectrometry–guided isolation lead to the discovery of Brassicapeptins A to D, four new cyclic lipopeptides from the culture broth of *P. brassicacearum* Root401. Their structures were determined using mass spectrometry including HR-ESI-MS and HR-ESI-MS/MS, 1D and 2D NMR data and Marfey's analysis. The isolated brassicapaptins represent a novel sub group of cyclic lipopeptides, with notable structural differences including a different fatty acid starter unit and a smaller ring structure that is formed intramolecularly between the six C-terminal amino acid residues, comparison to the previously described syringopeptins which are also produced by *Pseudomonas* strains (Grgurina et al., 2005; Grgurina et al., 2002; Isogai et al., 1995) (**Figure 6B**).

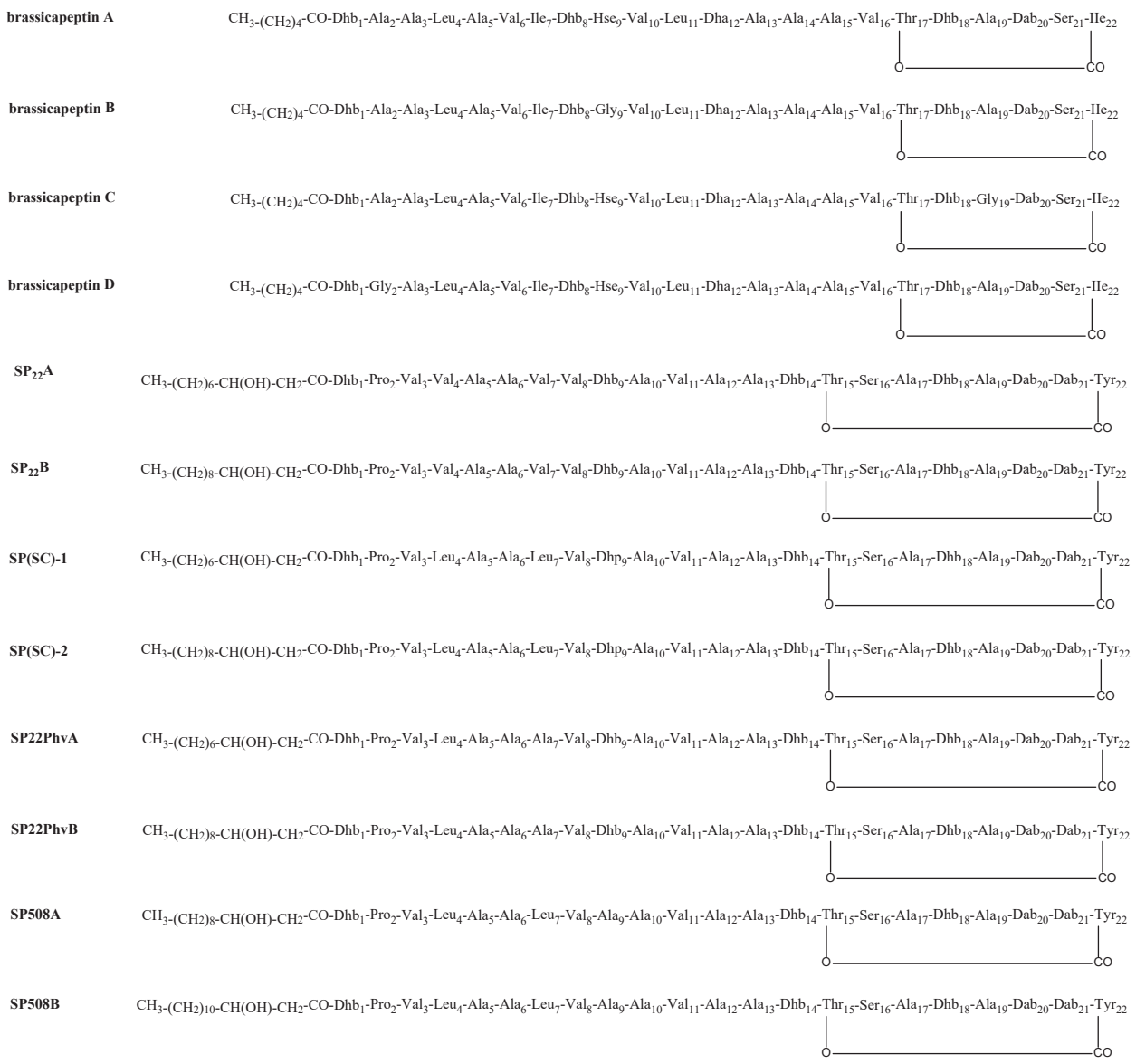

Figure 6B. Structural comparison between *P. brassicacearum* Root401 brassicapeptins and previously identified syringopeptins.

Chromone derivatives is a widespread characteristic within the fungi *Palmiascoma qujingense* ST006189

The genus *Palmiascoma* was first introduced by Liu et al. in 2015 (Liu et al., 2015). A species of this genus, i.e. *P. qujingense*, was reported as a pathogenic fungi, which can cause branch blight on *Juglans regia* (Wang et al., 2022). Until now, there is no report about natural products produced by this genus. In the present work (Chapter 5), we investigated the potential of *P. qujingense* ST006189 for the production of structurally diverse chromone derivatives. An OSMAC approach revealed that a high yield of chromone derivatives was observed in the extract after 26 days fermentation in Medium 5367A. Subsequently, a mass spectrometry–guided isolation resulted in the discovery of four new monomeric chromone derivatives and three new dimeric chromone derivatives, together with 2 known monomeric chromone derivatives and one polyketide derivative (**Figure 6C**).

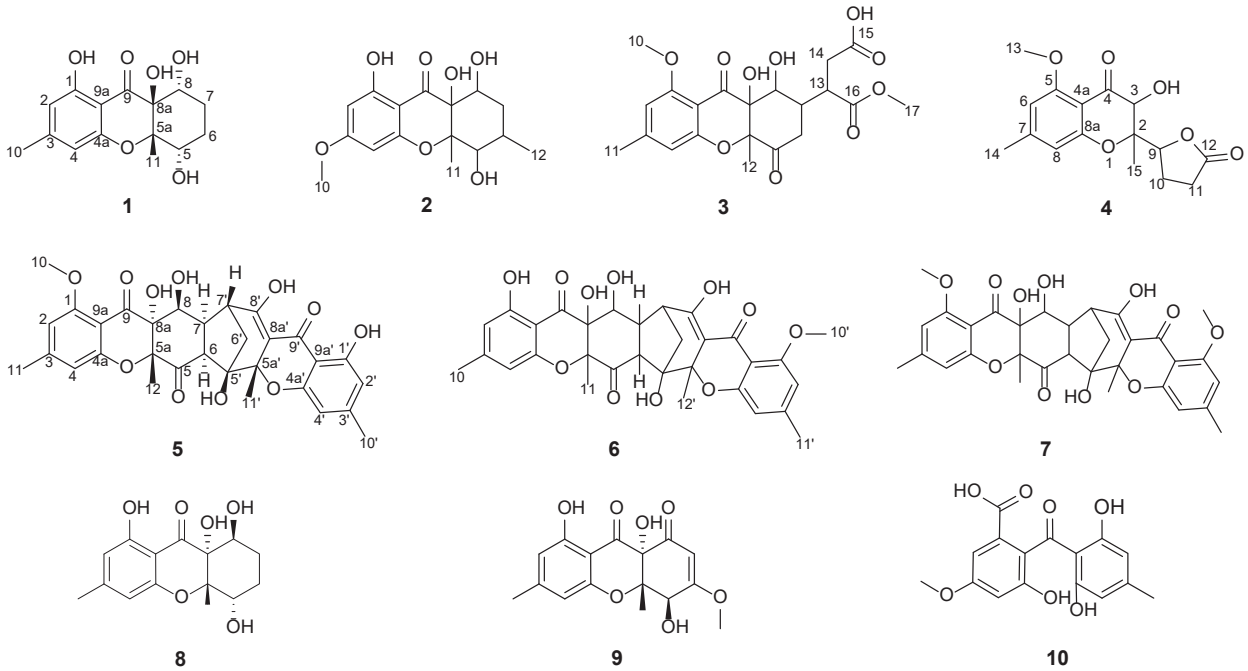

Figure 6C. Compounds isolated from *P. qujingense* ST006189.

In summary, 23 novel metabolites were obtained using a traditional bioactivity-guided (Chapter 2) and mass spectrometry-guided strategy (belongs to chemical signature-guided strategy, Chapter 3 and 5). A novel sub group of cyclic lipopeptides, i.e. brassicapeptins, was discovered, using a combination of mass spectrometry-guided strategy and genome-guided strategy from a strain of the genus *Pseudomonas*, which has been well researched (Chapter 4). Undoubtedly, traditional strategies continued to provide lead compounds for the discovery of novel natural products from microorganisms, which have not yet been fully researched. These include for example *T. discolor* sv11 (Chapter 2 and 3) and *P. qujingense* ST006189 (Chapter 2), since not much was known about natural products produced by these microorganisms when we start our research. On the other hand, the limitations of conventional strategies may be addressed by modern genomics-based discovery approaches.

References

Achan, J., Talisuna, A. O., Erhart, A., Yeka, A., Tibenderana, J. K., Baliraine, F. N., Rosenthal, P. J., & D'Alessandro, U. (**2011**). Quinine, an old anti-malarial drug in a modern world: role in the treatment of malaria. *Malaria journal,* 10, 1-12.

Akinpelu, O. I., Lawal, M. M., Kumalo, H. M., & Mhlongo, N. N. (**2020**). Drug repurposing: Fusidic acid as a potential inhibitor of M. tuberculosis FtsZ polymerization–Insight from DFT calculations, molecular docking and molecular dynamics simulations. *Tuberculosis,* 121, 101920.

Artsimovitch, I., Seddon, J., & Sears, P. (**2012**). Fidaxomicin is an inhibitor of the initiation of bacterial RNA synthesis. *Clinical infectious diseases,* 55, S127-S131.

Atanasov, A. G., Waltenberger, B., Pferschy-Wenzig, E.-M., Linder, T., Wawrosch, C., Uhrin, P., Temml, V., Wang, L., Schwaiger, S., & Heiss, E. H. (**2015**). Discovery and resupply of pharmacologically active plant-derived natural products: A review. *Biotechnology advances,* 33, 1582-1614.

Atanasov, A. G., Zotchev, S. B., Dirsch, V. M., & Supuran, C. T. (**2021**). Natural products in drug discovery: advances and opportunities. *Nature reviews Drug discovery,* 20, 200-216.

Badros, A., Singh, Z., Dhakal, B., Kwok, Y., MacLaren, A., Richardson, P., Trikha, M., & Hari, P. (**2017**). Marizomib for central nervous system ‐ multiple myeloma. *British Journal of Haematology,* 177, 221-225.

Bar-On, Y. M., Phillips, R., & Milo, R. (**2018**). The biomass distribution on Earth. *Proceedings of the National Academy of Sciences,* 115, 6506-6511.

Bills, G. F., & Gloer, J. B. (**2016**). Biologically Active Secondary Metabolites from the Fungi. *Microbiol Spectr,* 4.

Black, W., & Mcnellis, D. A. (**1971**). Comparative in-vitro sensitivity of Nocardia species to fusidic acid and sulphonamides. *Journal of Medical Microbiology,* 4, 293-295.

Blowey, D. L. (**2016**). Diuretics in the treatment of hypertension. *Pediatric nephrology,* 31, 2223-2233.

Bonamonte, D., Belloni Fortina, A., Neri, L., & Patrizi, A. (**2014**). Fusidic acid in skin infections and infected atopic eczema. *G Ital Dermatol Venereol,* 149, 453-459.

Borel, J., Kis, Z., & Beveridge, T. (**1995**). The history of the discovery and development of cyclosporine (Sandimmune®). *The search for anti-inflammatory drugs: Case histories from concept to clinic*, 27-63.

Bota, D. A., Mason, W., Kesari, S., Magge, R., Winograd, B., Elias, I., Reich, S. D., Levin, N., Trikha, M., & Desjardins, A. (**2021**). Marizomib alone or in combination with bevacizumab in patients with recurrent glioblastoma: Phase I/II clinical trial data. *Neuro-oncology advances,* 3, vdab142.

Bradner, W. (**2001**). Mitomycin C: a clinical update. *Cancer treatment reviews,* 27, 35-50.

Brinkmann, V., Billich, A., Baumruker, T., Heining, P., Schmouder, R., Francis, G., Aradhye, S., & Burtin, P. (**2010**). Fingolimod (FTY720): discovery and development of an oral drug to treat multiple sclerosis. *Nature reviews Drug discovery,* 9, 883-897.

Burgos, R. M., & Rodvold, K. A. (**2019**). Omadacycline: A novel aminomethylcycline. *Infection and Drug Resistance,* 12, 1895.

Canzi, A. M., Weber, P., & Boussougant, Y. (**1987**). [Activity of fusidic acid on strictly anaerobic bacteria]. *Pathol Biol (Paris),* 35, 577-580.

Capdevila, J., Ducreux, M., Carbonero, R. G., Grande, E., Halfdanarson, T., Pavel, M., Tafuto, S., Welin, S., Valentí, V., & Salazar, R. (**2022**). STREPTOZOTOCIN. 1982-2022: FORTY YEARS FROM THE FDA'S APPROVAL TO TREAT PANCREATIC NEUROENDOCRINE TUMORS. *Neuroendocrinology*.

Cephalotaxus Research Coordinating Group. (**1976**). Cephalotaxine esters in the treatment of acute leukemia: A preliminary clinical assessment. *Chinese Medical Journal,* 2, 263-272.

Charan, R. D., Schlingmann, G., Janso, J., Bernan, V., Feng, X., & Carter, G. T. (**2004**). Diazepinomicin, a new antimicrobial alkaloid from a marine Micromonospora sp. *Journal of natural products,* 67, 1431-1433.

Chen, Y., Lear, T. B., Evankovich, J. W., Larsen, M. B., Lin, B., Alfaras, I., Kennerdell, J. R., Salminen, L., Camarco, D. P., & Lockwood, K. C. (**2021**). A high-throughput screen for TMPRSS2 expression identifies FDA-approved compounds that can limit SARS-CoV-2 entry. *Nature communications,* 12, 1-15.

Chopra, I., & Roberts, M. (**2001**). Tetracycline antibiotics: mode of action, applications, molecular biology, and epidemiology of bacterial resistance. *Microbiology and molecular biology reviews,* 65, 232-260.

Cohen, D. J., Loertscher, R., Rubin, M. F., Tilney, N. L., Carpenter, C. B., & Strom, T. B. (**1984**). Cyclosporine: a new immunosuppressive agent for organ transplantation. *Annals of internal medicine,* 101, 667-682.

Collignon, P., & Turnidge, J. (**1999**). Fusidic acid in vitro activity. *International journal of antimicrobial agents,* 12, S45-S58.

Colombo, N., Kutarska, E., Dimopoulos, M., Bae, D.-S., Rzepka-Gorska, I., Bidzinski, M., Scambia, G., Engelholm, S. A., Joly, F., & Weber, D. (**2012**). Randomized, open-label, phase III study comparing patupilone (EPO906) with pegylated liposomal doxorubicin in platinum-refractory or-resistant patients with recurrent epithelial ovarian, primary fallopian tube, or primary peritoneal cancer. *Journal of Clinical Oncology,* 30, 3841-3847.

Conlin, A., Fornier, M., Hudis, C., Kar, S., & Kirkpatrick, P. (**2007**). Ixabepilone. *Nature reviews Drug discovery,* 6, 953-955.

Costa, M., Bernardi, J., Fiuza, T., Costa, L., Brandão, R., & Pereira, M. E. (**2016**). N-acetylcysteine protects memory decline induced by streptozotocin in mice. *Chemico-biological interactions,* 253, 10-17.

Cragg, G. M., & Newman, D. J. (**2013**). Natural products: a continuing source of novel drug leads. *Biochimica et Biophysica Acta (BBA)-General Subjects,* 1830, 3670-3695.

Crits-Christoph, A., Diamond, S., Butterfield, C. N., Thomas, B. C., & Banfield, J. F. (**2018**). Novel soil bacteria possess diverse genes for secondary metabolite biosynthesis. *Nature,* 558, 440-444.

Daniel, R. (**2004**). The soil metagenome–a rich resource for the discovery of novel natural products. *Current opinion in biotechnology,* 15, 199-204.

Davies, J., & Davies, D. (**2010**). Origins and evolution of antibiotic resistance. *Microbiology and molecular biology reviews,* 74, 417-433.

Debono, M., Abbott, B. J., Molloy, R. M., Fukuda, D. S., HUNT, A. H., Daupert, V. M., Counter, F. T., Ott, J. L., Carrell, C. B., & Howard, L. C. (**1988**). ENZYMATIC AND CHEMICAL MODIFICATIONS OF IPOPEPTIDE ANTIBIOTIC A21978C: THE SYNTHESIS AND EVALUATION OF DAPTOMYCIN (LY146032). *The Journal of antibiotics,* 41, 1093-1105.

Du, X., Liu, D., Huang, J., Zhang, C., Proksch, P., & Lin, W. (**2018**). Polyketide derivatives from the sponge associated fungus Aspergillus europaeus with antioxidant and NO inhibitory activities. *Fitoterapia,* 130, 190-197.

Ebenezer, O., Jordaan, M. A., Carena, G., Bono, T., Shapi, M., & Tuszynski, J. A. (**2022**). An Overview of the Biological Evaluation of Selected Nitrogen-Containing Heterocycle Medicinal Chemistry Compounds. *International journal of molecular sciences,* 23, 8117.

Eliopoulos, G. M., Willey, S., Reiszner, E., Spitzer, P., Caputo, G., & Moellering Jr, R. (**1986**). In vitro and in vivo activity of LY 146032, a new cyclic lipopeptide antibiotic. *Antimicrobial agents and chemotherapy,* 30, 532-535.

Feil, H., Feil, W. S., Chain, P., Larimer, F., DiBartolo, G., Copeland, A., Lykidis, A., Trong, S., Nolan, M., & Goltsman, E. (**2005**). Comparison of the complete genome sequences of Pseudomonas syringae pv. syringae B728a and pv. tomato DC3000. *Proceedings of the National Academy of Sciences,* 102, 11064-11069.

Feling, R. H., Buchanan, G. O., Mincer, T. J., Kauffman, C. A., Jensen, P. R., & Fenical, W. (**2003**). Salinosporamide A: a highly cytotoxic proteasome inhibitor from a novel microbial source, a marine bacterium of the new genus Salinospora. *Angewandte Chemie International Edition,* 42, 355-357.

Fleming, A. (**1929**). On the Antibacterial Action of Cultures of a Penicillium, with Special Reference to their Use in the Isolation of B. influenzæ. *British Journal of Experimental Pathology,* 10, 226–236.

Furman, B. L. (**2015**). Streptozotocin‐induced diabetic models in mice and rats. *Current protocols in pharmacology,* 70, 5.47. 41-45.47. 20.

Gamal, A., Chu, S., McCormick, T. S., Borroto-Esoda, K., Angulo, D., & Ghannoum, M. A. (**2021**). Ibrexafungerp, a Novel Oral Triterpenoid Antifungal in Development: Overview of Antifungal Activity Against Candida glabrata. *Front Cell Infect Microbiol,* 11, 642358.

Geers, A. U., Buijs, Y., Strube, M. L., Gram, L., & Bentzon-Tilia, M. (**2021**). The natural product biosynthesis potential of the microbiomes of Earth-bioprospecting for novel anti-microbial agents in the meta-omics era. *Computational and structural biotechnology journal*.

Getzke, F., Hassani, M. A., Crüsemann, M., Malisic, M., Zhang, P., Ishigaki, Y., Böhringer, N., Jiménez Fernández, A., Wang, L., & Ordon, J. (**2023**). Cofunctioning of bacterial

exometabolites drives root microbiota establishment. *Proceedings of the National Academy of Sciences,* 120, e2221508120.

Godtfredsen, W., Jahnsen, S., Lorck, H., Roholt, K., & Tybring, L. (**1962**). Fusidic acid: a new antibiotic. *Nature,* 193, 987-987.

Goldstein, E. J., Babakhani, F., & Citron, D. M. (**2012**). Antimicrobial activities of fidaxomicin. *Clinical infectious diseases,* 55, S143-S148.

Gomes, N., Valentao, P., Andrade, P., & Pereira, R. (**2020**). Plitidepsin to treat multiple myeloma. *Drugs of Today (Barcelona, Spain: 1998),* 56, 337-347.

Grgurina, I., Bensaci, M., Pocsfalvi, G., Mannina, L., Cruciani, O., Fiore, A., Fogliano, V., Sorensen, K. N., & Takemoto, J. Y. (**2005**). Novel cyclic lipodepsipeptide from Pseudomonas syringae pv. lachrymans strain 508 and syringopeptin antimicrobial activities. *Antimicrobial agents and chemotherapy,* 49, 5037-5045.

Grgurina, I., Mariotti, F., Fogliano, V., Gallo, M., Scaloni, A., Iacobellis, N. S., Cantore, P. L., Mannina, L., van Axel Castelli, V., & Greco, M. L. (**2002**). A new syringopeptin produced by bean strains of Pseudomonas syringae pv. syringae. *Biochimica et Biophysica Acta (BBA)-Protein Structure and Molecular Enzymology,* 1597, 81-89.

Grove, J. F., MacMillan, J., Mulholland, T., & Rogers, M. T. (**1952**). 762. Griseofulvin. Part IV. Structure. *Journal of the Chemical Society (Resumed)*, 3977-3987.

Gull, K., & Trinci, A. (**1973**). Griseofulvin inhibits fungal mitosis. *Nature,* 244, 292-294.

Harvey, A. L., Edrada-Ebel, R., & Quinn, R. J. (**2015**). The re-emergence of natural products for drug discovery in the genomics era. *Nature reviews Drug discovery,* 14, 111-129.

Henary, M., Kananda, C., Rotolo, L., Savino, B., Owens, E. A., & Cravotto, G. (**2020**). Benefits and applications of microwave-assisted synthesis of nitrogen containing heterocycles in medicinal chemistry. *RSC advances,* 10, 14170-14197.

Herman, L. L., & Bashir, K. (**2021**). Hydrochlorothiazide. In *StatPearls [Internet]*: StatPearls Publishing.

Hochlowski, J., Swanson, S., Ranfranz, L., Whittern, D., Buko, A., & McAlpine, J. (**1987**). Tiacumicins, a novel complex of 18-membered macrolides II. Isolation and structure determination. *The Journal of antibiotics,* 40, 575-588.

Hou, C., & Zhang, Z. (**1981**). Intrathecal injection of harringtonine and homoharringtonine in treating central nervous system leukemia--clinical analysis of 26 cases (author's transl). *Zhonghua yi xue za zhi,* 61, 530-532.

Hübschle, C. B., Sheldrick, G. M., & Dittrich, B. (**2011**). ShelXle: a Qt graphical user interface for SHELXL. *Journal of applied crystallography,* 44, 1281-1284.

Hutchings, M. I., Truman, A. W., & Wilkinson, B. (**2019**). Antibiotics: past, present and future. *Current opinion in microbiology,* 51, 72-80.

Ibrahim, N. K. (**2021**). Ixabepilone: Overview of Effectiveness, Safety, and Tolerability in Metastatic Breast Cancer. *Frontiers in Oncology,* 11, 2549.

Illingworth, D. R. (**1994**). Therapeutic use of lovastatin in the treatment of hypercholesterolemia. *Clinical therapeutics,* 16, 2-26; discussion 21.

Isogai, A., Iguchi, H., Nakayama, J., Kusai, A., Takemoto, J. Y., & Suzuki, A. (**1995**). Structural analysis of new syringopeptins by tandem mass spectrometry. *Bioscience, biotechnology, and biochemistry,* 59, 1374-1376.

Jevitt, L. A., Smith, A. J., Williams, P. P., Raney, P. M., McGowan Jr, J. E., & Tenover, F. C. (**2003**). In vitro activities of daptomycin, linezolid, and quinupristin-dalfopristin against a challenge panel of staphylococci and enterococci, including vancomycin-intermediate Staphylococcus aureus and vancomycin-resistant Enterococcus faecium. *Microbial Drug Resistance,* 9, 389-393.

Jin, H., Yamashita, A., Maekawa, S., Yang, P., He, L., Takayanagi, S., Wakita, T., Sakamoto, N., Enomoto, N., & Ito, M. (**2008**). Griseofulvin, an oral antifungal agent, suppresses hepatitis C virus replication in vitro. *Hepatology Research,* 38, 909-918.

Jin, Z. (**2016**). Muscarine, imidazole, oxazole and thiazole alkaloids. *Natural product reports,* 33, 1268-1317.

Joule, J. A. (**2016**). Natural products containing nitrogen heterocycles—some highlights 1990–2015. *Advances in Heterocyclic Chemistry,* 119, 81-106.

Jungnickel, P., Cantral, K., & Maloley, P. (**1992**). Pravastatin: a new drug for the treatment of hypercholesterolemia. *Clinical pharmacy,* 11, 677-689.

Katz, L., & Baltz, R. H. (**2016**). Natural product discovery: past, present, and future. *Journal of Industrial Microbiology and Biotechnology,* 43, 155-176.

Kawamori, R., Tajima, N., Iwamoto, Y., Kashiwagi, A., Shimamoto, K., Kaku, K., & Group, V. P.-S. (**2009**). Voglibose for prevention of type 2 diabetes mellitus: a randomised, double-blind trial in Japanese individuals with impaired glucose tolerance. *The Lancet,* 373, 1607-1614.

Kerru, N., Gummidi, L., Maddila, S., Gangu, K. K., & Jonnalagadda, S. B. (**2020**). A review on recent advances in nitrogen-containing molecules and their biological applications. *Molecules,* 25, 1909.

Koehn, F. E., & Carter, G. T. (**2005**). The evolving role of natural products in drug discovery. *Nature reviews Drug discovery,* 4, 206-220.

Kuhnert, E., Li, Y., Lan, N., Yue, Q., Chen, L., Cox, R. J., An, Z., Yokoyama, K., & Bills, G. F. (**2018**). Enfumafungin synthase represents a novel lineage of fungal triterpene cyclases. *Environ Microbiol,* 20, 3325-3342.

Lamb, Y. (**1991**). Overview of the role of mupirocin. *Journal of Hospital Infection,* 19, 27-30.

Landh, E., Wang, R., Moir, L. M., Traini, D., Young, P. M., & Ong, H. X. (**2022**). Prospective nanoparticle treatments for lymphangioleiomyomatosis. *Expert Opinion on Drug Delivery,* 19, 75-86.

Laube, H. (**2002**). Acarbose. *Clinical drug investigation,* 22, 141-156.

Lee, A. (**2021**). Ibrexafungerp: first approval. *Drugs,* 81, 1445-1450.

Lima, L. M., da Silva, B. N. M., Barbosa, G., & Barreiro, E. J. (**2020**). β-lactam antibiotics: An overview from a medicinal chemistry perspective. *European Journal of Medicinal Chemistry,* 208, 112829.

Ling, L. L., Schneider, T., Peoples, A. J., Spoering, A. L., Engels, I., Conlon, B. P., Mueller, A., Schäberle, T. F., Hughes, D. E., & Epstein, S. (**2015**). A new antibiotic kills pathogens without detectable resistance. *Nature,* 517, 455-459.

Liu, J., Mi, Y., Fu, M., Yu, W., Wang, Y., Lin, D., Bian, S., & Wang, J. (**2009**). Intensive induction chemotherapy with regimen containing intermediate dose cytarabine in the treatment of de novo acute myeloid leukemia. *American journal of hematology,* 84, 422-427.

Liu, J. K., Hyde, K. D., Jones, E. G., Ariyawansa, H. A., Bhat, D. J., Boonmee, S., Maharachchikumbura, S. S., McKenzie, E. H., Phookamsak, R., & Phukhamsakda, C. (**2015**). Fungal diversity notes 1–110: taxonomic and phylogenetic contributions to fungal species. *Fungal diversity,* 72, 1-197.

Liu, S., Moon, C. D., Zheng, N., Huws, S., Zhao, S., & Wang, J. (**2022**). Opportunities and challenges of using metagenomic data to bring uncultured microbes into cultivation. *Microbiome,* 10, 76.

Long, B. H. (**2008**). Fusidic acid in skin and soft-tissue infections. *Acta Dermato-Venereologica,* 88, 14-20.

Losada, A., Muñoz-Alonso, M. J., García, C., Sánchez-Murcia, P. A., Martínez-Leal, J. F., Domínguez, J. M., Lillo, M. P., Gago, F., & Galmarini, C. M. (**2016**). Translation elongation factor eEF1A2 is a novel anticancer target for the marine natural product plitidepsin. *Scientific reports,* 6, 1-15.

Lu, L.-h., Lin, S.-p., Liang, Y.-y., Song, T.-y., & Li, L.-y. (**1983**). Harringtonine in treatment of polycythemia vera. *Chinese Medical Journal,* 96, 533-535.

Ma, K.-W., Niu, Y., Jia, Y., Ordon, J., Copeland, C., Emonet, A., Geldner, N., Guan, R., Stolze, S. C., & Nakagami, H. (**2021**). Coordination of microbe–host homeostasis by crosstalk with plant innate immunity. *Nature Plants,* 7, 814-825.

Maha, A., Phainuphong, P., Rukachaisirikul, V., Saithong, S., Phongpaichit, S., Hadsadee, S., Jungsuttiwong, S., Preedanon, S., & Sakayaroj, J. (**2018**). Blennolide derivatives from the soil-derived fungus Trichoderma asperellum PSU-PSF14. *Tetrahedron,* 74, 5659-5664.

Mahalati, K., & Kahan, B. D. (**2001**). Clinical pharmacokinetics of sirolimus. *Clinical pharmacokinetics,* 40, 573-585.

Mason, W., Belanger, K., Nicholas, G., Vallieres, I., Mathieu, D., Desjardins, A., Kavan, P., Omuro, A., & Reymond, D. (**2010**). A phase II trial of TLN-4601 in patients with glioblastoma multiforme (GBM) at first progression. *Journal of Clinical Oncology,* 28, 2094-2094.

Miethke, M., Pieroni, M., Weber, T., Brönstrup, M., Hammann, P., Halby, L., Arimondo, P. B., Glaser, P., Aigle, B., & Bode, H. B. (**2021**). Towards the sustainable discovery and development of new antibiotics. *Nature Reviews Chemistry,* 5, 726-749.

Mir, L., Tounekti, O., & Orlowski, S. (**1996**). Bleomycin: revival of an old drug. *General Pharmacology: The Vascular System,* 27, 745-748.

Miwa, N., Kurosaki, K., Yoshida, Y., Kurokawa, M., Saito, S., & Shiraki, K. (**2005**). Comparative efficacy of acyclovir and vidarabine on the replication of varicella-zoster virus. *Antiviral research,* 65, 49-55.

Mohsin, N. u. A., Irfan, M., Hassan, S. u., & Saleem, U. (**2020**). Current strategies in development of new chromone derivatives with diversified pharmacological activities: a review. *Pharmaceutical chemistry journal,* 54, 241-257.

Muszalska, I., Sobczak, A., Dołhań, A., & Jelińska, A. (**2014**). Analysis of sartans: a review. *Journal of pharmaceutical Sciences,* 103, 2-28.

Newman, D. J. (**2019**). From natural products to drugs. *Physical Sciences Reviews,* 4, DOI: 10.1515/psr-2018-0111.

Newman, D. J., & Cragg, G. M. (**2020**). Natural products as sources of new drugs over the nearly four decades from 01/1981 to 09/2019. *Journal of natural products,* 83, 770-803.

Pankey, G. A. (**2005**). Tigecycline. *Journal of antimicrobial Chemotherapy,* 56, 470-480.

Paoli, L., Ruscheweyh, H.-J., Forneris, C. C., Hubrich, F., Kautsar, S., Bhushan, A., Lotti, A., Clayssen, Q., Salazar, G., & Milanese, A. (**2022**). Biosynthetic potential of the global ocean microbiome. *Nature,* 607, 111-118.

Peláez, F., Cabello, A., Platas, G., Díez, M. T., González del Val, A., Basilio, A., Martán, I., Vicente, F., Bills, G. E., Giacobbe, R. A., Schwartz, R. E., Onish, J. C., Meinz, M. S., Abruzzo, G. K., Flattery, A. M., Kong, L., & Kurtz, M. B. (**2000**). The discovery of enfumafungin, a novel antifungal compound produced by an endophytic Hormonema species biological activity and taxonomy of the producing organisms. *Syst Appl Microbiol,* 23, 333-343.

Phillips, N. A., Rocktashel, M., & Merjanian, L. (**2023**). Ibrexafungerp for the Treatment of Vulvovaginal Candidiasis: Design, Development and Place in Therapy. *Drug Design, Development and Therapy*, 363-367.

Rebacz, B., Larsen, T. O., Clausen, M. H., Rønnest, M. H., Löffler, H., Ho, A. D., & Krämer, A. (**2007**). Identification of griseofulvin as an inhibitor of centrosomal clustering in a phenotype-based screen. *Cancer research,* 67, 6342-6350.

Reis, J., Gaspar, A., Milhazes, N., & Borges, F. (**2017**). Chromone as a privileged scaffold in drug discovery: recent advances: miniperspective. *Journal of medicinal chemistry,* 60, 7941-7957.

Robak, T., Korycka, A., Kasznicki, M., Wrzesien-Kus, A., & Smolewski, P. (**2005**). Purine nucleoside analogues for the treatment of hematological malignancies: pharmacology and clinical applications. *Current Cancer Drug Targets,* 5, 421-444.

Rossini, A. A., Like, A. A., Chick, W. L., Appel, M. C., & Cahill Jr, G. (**1977**). Studies of streptozotocin-induced insulitis and diabetes. *Proceedings of the National Academy of Sciences,* 74, 2485-2489.

Rossiter, S. E., Fletcher, M. H., & Wuest, W. M. (**2017**). Natural products as platforms to overcome antibiotic resistance. *Chemical reviews,* 117, 12415-12474.

Roth, P., Gorlia, T., Reijneveld, J. C., De Vos, F. Y. F. L., Idbaih, A., Frenel, J.-S., Le Rhun, E., Sepulveda Sánchez, J. M., Perry, J. R., & Masucci, L. (2021). EORTC 1709/CCTG CE. 8: A phase III trial of marizomib in combination with temozolomide-based radiochemotherapy versus temozolomide-based radiochemotherapy alone in patients with newly diagnosed glioblastoma. In: Wolters Kluwer Health.

Rutledge, P. J., & Challis, G. L. (**2015**). Discovery of microbial natural products by activation of silent biosynthetic gene clusters. *Nature reviews microbiology,* 13, 509-523.

Sadorn, K., Saepua, S., Punyain, W., Saortep, W., Choowong, W., Rachtawee, P., & Pittayakhajonwut, P. (**2020**). Chromanones and aryl glucoside analogs from the entomopathogenic fungus Aschersonia confluens BCC53152. *Fitoterapia,* 144, 104606.

Schatz, A., Bugle, E., & Waksman, S. A. (**1944**). Streptomycin, a substance exhibiting antibiotic activity against gram-positive and gram-negative bacteria.∗. *Proceedings of the society for Experimental Biology and Medicine,* 55, 66-69.

Scherlach, K., & Hertweck, C. (**2021**). Mining and unearthing hidden biosynthetic potential. *Nature communications,* 12, 1-12.

Schwartz, R. E., Smith, S. K., Onishi, J. C., Meinz, M., Kurtz, M., Giacobbe, R. A., Wilson, K. E., Liesch, J., Zink, D., & Horn, W. (**2000**). Isolation and structural determination of enfumafungin, a triterpene glycoside antifungal agent that is a specific inhibitor of glucan synthesis. *Journal of the American Chemical Society,* 122, 4882-4886.

Scott, L. J. (**2020**). Siponimod: a review in secondary progressive multiple sclerosis. *CNS drugs,* 34, 1191-1200.

Sekurova, O. N., Schneider, O., & Zotchev, S. B. (**2019**). Novel bioactive natural products from bacteria via bioprospecting, genome mining and metabolic engineering. *Microbial biotechnology,* 12, 828-844.

Sheldrick, G. M. (**2015a**). Crystal structure refinement with SHELXL. *Acta Crystallographica Section C: Structural Chemistry,* 71, 3-8.

Sheldrick, G. M. (**2015b**). SHELXT–Integrated space-group and crystal-structure determination. *Acta Crystallographica Section A: Foundations and Advances,* 71, 3-8.

Shigematsu, N., Ueda, H., Takase, S., Tanaka, H., Yamamoto, K., & TADA, T. (**1994**). FR901228, a novel antitumor bicyclic depsipeptide produced by Chromobacterium violaceum No. 968 II. Structure determination. *The Journal of antibiotics,* 47, 311-314.

Shoichet, B. K. (**2004**). Virtual screening of chemical libraries. *Nature,* 432, 862-865.

Siddiqui, I. N., Zahoor, A., Hussain, H., Ahmed, I., Ahmad, V. U., Padula, D., Draeger, S., Schulz, B., Meier, K., & Steinert, M. (**2011**). Diversonol and blennolide derivatives from the endophytic fungus Microdiplodia sp.: absolute configuration of diversonol. *Journal of natural products,* 74, 365-373.

Silvani, A., Gaviani, P., Fiumani, A., Scaioli, V., Lamperti, E., Eoli, M., Botturi, A., & Salmaggi, A. (**2009**). Systemic sagopilone (ZK-EPO) treatment of patients with recurrent malignant gliomas. *Journal of neuro-oncology,* 95, 61-64.

Singh, S. P., & Sashidhara, K. V. (**2017**). Lipid lowering agents of natural origin: An account of some promising chemotypes. *European Journal of Medicinal Chemistry,* 140, 331-348.

Solecka, J., Zajko, J., Postek, M., & Rajnisz, A. (**2012**). Biologically active secondary metabolites from Actinomycetes. *Open Life Sciences,* 7, 373-390.

Spek, A. L. (**2015**). PLATON SQUEEZE: a tool for the calculation of the disordered solvent contribution to the calculated structure factors. *Acta Crystallographica Section C: Structural Chemistry,* 71, 9-18.

Spek, A. L. (2019). PLATON. A Multipurpose Crystallographic Tool. Utrecht University, The Netherlands. In.

Steenbergen, J. N., Alder, J., Thorne, G. M., & Tally, F. P. (**2005**). Daptomycin: a lipopeptide antibiotic for the treatment of serious Gram-positive infections. *Journal of antimicrobial Chemotherapy,* 55, 283-288.

Thakuria, B., & Lahon, K. (**2013**). The beta lactam antibiotics as an empirical therapy in a developing country: an update on their current status and recommendations to counter the resistance against them. *Journal of clinical and diagnostic research: JCDR,* 7, 1207.

Thomford, N. E., Senthebane, D. A., Rowe, A., Munro, D., Seele, P., Maroyi, A., & Dzobo, K. (**2018**). Natural products for drug discovery in the 21st century: innovations for novel drug discovery. *International journal of molecular sciences,* 19, 1578.

Tribe, H. T. (**1998**). The discovery and development of cyclosporin. *Mycologist,* 12, 20-22.

Tse, E. G., Korsik, M., & Todd, M. H. (**2019**). The past, present and future of anti-malarial medicines. *Malaria journal,* 18, 1-21.

Turner, J., Muraoka, A., Bedenbaugh, M., Childress, B., Pernot, L., Wiencek, M., & Peterson, Y. K. (**2022**). The Chemical Relationship Among Beta-Lactam Antibiotics and Potential Impacts on Reactivity and Decomposition. *Frontiers in microbiology,* 13.

Turnidge, J. (**1999**). Fusidic acid pharmacology, pharmacokinetics and pharmacodynamics. *Int J Antimicrob Agents,* 12 Suppl 2, S23-34.

Ueda, H., Manda, T., Matsumoto, S., Mukumoto, S., Nishigaki, F., Kawamura, I., & Shimomura, K. (**1994**). FR901228, a novel antitumor bicyclic depsipeptide produced by Chromobacterium violaceum No. 968 III. Antitumor activities on experimental tumors in mice. *The Journal of antibiotics,* 47, 315-323.

Ueda, H., Nakajima, H., Hori, Y., Fujita, T., Nishimura, M., Goto, T., & Okuhara, M. (**1994**). FR901228, a novel antitumor bicyclic depsipeptide produced by Chromobacterium violaceum No. 968 I. Taxonomy, fermentation, isolation, physico-chemical and biological properties, and antitumor activity. *The Journal of antibiotics,* 47, 301-310.

Umezawa, H., Ishizuka, M., Maeda, K., & Takeuchi, T. (**1967**). Studies on bleomycin. *Cancer,* 20, 891-895.

Veeresham, C. (**2012**). Natural products derived from plants as a source of drugs. *Journal of advanced pharmaceutical technology & research,* 3, 200.

Venkatesh, P., & Kasi, A. (**2019**). Anthracyclines.

Venugopal, A. A., & Johnson, S. (**2012**). Fidaxomicin: a novel macrocyclic antibiotic approved for treatment of Clostridium difficile infection. *Clinical infectious diseases,* 54, 568-574.

Vezina, C., Kudelski, A., & Sehgal, S. (**1975**). Rapamycin (AY-22, 989), a new antifungal antibiotic I. taxonomy of the producing streptomycete and isolation of the active principle. *The Journal of antibiotics,* 28, 721-726.

Vitaku, E., Smith, D. T., & Njardarson, J. T. (**2014**). Analysis of the structural diversity, substitution patterns, and frequency of nitrogen heterocycles among US FDA approved pharmaceuticals: miniperspective. *Journal of medicinal chemistry,* 57, 10257-10274.

Wagner, A. J., Ravi, V., Riedel, R. F., Ganjoo, K., Van Tine, B. A., Chugh, R., Cranmer, L., Gordon, E. M., Hornick, J. L., & Du, H. (**2021**). nab-Sirolimus for patients with malignant perivascular epithelioid cell tumors. *Journal of Clinical Oncology,* 39, 3660-3670.

Waksman, S. A., & Woodruff, H. B. (**1940**). Bacteriostatic and bactericidal substances produced by a soil Actinomyces. *Proceedings of the society for Experimental Biology and Medicine,* 45, 609-614.

Wang, F., Zeng, Q., Lv, Y., Xu, X., Han, S., Yang, H., Li, S., Lin, T., Yang, H., & Liu, Y. (**2022**). Branch blight of Juglans regia caused by Palmiascoma qujingense in China. *Plant Disease,* 106, 2992.

Wang, Q., Zhang, Y., Wang, M., Tan, Y., Hu, X., He, H., Xiao, C., You, X., Wang, Y., & Gan, M. (**2017**). Neo-actinomycins A and B, natural actinomycins bearing the 5H-oxazolo [4, 5-b] phenoxazine chromophore, from the marine-derived Streptomyces sp. IMB094. *Scientific reports,* 7, 1-8.

Wassner, C., Bradley, N., & Lee, Y. (**2020**). A review and clinical understanding of tenofovir: tenofovir disoproxil fumarate versus tenofovir alafenamide. *Journal of the International Association of Providers of AIDS Care (JIAPAC),* 19, 2325958220919231.

White, K. M., Rosales, R., Yildiz, S., Kehrer, T., Miorin, L., Moreno, E., Jangra, S., Uccellini, M. B., Rathnasinghe, R., & Coughlan, L. (**2021**). Plitidepsin has potent preclinical efficacy against SARS-CoV-2 by targeting the host protein eEF1A. *Science,* 371, 926-931.

Wiemann, P., & Keller, N. P. (**2014**). Strategies for mining fungal natural products. *Journal of Industrial Microbiology and Biotechnology,* 41, 301-313.

Winer, E. S., & DeAngelo, D. J. (**2018**). A review of omacetaxine: a chronic myeloid leukemia treatment resurrected. *Oncology and Therapy,* 6, 9-20.

Wolters, J. E., van Mechelen, R. J., Al Majidi, R., Pinchuk, L., Webers, C. A., Beckers, H. J., & Gorgels, T. G. (**2021**). History, presence, and future of mitomycin C in glaucoma filtration surgery. *Current Opinion in Ophthalmology,* 32, 148-159.

Wu, L., Li, X., Su, J., Chang, C., He, Q., Zhang, X., Xu, L., Song, L., & Pu, Q. (**2009**). Effect of low-dose cytarabine, homoharringtonine and granulocyte colony-stimulating factor priming regimen on patients with advanced myelodysplastic syndrome or acute myeloid leukemia transformed from myelodysplastic syndrome. *Leukemia & lymphoma,* 50, 1461-1467.

Yang, L. P. (**2011**). Romidepsin. *Drugs,* 71, 1469-1480.

Ye, J., Wang, X., Feng, G., Liang, G., & Liu, Z. (**1988**). Small-dose Harringtonine induces complete remission in patients with acute promyelocytic leukemia. *Leukemia,* 2, 427-429.

Zhang, M. M., Qiao, Y., Ang, E. L., & Zhao, H. (**2017**). Using natural products for drug discovery: the impact of the genomics era. *Expert opinion on drug discovery,* 12, 475-487.

Zhang, Z. (**1981**). Clinical analysis of the therapeutic effect of semisynthetic harringtonine in treating 55 cases of nonlymphocytic leukemia (author's transl). *Zhonghua nei ke za zhi,* 20, 667-669.